TESIS DE LA UNIVERSIDAD DE ZARAGOZA

2019

54

Javier Fernández Pato

Performance assessment of Finite Volume methods in transient simulations of hydraulic processes

Departamento

Ciencia y Tecnología de Materiales y Fluidos

Director/es

GARCÍA, REINALDO
GARCÍA NAVARRO, PILAR

ISSN 2254-7606

Prensas de la Universidad
Universidad Zaragoza

ISSN 2254-7606

Universidad Zaragoza
1542

Tesis Doctoral

PERFORMANCE ASSESSMENT OF FINITE VOLUME METHODS IN TRANSIENT SIMULATIONS OF HYDRAULIC PROCESSES

Autor

Javier Fernández Pato

Director/es

GARCÍA, REINALDO
GARCÍA NAVARRO, PILAR

UNIVERSIDAD DE ZARAGOZA

Ciencia y Tecnología de Materiales y Fluidos

2019

Performance assessment of Finite Volume methods in transient simulations of hydraulic processes

A dissertation presented for the degree of Doctor of Philosophy (Industrial Doctorate) by:

Javier Fernández Pato

Supervised by:

Prof. Dr. Pilar García-Navarro (*University of Zaragoza*)
Dr. Reinaldo García (*Hydronia LCC*)

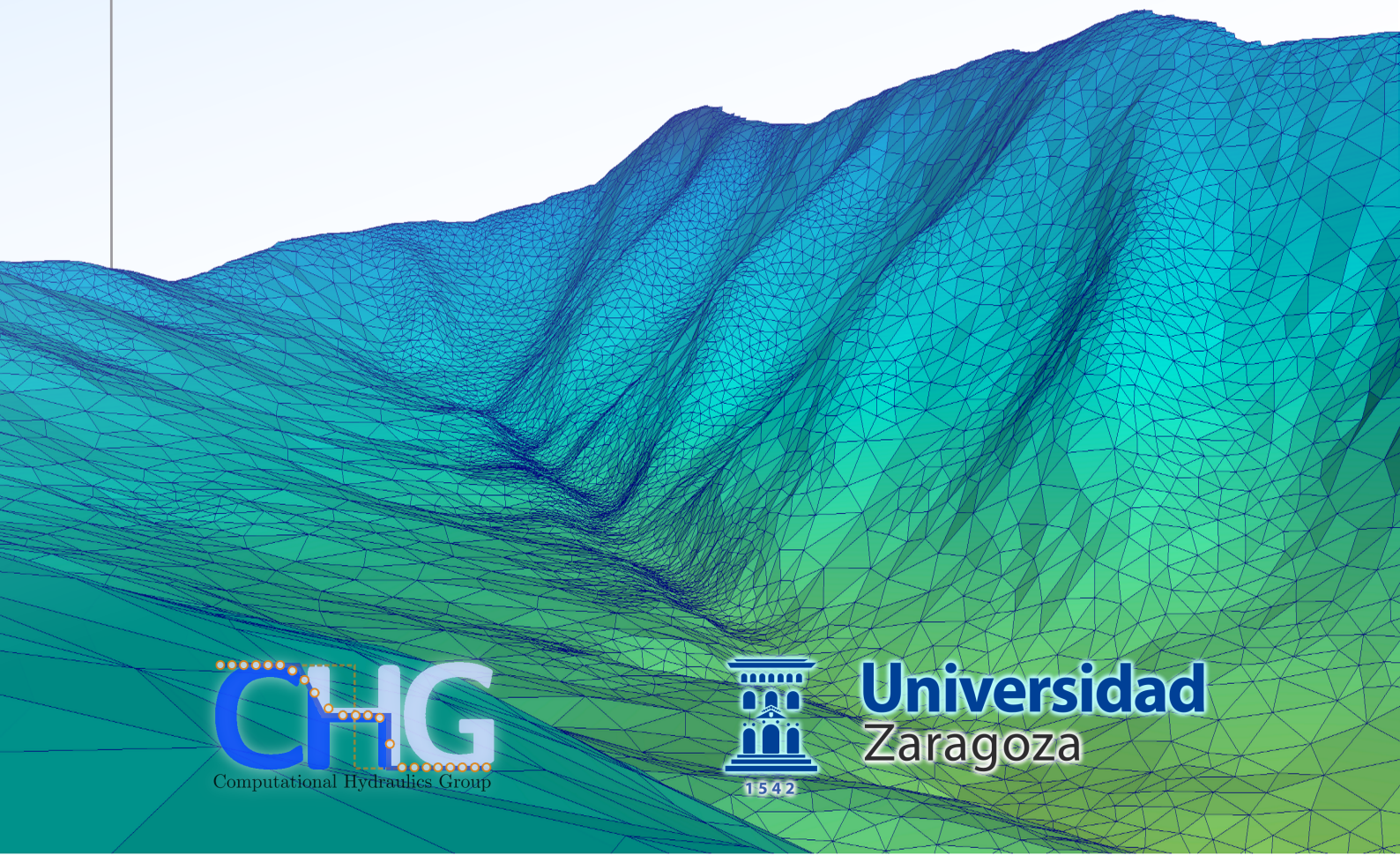

Computational Hydraulics Group

Universidad Zaragoza
1542

Performance assessment of Finite Volume methods in transient simulations of hydraulic processes

Abstract

In this thesis, the development of a hydraulic/hydrological numerical simulation model is presented. It considers the coupling of surface-subsurface flows, paying special attention to the interactions among submodels. The surface flow is formulated by means of 2D Shallow Water flow equations and 2D Zero-Inertia flow model and includes hydrological components as rainfall or infiltration. Both models are discretized using a hybrid implicit-explicit finite volume scheme and a full comparison is carried out in terms of accuracy and efficiency in several synthetic and real world applications. The efficiency of the implicit scheme is evaluated in every test case in order to emphasize it as a feasible acceleration technique for certain situations. When rainfall-runoff simulations are considered, a correct estimation of the infiltration water losses is of crucial relevance. With the aim of improving the Green-Ampt infiltration model, a novel technique based on the fractional calculus is combined with the surface flow models, leading to promising improvements in the numerical results. On the other hand, two subsurface submodels are presented in this work: 1) A 2D vertical-averaged groundwater flow model based on Darcy's law and Dupuit approximation. The coupling between surface and groundwater flows takes place in the border connecting the phreatic level with the soil surface, leading to infiltration/exfiltration processes. 2) A drainage model based on 1D Shallow Water equations capable of simulating transient flows in a pipe which can be locally pressurized. The pipe pressurization is estimated by means of the Preissmann slot method. In this case, the coupling with the surface occurs at local points such as manholes, where the exchange surface-sewer flux is calculated. Both subsurface submodels are tested and validated independently with several analytical and experimental cases. Overall, the synthetic, analytical and experimental test cases presented in this thesis point out the good applicability of each submodel and of both coupled models.

Análisis de la aceleración de cálculo en simulaciones de procesos hidráulicos mediante Volúmenes Finitos

Resumen

En esta tesis se presenta el desarrollo de un modelo numérico para simulaciones hidráulicas/hidrológicas. Se considera el acoplamiento de flujos superficiales y subterráneos, poniendo una atención especial a la interacción ente ambos. El flujo superficial está formulado mediante las ecuaciones de aguas poco profundas en 2D, así como el modelo Cero-Inercia en 2D e incluye componentes hidrológicas como lluvia o infiltración. Ambos modelos son discretizados usando un esquema híbrido implícito-explícito en volúmenes finitos. Así mismo, se realiza una comparación exhaustiva entre ambas discretizaciones temporales en términos de precisión y eficiencia en varias aplicaciones tanto sintéticas como reales. La eficiencia del esquema implícito es evaluada en cada caso test con el propósito de su consideración como posible estrategia de aceleración del cálculo para ciertas situaciones. Cuando se consideran simulaciones en las que interviene la transformación de lluvia en escorrentía, tiene especial relevancia la correcta estimación de las pérdidas de agua por infiltración. Con el propósito de mejorar el actual modelo de infiltración de Green-Ampt, en este trabajo se propone la aplicación de una nueva técnica basada en el cálculo fraccionario, que da lugar a mejoras considerables en los resultados numéricos. Por otro lado, se presentan dos modelos de flujo en el subsuelo: 1) Un modelo 2D de flujo subterráneo en medios porosos basado en la ley de Darcy y la aproximación de Dupuit. El acoplamiento entre la superficie y el subsuelo tiene lugar en la frontera que conecta el nivel freático con la superficie del suelo, lo que da lugar a los procesos de infiltración y exfiltración. 2) Un modelo de drenaje basado en las ecuaciones 1D de aguas poco profundas capaz de simular flujos transitorios en una tubería que pueden llegar a presurizarse localmente. La presurización de la tubería se estima mediante el método de la rendija de Preissmann. En este caso, el acoplamiento con la superficie tiene lugar en localizaciones puntuales como sumideros o alcantarillas, donde se calcula el flujo de intercambio entre modelos. Ambos modelos subsuperficiales son validados de forma independiente mediante varios casos test con solución analítica o datos experimentales. En general, los casos test

sintéticos, con solución analítica o datos experimentales presentados en esta tesis ponen de manifiesto la gran aplicabilidad de cada sub-modelo de forma particular y de ambos modelos acoplados.

Acknowledgements

There are a lot of people who should be thanked. First of all, I want to thank my advisors, Prof. Dr. Pilar García Navarro and Dr. Reinaldo García, who has developed a wonderful guidance across this learning journey. In particular, I would like to thank Pilar for the trust placed in me since my first contact with Computational Fluid Mechanics in the fifth year of Physics degree until the last step of this thesis. The unlimited patience she has shown during these years is also worth mentioning. I must also thank Reinaldo for putting his trust on me and offering me the great opportunity to carry out the development of this thesis within the Hydronia framework.

I must also thank my friends of the Computational Hydraulics Group and Fluid Mechanics area. All of them have contributed in one way or another to make this journey more enriching and interesting. I have learned many things from each one of you.

I would like to thank Dr. Javier Murillo, Dr. Pilar Brufau, Dr. Daniel Caviedes-Voullième, Dr. Mario Morales-Hernández and Dr. José Luis Gracia for providing remarkable and useful insights in this thesis and other collaborative works.

Last but not least, I must thank my family for their support along all these years, for all they have taught to me and for encouraging me to continue studying in every stage of my life. Finally, all my gratitude to Alexia who has lived these years with me and has supported and comprehended me in many ways.

The present thesis has been partially supported by the MINECO (Ministerio de Economía y Competitividad) by means of the Research Grant DI-14-06987. The project has also been partially funded by Hydronia Europe S.L.

Contents

List of Figures

List of Tables

CHAPTER 1

Introduction

The non-linear nature of the fluid mechanics equations generally requires numerical approximations to find the solution of certain problems. Great effort has been put to increase efficiency and accuracy of numerical methods in order to obtain solutions to real-world complex problems in affordable computational times. In particular, Computational Hydraulics has taken great advantage from numerical models in the last decades. [25, 16, 11, 40, 41, 32, 61, 104].

Nowadays, a proper water resources management has to consider a hydrogeological system as an integrated domain where surface water and groundwater interact. Obviouosly, the degree of complexity of the problem increases if several coupled sub-models are involved. A global conceptualization is required in order to couple different physical laws and mathematical models within different sub-domains. Consistent coupling mechanics need to be considered and formulated in order to establish a suitable communication among models.

In this thesis, a coupled surface-subsurface water flow model is considered. Figure 1.1 shows an sketch of the hydraulic/hydrological processes and situations that can be found in natural and man-made domains. By assuming an arbitrary datum from where all the vertical coordinates are referenced, three main frontiers can be

remarked in this scheme: a pervious-impervious interface (z_s), a separation between saturated and unsaturated regions, which is termed phreatic level or phreatic surface (h_s) and the surface bed level (z). Regarding the surface flow, the water depth (h) is always referenced to the bed level (z). From rainfall and natural runoff to the water flow in sewer systems, all the processes are likely to be connected [34, 92, 72]. Hence, the interaction among models should be addressed carefully.

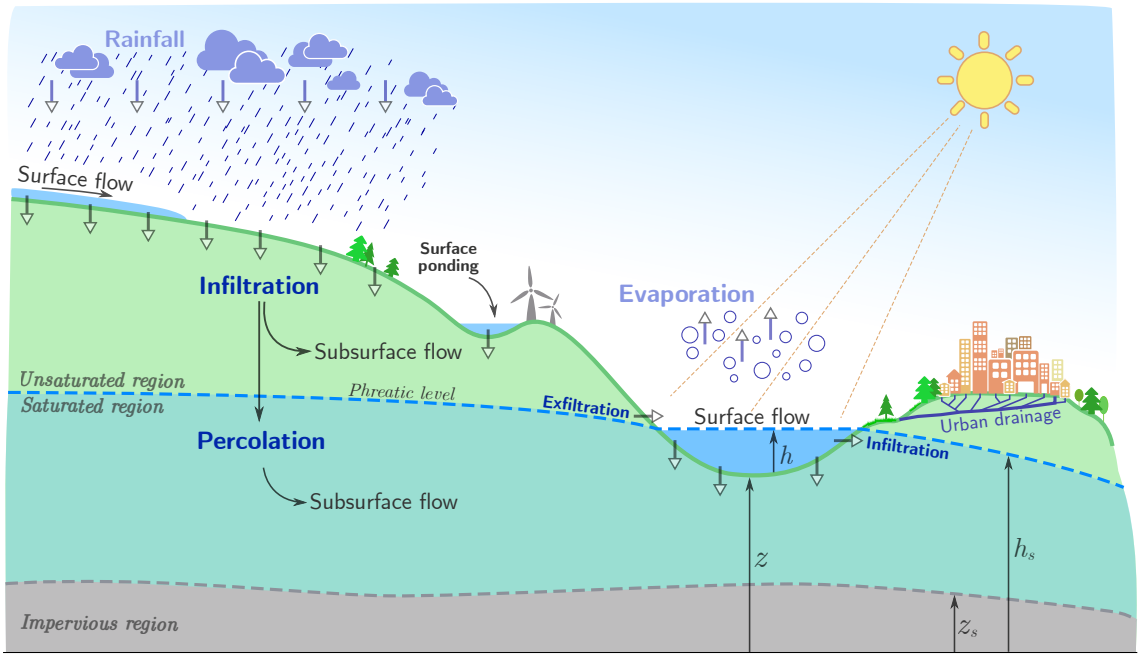

Figure 1.1: Schematic view of all the hydraulic/hydrological processes involved in a real-world situation.

This full environment is conceptualized and simulated by means of several sub-models. On the one hand, surface flow is addressed from two different perspectives of different complexity: 1) 2D Shallow Water equations (SW) [97] and 2) 2D Zero-Inertia model (ZI) [74]. Both models are supplied with mass source/sink terms of rainfall/infiltration, the latter modeled by three empirical laws (Horton [33], Green-Ampt [77, 57, 76] and SCS-CN model [66, 59]). In the last years, fractional-order derivatives have been applied to hydrological modeling [9, 85, 86, 6], water movement in soils [71, 87] and solute transport modeling in both overland [21] and subsurface flows [54, 87], since the classical advection-dispersion equation seems to fail to capture some important solute transport features.

Fractional derivatives, unlike ordinary derivatives, provide an excellent instrument for the description of memory and hereditary complex processes. For this

reason, although fractional calculus dates from XVII century, it has recently become a research area of growing interest due mainly to the ever-widening range of applications in Physics, Engineering, Chemistry, Biology, Economics. A general overview on this research area is provided in [37, 53, 58, 68, 81]. In particular, fractional calculus is a key tool in the study of anomalous diffusion: subdiffusion and superdiffusion processes. These processes are described in detail in the excellent report [58] and the authors focus the discussion on the case that the mean square displacement of the particles growths as a power-law pattern in the course of the time, unlike the Brownian motion.

Regarding the infiltration calculation, a fractional-order Green-Ampt infiltration model, which is a generalization of the classical model, was proposed in the recent literature for a better fitting to experimental data [28, 96]. Namely, in [96], a FOGA model is proposed for predicting the infiltration rates into columns of non-homogeneous soil. This curve can exhibit a non-monotonic behavior, which facilitates the soil infiltration recovery during dry periods. In this thesis, the FOGA model is combined with a distributed 2D surface flow model in order to improve the modelization of the infiltration process in river catchments.

On the other hand, the subsurface is conceptualized by two flow types: 1) A 2D groundwater flow model through which the evolution of the phreatic level is simulated and 2) a 1D drainage model that allows a representation of sewer systems that normally operate under free flow conditions but can be locally pressurized. The first one in based on a Dupuit model of groundwater flow in the form of a 2D Darcy's equation [102] which allows to compute the temporal evolution of the phreatic level in a distributed domain.

Groundwater modeling has become a useful tool in the field of hydrogeology to analyze the response of the groundwater to surface water changes, to evaluate the recharge of aquifers or to predict the soil water quality due to human impacts [108].

The increase of computing power of personal computers along the last decades has made also possible to model large scale ground systems. However, the main issue when dealing with large domains is usually the lack of geological and hydrogeological data to perform a proper characterization of the soil [108].

The urban drainge model allows the possibility of having an underground pipe

network connected to the surface via manholes, drainage structures or culverts. The pipe flow is simulated by means of a 1D SW model combined with the Priessmann slot method which provides an estimation of the pressure head in the points in where the flow is locally pressurized. This method has been succesfully applied in recent years [75, 35, 44, 23].

Another key point of this thesis is the numerical simulation of mixed flows combining free surface and pressurized flows, which is a practical tool to prevent possible flood situations in urban environments. When dealing with intense storm events, the limited capacity of the drainage network conduits can cause undesirable flooding situations. Computational simulation of the involved processes can lead to a better management of the drainage network of urban areas. In particular, it is interesting to calculate simultaneuously the possible pressurization of the pipe network and the surface water dynamics in case of overflow. The underground drainage system assumes mostly free surface flow, that can be pressurized in specific situations.

Hydrologic/hydraulic modeling in urban environments is becoming a relevant tool to predict and evaluate the effects of storm events due to the failure of sewer systems. When this occurs, the flow within the pipe becomes pressurized and overflow appears in the linking elements as culverts or storage wells. The use of distributed models for the surface flow simulation provides a more detailed computation of the spatial variations of the variables of interest. Within the bidimensional domain on the surface, this leads to detailed distributions of numerical results, such as the water depth or the flow discharge. This is of special relevance in abrupt terrain topographies or in urban areas where the buildings dramatically condition the flow direction.

One of the difficulties of the numerical simulation of drainage networks is that they flow mostly under free surface conditions but they are likely to become locally pressurized due to the limited storage capacity. Under these conditions, a complete drainage system model should be able to solve steady and transient flows under pressurized and unpressurized situations and the transition between both flows (mixed flows). Many of the models developed to study the propagation of hydraulic waves solve both system of equations, e.g. [103]. For this purpose, a few numerical schemes derived from the Method of Characteristics (MOC) have been used. Other authors, e.g. [24, 44, 35] developed numerical simulations applying the 1D shallow water

equations within a slim slot over the pipe (Preissmann slot method). An estimation of the conduits pressure can be obtained from the water level in the slot. This technique has been widely used to simulate local transitions between pressurized and shallow flows but some stability problems have been reported [94] when simulating cases with abrupt transitions. This work is focused on the development of a coupled simulation model able to solve 2D overland flow in connection with a drainage system that can be exceptionally pressurized.

The interest in the development of efficient hydraulic/hydrologic models has increased over the last decades. A wide range of natural phenomena can be studied by means of numerical simulation tools for predictive purposes. Flood events, rainfall-runoff-infiltration processes, river swelling, phreatic level evolution or vegetation dynamics are some examples of topics of interest in which computer simulation can improve the management of natural hazards. It is traditionally accepted that the most accurate mathematical models for simulating surface flows are based on the Shallow Water (SW) equations. Nevertheless, the wide range of applicability of the SW models to any type of overland flow has a counterpoint in the usually high computational cost. In order to deal with this issue, simplified models have been developed (Kinematic Wave, Zero Inertia (a.k.a. Diffusion Wave), Gravity Wave). The Zero Inertia model is a usual choice for modeling overland flow under certain conditions [74, 50]. This model neglects all the inertia terms of the SW model momentum equations.

In computational fluid dynamics, the non-linearity of the governing equations combined with the usually huge number of cells and thence unknowns in a complex problem implies a large amount of computing effort and time. There is an interest in developing efficient numerical methods. In general terms, numerical schemes used to solve time dependent problems can be classified in two groups, attending to the time evaluation of the unknowns: explicit and implicit methods. Explicit schemes update the solution at every cell from the known values of the system at the current time, whereas implicit schemes generate a system of N equations with N unknowns, being N the number of computational cells multiplied by the number of variables to solve for each cell. Explicit schemes are restricted by numerical stability reasons.

The advantage of using implicit schemes is that they are, in theory, unconditionally stable, even though they may be less accurate than explicit schemes for unsteady

flows when using large time step sizes. A compromise is required between stability gain and accuracy loss on the results. Traditionally [106, 3, 93], this constitutes the main reason for using implicit methods in steady state computations. In these of problems, the accuracy loss during the transient state is not so important and the possibility of choosing a larger time step for the simulation often allows the faster calculation of the steady state. In order to maximize the simulation efficiency by means of large time step sizes, some authors have applied implicit methods to SW equations for solving 1D problems [14, 25] and 2D problems [15, 39, 47, 4, 89, 36].

There is a wide range of applications of implicit methods within the field of computational hydraulics in both surface and subsurface domains. Some simplified overland flow models have been applied in combination with an implicit numerical scheme [99, 100, 101]. For example, the Zero-Inertia simplification of the Shallow Water Equations, often termed as Diffusion Wave, has been reported as inefficient when discretized by means of an explicit scheme compared to the implicit ZI model [49, 50] or even the full SW equations [19, 98]. On the other hand, implicit schemes are well suited for the temporal discretization of the groundwater flow models. This is mainly due to the usually slow flow velocity which leads to very smooth transient situations. The are several examples of implicit subsurface modelization that can be found in the recent literature [73, 83, 84, 70, 8, 31, 55].

A fundamental point in the recent literature has been to get schemes that satisfy the preservation of steady-states such as still water equilibrium in shallow water system. The difficulty to build such schemes was pointed out by several authors and led to the notion of well-balanced schemes or Property-C [26]. The explicit implementation of the above scheme has proved to be well-balanced not only in cases of water at rest but also in moving water steady state situations [62]. According to that work, numerical experimentation proves that careless discretization of resistance may lead to a wrong equilibrium in steady state and to oversize and inadequate values for the discrete friction forces, specially in wet/dry fronts that can interfere with the stability of the numerical solution. The upwind unified treatment of all terms, including boundary shear stress, ensures Property-C even in steady cases with non-zero velocity [64].

Another relevant issue when dealing with shallow flows, regardless of the temporal scheme, is the correct treatment of wet/dry fronts in a flood wave advancing over

an irregular topography. This is a nontrivial challenge for the development of an accurate numerical scheme, as these situations frequently lead to extreme and non-physical velocities in the wet/dry front, causing instabilities and a drastic reduction in the numerical time step [65, 13]. In [56] a few techniques used in the last years are classified in four categories: thin film, element removal, depth extrapolation and negative depth. Each group has benefits and drawbacks regarding, for instance, the correct capture of the wet/dry interface or the local and global mass conservation. More recently, [62, 64] presented a novel procedure to deal with wet/dry fronts consisting of the water positivity preserving and the friction losses limitation. This is the strategy considered in the present work.

In the last decades, the effort has been put on a good balance between source terms and fluxes [26]. However, this is not enough when dealing with realistic scenarios where bed slope or friction terms play a dominant role over convective terms and unrealistic non-physical solutions such as negative values of water depth can appear due to the wrong estimation of the source amount. In those cases, one option is reducing the time step size until the positivity is guaranteed or the non-physical solutions are removed. The main drawback of this strategy is that the time step size may be decreased in many orders of magnitude hence rising the number of time steps done, and consequently the time needed to compute the solution. Therefore, a good philosophy could be to adopt a correct estimation of the source amount instead of reducing the time step size.

1.1 Goals

The main goals of this research can be summarized as follows:

- To formulate robust and well-balanced implicit numerical schemes for both 2D surface and subsurface domains in order to solve both transient and steady flows. Unstructured meshes are used in order to get a better fitting of irregular geometries, such as the curvature of a river meander or a steep mountain catchment.
- To apply and validate a robust and efficient wetting and drying procedure in combination with implicit surface flow models.

- The performance assessment of surface flow models (Shallow Water vs. Zero Inertia), linear matrix solvers (BiCGStab vs. Thomas algorithm) and temporal discretizarion of the numerical schemes (implicit vs. explicit). These comparisons are carried out in terms of results accuracy and computational costs and will lead to several recommendations in order to choose the optimal combination for each situation.

- The numerical implementation of several infiltration and rainfall-runoff conversion models, studying possible improvements taking advantage of new mathematical techniques as the fractional derivatives. A novel application of this method to 2D surface flow models for the simulation of real world domains is also addessed.

- To develop surface-groundwater and surface-urban drainage coupling models capable of dealing with both steady and transient situations.

1.2 Outline

This document is structured in five main chapters. Chapter 2 provides a detailed description of all the conceptual and mathematical models used including the formulation of 2D Shallow Water equations and 2D Zero-Inertia model for overland flow simulations, classical infiltration laws together with the proposed improvements based on the fractional calculus theory. The formulation for 2D groundwater flow and 1D drainage is also presented. Chapter 3 discusses the numerical techniques used for building the solution of all the governing equations, classified in two groups: scalar equations and system of equations. Chapters 4 and 5 present the numerical results reached in the framework of this thesis, classified in two main groups: Single model tests cases (Chapter 4) and multi-model test cases (Chapter 5). The description of the two linear matrix solvers used in this work (BiCGStab and Thomas algorithm) is addressed in Chapter 4, including a solver performance assessment for several test cases. Finally, Chapter 6 summarizes all the conclusions achieved from all the numerical tests performed in this work.

CHAPTER 2

Governing equations

2.1 Overland flow mathematical formulation

2.1.1 2D Shallow Water equations

Free surface flows are usually described in Hydraulics by means of the Shallow Water equations (SW), assuming that the vertical dimensions are small compared with the horizontal ones [97, 62]. The vertical pressure gradients are nearly hydrostatic and the horizontal velocity field is constant throughout the depth of the fluid. Vertically integrating allows the vertical velocity to be removed from the equations. These equations represent mass and momentum conservation along the main direction of the flow and are a good description for most of the surface flow problems. The system of equations can be expressed in 2D, under the hypothesis of mild slope, as follows:

$$\frac{\partial h}{\partial t} + \frac{\partial q_x}{\partial x} + \frac{\partial q_y}{\partial y} = R - f \tag{2.1}$$

$$\frac{\partial q_x}{\partial t} + \frac{\partial}{\partial x}\left(\frac{q_x^2}{h} + \frac{1}{2}gh^2\right) + \frac{\partial}{\partial y}\left(\frac{q_x q_y}{h}\right) = gh\left(S_{0x} - S_{fx}\right) \tag{2.2}$$

$$\frac{\partial q_y}{\partial t} + \frac{\partial}{\partial x}\left(\frac{q_x q_y}{h}\right) + \frac{\partial}{\partial y}\left(\frac{q_y^2}{h} + \frac{1}{2}gh^2\right) = gh\left(S_{0y} - S_{fy}\right) \tag{2.3}$$

where the conserved variables are h representing the water depth (see Figure 2.1) and $q_x = hu$ and $q_y = hv$ the unit discharges, with u and v the depth averaged components of the velocity vector $\mathbf{u}$ along the x and y coordinates respectively. The acceleration due to gravity is represented with g. The source terms on the right hand side of the equations are written in terms of the rainfall intensity R, the soil infiltration rate f, which will be properly define later, and the bed slopes of the bottom level z in the x and y direction, S_{0x} and S_{0y}, respectively, given by:

$$S_{0x} = -\frac{\partial z}{\partial x}, \qquad S_{0y} = -\frac{\partial z}{\partial y} \tag{2.4}$$

The terms S_{fx}, S_{fy} represent the friction losses in both directions, which can be expressed in terms of the shear stress τ:

$$S_{fx} = \frac{\tau_x}{\rho g h}, \qquad S_{fy} = \frac{\tau_y}{\rho g h} \tag{2.5}$$

Friction in models based on SW equations is frequently modeled by the Manning's roughness coefficient n:

$$\tau_x = \rho g h \frac{n^2 u\sqrt{u^2+v^2}}{h^{4/3}}, \qquad \tau_y = \rho g h \frac{n^2 v\sqrt{u^2+v^2}}{h^{4/3}} \tag{2.6}$$

that represents the turbulent shear stress at the fluid-bed interface. In case of considering cases of not pure water flows, such as mud or viscous flows, this term should be modificated in order to take into account other friction laws, including viscous stress or yield stress [64]. In this thesis, when dealing with viscous flows, the next formulation is followed:

$$\tau_x = 3\mu(T)\frac{u}{h}, \qquad \tau_y = 3\mu(T)\frac{v}{h} \tag{2.7}$$

where $\mu(T)$ is the dynamic viscosity of the fluid, which depends on the temperature T.

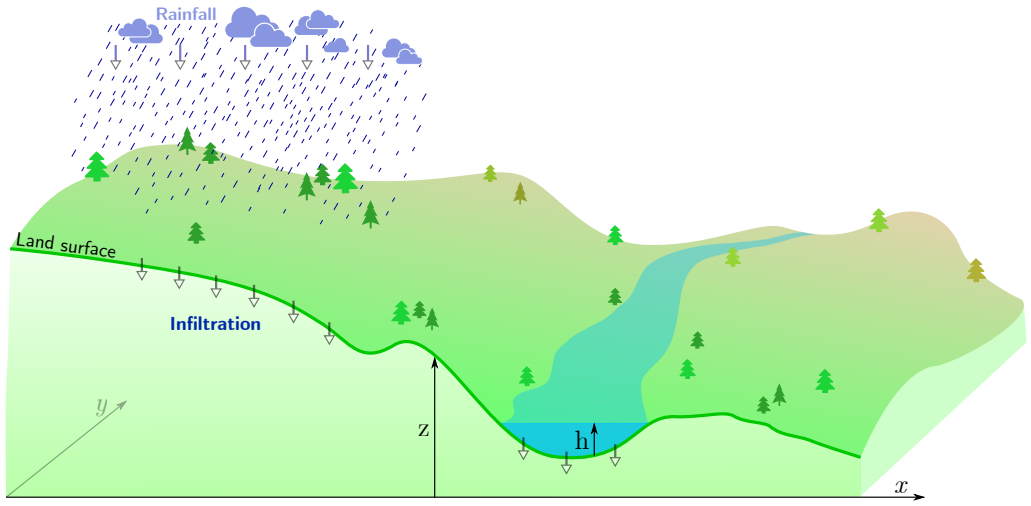

Figure 2.1: Coordinates representing water depth h and bed level z.

The 2D Shallow Water equations conform a hyperbolic non-linear system that can also be written using a general conservative formulation:

$$\frac{\partial \mathbf{U}}{\partial t} + \frac{\partial \mathbf{F}}{\partial x} + \frac{\partial \mathbf{G}}{\partial y} = \mathbf{S} \tag{2.8}$$

or

$$\frac{\partial \mathbf{U}}{\partial t} + \nabla \cdot \mathbf{E} = \mathbf{S} \tag{2.9}$$

being $\mathbf{E} = (\mathbf{F}, \mathbf{G})$, where

$$\mathbf{U} = (h, q_x, q_y)^T, \qquad q_x = hu, \qquad q_y = hv \tag{2.10}$$

$$\mathbf{F} = \left(q_x, \frac{q_x^2}{h} + \frac{1}{2}gh^2, \frac{q_x q_y}{h}\right)^T, \qquad \mathbf{G} = \left(q_y, \frac{q_x q_y}{h}, \frac{q_y^2}{h} + \frac{1}{2}gh^2\right)^T \tag{2.11}$$

$$\mathbf{S} = \left(R - f, gh\left(S_{0x} - S_{fx}\right), gh\left(S_{0y} - S_{fy}\right)\right)^T \tag{2.12}$$

The Jacobian matrix of the flux in the normal-pointing direction is [93, 62]:

$$\mathbf{J}_n = \frac{\partial \mathbf{E}\cdot\mathbf{n}}{\partial \mathbf{U}} = \mathbf{A}n_x + \mathbf{B}n_y \tag{2.13}$$

where

$$\mathbf{A} = \frac{\partial \mathbf{F}}{\partial \mathbf{U}} = \begin{pmatrix} 0 & 1 & 0 \\ c^2 - u^2 & 2u & 0 \\ -uv & v & u \end{pmatrix} \quad , \quad \mathbf{B} = \frac{\partial \mathbf{G}}{\partial \mathbf{U}} = \begin{pmatrix} 0 & 0 & 1 \\ -uv & v & u \\ c^2 - v^2 & 0 & 2v \end{pmatrix} \tag{2.14}$$

in terms of the flow velocities and the surface wave speed $c = \sqrt{gh}$. Then:

$$\mathbf{J}_n = \begin{pmatrix} 0 & n_x & n_y \\ -u(\mathbf{u}\cdot\mathbf{n}) + c^2 n_x & \mathbf{u}\cdot\mathbf{n} + un_x & un_y \\ -v(\mathbf{u}\cdot\mathbf{n}) + c^2 n_y & vn_x & \mathbf{u}\cdot\mathbf{n} + vn_y \end{pmatrix} \tag{2.15}$$

The eigenvalues and eigenvectors are given by:

$$\lambda^1 = \mathbf{u}\cdot\mathbf{n} - c, \qquad \lambda^2 = \mathbf{u}\cdot\mathbf{n}, \qquad \lambda^3 = \mathbf{u}\cdot\mathbf{n} + c \tag{2.16}$$

$$\mathbf{e}^1 = \begin{pmatrix} 1 \\ u - cn_x \\ v - cn_y \end{pmatrix}, \qquad \mathbf{e}^2 = \begin{pmatrix} 0 \\ -cn_y \\ cn_x \end{pmatrix}, \qquad \mathbf{e}^3 = \begin{pmatrix} 1 \\ u + cn_x \\ v + cn_y \end{pmatrix} \tag{2.17}$$

so that the matrices that diagonalize the Jacobian are:

$$\mathbf{P} = (\mathbf{e}^1, \mathbf{e}^2, \mathbf{e}^3) = \begin{pmatrix} 1 & 0 & 1 \\ u - cn_x & -cn_y & u + cn_x \\ v - cn_y & cn_x & v + cn_y \end{pmatrix} \tag{2.18}$$

$$\mathbf{P}^{-1} = -\frac{1}{2c}\begin{pmatrix} -\mathbf{u}\cdot\mathbf{n} - c & n_x & n_y \\ 2(vn_x - un_y) & 2n_y & -2n_x \\ \mathbf{u}\cdot\mathbf{n} - c & -n_x & -n_y \end{pmatrix} \tag{2.19}$$

$$\mathbf{J}_n = \mathbf{P}\mathbf{\Lambda}\mathbf{P}^{-1}, \qquad \mathbf{P}^{-1}\mathbf{J}_n\mathbf{P} = \mathbf{\Lambda}, \qquad \mathbf{\Lambda} = \begin{pmatrix} \lambda^1 & 0 & 0 \\ 0 & \lambda^2 & 0 \\ 0 & 0 & \lambda^3 \end{pmatrix} \tag{2.20}$$

These properties are of interest for the type of methods used to discretize the equations in this thesis.

The surface flow is commonly characterized by means of the Froude number, defined as follows:

$$Fr = \frac{|\mathbf{u}|}{c}, \qquad |\mathbf{u}| = \sqrt{u^2 + v^2} \tag{2.21}$$

It allows the classification of the flux into three main regimes: subcritical $Fr < 1$, supercritical $Fr > 1$ and critical $Fr = 1$.

2.1.2 2D Zero-Inertia Model

Equations from (2.1) to (2.3), also known as Dynamic-Wave model, have been considered too complex for some applications. High computational costs are associated with that model when applied to domains with a large number of cells [11, 16, 40, 41, 32, 61]. There are some strategies to simplify the full system. One of the most commonly used is the Zero-Inertia model [74, 107], which neglects acceleration terms in (2.2) and (2.3). The resulting system can be expressed as follows:

$$\frac{\partial h}{\partial t} + \frac{\partial q_x}{\partial x} + \frac{\partial q_y}{\partial y} = R - f \tag{2.22}$$

$$\frac{\partial h}{\partial x} = S_{0x} - S_{fx} \tag{2.23}$$

$$\frac{\partial h}{\partial y} = S_{0y} - S_{fy} \tag{2.24}$$

By defining the water surface slopes in x and y directions as

$$\mathbf{S} = (S_x, S_y) = -\left(\frac{\partial(h+z)}{\partial x}, \frac{\partial(h+z)}{\partial y}\right) = -\nabla(h+z) \tag{2.25}$$

equations (2.23) and (2.24) lead to:

$$S_x = S_{fx}, \qquad S_y = S_{fy} \tag{2.26}$$

Hence, by replacing the friction slopes (2.6) in (2.26), the unit discharges in x and y direction can be written as:

$$q_x = \left(\frac{h^{5/3}}{n\sqrt{|\mathbf{S}|}} S_x\right), \qquad q_y = \left(\frac{h^{5/3}}{n\sqrt{|\mathbf{S}|}} S_y\right) \tag{2.27}$$

By replacing the unit discharges (2.27) in the continuity equation (2.22), the final ZI equation is obtained:

$$\frac{\partial h}{\partial t} + \nabla \cdot \mathbf{q} = \frac{\partial h}{\partial t} + \nabla\left(\frac{h^{5/3}}{n\sqrt{|\mathbf{S}|}} \mathbf{S}\right) = R - f \tag{2.28}$$

Equation (2.28) is a partial differential equation with parabolic character, where the water depth h is the sole variable to solve.

2.2 Infiltration models

Infiltration is the process by which surface water enters the soil. This process is mainly governed by two forces: gravity and capillarity action. In this section, three widely used laws are presented, SCS-CN, Horton and Green-Ampt methods. All of them formulate the soil infiltration capacity f_p and cumulative infiltration volume F in terms of several soil parameters.

It is important to highlight the difference between f_p and the actual infiltration rate f. In absence of ponding surface water, a rain event starting with a weak rainfall intensity ($R \leq f_p$) leads to all the rain completely infiltrating into the soil. On the other hand, if the rain intensity exceeds the soil infiltration capacity the

surface becomes ponded. Therefore:

$$f(t) = \begin{cases} R(t) & \text{if } R(t) \leq f_p(t) \\ f_p(t) & \text{if } R(t) > f_p(t) \end{cases} \tag{2.29}$$

The cumulative infiltration $F(t)$, up to time t, can be calculated by integrating the infiltration rate f as:

$$F(t) = \int_0^t f(t)dt \tag{2.30}$$

2.2.1 SCS-CN model

The Soil Conservation Service-Curve Number (SCS-CN) runoff model was originally developed by the USDA Natural Resources Conservation Service for estimating runoff from rainfall events on agricultural watersheds [66]. Nowadays it is also used for urban hydrology. The main parameter of the method is the Curve Number (CN) which is essentially a coefficient for reducing the total precipitation to runoff or surface water potential, by taking into account the losses (evaporation, absorption, transpiration and surface storage). In general terms, the higher the CN value the higher the runoff potential.

Let us define the concepts of runoff or effective precipitation RO, rainfall volume RV, initial water abstraction which infiltrates before runoff begins I_a and the potential maximum retention S. Hence, the potential runoff can be calculated as $RV - I_a$. The main hypothesis of SCS-CN method is assuming equal relations between the real quantities and the potential quantities, as follows:

$$\frac{F}{S} = \frac{RO}{RV - I_a} \tag{2.31}$$

On the other hand, the water mass balance on the catchment lead us to:

$$RV = RO + F + I_a \tag{2.32}$$

By combining (2.31) and (2.32) and taking into consideration that the runoff cannot begin until the initial abstraction has been met:

$$RO = \begin{cases} \frac{(RV-I_a)^2}{RV-I_a+S} & (RV > I_a) \\ 0 & (RV \leq I_a) \end{cases} \tag{2.33}$$

The potential maximum retention S is estimated (in mm) by means of the Curve Number:

$$S = \frac{25400}{CN} - 254 \tag{2.34}$$

The initial abstraction is assumed proportional to S:

$$I_a = \alpha S \tag{2.35}$$

where traditionally $\alpha = 0.2$ for every watersheds [66] but recent studies suggest that there is a wide range of values that work better than this value, depending on the soil properties. The influence of this parameter was studied in [17].

It is important to remark that SCS-CN method was not designed to consider time. When the method is implemented in a time-advancing simulator, the runoff is calculated for every cell in every time step, using the cumulative rainfall since the beginning of the storm.

For the determination of the Curve Number the guidelines provided in [66] should be followed. Another important fact that needs to be considered is the Antecedent Moisture Content (AMC) or Antecedent Runoff Condition (ARC), which represents the preceding relative moisture of the soil prior to the storm event [90]. This parameter results useful in order to account for the CN variation among storm events. Three possible assumptions can be considered: dry conditions (AMC I), average conditions (AMC II) or wet conditions (AMC III) (see Table 2.1).

Traditionally [90], the Curve Number for dry or wet conditions has been recalculated in terms of the standard conditions according to (2.36) and (2.37):

AMC	Total 5-day rainfall (dormant season)	Total 5-day rainfall (growing season)
I	Less than 13 mm	Less than 36 mm
II	13 mm to 28 mm	36 mm to 53 mm
III	More than 28 mm	More than 53 mm

Table 2.1: AMC groups (adaptation from Mishra et al [59].)

$$CN(I) = \frac{4.2CN(II)}{10 - 0.058CN(II)} \tag{2.36}$$

$$CN(III) = \frac{23CN(II)}{10 - 0.13CN(II)} \tag{2.37}$$

On the other hand, some newer references [67, 59] recommend to use a conversion table to compute both values.

The SCS-CN method can be extended in order to estimate the temporal distribution of the water losses. By combining again (2.31) and (2.32) but solving for F:

$$F = \frac{S\,(RV - I_a)}{RV - I_a + S}, \qquad RV \geq I_a \tag{2.38}$$

By differentiating (2.38), taking into account that I_a and S are constant magnitudes, the following expression for the infiltration rate is obtained [90]:

$$f = \frac{dF}{dt} = \frac{S^2 R}{RV - I_a + S} \tag{2.39}$$

being R the rainfall rate, defined as follows:

$$R = \frac{dRV}{dt} \tag{2.40}$$

2.2.2 Horton model

Horton's infiltration model [88, 33] suggests an exponential equation (2.41) for modeling the soil infiltration capacity f_p:

$$f_p = f_c + (f_0 - f_c)\, e^{-kt} \tag{2.41}$$

where f_0 and f_c are the initial and final infiltration capacities, both measured in m/s and k represents the rate of decrease in the capacity $(1/s)$.

The parameters f_0 and k have no clear physical basis, so they must be estimated from calibrating the model against experimental data. A good source for experimental values of these parameters for different types of soils can be found in [78] and is summarized in [69]. Tables 2.2 and 2.3 show the parameters for some general types of soil, as presented in [2]. Note that no k values are shown. A value of $k = 4.14hr^{-1}$ is recommended in the absence of any field data [2].

Soil type	f_0 (mm/hr)
Dry sandy soils with few to no vegetation	127
Dry loam soils with few to no vegetation	76.2
Dry clay soils with few to no vegetation	25.4
Dry sandy soils with dense vegetation	254
Dry loam soils with dense vegetation	152.4
Dry clay soils with dense vegetation	50.8
Moist sandy soils with few to no vegetation	43.18
Moist loam soils with few to no vegetation	25.4
Moist clay soils with few to no vegetation	7.62
Moist sandy soils with dense vegetation	83.82
Moist loam soils with dense vegetation	50.8
Moist clay soils with dense vegetation	17.78

Table 2.2: Horton initial infiltration for different soils. Source: Akan [2].

Soil type	f_c (mm/hr)
Clay loam, silty clay loams	0 - 1.3
Sandy clay loam	1.3 - 3.8
Silt loam, loam	3.8 - 7.6
Sand, loamy sand, sandy loams	7.6 - 11.4

Table 2.3: Horton final infiltration for different soils. Source: Akan [2].

2.2.3 Green-Ampt model

The Green-Ampt model [29, 57, 90] assumes a sharp wetting front at the position $z = s(t)$ (see Figure 2.2) separating a saturated soil region $0 \leq z \leq s(t)$ with a water

content equal to the porosity θ_s from the unsaturated region $s(t) < z$ with an initial water content θ_i. Additionally, the water suction at the wetting front, denoted by Ψ, is assumed to remain constant. Also, the vertical hydraulic flux per unit area in the saturated area q_s is given by Darcy's law

$$q_s = K_s \frac{\partial H}{\partial z} \tag{2.42}$$

where $H(z,t) = \Psi + z$ is the hydraulic head and K_s is the saturated hydraulic conductivity.

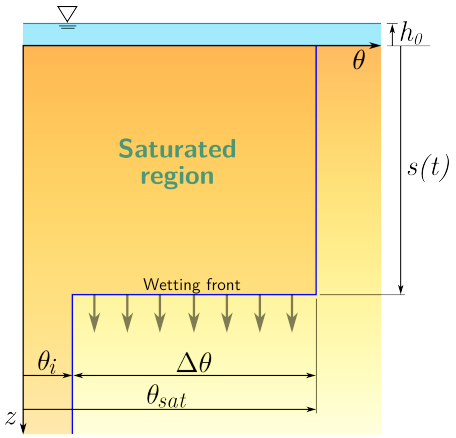

Figure 2.2: Sketch of the variables of the Green-Ampt infiltration wetting front.

The main assumption in the saturated region ($0 \leq z \leq s(t)$) is that q is constant in the vertical direction:

$$\frac{\partial q}{\partial z} = \frac{\partial}{\partial z}\left(K_s \frac{\partial H}{\partial z}\right) = 0 \tag{2.43}$$

The surface water depth is used to define the upper boundary condition $H(0,t) = h_0$, assuming manometric pressure. The lower boundary condition, at the wetting front position, is set as $H(s,t) = s + \Psi$. Hence, the solution of (2.43) can be easily obtained and is given by

$$H(z,t) = \frac{s + \Psi - h_0}{s} z + h_0 \tag{2.44}$$

Considering the saturated region (Figure 2.2) as a control volume Ω with a

contour $\partial\Omega$, the following integral mass balance equation can be obtained:

$$\frac{d}{dt}\int_{\Omega}\rho d\Omega + \oint_{c}\rho\left(\mathbf{v}-\mathbf{v}_{c}\right)\cdot\mathbf{n}dc = 0 \tag{2.45}$$

being $\mathbf{v}$ and $\mathbf{v}_c$ the fluid and control volume velocities, respectively.

Assuming that ρ is constant,

$$\frac{d\Omega}{dt} + \int_{soil}\left(\mathbf{v}\cdot\mathbf{n}\right)dc = 0 \tag{2.46}$$

Hence, taking into account that $dc = \theta ds$:

$$\Delta\theta\frac{ds}{dt} - f_p = 0 \Rightarrow f_p = \Delta\theta\frac{ds}{dt} \tag{2.47}$$

where $\Delta\theta = \eta - \theta_i$, being η the porosity and θ_i the initial water content.

Hence, assuming that $q = f_p$:

$$\Delta\theta\frac{ds}{dt} = q, \quad s(0) = 0 \tag{2.48}$$

By combining (2.42), (2.44) and (2.48), the Green-Ampt equation is obtained:

$$\Delta\theta\frac{ds}{dt} = K_s\frac{s+\Psi-h_0}{s} \tag{2.49}$$

Once the function $s(t)$ is known, the infiltration capacity f_p comes from (2.47) and the cumulative infiltration is evaluated as

$$F(t) = \Delta\theta\, s(t) \tag{2.50}$$

The most common soil parameters are shown in Table 2.4, as presented in [76].

Soil type	θ_s	S_f (cm)	K_s (cm/h)
Sand	0.437 (0.374-0.500)	4.95 (0.97-25.36)	11.78
Loamy sand	0.437 (0.363-0.506)	6.13 (1.35-27.94)	2.99
Sandy loam	0.453 (0.351-0.565)	11.01 (2.67-45.47)	1.09
Loam	0.463 (0.375-0.551)	8.89 (1.33-59.38)	0.66
Silt loam	0.501 (0.420-0.582)	16.68 (2.92-95.39)	0.34
Sandy clay loam	0.398 (0.332-0.464)	21.85 (4.42-108.0)	0.15
Clay loam	0.464 (0.409-0.519)	20.88 (4.79-91.10)	0.10
Silty clay loam	0.471 (0.418-0.524)	27.30 (5.67-131.50)	0.10
Sandy clay	0.430 (0.370-0.490)	23.90 (4.08-140.2)	0.06
Silty clay	0.479 (0.425-0.533)	29.22 (6.13-139.4)	0.05
Clay	0.475 (0.427-0.523)	31.63 (6.39-156.5)	0.03

Table 2.4: Mean values and standard deviation for Green-Ampt model parameters. Source: Rawls et al. 1983 [76].

2.2.4 Fractional Order Green-Ampt model

In [96] the Green-Ampt infiltration model is generalized by considering the subsurface hydraulic flux as a fractional-order derivative of H. This is justified by means of several empirical results that highlight some deviations of this theoretical model from the field infiltration measurements in heterogeneous media and a generalized Darcy's law is used to improve the numerical results. As in the Green-Ampt infiltration method, the vertical water movement is characterized by means of the flux:

$$q = K_\alpha D_z^\alpha H, \qquad D_z^\alpha \equiv \frac{D^\alpha}{Dz^\alpha} \tag{2.51}$$

where K_α is the hydraulic conductivity with the proper dimensions for the fractional model [length$^\alpha$/time], allowing the correct physical dimensions for the hydraulic flux [length/time]. In addition, D_z^α denotes the Caputo fractional derivative [22] of order α with $0 < \alpha \leq 1$, which is defined by

$$D_z^\alpha g(z,t) = \left[J^{1-\alpha} \left(\frac{\partial g}{\partial z} \right) \right] (z,t) \tag{2.52}$$

and

$$(J^{1-\alpha}g)(z,t) = \frac{1}{\Gamma(1-\alpha)}\int_{r=0}^{z}(z-r)^{-\alpha}g(r,t)\,dr \tag{2.53}$$

is the Riemann-Liouville fractional integral operator of order $1-\alpha$ where Γ denotes the Euler's Gamma function. It is well known [22] that if $\alpha = 1$, then the operator D_z^1 coincides with the partial derivative $\frac{\partial}{\partial z}$. Thus, the fractional-order Green-Ampt infiltration law (FOGA) can be described as a generalization of the classical version of this law.

Using that the Caputo fractional derivative of the function $g(z) = z^j$ is given by [22]

$$(D_z^\alpha g)(z) = \begin{cases} 0 & \text{if } j = 0 \\ \frac{\Gamma(j+1)}{\Gamma(j+1-\alpha)}z^{j-\alpha} & \text{if } j \in \mathbb{N} \text{ or } j \notin \mathbb{N} \text{ and } j > 0 \end{cases} \tag{2.54}$$

it is possible to derive the FOGA infiltration law by using the fractional Darcy's law given in (2.51). The balance of the subsurface flux $q = cte$ leads to a simple governing equation for the saturated region $0 \le z \le s(t)$, and the function H is the solution of the following problem:

$$\frac{\partial q}{\partial z} = K_\alpha \frac{\partial}{\partial z}\left(D_z^\alpha H\right) = 0, \tag{2.55a}$$

$$H(0,t) = h_0, \tag{2.55b}$$

$$H(s,t) = s + \Psi. \tag{2.55c}$$

It is worth noting that in general the Caputo fractional derivative lacks the property $\frac{\partial}{\partial z}\left(D_z^\alpha H\right) \neq D_z^{1+\alpha}H$ and thus the solution of problem (2.55) is not a linear combination of the functions 1 and z (see for example [22]). The solution of the problem (2.55) is given by

$$H(z,t) = \frac{s+\Psi-h_0}{s^\alpha}z^\alpha + h_0\,, \quad 0 \le z \le s. \tag{2.56}$$

and therefore it is now a linear combination of 1 and z^α.

Hence, the subsurface hydraulic flux is given by

$$q = K_\alpha D_z^\alpha H = K_\alpha \Gamma(\alpha+1)\frac{s+\Psi-h_0}{s^\alpha} \tag{2.57}$$

where (2.51) and (2.54) have been used with $j = 1$ and $j = \alpha$. Replacing the expression of the flux (2.57) into the mass balance equation (2.48), the following initial-value problem for the wetting front is obtained

$$\Delta\theta\frac{ds}{dt} = K_\alpha \Gamma(\alpha+1)\frac{s+\Psi-h_0}{s^\alpha}, \quad s(0) = 0 \tag{2.58}$$

Note that if $\alpha = 1$, then the initial-value problem (2.58) that governs the wetting front s at each time level coincides with the classical Green-Ampt infiltration model (see (2.49)) and one would recover the solution of that model. In this sense, the FOGA model generalizes the classical Green-Ampt infiltration model.

From (2.57), one observes that $D_z^\alpha H$ has dimensions [length$^{1-\alpha}$] and therefore the dimensions of K_α must be [length$^\alpha$/time] so that the subsurface hydraulic flux q has the correct physical dimensions [length/time].

Table 2.5 shows a summary of the intermediate equations for both GA and FOGA models. Note that if $\alpha = 1$, both GA and FOGA models are governed by the same differential equation.

GA	FOGA
$q = K_s \frac{\partial H}{\partial z}$	$q = K_\alpha D_z^\alpha H$
$\downarrow$	$\downarrow$
$\frac{\partial q}{\partial z} = K_s \frac{\partial}{\partial z}\left(\frac{\partial H}{\partial z}\right) = 0$	$\frac{\partial q}{\partial z} = K_\alpha \frac{\partial}{\partial z}\left(D_z^\alpha H\right) = 0$
$\downarrow$	$\downarrow$
$H(z,t) = \frac{s+\Psi-h_0}{s} z + h_0$	$H(z,t) = \frac{s+\Psi-h_0}{s^\alpha} z^\alpha + h_0$
$\downarrow$	$\downarrow$
$q = K_s \frac{s+\Psi-h_0}{s}$	$q = K_\alpha \Gamma(\alpha+1) \frac{s+\Psi-h_0}{s^\alpha}$
$\downarrow$	$\downarrow$
$\Delta\theta \frac{ds}{dt} = K_s \frac{s+\Psi}{s}$	$\Delta\theta \frac{ds}{dt} = K_\alpha \Gamma(\alpha+1) \frac{s+\Psi}{s^\alpha}$

Table 2.5: Summary of GA and FOGA models.

2.3 Groundwater flow mathematical formulation

By combining the Darcy's law for saturated flow in porous media [20] with the continuity equation for flows in porous media:

$$\mathbf{v} = -K_s \nabla h_s \Rightarrow \mathbf{q} = (h_s - z_s)\mathbf{v} = -K_s(h_s - z_s)\nabla h_s \tag{2.59}$$

$$\eta \frac{\partial (h_s - z_s)}{\partial t} + \nabla \mathbf{q}_s = S_s \tag{2.60}$$

$$\eta \frac{\partial h_s}{\partial t} - K_s \nabla \left[(h_s - z_s)\nabla h_s\right] = S_s \tag{2.61}$$

where K_s represents the saturated hydraulic conductivity and S_s the source terms. Figure 2.3 shows the coordinate system for the groundwater flow model.

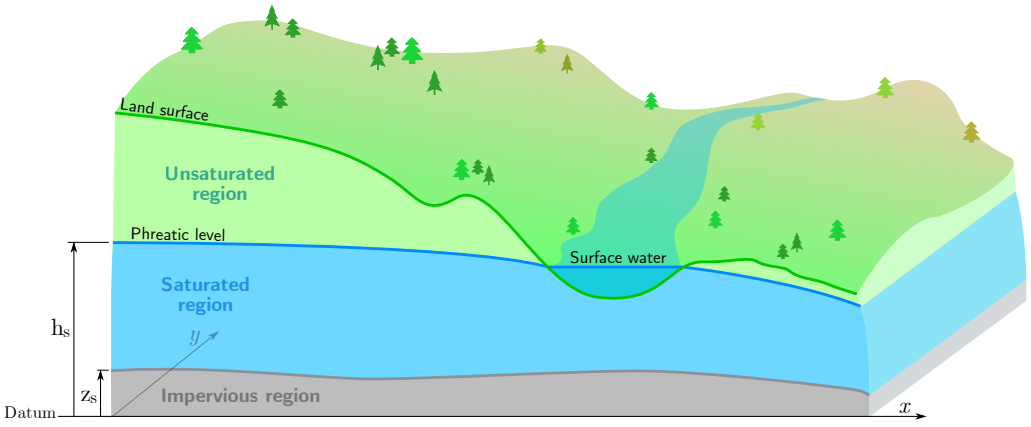

Figure 2.3: Subsurface coordinate system.

2.4 Drainage flow mathematical formulation

It is generally accepted that unsteady open channel water flows can be simulated using the 1D Shallow Water or St. Venant equations. These equations represent mass and momentum conservation along the main direction of the flow and are a good description for most of the pipe flow kind problems. They can be written in a conservative form as follows:

$$\frac{\partial A}{\partial t} + \frac{\partial Q}{\partial x} = q_e \tag{2.62}$$

$$\frac{\partial Q}{\partial t} + \frac{\partial}{\partial x}\left(\frac{Q^2}{A} + gI_1\right) = gI_2 + gA\left(S_0^{1D} - S_f^{1D}\right) \tag{2.63}$$

where A is the wetted cross section, Q is the discharge, I_1 represents the hydrostatic pressure force term, q_e is the exchange discharge per unit length and I_2 accounts for the pressures forces due to channel width changes (see Figure 2.4):

$$I_1 = \int_0^{h(x,t)} (h_p - \gamma)\,\sigma(x,\gamma)d\gamma \tag{2.64}$$

$$I_2 = \int_0^{h(x,t)} (h_p - \gamma)\,\frac{\partial \sigma(x,\gamma)}{\partial x}d\gamma \tag{2.65}$$

$$\sigma = \frac{\partial A(x,\gamma)}{\partial \gamma} \tag{2.66}$$

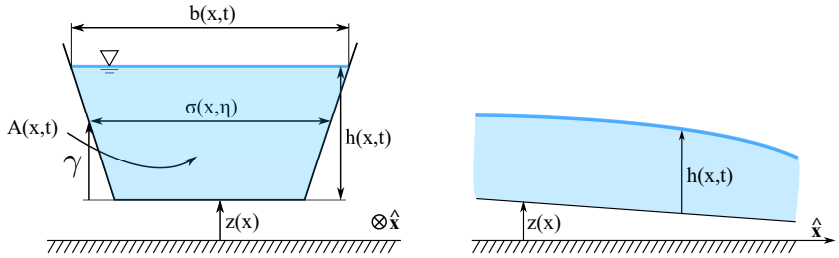

Figure 2.4: Coordinate system for 1D Shallow Water equations.

The remaining terms, S_0^{1D} and S_f^{1D}, represent the bed slope and the energy grade line (defined in terms of the Manning roughness coefficient), respectively:

$$S_0^{1D} = -\frac{\partial z_p}{\partial x}, \qquad S_f^{1D} = \frac{Q\,|Q|\,n_{1D}^2}{A^2 R^{4/3}} \tag{2.67}$$

where $R = A/P$, P being the wetted perimeter.

Note that the superindex $1D$ is added to the source terms S_0^{1D} and S_f^{1D} in order to distinguish them from the ones corresponding to the $2D$ SW model. The coordinate system used for the formulation is shown in Figure 2.4. It is useful to rewrite the equation system in a vectorial form:

$$\frac{\partial \mathbf{U}}{\partial t} + \frac{\partial \mathbf{F}}{\partial x} = \mathbf{S} \tag{2.68}$$

where

$$\mathbf{U} = (A, Q)^T, \qquad \mathbf{F} = \left(Q, \frac{Q^2}{A} + gI_1\right)^T, \qquad \mathbf{S} = \left(0, gI_2 + gA\left(S_0^{1D} - S_f^{1D}\right)\right)^T \tag{2.69}$$

In those cases in which $\mathbf{F} = \mathbf{F}(\mathbf{U})$, when $I_2 = 0$, it is possible to rewrite the conservative system by means of the Jacobian matrix of the system:

$$\frac{\partial \mathbf{U}}{\partial t} + \mathbf{J}\frac{\partial \mathbf{U}}{\partial x} = \mathbf{S}, \qquad \mathbf{J} = \frac{\partial \mathbf{F}}{\partial \mathbf{U}} = \begin{pmatrix} 0 & 1 \\ c^2 - u^2 & 2u \end{pmatrix} \tag{2.70}$$

where $u = Q/A$ is the flow velocity and c is the wave speed, defined as follows:

$$c = \sqrt{g\frac{\partial I_1}{\partial A}} \tag{2.71}$$

The system matrix can be made diagonal by means of its set of real eigenvalues and eigenvectors, which represent the speed of propagation of the information:

$$\lambda^{1,2} = u \pm c, \qquad \mathbf{e}^{1,2} = (1, u \pm c)^T \tag{2.72}$$

As in 2D SW model, it is very common to characterize the flow type by means of the Froude number $Fr = u/c$, allowing the classification of the flux into three main regimes: subcritical $Fr < 1$, supercritical $Fr > 1$ and critical $Fr = 1$.

2.4.1 Preissmann slot method

Water flow numerical simulation in pipe systems may require to model transitions between surface flow and pressurized flow in steady and transient situations. The governing equations for both flow types are different and this must be taken into account in order to get a complete numerical model for solving dynamically transients. For the sake of completeness, the 1D pressurized flow governing equations are presented in Appendix A.

In this section, the mathematical model is reformulated by means of the Preissmann slot method. This technique provides a reasonable estimation of the water pressure in cases of simulating pipe networks mainly unpressurized, with isolated points of pressurization. The Preissmann slot approach assumes that the top of the pipe or closed channel is connected to a hypothetical narrow slot, open to the atmosphere, so the shallow water equations can be applied including this slot (see Fig. 2.5). The slot width is ideally chosen equaling the speed of gravity waves in the slot to the water hammer wave speed, so the water level in the slot is equal to the pressure head level. The water hammer flow comes from the capacity of the pipe system to change the area and fluid density, so forcing the equivalence between both models requires that the slot stores as much fluid as the pipe would by means of a change in area and fluid density. The pressure term and the wavespeed, assuming rectangular cross section, for $A \leq bH_{max}$ are:

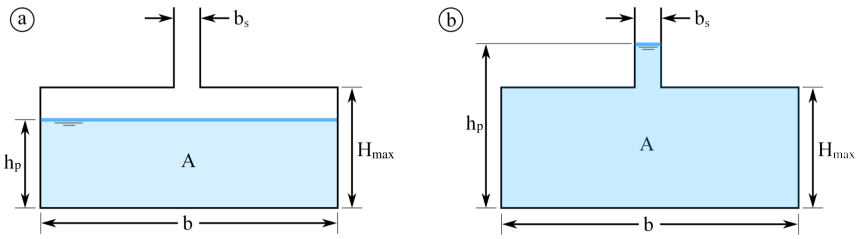

Figure 2.5: Possible flow conditions in the pipe: a) Free surface flow, b) Pressurized flow.

$$h_p = \frac{A}{b} \tag{2.73}$$

$$I_1 = \frac{A^2}{2b} \tag{2.74}$$

$$c = \sqrt{g\frac{\partial I_1}{\partial A}} = \sqrt{g\frac{A}{b}} \tag{2.75}$$

and for $A > bH_{max}$:

$$h_p = H_{max} + \frac{A - bH_{max}}{b_s} \tag{2.76}$$

$$I_1 = bH_{max}\left(\frac{A - bH_{max}}{b_s} + \frac{H_{max}}{2}\right) + \frac{(A - bH_{max})^2}{2b_s} \tag{2.77}$$

$$c = \sqrt{g\frac{\partial I_1}{\partial A}} = \sqrt{g\frac{A}{b_s}} \tag{2.78}$$

The ideal choice for the slot width results in:

$$c_{WH} = c \Rightarrow b_s = g\frac{A_f}{c_{WH}^2} \tag{2.79}$$

in which A_f is the full pipe cross-section.

CHAPTER 3

Discretization using Finite Volume schemes

3.1 Scalar equations

In this section, a conservative first-order implicit upwind scheme for scalar non-linear equations is presented and applied to the inviscid Burgers' equation, as a simple example.

3.1.1 1D non-linear equations

As starting point, let us consider a generic 1D non-linear scalar equation:

$$\frac{\partial u}{\partial t} + \frac{\partial f}{\partial x} = 0, \qquad a = \frac{\partial f}{\partial u} \tag{3.1}$$

where a represents the wave speed and u, f the conserved variable and its flux, respectively.

By considering a control volume Ω (which becomes a lenght in 1D) and by integrating (3.1), assuming a fixed-in-time control volume:

$$\frac{d}{dt}\int_{\Omega} u\, d\Omega + \int_{\Omega} \frac{\partial f}{\partial x} d\Omega = 0 \tag{3.2}$$

In order to obtain a numerical solution, the spatial domain is discretized in a set of grid cells $\Omega_i = \left[x_{i-1/2}, x_{i+1/2}\right]$ (see Figure 3.1):

$$\frac{d}{dt}\int_{x_{i-1/2}}^{x_{i+1/2}} u\, dx + \int_{x_{i-1/2}}^{x_{i+1/2}} \frac{\partial f}{\partial x} dx = 0 \tag{3.3}$$

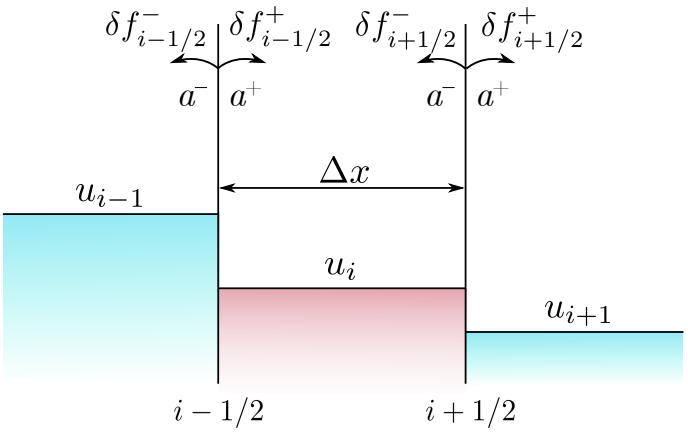

Figure 3.1: Discretization of the 1D domain in computational cells.

By considering that the finite volume method considers the spatially averaged value of the variables:

$$\int_{x_{i-1/2}}^{x_{i+1/2}} u\, dx = u_i \Delta x, \qquad \int_{x_{i-1/2}}^{x_{i+1/2}} \frac{\partial f}{\partial x} dx = \delta f_i \tag{3.4}$$

Hence, by replacing (3.4) in (3.3):

$$\frac{\Delta u_i}{\Delta t} + \frac{1}{\Delta x}\delta f_i = 0 \tag{3.5}$$

where $\Delta u_i = u_i^{n+1} - u_i^n$ and $\delta f_i^n = f_i^n - f_{i-1}^n$. Following [12] the flux can be split as follows:

$$\begin{aligned}\delta f_i &= \left(\delta f^+_{i-1/2} + \delta f^-_{i+1/2}\right) = \\ &= \left[(f_i - f_{i-1})^+ + (f_{i+1} - f_i)^-\right] = \\ &= \tilde{a}^+_{i-1/2}\delta u_{i-1/2} + \tilde{a}^-_{i+1/2}\delta u_{i+1/2}\end{aligned} \tag{3.6}$$

where

$$\tilde{a}^{\pm} = \frac{1}{2}\left(a \pm |a|\right) \tag{3.7}$$

An implicit discretization of this equation can be done as follows:

$$\frac{\Delta u_i}{\Delta t} + \frac{1}{\Delta x}\left[\theta\delta f_i^{n+1} + (1-\theta)\delta f_i^n\right] = 0 \tag{3.8}$$

The discretization is done in terms of the weight θ for sake of availability to select a fully-implicit ($\theta = 1$) or a fully-explicit method ($\theta = 0$). The fluxes evaluated in $n+1$ needs to be linearized in order to achieve a discrete linear equation. This linearization can be done by means of the first order Taylor series:

$$\begin{aligned}\delta f_i^{n+1} &= \delta f_i^n + \frac{df}{du}\Delta u_i = \\ &= \left(f_i^+ - f_{i-1}^+\right)^n + a_i^+\Delta u_i - a_{i-1}^+\Delta u_{i-1} + \\ &+ \left(f_{i+1}^- - f_i^-\right)^n + a_{i+1}^-\Delta u_{i+1} - a_i^-\Delta u_i\end{aligned} \tag{3.9}$$

By replacing (3.9) in (3.8) and rearranging in a coefficient form:

$$A\Delta u_{i-1} + B\Delta u_i + C\Delta u_{i+1} = k \tag{3.10}$$

where

$$A = -\theta\frac{\Delta t}{\Delta x}\left(a^+_{i-1}\right)^n, \qquad B = 1 + \theta\frac{\Delta t}{\Delta x}\left|a_i\right|^n, \qquad C = \theta\frac{\Delta t}{\Delta x}\left(a^-_{i+1}\right)^n \tag{3.11}$$

$$k = -\frac{\Delta t}{\Delta x}\left(\delta f^{+}_{i-1/2} + \delta f^{-}_{i+1/2}\right)^{n} \tag{3.12}$$

Stability condition

The time step choice when using explicit schemes is limited in order to avoid the interaction among the other outwards waves from the neighbour Riemann problems taking into account the wave speed a and the half-length of the cell $\Delta x/2$. Hence, the stability of the numerical solution is guaranteed if the time step Δt satisfies the following relation:

$$\Delta t = \mathrm{CFL}\frac{\Delta x}{\max\left(|\tilde{a}_w|\right)} \tag{3.13}$$

being $\tilde{a}_w$ the average wave speed evaluated at each wall of the grid and CFL the Courant-Friedrich-Levy number which is limited to $\mathrm{CFL} \leq 1$ for 1D explicit schemes.

Numerical example

The 1D inviscid Burgers's equation is a simple non-linear and homogeneous scalar hyperbolic case with shock:

$$\frac{\partial h}{\partial t} + \frac{\partial f}{\partial x} = 0, \qquad f = \frac{h^2}{2} \tag{3.14}$$

It can be expressed in conservation or non-conservation (advection) forms, as follows:

$$\frac{\partial h}{\partial t} + \frac{\partial}{\partial t}\left(\frac{h^2}{2}\right) = 0 \Rightarrow \frac{\partial h}{\partial t} + h\frac{\partial h}{\partial x} = 0 \tag{3.15}$$

As example initial condition, let us consider a squared wave defined by:

$$u(x,0) = \begin{cases} h_1 & \forall x \in (-\infty, x_1)\bigcup(x_2, \infty) \\ h_2 & \forall x \in [x_1, x_2] \end{cases} \tag{3.16}$$

with an analytical solution [14] given by:

$$t_c = 2\frac{x_2 - x_1}{h_2 + h_1} \tag{3.17}$$

$$t \leq t_c \Rightarrow u(x,t) = \begin{cases} h_1 & \forall x \in (-\infty, x_1 + h_1 t) \bigcup \left(x_2 + \frac{h_2+u_1}{2}t, \infty\right) \\ \frac{x-x_1}{t} & \forall x \in [x_1 + h_1 t, x_1 + h_2 t) \\ h_2 & \forall x \in \left[x_1 + h_2 t, x_2 + \frac{h_2+u_1}{2}t\right] \end{cases} \tag{3.18}$$

$$t > t_c \Rightarrow h(x,t) = \begin{cases} h_1 & \forall x \in (-\infty, x_1 + h_1 t) \bigcup \left(x_1 + (h_2 + h_1)\sqrt{t t_c}, \infty\right) \\ \frac{x-x_1}{t} & \forall x \in \left[x_1 + h_1 t, x_1 + (h_2 + h_1)\sqrt{t t_c}\right) \end{cases} \tag{3.19}$$

For this example, let us choose $x_1 = 33.5, x_2 = 77.5$ and positive values of the function ($h_1 = 1, h_2 = 3$). The spatial discretization was done by a uniform grid of 400 cells with $\Delta x = 0.25$. The numerical results at times $t_1 = 3s, t_2 = 6s, t_3 = 9s$ for both explicit ($\theta = 0$) and implicit ($\theta = 1$) time discretization and for several CFL values are presented and compared with the above analytical solution in the Figures from 3.2 to 3.7. The results show that the implicit methodology provides inconditionally stable solutions but the larger the CFL, the more diffusive becomes the numerical solutions. When using an explicit scheme, the solution becomes unstable for CFL > 1, as expected (Figure 3.7).

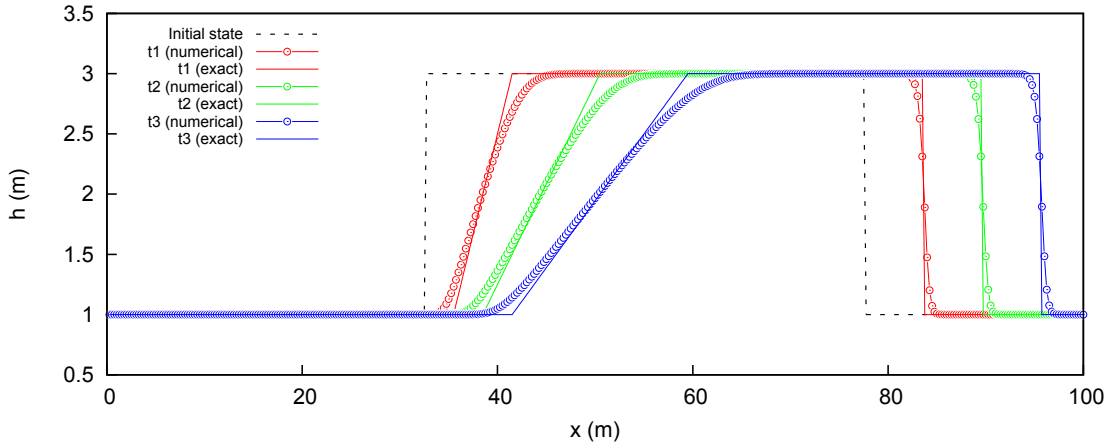

Figure 3.2: Fully implicit, CFL=0.2

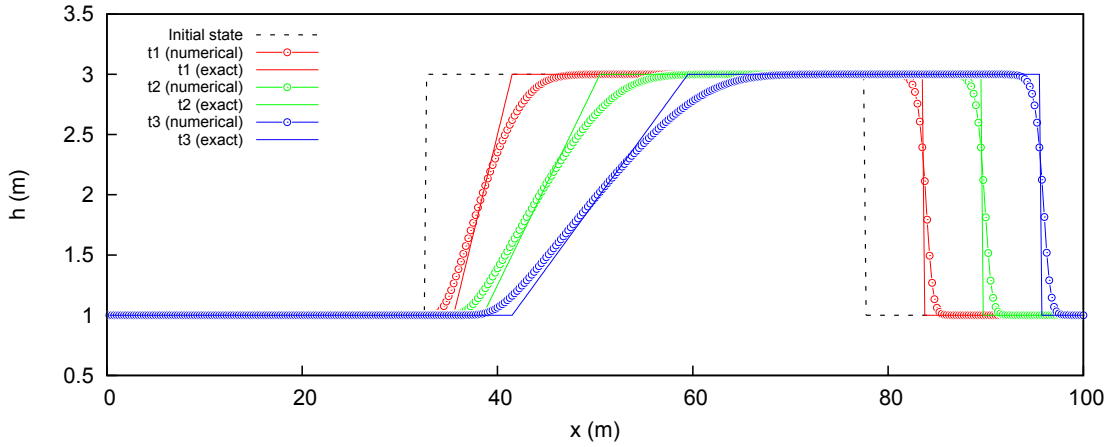

Figure 3.3: Fully implicit, CFL=1

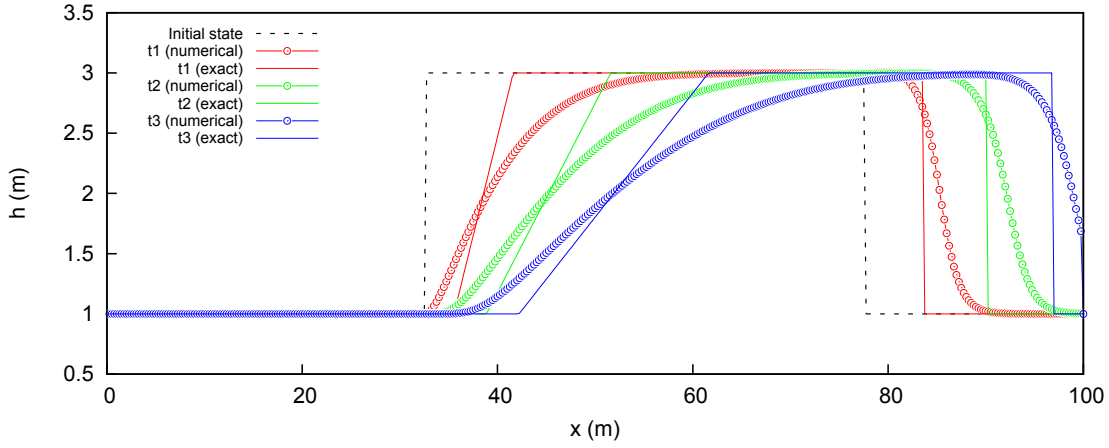

Figure 3.4: Fully implicit, CFL=10

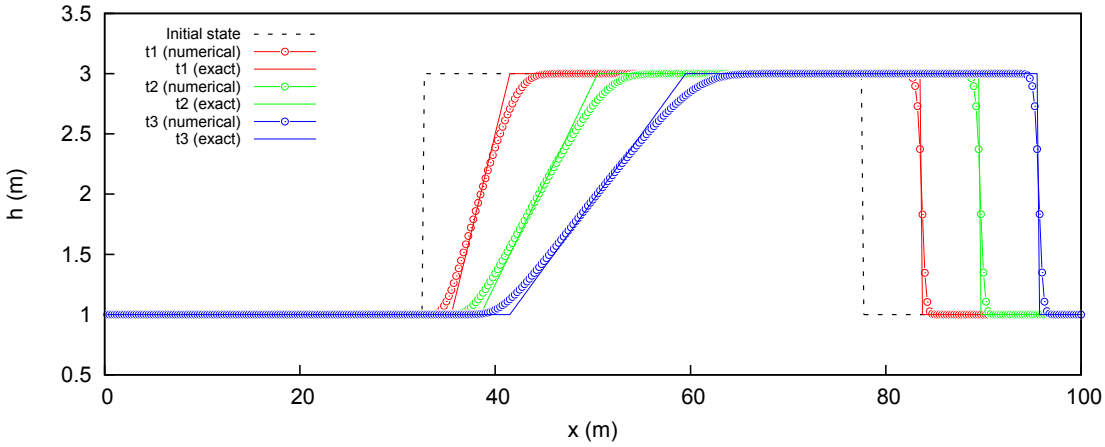

Figure 3.5: Fully explicit, CFL=0.2

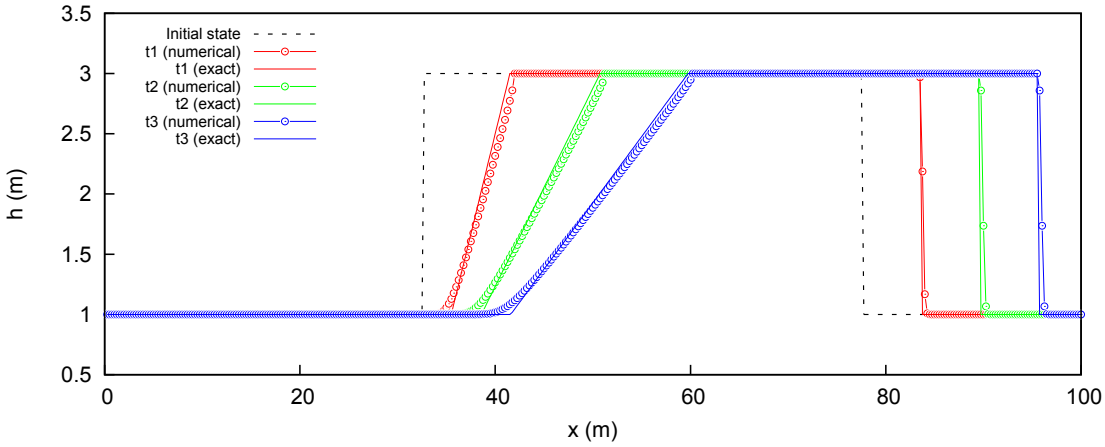

Figure 3.6: Fully explicit, CFL=1

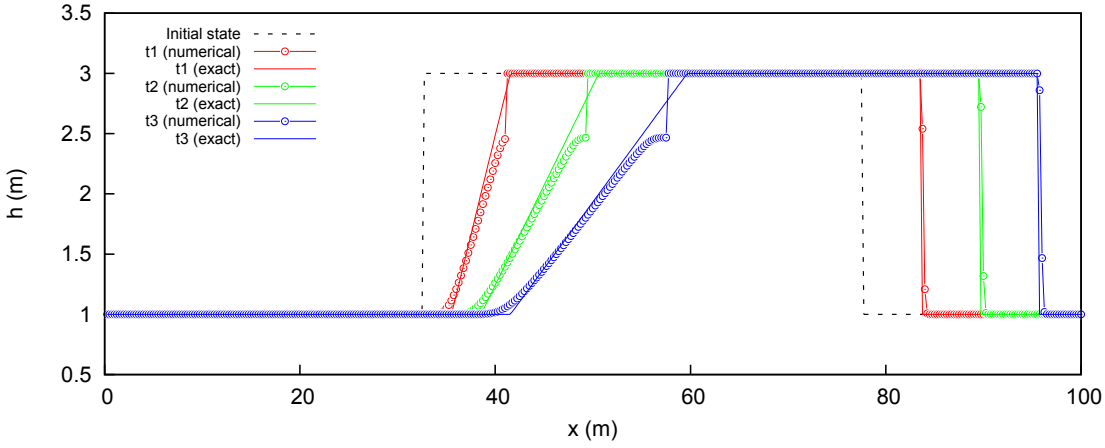

Figure 3.7: Fully explicit, CFL=1.1

3.1.2 2D non-linear equations

As in 1D case, let us consider a generic non-linear bidimensional scalar equation as starting point:

$$\frac{\partial u}{\partial t} + \nabla \mathbf{f} = 0, \qquad \mathbf{f} = (f_x, f_y), \qquad \mathbf{a} = (a_x, a_y) = \frac{d\mathbf{f}}{du} \tag{3.20}$$

where $\mathbf{a}$ represents the wave speed vector and u and $\mathbf{f}$ are the conserved variable and its flux, respectively. By considering a control volume Ω (area in 2D) and by integrating (3.20) assuming a fixed-in-time control volume:

$$\frac{d}{dt}\int_\Omega u d\Omega + \int_\Omega \nabla \mathbf{f} d\Omega = 0 \tag{3.21}$$

Invoking Gauss' theorem:

$$\frac{d}{dt}\int_\Omega u d\Omega + \int_{\partial\Omega} (\mathbf{f}\cdot\mathbf{n})\, \partial\Omega = 0 \tag{3.22}$$

where $\mathbf{n}$ is the outward-pointing normal vector to the surface $\partial\Omega$.

Considering as control volume Ω a grid cell of area S_i with N_w polygonal faces of length l_w, each with an outward-pointing normal vector n_w (see Figure 3.8) and assuming a piecewise constant representation, Equation (3.22) can be written in a discrete form

$$\frac{\Delta u_i}{\Delta t} S_i + \sum_{j,w=1}^{N_w} (\delta \mathbf{f}\cdot\mathbf{n})_w^- \, l_w = 0 \tag{3.23}$$

where superscript n indicates the time level and:

$$(\delta \mathbf{f}\cdot\mathbf{n})_w^- = (\tilde{\mathbf{a}}\cdot\mathbf{n})_w^- \, \delta u_w \tag{3.24}$$

where $\delta u_w = u_j - u_i$ with u_i and u_j being the cell average values of the variable u at two adjacent cells and

$$\tilde{\mathbf{a}}_w = \frac{\mathbf{f}_j - \mathbf{f}_i}{u_j - u_i} \tag{3.25}$$

is the average advection speed at the cell edge.

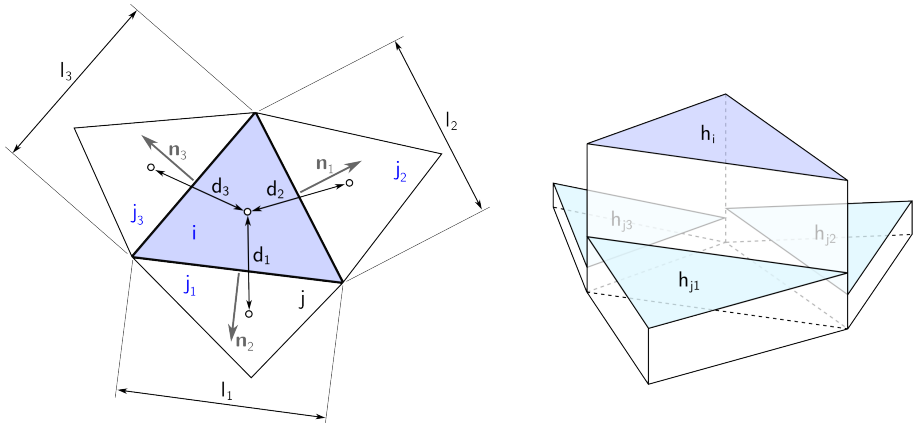

Figure 3.8: Cell connectivity sketch in a triangular unstructured mesh.

Note that, as in the 1D case and following the upwind philosophy, only the incoming components of the information (-) are taken into account in Equation (3.23). The temporal discretization can be done in terms of a weight θ to select a fully-implicit ($\theta = 1$) or a fully-explicit method ($\theta = 0$), as before:

$$\frac{\Delta u_i}{\Delta t} S_i + \theta \sum_{j,w=1}^{N_w} \left[(\delta \mathbf{f} \cdot \mathbf{n})_w^-\right]^{n+1} l_w + (1-\theta) \sum_{j,w=1}^{N_w} \left[(\delta \mathbf{f} \cdot \mathbf{n})_w^-\right]^{n} l_w = 0 \tag{3.26}$$

The fluxes at $n+1$ time can be linearized as follows [14]:

$$\delta \mathbf{f}_w^{n+1} \simeq \delta \mathbf{f}_w^n + \mathbf{a}_j^n \Delta u_j - \mathbf{a}_i^n \Delta u_i \tag{3.27}$$

where $\Delta u_j = u_j^{n+1} - u_j^n$. Note that the advection speeds are evaluated at the cell centers in (3.27). It is worth mentioning that this first order Taylor expansion is a valid technique for equations with weak non-linearities. Otherwise, an iterative method should be applied in order to linearize the equation (e.g. Picard fixed-point iterations method (see Appendix C for further details))

Therefore, projecting on the normal-pointing direction the ingoing component of the

flux:

$$\left[(\delta\mathbf{f}\cdot\mathbf{n})_w^-\right]^{n+1} \simeq \left[(\delta\mathbf{f}\cdot\mathbf{n})_w^-\right]^n + \left(\mathbf{a}_j^n\cdot\mathbf{n}_w\right)^- \Delta u_j - \left(\mathbf{a}_i^n\cdot\mathbf{n}_w\right)^- \Delta u_i \tag{3.28}$$

By replacing (3.28) in (3.26):

$$\Delta u_i - \theta\frac{\Delta t}{S_i}\sum_{j,w=1}^{N_w}\left(\mathbf{a}_i^n\cdot\mathbf{n}_w\right)^- l_w\Delta u_i + \theta\frac{\Delta t}{S_i}\sum_{j,w=1}^{N_w}\left(\mathbf{a}_j^n\cdot\mathbf{n}_w\right)^- l_w\Delta u_j = -\frac{\Delta t}{S_i}\sum_{j,w=1}^{N_w}\left[(\delta\mathbf{f}\cdot\mathbf{n})_w^-\right]^n l_w \tag{3.29}$$

Finally, by reordering in a compact coefficient scheme:

$$a_i\Delta u_i + \sum_{j,w=1}^{N_w} b_w\Delta u_j = k_i \tag{3.30}$$

where

$$a_i = 1 - \theta\frac{\Delta t}{S_i}\sum_{j,w=1}^{N_w}\left(\mathbf{a}_i^n\cdot\mathbf{n}_w\right)^- l_w, \tag{3.31}$$

$$b_w = \theta\frac{\Delta t}{S_i}\left(\mathbf{a}_j^n\cdot\mathbf{n}_w\right)^- l_w \tag{3.32}$$

$$k_i = -\frac{\Delta t}{S_i}\sum_{j,w=1}^{N_w}\left(\tilde{\mathbf{a}}^n\cdot\mathbf{n}\right)_w^-\delta u_w^n l_w \tag{3.33}$$

Stability condition

For 1D explicit numerical schemes, the time step is chosen for ensuring the no-interaction among the other outward waves from the neighbour Riemann problems, taking into account the wave speed and the half-length of the cell $\Delta x/2$. However, the process is more complicated for 2D problems, specially if the spatial discretiza-

tion is done by means of unstructured meshes. Let us define the equivalent distance to Δx:

$$\Delta x'_i = \frac{S_i}{\max_{1,N_w}(l_w)} \tag{3.34}$$

When using an explicit scheme, the limited time step for each face is given by:

$$\Delta t_{i,w} = \frac{\min(\Delta x'_i, \Delta x'_j)}{\max(|\tilde{\mathbf{a}}_w \cdot \mathbf{n}|)} \tag{3.35}$$

The stability is given by the Courant-Friedrich-Levy (CFL) number,

$$\mathrm{CFL} = \frac{\Delta t}{\min_{Mesh}(\Delta t_{i,w})} \tag{3.36}$$

so that

$$\Delta t = \mathrm{CFL}\, \min_{Mesh}(\Delta t_{i,w}) \tag{3.37}$$

where $\min_{Mesh}(\Delta t_{i,w})$ represents the minimum $\Delta t_{i,w}$ value along the whole computational mesh.

In case of using structured 2D meshes, the maximum CFL number for the explicit scheme is 1/2, whereas CFL=1 is allowed for some unstructured triangular meshes. On the other hand, implicit schemes benefit from theoretical unconditional stability. Hence, CFL number becomes a multiplicative factor of the maximum time step allowed by the explicit scheme for stability reasons.

Numerical example

As an illustrative example, let us consider the 2D inviscid Burgers' equation:

$$\frac{\partial u}{\partial t} + \nabla \cdot \mathbf{f} = 0, \qquad \mathbf{f} = \left(\frac{u^2}{2}, \frac{u^2}{2}\right) \tag{3.38}$$

$$\frac{\partial u}{\partial t} + u\frac{\partial u}{\partial x} + u\frac{\partial u}{\partial y} = 0 \tag{3.39}$$

Figures 3.9 and 3.10 show the initial conditions and the analytical solution of two Riemann problems proposed in [5]. The numerical solutions for various CFL numbers using square mesh are shown in figures 3.11 to 3.16. The same conclusion as in the 1D case is reached, the larger the CFL value, the more diffusive is the numerical solution.

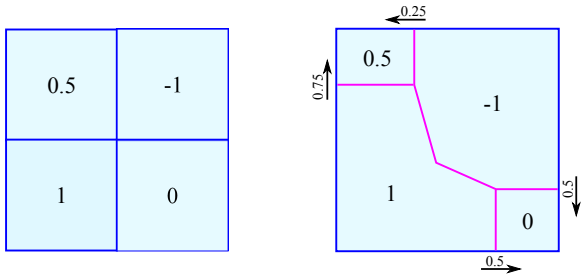

Figure 3.9: Riemann problem 1. Initial conditions and analytic solution (pink lines).

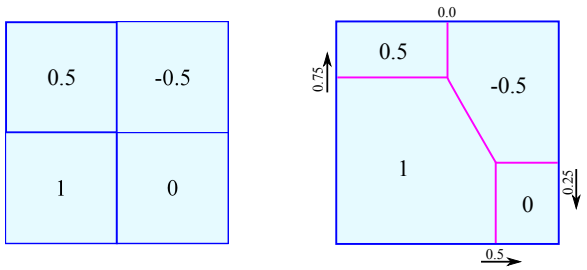

Figure 3.10: Riemann problem 2. Initial conditions and analytic solution (pink lines).

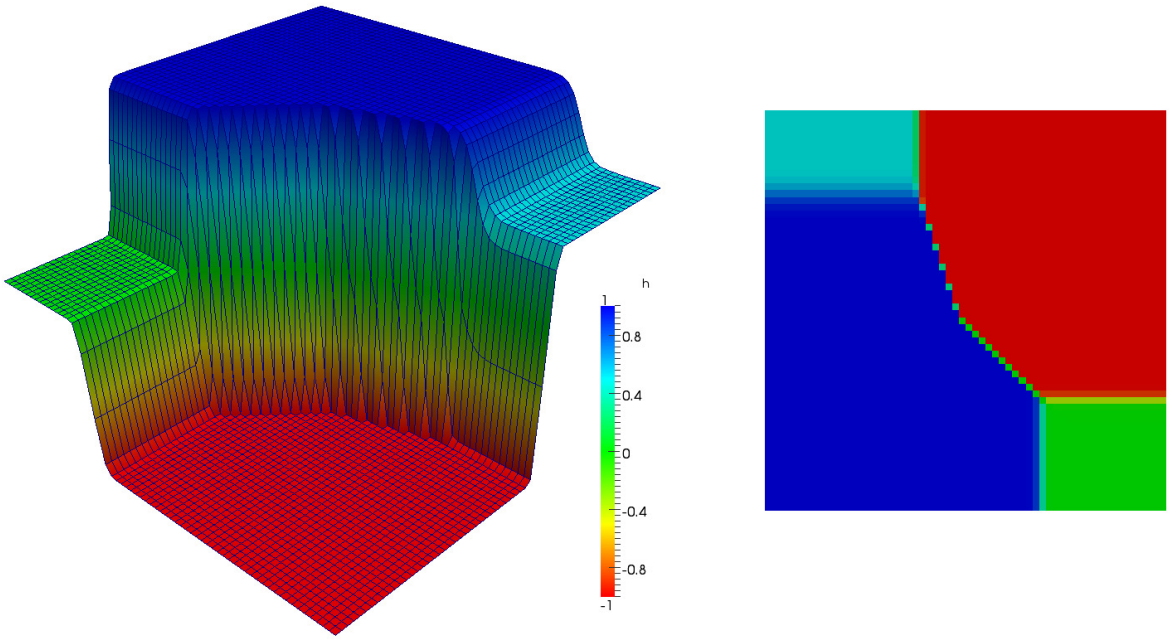

Figure 3.11: Riemann problem 1. Fully explicit, CFL=0.5.

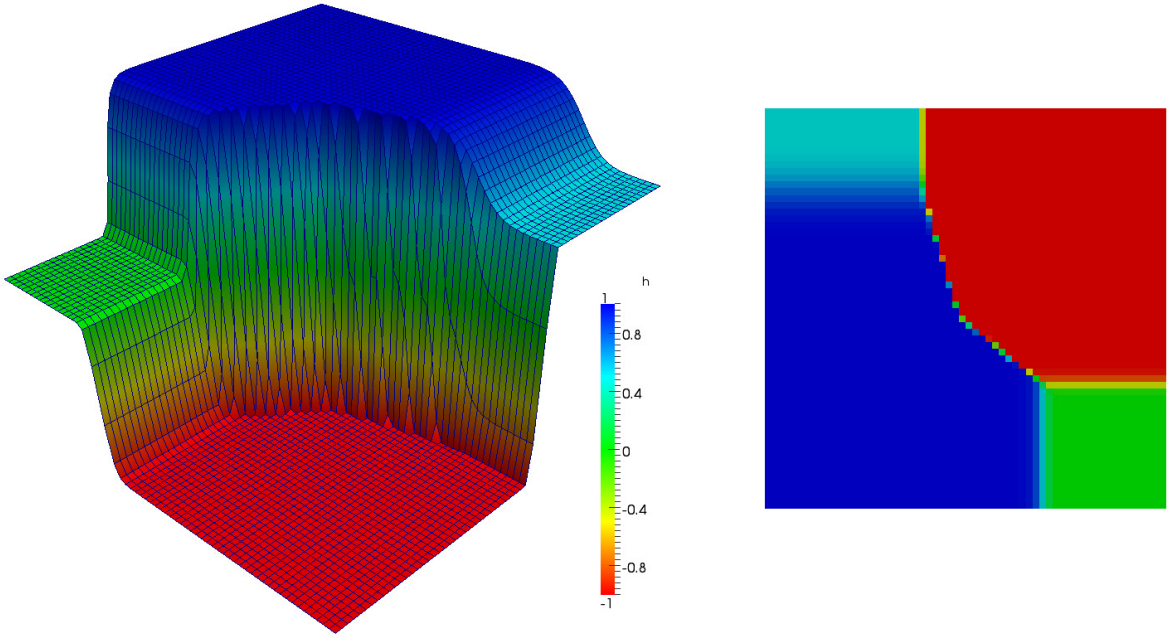

Figure 3.12: Riemann problem 1. Fully implicit, CFL=0.5.

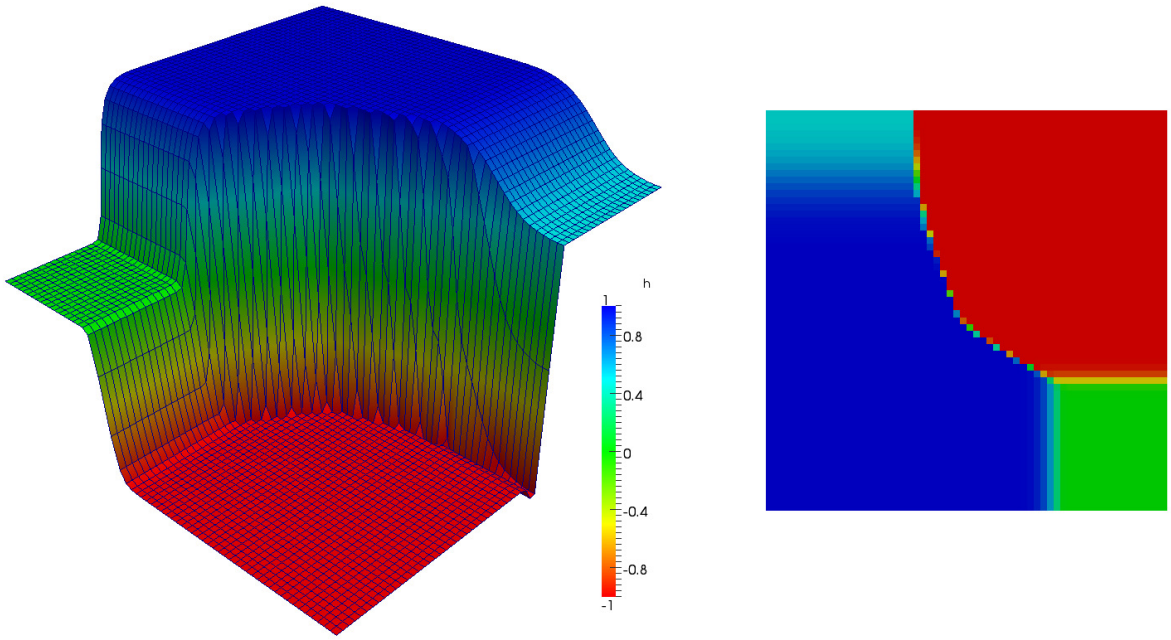

Figure 3.13: Riemann problem 1. Fully implicit, CFL=2.0.

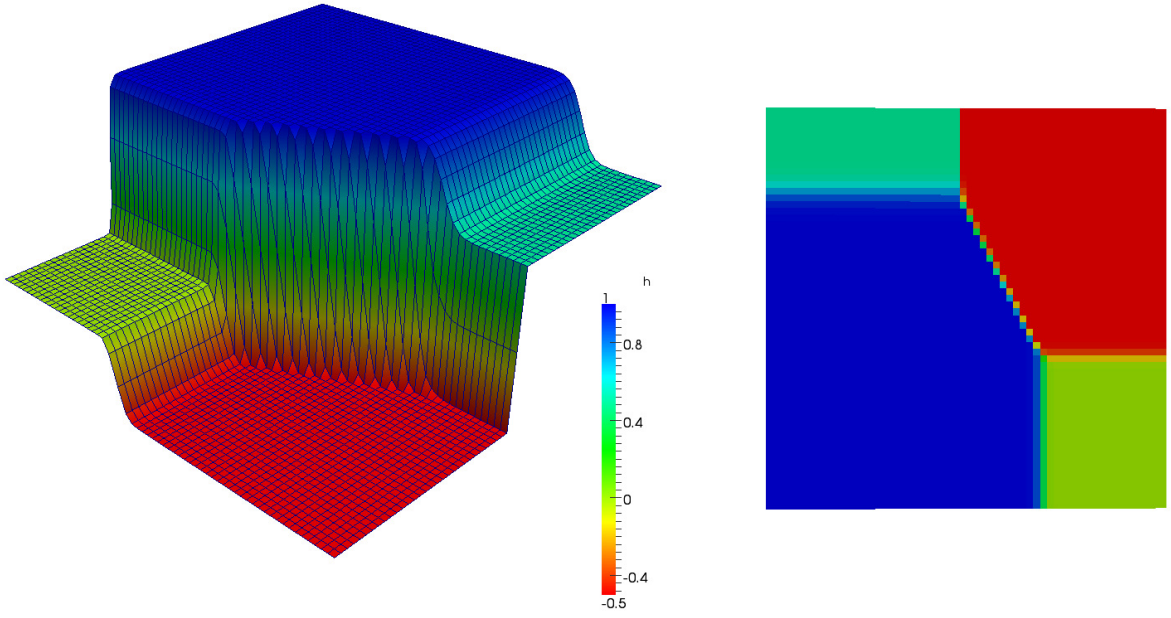

Figure 3.14: Riemann problem 2. Fully explicit, CFL=0.5.

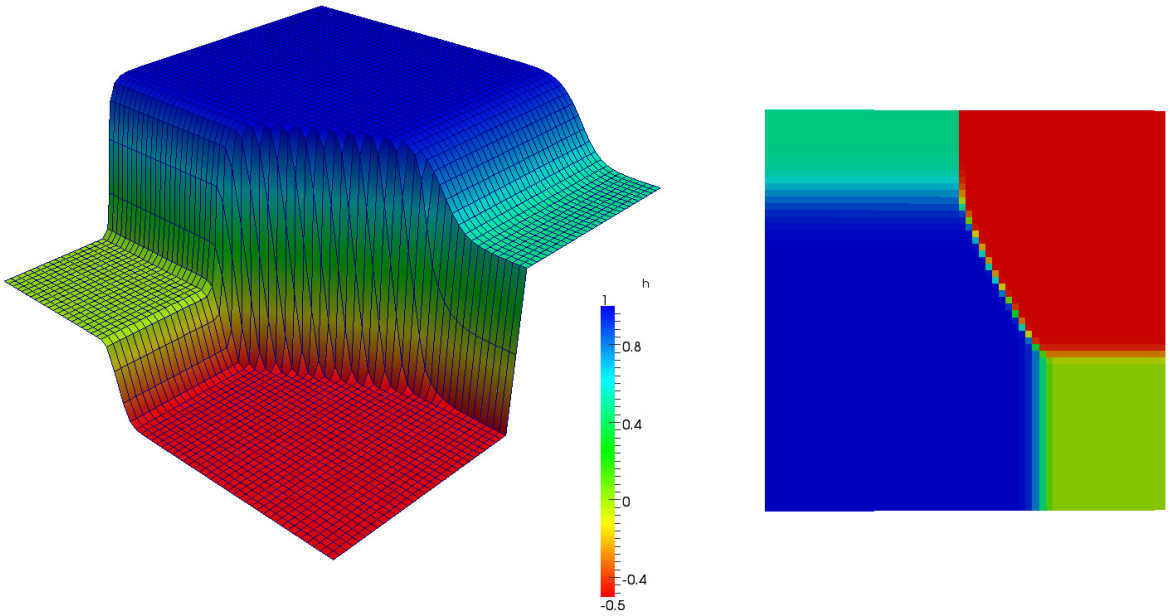

Figure 3.15: Riemann problem 2. Fully implicit, CFL=0.5.

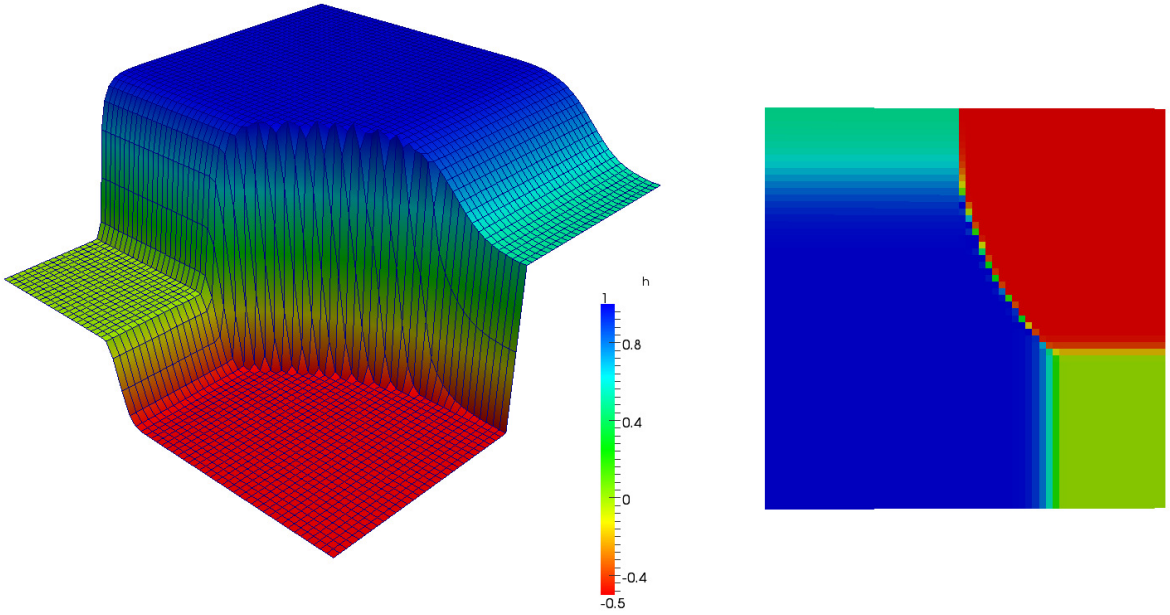

Figure 3.16: Riemann problem 2. Fully implicit, CFL=2.0.

3.1.3 Application to 2D Zero-Inertia model

In this section, the Zero-Inertia model equation (2.28) is discretized by applying the 2D Implicit cell centered upwind Finite Volume scheme described. For simplicity of the notation, let us define:

$$\alpha(h) = \frac{h^{5/3}}{n\sqrt{|\mathbf{S}|}} \Rightarrow \mathbf{q} = \alpha(h)\mathbf{S} = -\alpha(h)\nabla(h+z) \tag{3.40}$$

Hence, (2.28) is transformed as follows:

$$\frac{\partial h}{\partial t} + \nabla\mathbf{f} = R - f, \qquad \mathbf{f} = \mathbf{q} \tag{3.41}$$

This is an example of non-linear equation that requires iterations in the linearization process due to the dependency $\alpha(h)$. By following the previous procedure for a general 2D non-linear scalar equation:

$$\begin{aligned}\frac{h^{n+1}-h^n}{\Delta t}\Omega =& \theta \int_{\partial\Omega} \left[\mathbf{q}^{n+1}(h)\cdot\mathbf{n}\right]\partial\Omega + \\ &+ (1-\theta)\int_{\partial\Omega}\left[\mathbf{q}^{n}(h)\cdot\mathbf{n}\right]\partial\Omega + (R-f)^n\Omega\end{aligned} \tag{3.42}$$

Considering the control volume Ω as equal to the area A_i of cell i with N_w polygonal faces of length l_w, each with an outer-pointing normal vector $\mathbf{n}_w$ and distance between centroids of the cells i and j defined as d_w:

$$q_w^{n+\theta} = \alpha_w^{n+\theta}(h)\frac{h_j^{n+\theta} + z_j - h_i^{n+\theta} - z_i}{d_w} \tag{3.43}$$

where

$$\alpha_w^{n+\theta}(h) = \frac{\left(h_w^{n+\theta}\right)^{5/3}}{n_w\sqrt{|\mathbf{S}|_w}} \tag{3.44}$$

The coefficients $\alpha_w^{n+\theta}(h)$ are non-linear functions of h. In case of choosing an

implicit time integration ($\theta \neq 0$), a linearization is necessary in order to solve the equation system. In this model, this is done by means of the Picard iteration method. Hence, evaluating α_w at an intermediate step (iteration) m and the unknowns h at time level $n+1$ yields:

$$h_i^{n+1,m+1} - h_i^n = \frac{\Delta t}{A_i} \sum_{j,w=1}^{N_w} \left[\alpha_w^{n+1,m}(h) \frac{h_j^{n+1,m+1} + z_j - h_i^{n+1,m+1} - z_i}{d_w} \right] l_w + (R-f)_i^n \Delta t \tag{3.45}$$

Note that $\alpha_w^{n+1,m}$ coefficients are average-evaluated at every cell edge. The next step is to reorder equation (3.45). For simplicity of notation, temporal indexes are not shown:

$$\alpha_w^{n+1,m}(h) \equiv \alpha_w^m(h), \qquad h_{i,j}^{n+1,m+1} \equiv h_{i,j}^{m+1} \tag{3.46}$$

Hence whenever m or $m+1$ superindexes are shown, they refer to time $n+1$ in the corresponding iteration. Following this convention and rearranging:

$$\begin{aligned} \left(1 + \frac{\Delta t}{A_i} \sum_{w=1}^{N_w} \alpha_w^m(h) \frac{l_w}{d_w} \right) h_i^{m+1} - \frac{\Delta t}{A_i} \sum_{j,w=1}^{N_w} \alpha_w^m(h) \frac{l_w}{d_w} h_j^{m+1} = \\ h_i^n - \frac{\Delta t}{A_i} \sum_{j,w=1}^{N_w} \alpha_w^m(h) \frac{l_w}{d_w} (z_i - z_j) + R \Delta t \end{aligned} \tag{3.47}$$

Equation (3.47) can be rewritten in a coefficient form. Additionally, the generalization of the time integration is recovered by means of the parameter θ, as shown below:

$$a_i h_i^{m+1} + \sum_{j,w=1}^{N_w} b_w h_j^{m+1} = k_i \tag{3.48}$$

where

$$a_i = 1 + \theta \frac{\Delta t}{A_i} \sum_{w=1}^{N_w} \alpha_w^m(h) \frac{l_w}{d_w} \tag{3.49}$$

$$b_w = -\theta \frac{\Delta t}{A_i} \alpha_w^m(h) \frac{l_w}{d_w} \tag{3.50}$$

$$\begin{aligned} k_i = h_i^n - \theta \frac{\Delta t}{A_i} \sum_{j,w=1}^{N_w} \alpha_w^m(h) \frac{l_w}{d_w} (z_i - z_j) - \\ (1-\theta) \frac{\Delta t}{A_i} \sum_{j,w=1}^{N_w} \alpha_w^m(h) \frac{l_w}{d_w} \left(h_i^n - h_j^n + z_i - z_j\right) + (R-f)_i^n \Delta t \end{aligned} \tag{3.51}$$

Expressions (3.48) to (3.51) together with the proper boundary conditions represent a system of equations conforming a $N \times N$ matrix, being N the number of computational cells. For a structured rectangular mesh (Figure 3.17, left), this results in a penta-diagonal matrix, as follows:

$$\begin{pmatrix} a_1 & b_w & & b_w & & & & \\ b_w & a_2 & b_w & & b_w & & & \\ & b_w & a_3 & b_w & & \ddots & & \\ \ddots & & \ddots & \ddots & \ddots & & \ddots & \\ & b_{j1} & & b_{j4} & a_i & b_{j2} & & b_{j3} \\ & & \ddots & & \ddots & \ddots & \ddots & \\ & & & \ddots & & b_w & a_{N-1} & b_w \\ & & & & b_w & & b_w & a_N \end{pmatrix} \begin{pmatrix} h_1 \\ h_2 \\ h_3 \\ \vdots \\ h_i \\ \vdots \\ h_{N-1} \\ h_N \end{pmatrix} = \begin{pmatrix} k_1 \\ k_2 \\ k_3 \\ \vdots \\ k_i \\ \vdots \\ k_{N-1} \\ k_N \end{pmatrix} \tag{3.52}$$

whereas an unstructured triangular mesh (Figure 3.17, right) generates a non-structured matrix in which the population depends on the mesh neighbour connectivity:

$$\begin{pmatrix} a_1 & & b_w & & & b_w & & b_w \\ b_w & a_2 & & b_w & b_w & & & \\ & b_w & a_3 & & & b_w & & b_w \\ & & & \ddots & & & & \\ & & & & \ddots & & & \\ b_w & & b_w & & & a_{N-2} & & b_w \\ & b_w & b_w & b_w & & & a_{N-1} & \\ b_w & & b_w & & b_w & & & a_N \end{pmatrix} \begin{pmatrix} h_1 \\ h_2 \\ h_3 \\ \vdots \\ \vdots \\ h_{N-2} \\ h_{N-1} \\ h_N \end{pmatrix} = \begin{pmatrix} k_1 \\ k_2 \\ k_3 \\ \vdots \\ \vdots \\ k_{N-2} \\ k_{N-1} \\ k_N \end{pmatrix} \tag{3.53}$$

The linear system conformed by the matrix and the RHS vector needs to be solved by means of a matrix inversion technique.

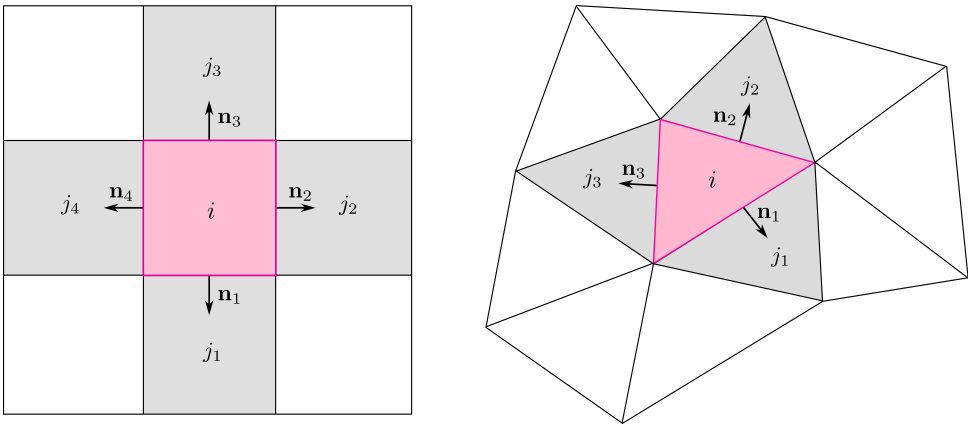

Figure 3.17: Inner cells for structured rectangular (left) and unstructured triangular (right) meshes.

Boundary conditions

Apart from the internal elements scheme, it is necessary to formulate adequately several types of boundary conditions. In this work, three different boundary conditions are used: closed boundaries, h-fixed and free outflow.

- *Closed boundary*: For the closed boundary cells (Figure 3.18), it is assumed that there is not any contribution from the boundary wall ($w = wB$), so the corresponding term in the sums of the system (3.48) should not be considered:

$$a_{iB}h_{iB}^{m+1} + \sum_{\substack{j,w=1 \\ j=w\neq wB}}^{N_w} b_w h_j^{m+1} = k_{iB} \tag{3.54}$$

with

$$a_{iB} = 1 + \theta\frac{\Delta t}{A_{iB}} \sum_{\substack{w=1 \\ w\neq wB}}^{N_w} \alpha_w^m(h)\frac{l_w}{d_w} \tag{3.55}$$

$$b_w = -\theta\frac{\Delta t}{A_{iB}}\alpha_w^m(h)\frac{l_w}{d_w} \tag{3.56}$$

$$\begin{aligned} k_{iB} = h_{iB}^n - \theta\frac{\Delta t}{A_{iB}} \sum_{\substack{j,w=1 \\ j=w\neq wB}}^{N_w} \alpha_w^m(h)\frac{l_w}{d_w}\left(z_{iB} - z_j\right) - \\ (1-\theta)\frac{\Delta t}{A_{iB}} \sum_{\substack{j,w=1 \\ j=w\neq wB}}^{N_w} \alpha_w^m(h)\frac{l_w}{d_w}\left(h_{iB}^n - h_j^n + z_{iB} - z_j\right) + R\Delta t \end{aligned} \tag{3.57}$$

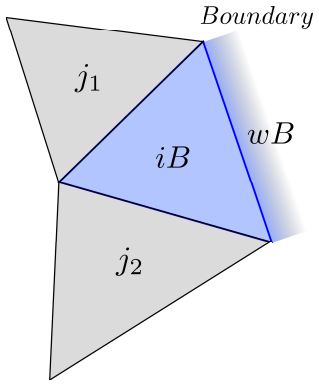

Figure 3.18: Closed boundary cell.

- *h-fixed*: In this case, the water depth for the boundary cell iB is imposed into the system matrix (3.48) at time level $n+1$ as follows:

$$h_{iB}^{n+1} = h_{fixed} \tag{3.58}$$

This boundary condition can also be used to represent water depth variations in time $h(t)$.

- *Inlet discharge*:

In order to impose an inflow discharge (Q-fixed or $Q(t)$) as inlet boundary condition, the system (3.48) is modified as follows:

$$a_{iB} = 1, \quad b_w = 0, \quad c_{iB} = h_{iB}^n + \frac{\Delta t}{A_i} Q_{in} \tag{3.59}$$

The equation for the boundary cell iB becomes trivial and the inlet discharge Q_{in} is imposed within the right hand side of the system. Note that the inlet discharge is assumed to be normal to the boundary cell wall.

- *Free outflow*: Free outflow is modeled by setting to zero the first spatial derivative of the water depth respect to the normal direction of the outlet wall of the boundary cell. This is done by calculating the water depth in the boundary cell (h_{iB}) as the average value of the two adjacent cells (see Figure 3.20, left):

$$h_{iB}^{n+1} = \frac{1}{2} \left(h_{j1}^{n+1} + h_{j2}^{n+1} \right) \tag{3.60}$$

The implementation of h-fixed, or free outflow boundary conditions is carried out by modifying the linear system (3.48) as follows:

$$a_{iB} = 1, \quad b_w = 0, \quad c_{iB} = h_{iB}^{n+1} \tag{3.61}$$

In general, the scheme for the cells adjacent to these boundary cells (see Figure 3.19) needs to be reformulated, in order to extract from the equation of this cell the known information about h_{iB} and add it to the free vector k_i. Hence, the system (3.48) is modified for the cells adjacent to boundaries as follows:

$$a_i h_i^{m+1} + \sum_{\substack{j,w=1 \\ j=w \neq iB}}^{N_w} b_w h_j^{m+1} = k_i \tag{3.62}$$

$$a_i = 1 + \theta \frac{\Delta t}{A_i} \sum_{w=1}^{N_w} \alpha_w^m(h) \frac{l_w}{d_w} \tag{3.63}$$

$$b_w = -\theta \frac{\Delta t}{A_i} \alpha_w^m(h) \frac{l_w}{d_w} \tag{3.64}$$

$$k_i = h_i^n - \theta \frac{\Delta t}{A_i} \sum_{j,w=1}^{N_w} \alpha_w^m(h) \frac{l_w}{d_w} (z_i - z_j) - (1-\theta) \frac{\Delta t}{A_i} \sum_{j,w=1}^{N_w} \alpha_w^m(h) \frac{l_w}{d_w} \left(h_i^n - h_j^n + z_i - z_j \right) + R\Delta t + \theta \frac{\Delta t}{A_i} \alpha_w^m(h) \frac{l_w}{d_w} h_{iB}^{n+1} \tag{3.65}$$

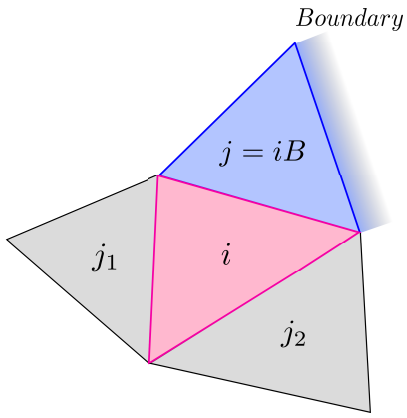

Figure 3.19: Cell i adjacent to an h-fixed boundary.

On the other hand, as the discharge is not explicitly solved in the ZI model, a reconstruction of this variable is carried out at every boundary cell iB associated to free outflow, by following the next procedure (see Figure 3.20, right):

- First, the unit discharge is defined at the inner walls of the cell iB and projected onto the normal vector as follows:

$$\mathbf{q}_{w1} = \alpha_{w1} \frac{h_{j1}^{n+1,m+1} + z_{j1} - h_{iB}^{n+1,m+1} - z_{iB}}{d_{w1}} (-\mathbf{n}_1) \tag{3.66}$$

$$\mathbf{q}_{w2} = \alpha_{w2} \frac{h_{j2}^{n+1,m+1} + z_{j2} - h_{iB}^{n+1,m+1} - z_{iB}}{d_{w2}} (-\mathbf{n}_2) \tag{3.67}$$

- The cell unit discharge $\mathbf{q}_{iB}$ is built as the sum of all vectors:

$$\mathbf{q}_{iB} = \mathbf{q}_{w1} + \mathbf{q}_{w2} \tag{3.68}$$

- The outlet unit discharge q_{out} is obtained by projecting $\mathbf{q}_{iB}$ onto the boundary wall normal vector $\mathbf{n}_{out}$:

$$q_{out} = \mathbf{q}_{iB} \cdot \mathbf{n}_{out} \tag{3.69}$$

- Finally, the full outlet discharge is computed by integrating the unitary discharge for each cell all along the outlet boundary.

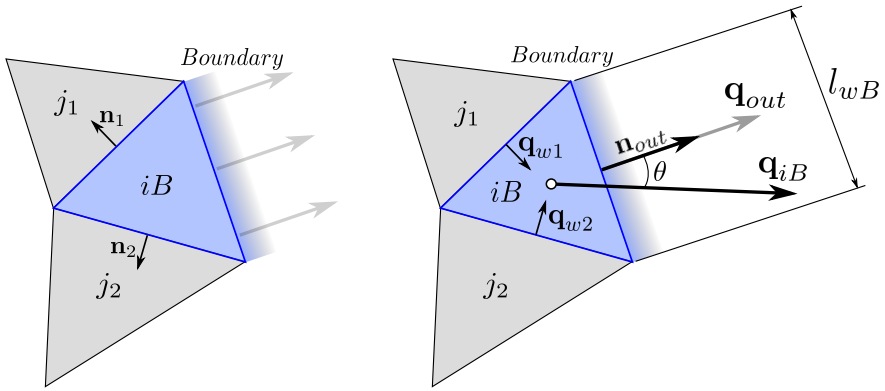

Figure 3.20: Free outflow boundary cell (left) and discharge integration scheme (right).

- *Inlet discharge*: By following the same procedure as for the outlet discharge, the inlet discharge hydrographs can be transformed into water depth variations in order to obtain an adequate boundary variable for the ZI equation.

Depth-positivity-preservation condition

In order to preserve the positive values of the water depth variable, a numerical fix proposed in [98] is used in this work. This condition automatically corrects the

value of water depth at each cell interface, avoiding non-physical negative values in complex situations, like dry-wet fronts in natural floodplains.

At each cell interface w (see Figure 3.21), a single value for the bed elevation is defined as:

$$\hat{z}_w = max(z_i, z_j) \tag{3.70}$$

The non-negative water depth is reconstructed at either side (i,j) of the interface (w):

$$\hat{h}_{i,j} = max(0, H_{i,j} - \hat{z}_w), \qquad H_{i,j} = h_{i,j} + z_{i,j} \tag{3.71}$$

The corresponding value of the water depth at the interface is obtained by averaging the values

$$\hat{h}_w = \frac{\hat{h}_i + \hat{h}_j}{2} \tag{3.72}$$

Then, the face-averaged α_w coefficients

$$\alpha_w^{n+\theta}(h) = \frac{\left(h_w^{n+\theta}\right)^{5/3}}{n_w \sqrt{|\mathbf{S}|_w}} \tag{3.73}$$

required in (3.49),(3.50) and (3.51) are calculated by using (3.72).

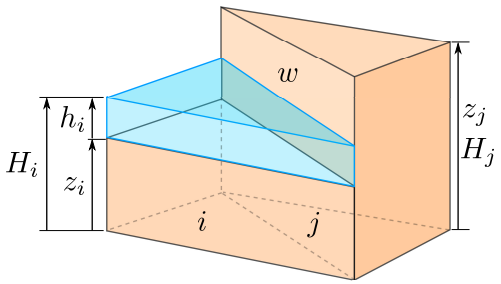

Figure 3.21: Cell interface with a dry-wet situation.

3.1.4 Application to 2D Groundwater flow model

Equation (2.61) is discretized by means of the same Finite Volume scheme. Hence by repeating the same steps and considering each cell as a control volume Ω, and by integrating (2.61) over a fixed cell:

$$\int_{\Omega} \eta \frac{\partial h}{\partial t} d\Omega = \int_{\Omega} K_s \nabla \left[(h - z) \nabla h \right] d\Omega + \int_{\Omega} S d\Omega \tag{3.74}$$

By applying a backwards Euler method for the time derivative, assuming η and k constant:

$$\begin{aligned} \eta \frac{h^{n+1} - h^n}{\Delta t} \Omega =& \theta K_s \int_{\partial\Omega} \left[\mathbf{f}^{n+1}(h) \mathbf{n} \right] \partial\Omega + \\ & (1 - \theta) K_s \int_{\partial\Omega} \left[\mathbf{f}(h)^n \mathbf{n} \right] \partial\Omega + S\Omega \end{aligned} \tag{3.75}$$

The flux of this model $\mathbf{f} = (h - z)\nabla h$ is a non-linear function of h. Considering the control volume Ω as equal to a finite volume A_i of the cell i with N_w polygonal faces of lenght l_w, each with an outer-pointing normal vector $\mathbf{n}_w$ and distance between centroids of the cells i and j defined as d_w:

$$\begin{aligned} \eta \frac{h_i^{n+1} - h_i^n}{\Delta t} A_i =& \theta K_s \sum_{j,w=1}^{N_w} \left(h_w^{n+1} - z_w \right) \frac{h_j^{n+1} - h_i^{n+1}}{d_w} l_w + \\ & (1 - \theta) K_s \sum_{j,w=1}^{N_w} \left(h_w^n - z_w \right) \frac{h_j^n - h_i^n}{d_w} l_w + S_i A_i \end{aligned} \tag{3.76}$$

This requires a linearization which is done by means of the fixed-point Picard iterations:

$$\begin{aligned} h_i^{n+1,m+1} - h_i^n =& \theta \frac{K_s \Delta t}{\eta A_i} \sum_{j,w=1}^{N_w} \left(h_w^{n+1,m} - z_w \right) \frac{h_j^{n+1,m+1} - h_i^{n+1,m+1}}{d_w} l_w + \\ & (1-\theta) \frac{K_s \Delta t}{\eta A_i} \sum_{j,w=1}^{N_w} \left(h_w^n - z_w \right) \frac{h_j^n - h_i^n}{d_w} l_w + \frac{\Delta t}{n} S_i \end{aligned} \tag{3.77}$$

The next step is to reorder equation (3.77). For simplicity of notation, temporal indices will not be shown:

$$h_w^{n+1,m} \equiv h_w^m, \qquad h_{i,j}^{n+1,m+1} \equiv h_{i,j}^{m+1} \tag{3.78}$$

Hence, whenever m or $m+1$ superindices are shown, it refers to time $n+1$ in the corresponding iteration. By reordering:

$$\begin{aligned} \left[1 + \theta \frac{K_s \Delta t}{\eta A_i} \sum_{w=1}^{N_w} \left(h_w^m - z_w \right) \frac{l_w}{d_w} \right] h_i^{m+1} - \theta \frac{K_s \Delta t}{\eta A_i} \sum_{j,w=1}^{N_w} \left(h_w^m - z_w \right) \frac{l_w}{d_w} h_j^{m+1} = \\ h_i^n + (1-\theta) \frac{K_s \Delta t}{\eta A_i} \sum_{j,w=1}^{N_w} \left(h_w^n - z_w \right) \frac{l_w}{d_w} \left(h_j - h_i \right) + \frac{\Delta t}{\eta} S_i \end{aligned} \tag{3.79}$$

Rewriting in a coefficient form:

$$a_i h_i^{m+1} + \sum_{j,w=1}^{N_w} b_w h_j^{m+1} = c_i \tag{3.80}$$

where

$$a_i = 1 + \theta \frac{K_s \Delta t}{\eta A_i} \sum_{w=1}^{N_w} \left(h_w^m - z_w \right) \frac{l_w}{d_w} \tag{3.81}$$

$$b_w = -\theta \frac{K_s \Delta t}{\eta A_i} \left(h_w^m - z_w \right) \frac{l_w}{d_w} \tag{3.82}$$

$$c_i = h_i^n + (1-\theta)\frac{K_s \Delta t}{\eta A_i} \sum_{j,w=1}^{N_w} \left(h_w^n - z_w\right) \frac{l_w}{d_w} \left(h_j - h_i\right) + \frac{\Delta t}{\eta} S_i \tag{3.83}$$

3.2 Systems of equations

3.2.1 Application to 1D Shallow Water equations

The extension of the numerical scheme (3.10) to 1D Shallow Water equations is next presented. Let us consider the system (2.62) and (2.63), here rewritten in conservative form:

$$\frac{\partial \mathbf{U}}{\partial t} + \frac{\partial \mathbf{F}}{\partial x} = \mathbf{S} \tag{3.84}$$

Following [79], in order to provide a local linearization of the fluxes

$$\delta \mathbf{F} = \tilde{\mathbf{J}} \delta \mathbf{U} \tag{3.85}$$

it is necessary to build an approximate Jacobian matrix $\tilde{\mathbf{J}}$ whose eigenvalues and eigenvectors satisfy:

$$\delta \mathbf{U}_{i+1/2} = \mathbf{U}_{i+1} - \mathbf{U}_i = \sum_{k=1}^{2} \left(\tilde{\alpha}_k \tilde{\mathbf{e}}_k\right)_{i+1/2} \tag{3.86}$$

$$\delta \mathbf{F}_{i+1/2} = \mathbf{F}_{i+1} - \mathbf{F}_i = \tilde{\mathbf{J}}_{i+1/2} \delta \mathbf{U}_{i+1/2} = \sum_{k=1}^{2} \left(\tilde{\lambda}_k \tilde{\alpha}_k \tilde{\mathbf{e}}_k\right)_{i+1/2} \tag{3.87}$$

The eigenvalues and eigenvectors are expressed in terms of the average flux velocity and wave speed:

$$\tilde{\lambda}_k = \left(\tilde{u} \pm \tilde{c}\right), \qquad \tilde{\mathbf{e}}_k = \left(\tilde{u} \pm \tilde{c}\right)^T \tag{3.88}$$

where

$$\tilde{u}_{i+1/2} = \frac{Q_{i+1}\sqrt{A_i} + Q_i\sqrt{A_{i+1}}}{\sqrt{A_i A_{i+1}}\left(\sqrt{A_{i+1}} + \sqrt{A_i}\right)} \tag{3.89}$$

$$\tilde{c}_{i+1/2} = \sqrt{\frac{g}{2}\left[\left(\frac{A}{b}\right)_i + \left(\frac{A}{b}\right)_{i+1}\right]} \tag{3.90}$$

The wave strenght coefficients $\tilde{\alpha}_k$ represent the variable variation coordinates in the Jacobian matrix basis and are given by

$$\tilde{\alpha}_1 = \frac{\tilde{\lambda}_2 \delta A - \delta Q}{2\tilde{c}}, \qquad \tilde{\alpha}_2 = \frac{-\tilde{\lambda}_1 \delta A + \delta Q}{2\tilde{c}} \tag{3.91}$$

Following [26], the source terms of the equation system (3.84) are also expressed on the basis of eigenvectors:

$$\left(\tilde{\mathbf{S}}\Delta x\right)_{i+1/2} = \left(\sum_{k+} \tilde{\beta}_k \tilde{\mathbf{e}}_k\right)_{i+1/2} + \left(\sum_{k-} \tilde{\beta}_k \tilde{\mathbf{e}}_k\right)_{i+1/2} \tag{3.92}$$

in which the source streghts $\tilde{\beta}_k$ take the role of $\tilde{\alpha}_k$ coefficients for the fluxes:

$$\tilde{\beta}_1 = -\frac{1}{2\tilde{c}}\left\{g\tilde{A}\left[\left(\tilde{S}_0 - \tilde{S}_f\right)\Delta x - \delta h + \frac{1}{\tilde{b}}\delta A\right]\right\}, \qquad \tilde{\beta}_2 = -\tilde{\beta}_1 \tag{3.93}$$

The reader is referred to Appendix B for further details on the calculation of α and β coefficients.

Then, the complete discretization of the system becomes:

$$\mathbf{U}_i^{n+1} = \mathbf{U}_i^n - \frac{\Delta t}{\Delta x}\left[\left(\sum_{k+}\left(\tilde{\lambda}_k\tilde{\alpha}_k - \tilde{\beta}_k\right)\tilde{\mathbf{e}}_k\right)_{i+1/2} + \left(\sum_{k-}\left(\tilde{\lambda}_k\tilde{\alpha}_k - \tilde{\beta}_k\right)\tilde{\mathbf{e}}_k\right)_{i+1/2}\right] \tag{3.94}$$

The upwind finite volume philosophy, when adapted to conservation laws with source terms, helps to formulate well-balanced schemes by means of a unified formulation of the flux derivatives and source terms as reported in [62, 26].

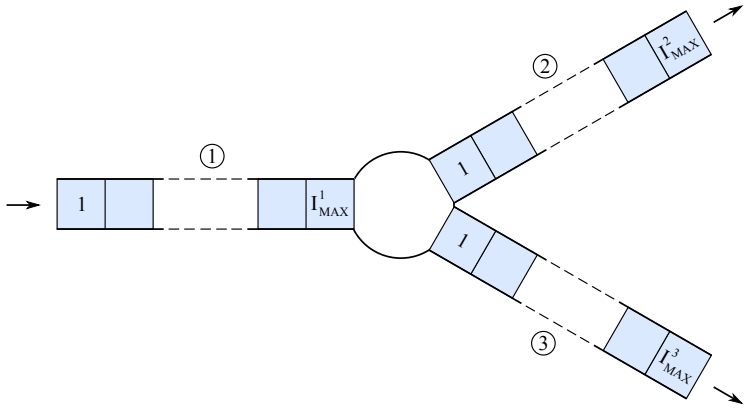

Figure 3.22: Example of pipe junction.

External boundary conditions

In order to solve a numerical problem, it is necessary to characterize the domain limits by imposing some physical boundary conditions (BC). The number of boundary conditions depends on the flow regime (subcritical or supercritical). Hence, there are four posibilities for a 1D numerical problem (see Table 3.1).

Flow regime and boundary	Number of physical BC to impose
Upstream subcritical flow	1
Upstream supercritical flow	2
Downstream subcritical flow	1
Downstream supercritical flow	0

Table 3.1: 1D SW model boundary conditions.

Internal boundary conditions

In the cases that consider pipe junctions, internal boundary conditions are necessary in order to model this feature. Figure 3.22 shows an example of a 3 pipe junction.

The water level equality condition is imposed at the junction for all the pipes:

$$h_2(1) = h_3(1) = h_1\left(I^1_{MAX}\right) \tag{3.95}$$

Discharge continuity condition is formulated depending on the flow regime. If water flows in a subcritical regime at the junction:

$$Q_1\left(I^1_{MAX}\right) = Q_2(1) + Q_3(1) \tag{3.96}$$

On the other hand, if the flow regime is supercritical:

$$Q_2(1) = Q_3(1) = \frac{1}{2}Q_1\left(I^1_{MAX}\right) \tag{3.97}$$

Storage wells are another common junction type. For these cases, the boundary conditions are modified as follows:

$$h_1 = h_2 = h_3 = H_{well}, \qquad \sum_{i=1}^{N} Q_i = A_{well}\frac{dH_{well}}{dt} \tag{3.98}$$

where A_{well} and H_{well} are the well top area and depth, respectively.

Stability condition

The Courant-Friedrichs-Lewy (CFL) condition is applied on every branch j of the network:

$$\Delta t^j_{max} = \frac{\Delta x^j}{max\left(|u^j| + c^j\right)} \tag{3.99}$$

Then, the minimum of all the computed time steps is chosen:

$$\Delta t_{max} = \min\left\{\Delta t^j_{max}\right\}, \qquad CFL = \frac{\Delta t}{\Delta t_{max}} \leq 1 \tag{3.100}$$

3.2.2 Application to 2D Shallow Water equations

The extension of the scheme (3.30) to system of equations is next described for the 2D Shallow Water equations. Let us consider a system of equations, written in conservative form:

$$\frac{\partial \mathbf{U}}{\partial t} + \frac{\partial \mathbf{F}}{\partial x} + \frac{\partial \mathbf{G}}{\partial y} = \mathbf{S} \tag{3.101}$$

The 2D extension of the finite volume method to a system of equations with source terms leads to:

$$\frac{d}{dt}\int_{\Omega} \mathbf{U} d\Omega + \int_{\Omega} (\nabla \cdot \mathbf{E}) d\Omega = \int_{\Omega} \mathbf{S} d\Omega \tag{3.102}$$

$$\frac{d}{dt}\int_{\Omega} \mathbf{U} d\Omega + \sum_{j,w=1}^{N_w} (\delta \mathbf{E} \cdot \mathbf{n})_w^- l_w = \sum_{j,w=1}^{N_w} \mathbf{S}_w^- l_w \tag{3.103}$$

Hence:

$$\frac{\Delta \mathbf{U}_i}{\Delta t} S_i + \sum_{j,w=1}^{N_w} (\delta \mathbf{E} \cdot \mathbf{n})_w^- l_w = \sum_{j,w=1}^{N_w} \mathbf{S}_w^- l_w \tag{3.104}$$

The focus in (3.104) is put on the flux and source terms contributions defined at the grid edges w. The difference in vector $\mathbf{U}$ across the grid edge and the source term can be projected onto the matrix eigenvectors basis, as follows:

$$\delta \mathbf{U}_w = \mathbf{U}_j - \mathbf{U}_i = \tilde{\mathbf{P}}_w \mathbf{A}_w, \qquad \mathbf{S}_w = \frac{1}{2}(\mathbf{S}_i + \mathbf{S}_j) = \tilde{\mathbf{P}}_w \mathbf{B}_w \tag{3.105}$$

being $\mathbf{A}$ and $\mathbf{B}$ the wave and source strength vectors, given by:

$$\mathbf{A}_w = (\alpha^1, \alpha^2, \alpha^3)_w^T, \qquad \mathbf{B}_w = (\beta^1, \beta^2, \beta^3)_w^T \tag{3.106}$$

Then, the flux and source terms in (3.102) can be expressed as follows:

$$\delta(\mathbf{E} \cdot \mathbf{n})_w = \mathbf{J}_n \delta \mathbf{U}_w = \sum_{m=1}^{3} (\tilde{\lambda} \alpha \tilde{\mathbf{e}})_w^m, \qquad \mathbf{S}_w = \sum_{m=1}^{3} (\beta \tilde{\mathbf{e}})_w^m \tag{3.107}$$

The time evaluation of the flux terms in (3.104) is done by means of the implicitness parameter θ:

$$\frac{\Delta \mathbf{U}_i}{\Delta t} S_i + \theta \sum_{j,w=1}^{N_w} \left[(\delta \mathbf{E} \cdot \mathbf{n})_w^- \right]^{n+1} l_w + (1-\theta) \sum_{j,w=1}^{N_w} \left[(\delta \mathbf{E} \cdot \mathbf{n})_w^- \right]^{n} l_w = \sum_{j,w=1}^{N_w} \left(\mathbf{S}_w^- \right)^n l_w \tag{3.108}$$

with a linearization for the fluxes given by [14]:

$$(\delta \mathbf{E} \cdot \mathbf{n})_w^{n+1} \approx (\delta \mathbf{E} \cdot \mathbf{n})_w^n + \mathbf{J}_{n,w} \Delta \mathbf{U}_j - \mathbf{J}_{n,w} \Delta \mathbf{U}_i \tag{3.109}$$

By replacing (3.109) in (3.108), upwinding the Jacobian and reordering:

$$\mathbf{aa}_i \Delta \mathbf{U}_i + \sum_{j,w=1}^{N_w} \mathbf{bb}_w \Delta \mathbf{U}_j = \mathbf{k}_i \tag{3.110}$$

with

$$\mathbf{aa}_i = \mathbf{I} - \theta \frac{\Delta t}{S_i} \sum_{w=1}^{N_w} \left(\mathbf{J}_{n,w}^- \right)^n l_w \tag{3.111}$$

$$\mathbf{bb}_w = \theta \frac{\Delta t}{S_i} \left(\mathbf{J}_{n,w}^- \right)^n l_w \tag{3.112}$$

$$\mathbf{k}_i = -\frac{\Delta t}{S_i} \sum_{w=1}^{N_w} \left[(\delta \mathbf{E} \cdot \mathbf{n})_w^- \right]^n l_w + \frac{\Delta t}{S_i} \sum_{w=1}^{N_w} \left(\mathbf{S}_w^- \right)^n l_w \tag{3.113}$$

Expressions (3.110) to (3.113) together with the proper boundary conditions represent a system of equations conforming a $3N_{cells} \times 3N_{cells}$ matrix built in terms of 3×3 block matrices as follows:

$$\tilde{\mathbf{A}} \mathbf{X} = \mathbf{k} \tag{3.114}$$

The linear system (3.114) needs to be solved by means of a matrix inversion technique. For a structured squared mesh, this results in a $3N_{cells} \times 3N_{cells}$ multi-diagonal-block matrix (3.115), whereas an unstructured triangular mesh generates

a $3N_{cells} \times 3N_{cells}$ block-matrix (3.116):

$$\begin{pmatrix} \mathbf{aa}_1 & \mathbf{bb}_w & & \mathbf{bb}_w & & & \\ \mathbf{bb}_w & \mathbf{aa}_2 & \mathbf{bb}_w & & \mathbf{bb}_w & & \\ & \ddots & \ddots & \ddots & & \ddots & \\ \mathbf{bb}_{j1} & & \mathbf{bb}_{j4} & \mathbf{aa}_i & \mathbf{bb}_{j2} & & \mathbf{bb}_{j3} \\ & \ddots & & \ddots & \ddots & \ddots & \mathbf{bb}_w \\ & & \mathbf{bb}_w & & \mathbf{bb}_w & \mathbf{aa}_{N-1} & \\ & & & \mathbf{bb}_w & & \mathbf{bb}_w & \mathbf{aa}_N \end{pmatrix} \begin{pmatrix} \Delta\mathbf{U}_1 \\ \Delta\mathbf{U}_2 \\ \vdots \\ \Delta\mathbf{U}_i \\ \vdots \\ \Delta\mathbf{U}_{N-1} \\ \Delta\mathbf{U}_N \end{pmatrix} = \begin{pmatrix} \mathbf{k}_1 \\ \mathbf{k}_2 \\ \vdots \\ \mathbf{k}_i \\ \vdots \\ \mathbf{k}_{N-1} \\ \mathbf{k}_N \end{pmatrix} \tag{3.115}$$

$$\begin{pmatrix} \mathbf{aa}_1 & & \mathbf{bb}_w & & \mathbf{bb}_w & & \mathbf{bb}_w \\ \mathbf{bb}_w & \mathbf{aa}_2 & & \mathbf{bb}_w & \mathbf{bb}_w & & \\ & \mathbf{bb}_w & \mathbf{aa}_3 & & & \mathbf{bb}_w & \mathbf{bb}_w \\ & & & \ddots & & & \\ & & & & \ddots & & \\ & \mathbf{bb}_w & \mathbf{bb}_w & \mathbf{bb}_w & & \mathbf{aa}_{N-1} & \\ \mathbf{bb}_w & & \mathbf{bb}_w & & \mathbf{bb}_w & & \mathbf{aa}_N \end{pmatrix} \begin{pmatrix} \Delta\mathbf{U}_1 \\ \Delta\mathbf{U}_2 \\ \Delta\mathbf{U}_3 \\ \vdots \\ \vdots \\ \Delta\mathbf{U}_{N-1} \\ \Delta\mathbf{U}_N \end{pmatrix} = \begin{pmatrix} \mathbf{k}_1 \\ \mathbf{k}_2 \\ \mathbf{k}_3 \\ \vdots \\ \vdots \\ \mathbf{k}_{N-1} \\ \mathbf{k}_N \end{pmatrix} \tag{3.116}$$

being

$$\mathbf{dd}_i = \begin{pmatrix} dd_i^{11} & dd_i^{12} & dd_i^{13} \\ dd_i^{21} & dd_i^{22} & dd_i^{23} \\ dd_i^{31} & dd_i^{32} & dd_i^{33} \end{pmatrix} \tag{3.117}$$

$$\mathbf{aa}_i = \begin{pmatrix} aa_i^{11} & aa_i^{12} & aa_i^{13} \\ aa_i^{21} & aa_i^{22} & aa_i^{23} \\ aa_i^{31} & aa_i^{32} & aa_i^{33} \end{pmatrix}, \qquad \mathbf{bb}_i = \begin{pmatrix} bb_i^{11} & bb_i^{12} & bb_i^{13} \\ bb_i^{21} & bb_i^{22} & bb_i^{23} \\ bb_i^{31} & bb_i^{32} & bb_i^{33} \end{pmatrix} \tag{3.118}$$

$$\Delta \mathbf{U}_i = \begin{pmatrix} \Delta \mathbf{U}^1 \\ \Delta \mathbf{U}^2 \\ \Delta \mathbf{U}^3 \end{pmatrix}_i, \qquad \mathbf{k}_i = \begin{pmatrix} k^1 \\ k^2 \\ k^3 \end{pmatrix}_i \tag{3.119}$$

The approximate Jacobian $\mathbf{J}_{n,w}$ of the 2D Shallow Water system (3.101)-(2.12) together with the source and wave strengths are constructed in terms of the averaged variables, corresponding to Roe's approximate Riemann solver [79]:

$$\tilde{u}_w = \frac{u_i\sqrt{h_i} + u_j\sqrt{h_j}}{\sqrt{h_i} + \sqrt{h_j}}, \qquad \tilde{v}_w = \frac{v_i\sqrt{h_i} + v_j\sqrt{h_j}}{\sqrt{h_i} + \sqrt{h_j}}, \qquad \tilde{c}_w = \sqrt{g\frac{h_i + h_j}{2}} \tag{3.120}$$

This results in the next eigenvalues and eigenvectors:

$$\tilde{\lambda}^1_w = (\tilde{\mathbf{u}} \cdot \mathbf{n} + \tilde{c})_w, \qquad \tilde{\lambda}^2_w = (\tilde{\mathbf{u}} \cdot \mathbf{n})_w, \qquad \tilde{\lambda}^3_w = (\tilde{\mathbf{u}} \cdot \mathbf{n} - \tilde{c})_w \tag{3.121}$$

$$\tilde{\mathbf{e}}^1_w = \begin{pmatrix} 1 \\ \tilde{u} + \tilde{c}n_x \\ \tilde{v} + \tilde{c}n_y \end{pmatrix}_w, \qquad \tilde{\mathbf{e}}^2_w = \begin{pmatrix} 0 \\ -\tilde{c}n_y \\ \tilde{c}n_x \end{pmatrix}_w, \qquad \tilde{\mathbf{e}}^3_w = \begin{pmatrix} 1 \\ \tilde{u} - \tilde{c}n_x \\ \tilde{v} - \tilde{c}n_y \end{pmatrix}_w \tag{3.122}$$

The wave strengths α and source strengths β coefficients in (3.106) are given by:

$$\alpha^{1,3}_w = \frac{\delta h_w}{2} \mp \frac{1}{2\tilde{c}_w}[\delta(hu)n_x + \delta(hv)n_y - \tilde{\mathbf{u}}\cdot\mathbf{n}\delta h]_w = \frac{\delta h_w}{2} \mp \frac{1}{2\tilde{c}_w}(\delta \mathbf{q}_w - \tilde{\mathbf{u}}_w \delta h_w)\mathbf{n} \tag{3.123}$$

$$\alpha^2_w = \frac{1}{\tilde{c}_w}[(\delta(hv) - \tilde{v}\delta h)n_x - (\delta(hu) - \tilde{u}\delta h)n_y]_w \tag{3.124}$$

$$\beta^1_w = -\frac{1}{2}\tilde{c}_w \left(\delta z + S_f d_n\right)_w = -\beta^3_w, \qquad \beta^2_w = 0 \tag{3.125}$$

The magnitude d_n is the normal distance between neighbour cell centers and $S_{f,w}$ represents the discrete energy grade line for the bidimensional case [62]:

$$S_{f,w} = \frac{\tilde{n}_w^2 \tilde{\mathbf{u}} \cdot \mathbf{n} \, |\tilde{\mathbf{u}}|}{\max\left(h_i, h_j\right)^{4/3}} \tag{3.126}$$

being

$$\tilde{n}_w = \frac{1}{2}\left(n_i + n_j\right) \tag{3.127}$$

the average Manning's roughness coefficient at the interface w.

Finally, by applying an upwind treatment to the fluxes and source terms:

$$\tilde{\lambda}_w^{\pm,m} = \frac{1}{2}(\tilde{\lambda} \pm |\tilde{\lambda}|)_w^m \tag{3.128}$$

$$\beta_w^{1-,3-} = \frac{1}{2}\beta_w^{1,3}[1 - sign(\tilde{\lambda}_w^{1,3})], \qquad \beta_w^2 = 0 \tag{3.129}$$

Boundary conditions

It is necessary to formulate adequately several boundary conditions in order to model any physical situation. Four different boundary conditions are used: closed boundaries, h-fixed, Q-fixed and free outflow (see Figure 3.23).

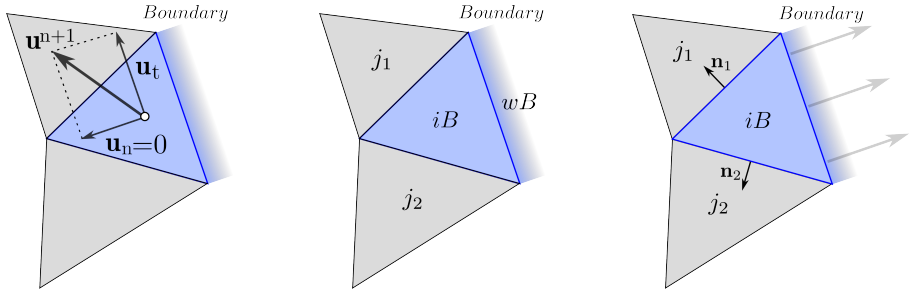

Figure 3.23: Closed wall (left), h- or Q-fixed (center) and free outflow (right) boundary conditions.

- *Closed boundaries*: They are considered as solid walls that completely block the water flow. When a closed boundary is chosen, the model sets zero normal flow across the boundary, but allows tangential velocities (see Figure 3.23, left).

- *h-fixed*: In order to impose fixed values of the water depth h, the boundary value h_{fixed} is set as the new value for the boundary cell iB at time $n+1$ (see Figure 3.23, center), as follows:

$$h_{iB}^{n+1} = h_{fixed} \tag{3.130}$$

- *Q-fixed*: The imposed inlet water discharge Q (Figure 3.23, center) needs to be converted to unit discharge x and y components, $q_x = hu$ and $q_y = hv$, respectively, by dividing by the inlet segment length L_{inlet} and taking into account the inlet direction (see Figure 3.24), as follows:

$$q_x = \frac{Q}{L_{inlet}} \cos\varphi, \qquad q_y = \frac{Q}{L_{inlet}} \sin\varphi \tag{3.131}$$

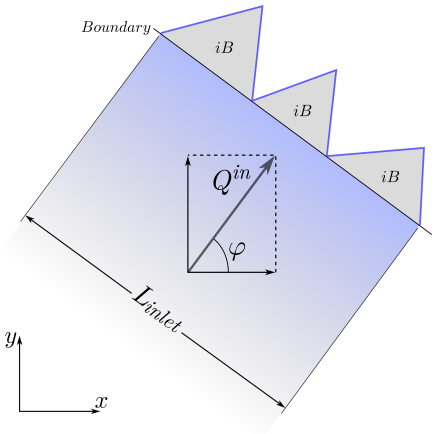

Figure 3.24: Inlet water discharge boundary condition.

- *Free outflow*: On free outflow boundary conditions (see Figure 3.23, right), the model calculates water depths and unit discharges applying the full equations from the internal cells. Hence, no condition is imposed on these nodes. This should be equivalent to assuming that spatial derivatives of water level $(h + z)$ and velocities are equal to zero.

Source terms limitation and wet/dry treatment

In this work, the strategy followed in [62] for an explicit Godunov finite volume scheme is adapted to the implicit scheme presented. First the discrete friction terms

are limited avoiding them to change the sign of the velocity within one time step. By splitting them into a sum of two components β_S^m (bed slope) and β_F^m (friction)

$$\beta^m = \beta_S^m + \beta_F^m, \qquad m = 1, 2, 3. \tag{3.132}$$

it is feasible to define the following quantities coming from the Riemann Problem between cells i and j at edge w:

$$\begin{aligned} q_i^* &= (hu_i + \alpha^1 \tilde{\mathbf{e}}_2^1) n_x + (hv_i + \alpha^1 \tilde{\mathbf{e}}_3^1) n_y - \beta_S^1 - \beta_F^1 \\ q_i^\nabla &= (hu_i + \alpha^1 \tilde{\mathbf{e}}_2^1) n_x + (hv_i + \alpha^1 \tilde{\mathbf{e}}_3^1) n_y - \beta_S^1 \end{aligned} \tag{3.133}$$

In case that $q_i^\nabla q_i^* < 0$ the effect of friction terms is overestimated to the extent that flow could move back, resulting in an impossible situation. Accordingly, the friction terms should be redefined as:

$$\beta_F^1 = \begin{cases} q_i^\nabla & \text{if} \quad q_i^\nabla q_i^* < 0 \\ \beta_F^1 & \text{otherwise} \end{cases}, \qquad \beta_F^3 = -\beta_F^1 \tag{3.134}$$

in order to preserve the sign of the discharge.

Additionally, negative values in the water depth can appear due to the wrong estimation of linearized source terms β^m in subcritical flow [62]. In order to avoid this undesirable situation, the following quantities can be defined with the aim of limiting the source terms amount:

$$\begin{aligned} h_i^* = h_i^n + \left(\alpha^1 - \frac{\beta^1}{\tilde{\lambda}^1}\right)_w \geq 0, \qquad h_j^{**} = h_j^n - \left(\alpha^2 - \frac{\beta^2}{\tilde{\lambda}^2}\right)_w \geq 0 \\ \beta_{min}^1 = (h_i^n + \alpha^1)\tilde{\lambda}^1, \qquad \beta_{min}^2 = (-h_j^n + \alpha^2)\tilde{\lambda}^2 \end{aligned} \tag{3.135}$$

Therefore:

- If $h_i^* < 0$ and $h_j^{**} > 0$, β^1 is redefined not only to ensure conservation, i.e., $\beta^2 = -\beta^1$ but also to produce a non-negative value h_j^{**}:

$$\beta^1 = \begin{cases} \beta^1_{min} & \text{if} \quad -\beta^1_{min} \geq \beta^2_{min} \\ \beta^1 & \text{otherwise} \end{cases}, \qquad \beta^2 = -\beta^1 \tag{3.136}$$

- If $h_i^* > 0$ and $h_j^{**} < 0$, β^2 is also redefined:

$$\beta^2 = \begin{cases} \beta^2_{min} & \text{if} \quad -\beta^2_{min} \geq \beta^1_{min} \\ \beta^2 & \text{otherwise} \end{cases}, \qquad \beta^1 = -\beta^2 \tag{3.137}$$

These cheap and simple corrections when discretizing the source terms allow to build robust solutions recovering the conventional CFL condition, avoiding large reductions in the time step size to ensure positive solutions [64]. The conservation property or C-property [7], which requires the preservation of equilibrium states, is ensured by a proper discretization of the explicit part in $\mathbf{k}$.

Time step size

As in the 2D scalar case (Section 3.1.2), the time step is dynamically chosen as follows:

$$\Delta t = \text{CFL} \min_{Mesh}(\Delta t_{i,w}) \tag{3.138}$$

where

$$\Delta t_{i,w} = \frac{\min(\Delta x'_i, \Delta x'_j)}{\max_{m=1,2,3}(|\tilde{\lambda}^m_w|)}, \qquad \Delta x'_i = \frac{S_i}{max_{1,N_w}(l_w)} \tag{3.139}$$

Therefore, the CFL number becomes a multiplicative factor of the maximum time step allowed by the explicit scheme. The present formulation follows closely the results in [62] where the influence of the source terms was controlled by means of the augmented Riemann solver.

3.3 Algorithm organization and coupling mechanisms

3.3.1 General flowchart for implicit models

All the implicit submodels presented in this thesis follows the same main steps. Within a simulation time loop (see Figure 3.25), two main algorithms run in every time step: 1) the matrix construction process and 2) the solution calculation by means of a matrix solver. If the system has a non-linear nature, these two steps are repeated within a linearization loop until convergence is achieved.

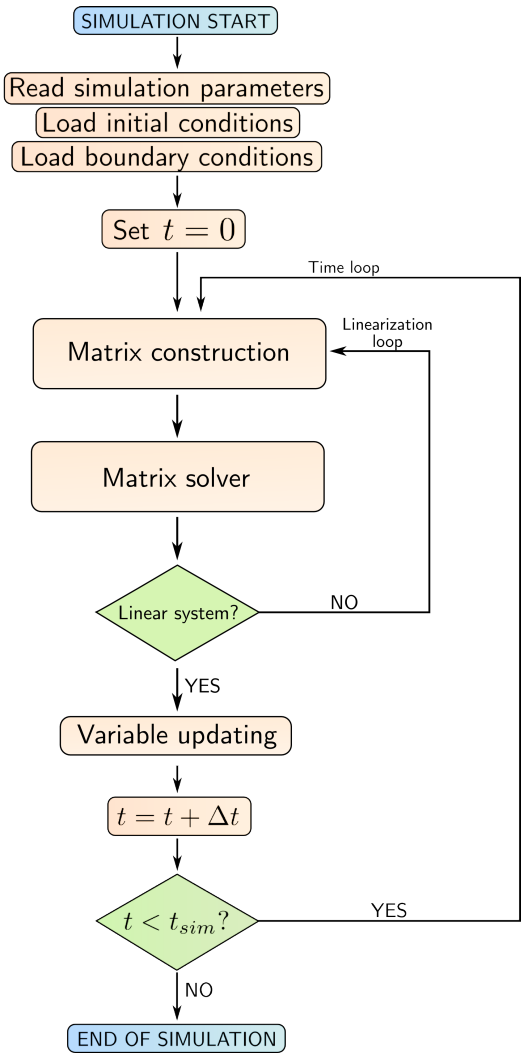

Figure 3.25: General flowchart for implicit models.

3.3.2 Overland and groundwater model coupling mechanisms

Overland and groundwater flow models are coupled by means of two ways: 1) The water exchange at the soil surface, which is computed by means of the infiltration rate f in the surface and 2) Infiltration/Exfiltration processes, based on the comparision between the surface water level $h + z$ with the groundwater phreatic level h_s.

- *Water exchange at the soil surface*:

Water exchange through the soil is one of the connection mechanisms between surface and groundwater flow models. Water from rainfall or surface flow infiltrates and may recharge the phreatic level (PL), as shown in Figure 3.26.

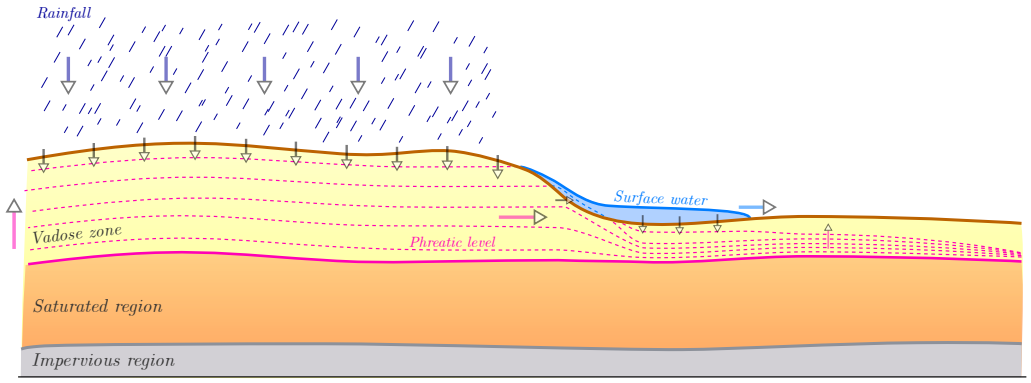

Figure 3.26: Phreatic level recharging and water exchange in a typical surface-groundwater interaction.

- *Infiltration*:

If the surface water level $h + z$ of the cell i exceeds the phreatic level h_s of the neighbour cell j, infiltration through the common wall occurs (Figure 4.78, left). The phreatic level is modified as follows:

$$(h + z)_i > h_{s,j} \Rightarrow h_{s,j} = (h + z)_i \tag{3.140}$$

- *Exfiltration*:

If the phreatic surface exceeds the water level value of the adjacent cell exfiltration occurs (Figure 4.78, right). This is modeled by applying a correction on the solution for the surface water depth h as follows:

$$(h+z)_i < h_{s,j} \Rightarrow h_i = h_{s,j} - z_i \tag{3.141}$$

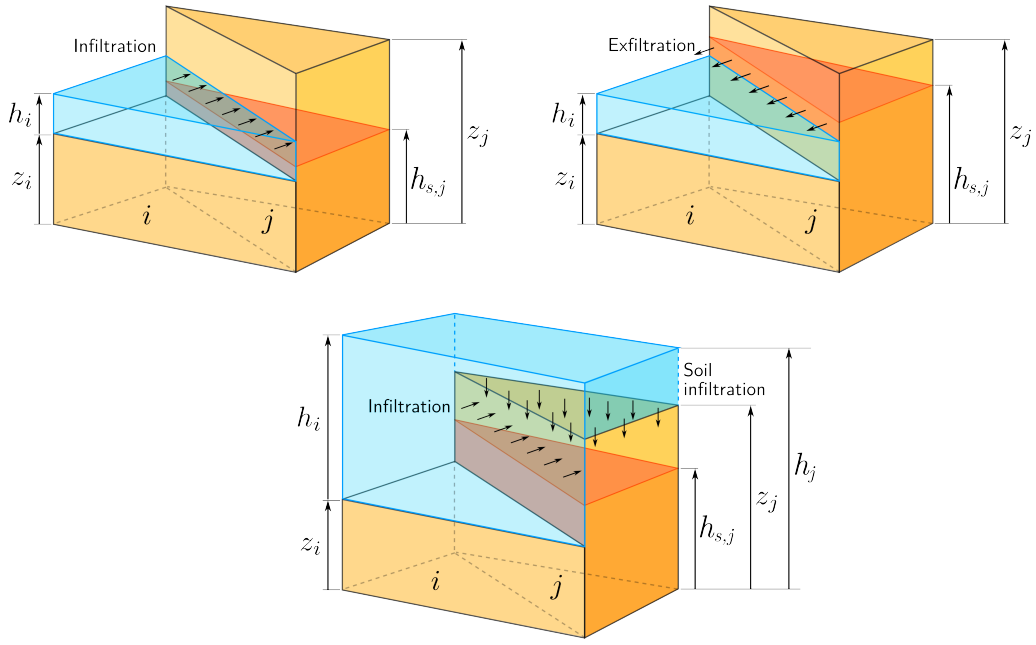

Figure 3.27: Infiltration (left), exfiltration (right) and an example of combination of exchange processes (lower).

Figure 3.28 shows a schematic flowchart with the main steps of the simulation for the surface-groundwater coupled model.

3.3.3 Using different time steps

In order to reduce the computational cost of the simulations a time step optimization strategy has been implemented. Since the groundwater flow is expected to be much slower that the overland flow and the model benefit from the inconditional stability of the implicit scheme, larger subsurface time steps shall be used. Both surface and subsurface model communicate every N-th surface time steps, as shown in Figure 3.29.

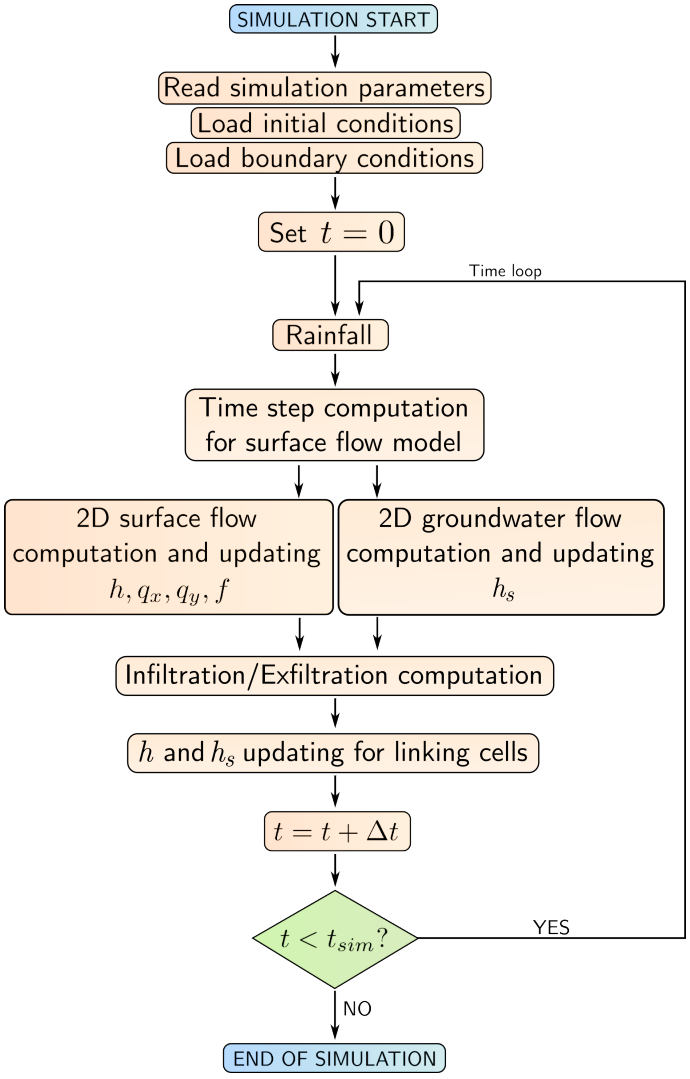

Figure 3.28: Surface-Groundwater coupled model flowchart.

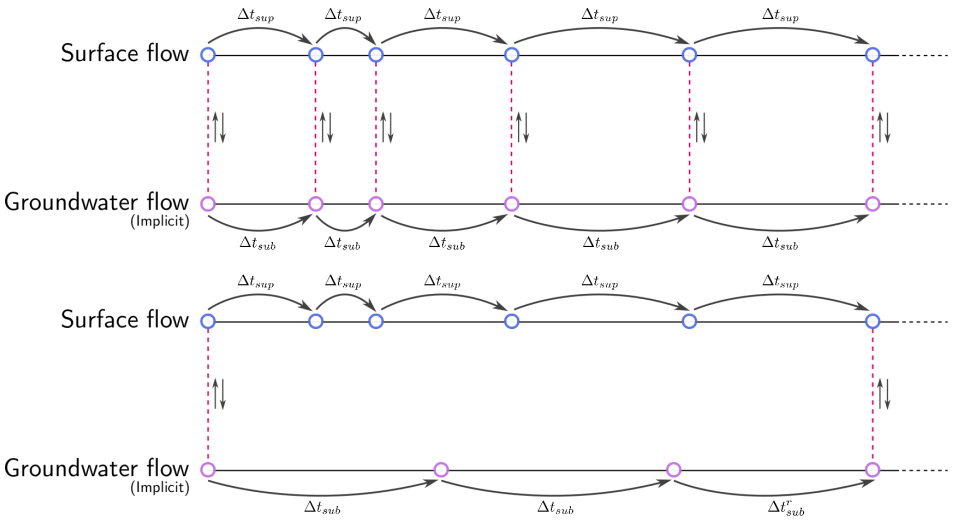

Figure 3.29: Same time step value for both surface and subsurface models (upper). Establishing the communication after N implicit time steps (lower).

3.3.4 2D overland flow + 1D drainage: Exchange between submodels

Several situations regarding the flow exchange between the surface flow and the sewer system can take place. Figure 3.30 displays all the possible scenarios: 1) Inflow into non-pressurized sewer, 2) Inflow into pressurized sewer, 3). Outflow over floodplain (wet or dry). Every time step, an internal algorithm compares the values of the surface water depth (h), pressure head in the pipe (h_p) and the distance between the bed of the flume and the invert level of the sewer ($H = z + (z_p + H_{max})$), in order to adequately estimate the exchange discharge in terms of the diameter of the manhole D_M, area of the manhole A_M, and a coefficient C which accounts for the energy losses at the manhole. The particular form used to formulate the exchange discharge Q_e follows closely the formulation suggested in [80].

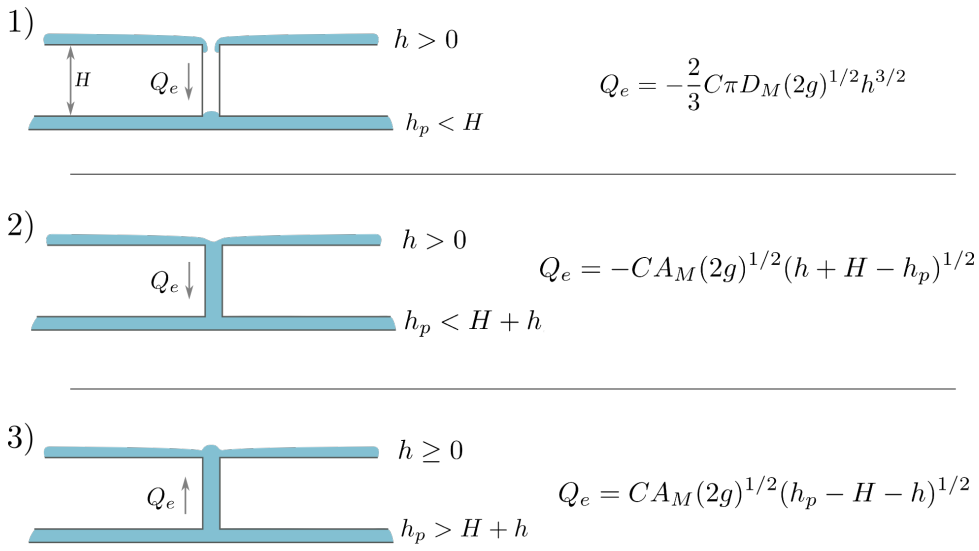

Figure 3.30: Possible hydraulic scenarios in the coupled model.

3.3.5 2D overland flow + 1D drainage: Time step synchronization

The 1D system is solved by means of a SW model scheme using an explicit time discretization ($\theta = 0$) and therefore it requires a control on the time step in order to avoid numerical instabilities. Hence the Courant-Friedrichs-Lewy (CFL) condition (see Section 3.2.1).

The coupled model can be built combining explicit drainage model with either the explicit 2D surface model or with the implicit 2D surface model. As the computation

progresses from the initial condition to the future times using a global time step, the fully explicit combination requires to use the most restrictive time step, so that

$$\Delta t = \min(\Delta t_{1D}, \Delta t_{2D}) \tag{3.142}$$

Figure 3.31 shows a schematic flowchart of the different model components.

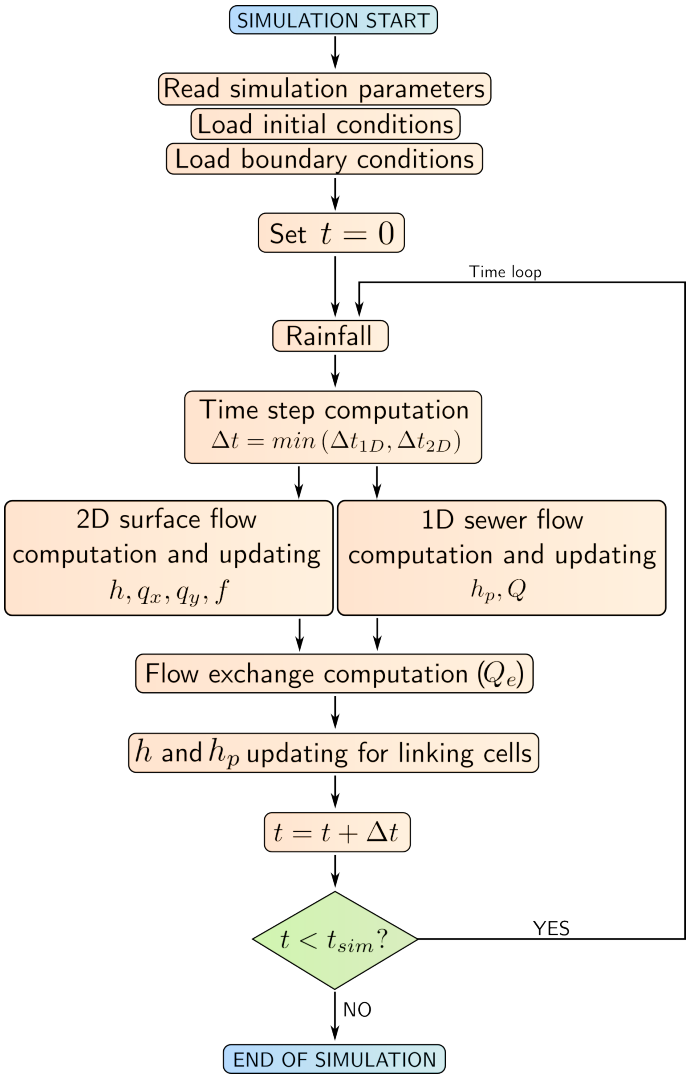

Figure 3.31: Surface-Sewer coupled model flowchart.

CHAPTER 4

Single model test cases

4.1 Zero-dimensional (0D) infiltration tests for unsteady rainfall conditions

In this section, a set of test cases is presented in order to evaluate the application of the infiltration models under different rainfall and initial conditions. The main goal is to understand the influence of their parameters before inserting them in a 2D model for the surface flow simulation.

4.1.1 SCS-CN model

Some illustrative and verification examples (see Table 4.1) are presented now in Figures 4.1(a) to 4.1(e). For all the cases the parameters considered are $CN = 80$ and $\alpha = 0.2$. Case 3 is taken from [90]. These examples show that the SCS model estimates the precipitation losses under steady (Cases 1 and 2) and unsteady rainfall patterns (Cases 3, 4 and 5). When rainfall stops, the model freezes the water losses (Cases 2, 4 and 5) even in the presence of surface water. This could be a possible

Case	Description
1	Steady rain event
2	Steady intermittent rain event
3	Unsteady storm pattern
4	Unsteady wet-dry-wet storm pattern
5	Natural storm pattern from dry conditions

Table 4.1: Summary of the SCS model test cases.

drawback when the model is applied to complex topographies where ponded areas are likely to appear.

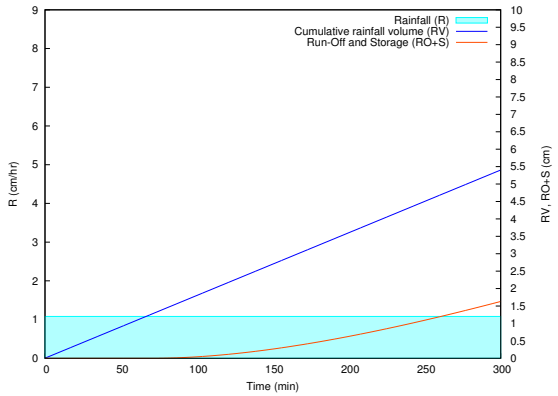

(a) SCS case 1

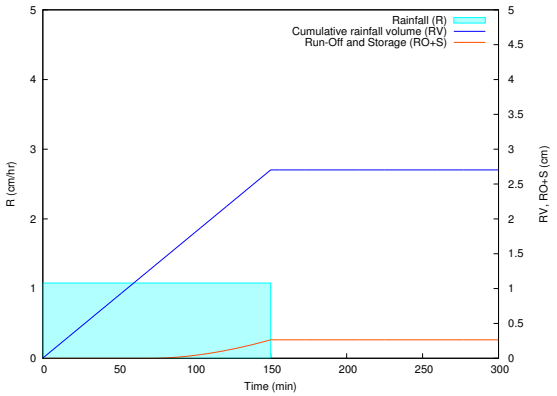

(b) SCS case 2

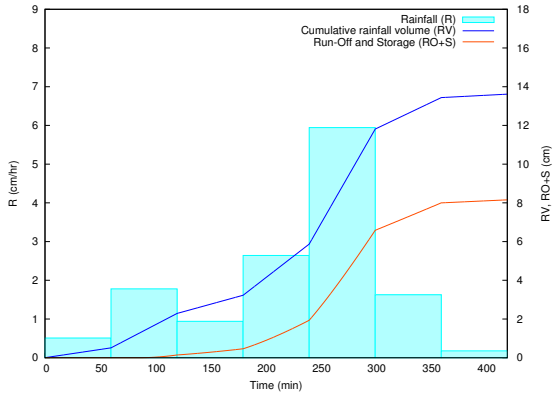

(c) SCS case 3

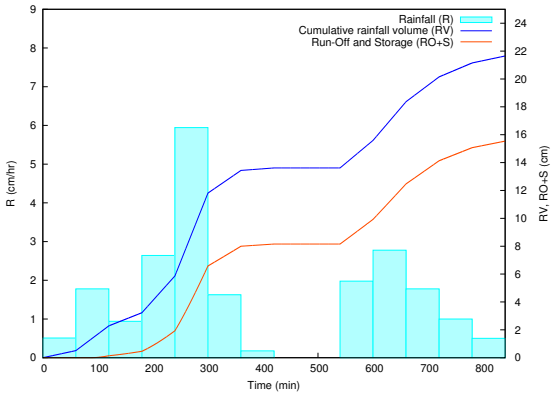

(d) SCS case 4

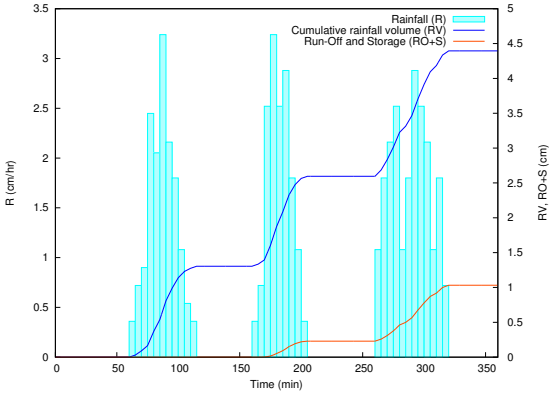

(e) SCS case 5

Figure 4.1: SCS model test cases.

4.1.2 Horton model

A case collection for testing the implementation of the Horton infiltration model is presented now. These cases try to consider all the possible phenomenology in terms of rainfall and initial conditions for a given setup. The same parameters have been considered for all the cases proposed: $f_0 = 8cm/h$, $f_c = 1.25cm/h$ and $k = 3h^{-1}$.

Case	Description
0	Ponded soil with no rain
1	Steady rain event with $R < f_c$
2	Steady rain event with $R > f_0$
3	Steady rain event with $f_c < R < f_0$
4	Steady rain event + Initial surface water with $R < f_c$
5	Steady rain event + Initial surface water 1 with $f_c < R < f_0$
6	Steady rain event + Initial surface water 2 with $f_c < R < f_0$
7	Steady intermittent rain event with $f_c < R < f_0$
8	Steady intermittent rain event + Initial surface water 1 with $f_c < R < f_0$
9	Steady intermittent rain event + Initial surface water 2 with $f_c < R < f_0$
10	Unsteady storm pattern
11	Unsteady wet-dry-wet storm pattern
12	Unsteady dry-wet-dry-wet storm pattern
13	Unsteady dry-wet-dry-wet storm pattern + Initial surface water 1
14	Unsteady dry-wet-dry-wet storm pattern + Initial surface water 2
15	Natural storm pattern from dry conditions
16	Natural storm pattern + Initial surface water 1
17	Natural storm pattern + Initial surface water 2
18	Natural storm pattern + Initial surface water + Water inlet 1
19	Natural storm pattern + Initial surface water + Water inlet 2
20	Natural storm pattern + Initial surface water + Water inlet 3

Table 4.2: Summary of the Horton infiltration cases.

Case 0. Ponded soil with no rain. The simplest case is a permanent ponded soil. The infiltration rate and cumulative infiltration curves predicted for this situation by the Horton model are shown in Figure 4.2.

Case 1. Steady rain event 1. If rainfall intensity is less than the asymptotic final infiltration rate ($R \leq f_c$), all the water coming from rainfall becomes infiltrated into the soil, as shown in Figure 4.3(a).

Case 2. Steady rain event 2. In this case, the rainfall intensity exceeds the soil infiltration capacity from the beginning $R > f_0$. This implies that the surface

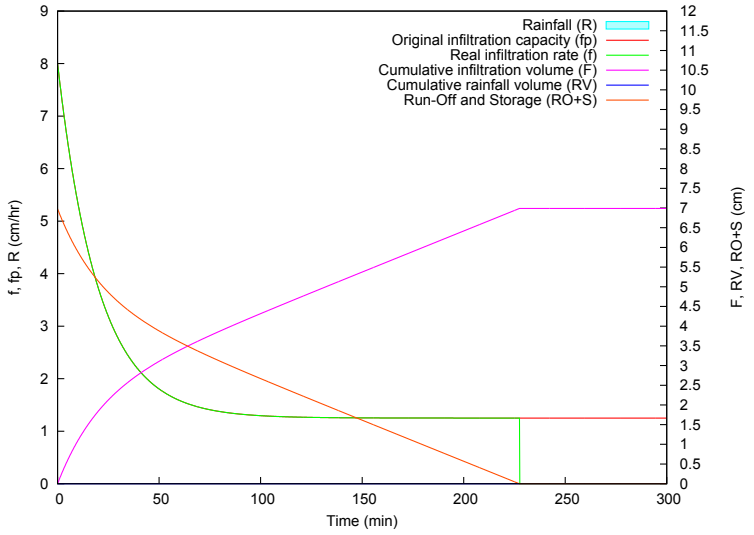

Figure 4.2: Horton infiltration Case 0 (Permanent ponded soil).

is continuously ponded and hence the actual infiltration rate is the same curve than the one infiltration capacity f_p predicted by Horton model (see Figure 4.3(b)).

Case 3. Steady rain event 3. In this case, the rainfall rate takes a value between f_c and f_0. Initially, the soil infiltration capacity is greater than the rain intensity, so all the water infiltrates. After a time of $25min$ (ponding time, t_p), the infiltration capacity falls below the rainfall rate and surface ponding begins (see Figure 4.3(c)).

Case 4, 5, 6. Steady rain event + Initial surface water. The purpose of these cases is to check the dominance of the initial surface water level over the rainfall. When all the surface water infiltrates, the rainfall intensity determines the real infiltration rate f (see Figures 4.3(d), 4.3(e), 4.3(f))

Case 7. Steady intermittent rain event. A test case with intermittent rainfall is presented now. No surface water is considered at the beginning, so the infiltration rate and the cumulative infiltration are frozen in time until rainfall starts (Figure 4.4(a)). In this point, all the rainfall is being infiltrated until the ponding time is met, since then the soil becomes ponded and both f_p and f curves coincide.

Case 8, 9. Steady intermittent rain event + Initial surface water. Two different water inputs are added now at the beginning in order to check the behaviour of the model (Figures 4.4(b), 4.4(c)). A small initial surface water depth lowers the soil infiltration capacity to $5.5cm/h$ but it remains larger than the later rainfall rate ($3cm/h$). This leads to a similar situation to that in Case 7. On the contrary, the soil infiltration capacity is lowered to $1.6cm/h$ in Case 9, which is lower than the $3cm/h$ rainfall intensity. Hence, the soil becomes immediately ponded when rainfall starts.

Case 10. Unsteady storm pattern. A more complex case is presented now using a storm pattern given by the hyetograph in Table 4.3.

Time (min)	Precipitation (cm/h)
0 - 10	1.5
10 - 20	3.0
20 - 30	8.0
30 - 40	5.0
40 - 50	4.0
50 - 60	3.0
60 - 70	0.8

Table 4.3: Storm pattern for Case 10.

In this case, an additional consideration should be taken into account. For the first 20 min, the rainfall intensity is less than the infiltration capacity (see Figure 4.5(a)), so the real infiltration rate is equal to the rainfall rate ($f = R$). Because of this fact, the actual infiltration capacity does not decay as given by Horton's equation. The reason, as indicated above, is the Horton's model assumption of water supply always exceeding the infiltration capacity from the beginning. Hence, the soil has more infiltration capacity and the real infiltration at $t = 20min$ needs to be computed, so the ponding time t_p must be determined by solving Equation (4.1):

$$F = \int_0^{t_p} R(t)dt = f_c t_p + \frac{f_0 - fc}{k}\left(1 - e^{-kt_p}\right) \tag{4.1}$$

where F stands for the cumulative infiltration (that is equal to the rainfall volume) until this ponding time.

Equation 4.1 needs to be solved by an iterative procedure, such as the Newton-

Raphson method. Thus, the infiltration capacity is now a function of the actual infiltrated water, not just a function of time. Finally, the real infiltration capacity a $t = 20min$ is calculated by evaluating (2.41) at $t = t_p$:

$$f_p = f_c + (f_0 - f_c)\, e^{-kt_p} \tag{4.2}$$

The rainfall intensity at $t = 20min$ exceeds the soil infiltration capacity at this time (see Figure 4.5(a)) so the real infiltration rate is equal to this capacity and decays following Horton's equation by replacing $f_c = f_p$ and $t = t - t'$, being $t' = 20min$:

$$f = f_c + (f_p - f_c)\, e^{-k(t-t')} \tag{4.3}$$

An additional consideration must be taken into account. It is possible that the recalculated infiltration capacity is greater than the actual rainfall rate. This implies a non-physical situation with negative storage or run-off. The reason for this behaviour is that the soil can not infiltrate more than the rainfall rate, so a limit in the recalculated infiltration capacity must be imposed:

$$f_p \leq R \tag{4.4}$$

The results for the infiltration rate, cumulative infiltration, cumulative rainfall and stored surface water (we are asumming that there is no run-off) are presented in Figure 4.5(a).

Case 11. Unsteady wet-dry-wet storm pattern. The motivation of this case is to check the behaviour of the Horton model under a very irregular storm pattern (see Table 4.4) with dry intermediate intervals. For the sake of simplicity, the recalculation of the infiltration capacity is done just in the first storm. The results are shown in Figure 4.5(b).

Case 12, 13, 14. Unsteady dry-wet-dry-wet storm pattern. Three cases of unsteady storms starting from dry conditions are presented now (Figure 4.5(c),

Time (min)	Precipitation (cm/h)
0 - 10	1.5
10 - 20	3.0
20 - 30	8.0
30 - 40	5.0
40 - 50	4.0
50 - 60	3.0
60 - 70	0.8
70 - 180	0.0
180 - 190	1.0
190 - 200	6.0
200 - 210	2.0
210 - 220	0.6
220 - 230	0.3

Table 4.4: Storm pattern for Case 11.

4.5(d), 4.5(e)). The first one (12) is the reference case and it assumes there is no surface water in the beginning. Then, two different initial water inputs are imposed. In the last one (14), there is surface water at all times and it can be seen that this fact dominates the infiltration rate, for any rainfall intensity.

Case 15, 16, 17. Natural storm pattern. These cases simulate a complex storm pattern with very irregular rainfall peaks and some dry periods, which is a common situation when simulation real-world events. The first case (15) is the reference case. As in the previous cases, it is shown that under ponding conditions, the rainfall intensity does not matter at all for the infiltration rate computation. The results are shown in Figures 4.6(a), 4.6(b) and 4.6(c).

Case 18, 19, 20. Natural storm pattern + Initial surface water + Water inlet For the sake of completeness, three full cases are presented now considering every kind of possible situations: unsteady storm patterns with intermediate dry periods, starting from no rain conditions but ponded soil, with an additional water input at *t=30 min*. This can be considered as the run-off from other computational cells, when the infiltration model is implemented in a distributed surface flow simulator. Three different inputs have been considered, in order to check the correct interaction between the surface water and the rainfall. The results are shown in Figures 4.6(d), 4.6(e), 4.6(f).

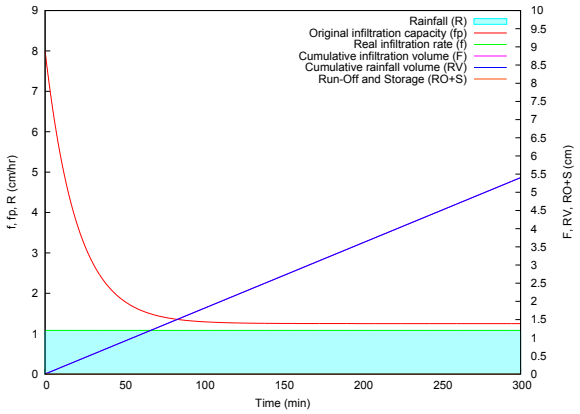

(a) Horton infiltration case 1

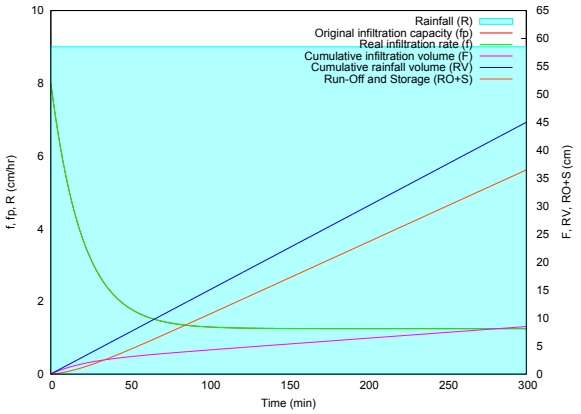

(b) Horton infiltration case 2

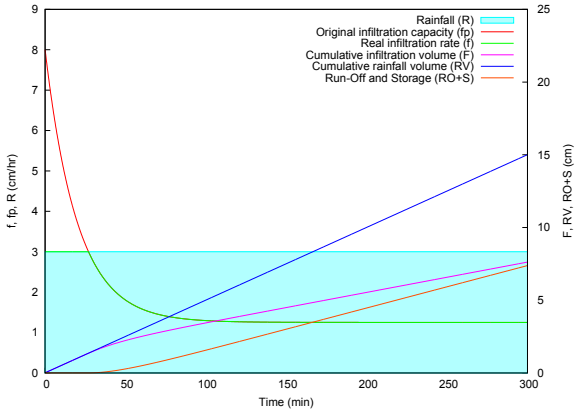

(c) Horton infiltration case 3

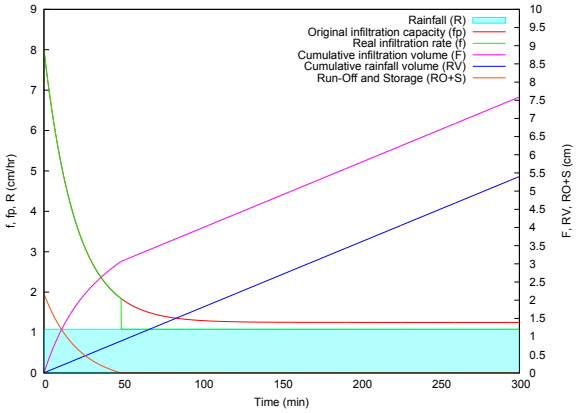

(d) Horton infiltration case 4

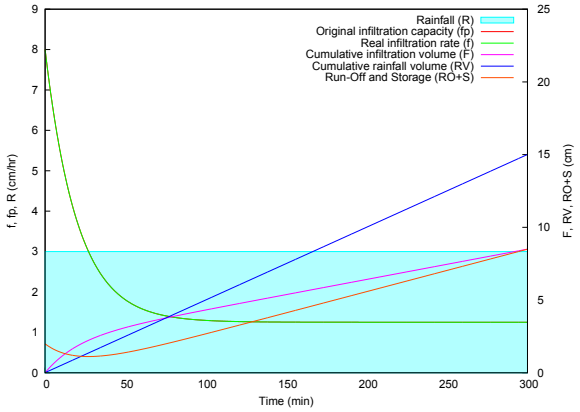

(e) Horton infiltration case 5

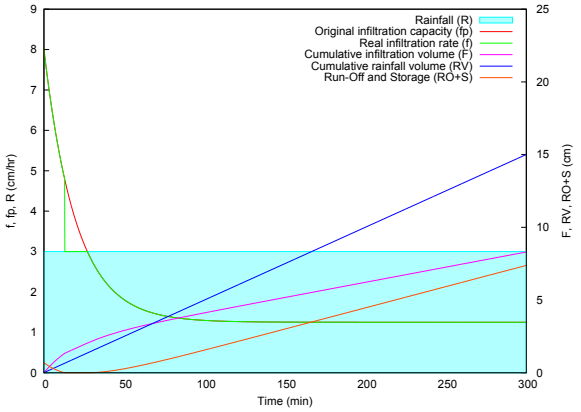

(f) Horton infiltration case 6

Figure 4.3: Horton model test cases 1 to 6.

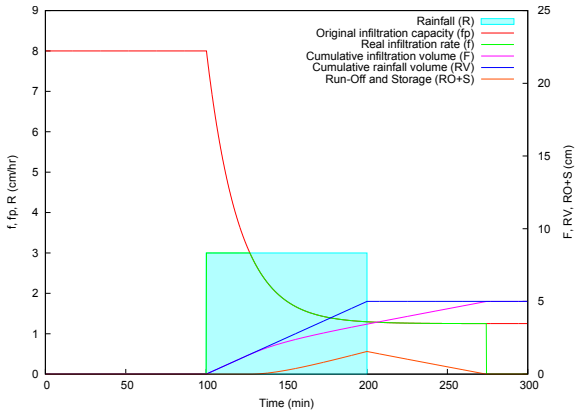

(a) Horton infiltration case 7

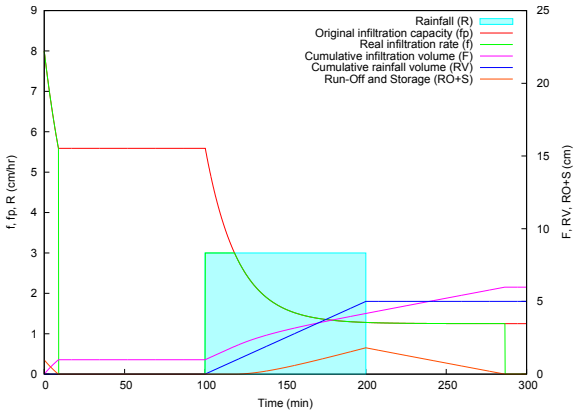

(b) Horton infiltration case 8

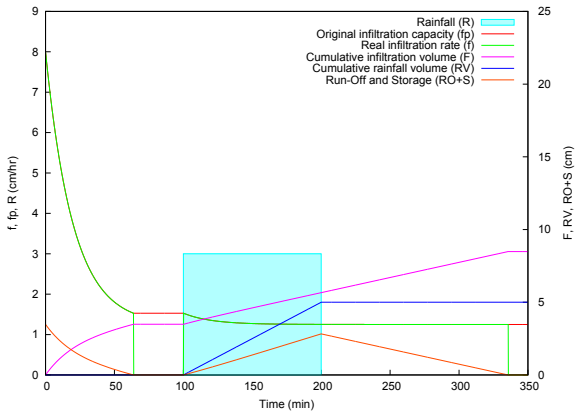

(c) Horton infiltration case 9

Figure 4.4: Horton model test cases 7 to 9.

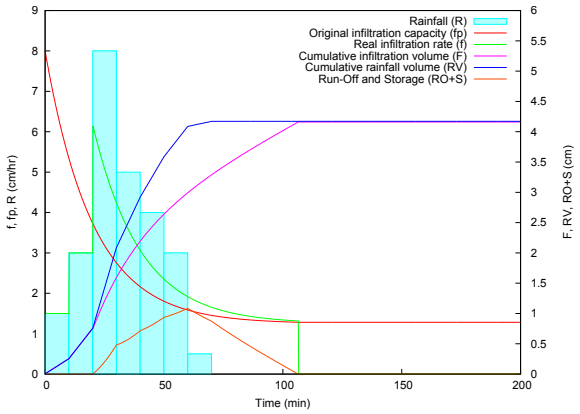

(a) Horton infiltration case 10

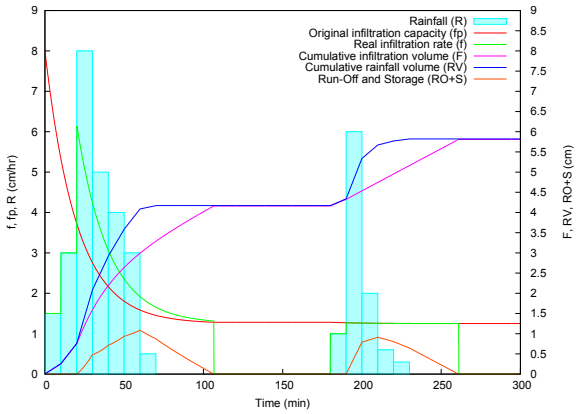

(b) Horton infiltration case 11

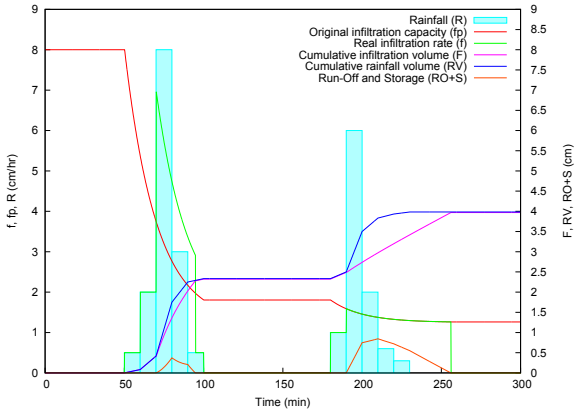

(c) Horton infiltration case 12

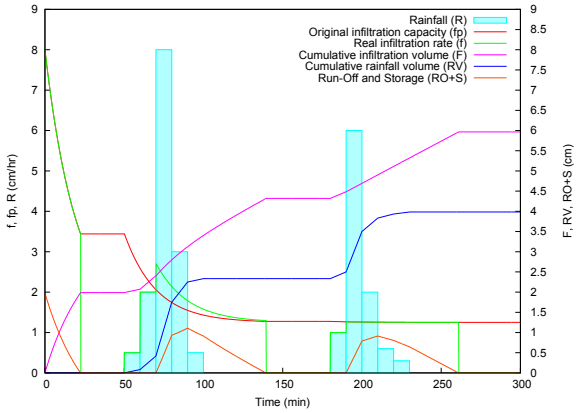

(d) Horton infiltration case 13

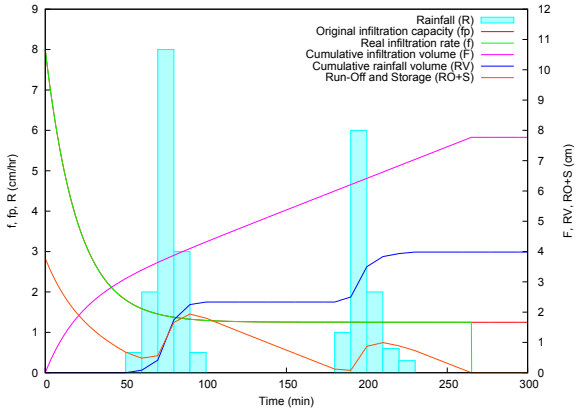

(e) Horton infiltration case 14

Figure 4.5: Horton model test cases 10 to 14.

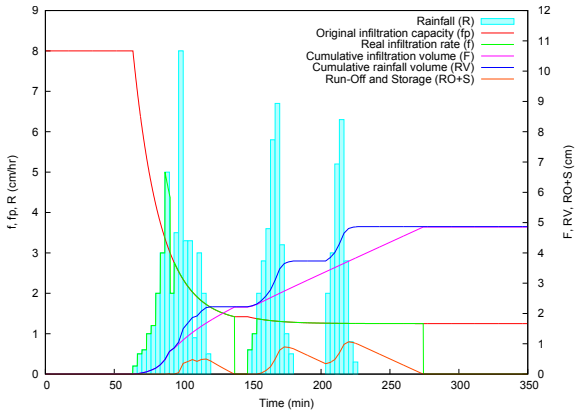

(a) Horton infiltration case 15

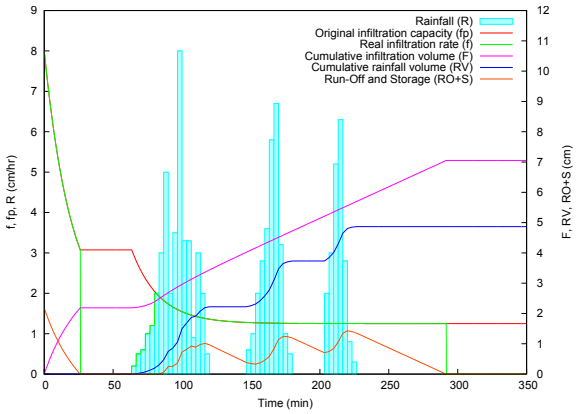

(b) Horton infiltration case 16

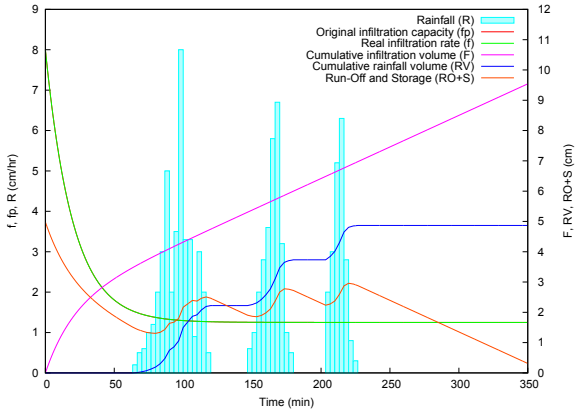

(c) Horton infiltration case 17

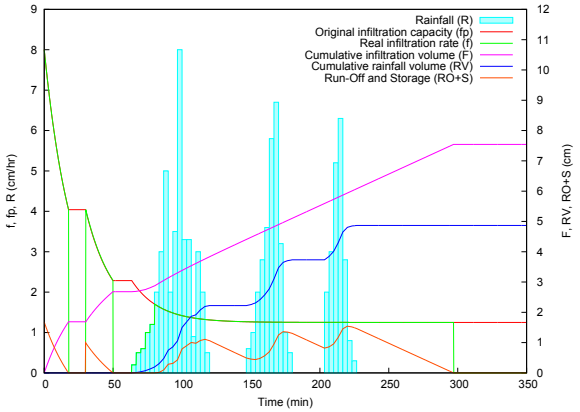

(d) Horton infiltration case 18

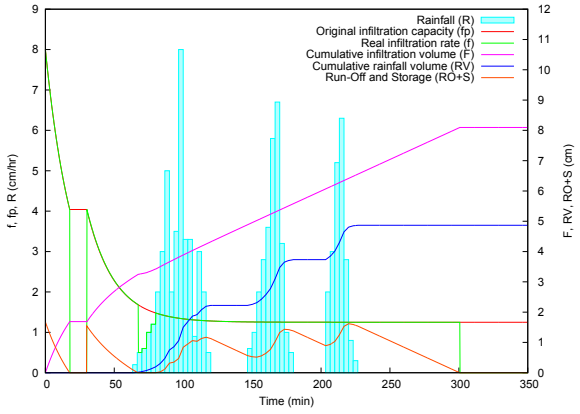

(e) Horton infiltration case 19

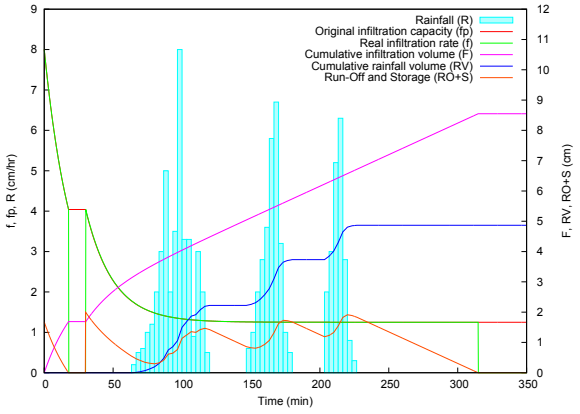

(f) Horton infiltration case 20

Figure 4.6: Horton model test cases 15 to 20.

4.1.3 Green-Ampt model

Some ilustrative examples are presented now (see Table 4.5), in order to understand the full application of the Green-Ampt model and how it works under different situations. The selected cases are, basically, the same used in the previous Horton model section with minor changes. The parameters chosen ($K = 1.27cm/s$, $\Psi = 2.54cm$ and $\Delta\theta = 0.20$) are the same for all the proposed cases, except for Case 6 which assumes an average suction head Ψ of $12,7cm$ for a better results visualization. Figures 4.7 to 5.12(f) show the results for all the cases.

Case	Description
0	Ponded soil with no rain
1	Steady rain event with $R < K$
2	Steady rain event with $R >> K$
3	Steady rain event with $R > K$
4	Steady rain event + Initial surface water with $R < K$
5	Steady rain event + Initial surface water 1 with $R > K$
6	Steady rain event + Initial surface water 2 with $R > K$
7	Steady intermittent rain event with $R > K$
8	Steady intermittent rain event + Initial surface water with $R > K$
09	Unsteady storm pattern
10	Unsteady wet-dry-wet storm pattern
11	Unsteady dry-wet-dry-wet storm pattern
12	Unsteady dry-wet-dry-wet storm pattern + Initial surface water 1
13	Unsteady dry-wet-dry-wet storm pattern + Initial surface water 2
14	Unsteady dry-wet-dry-wet storm pattern + Initial surface water 3
15	Natural storm pattern from dry conditions
16	Natural storm pattern + Initial surface water 1
17	Natural storm pattern + Initial surface water 2
18	Natural storm pattern + Initial surface water + Water inlet 1
19	Natural storm pattern + Initial surface water + Water inlet 2
20	Natural storm pattern + Initial surface water + Water inlet 3

Table 4.5: Summary of the Green-Ampt infiltration cases.

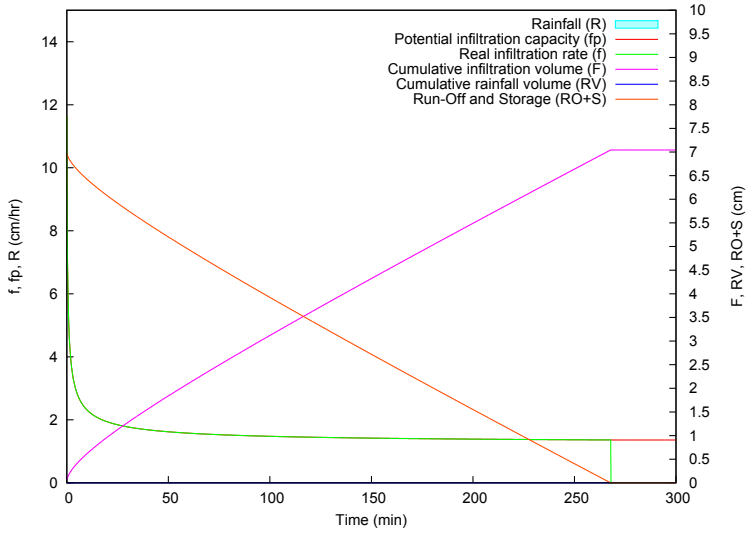

Figure 4.7: Green-Ampt infiltration case 0.

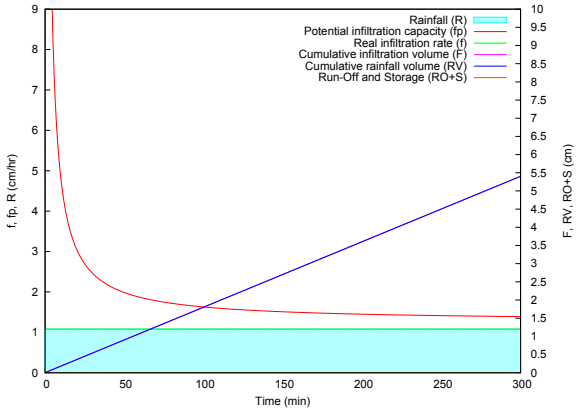

(a) Green-Ampt infiltration case 1

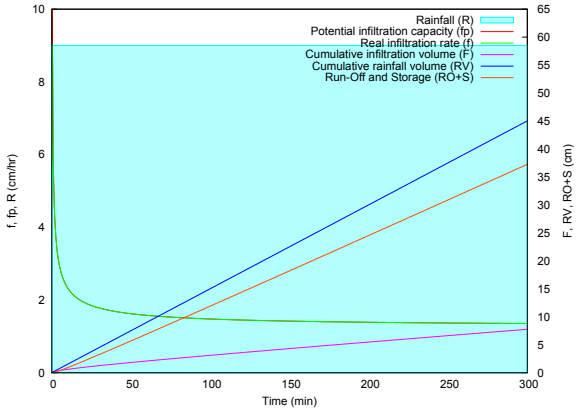

(b) Green-Ampt infiltration case 2

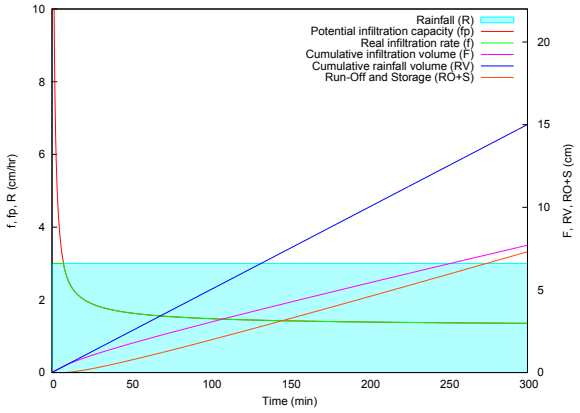

(c) Green-Ampt infiltration case 3

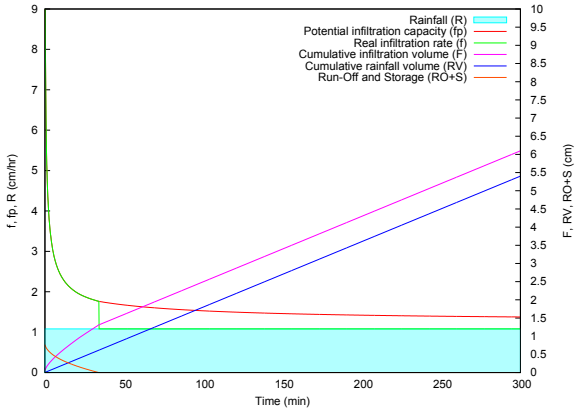

(d) Green-Ampt infiltration case 4

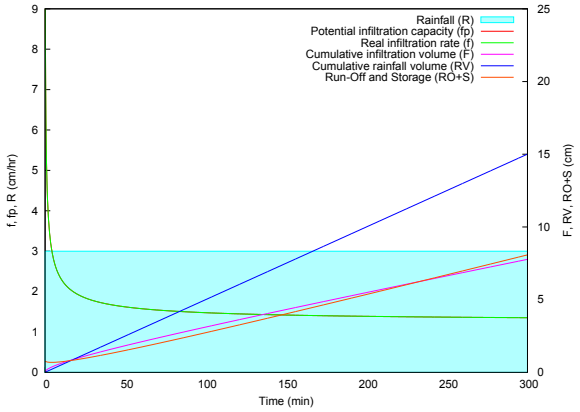

(e) Green-Ampt infiltration case 5

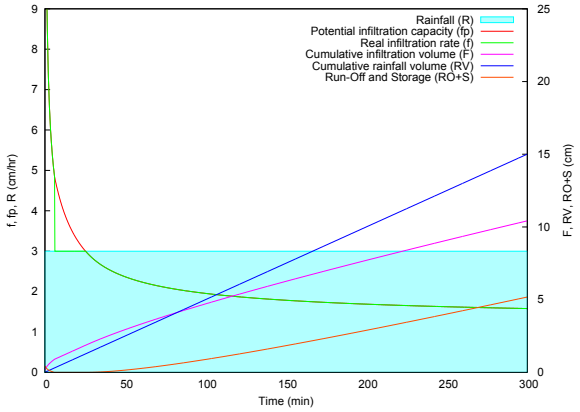

(f) Green-Ampt infiltration case 6

Figure 4.8: Green-Ampt model test cases 1 to 6.

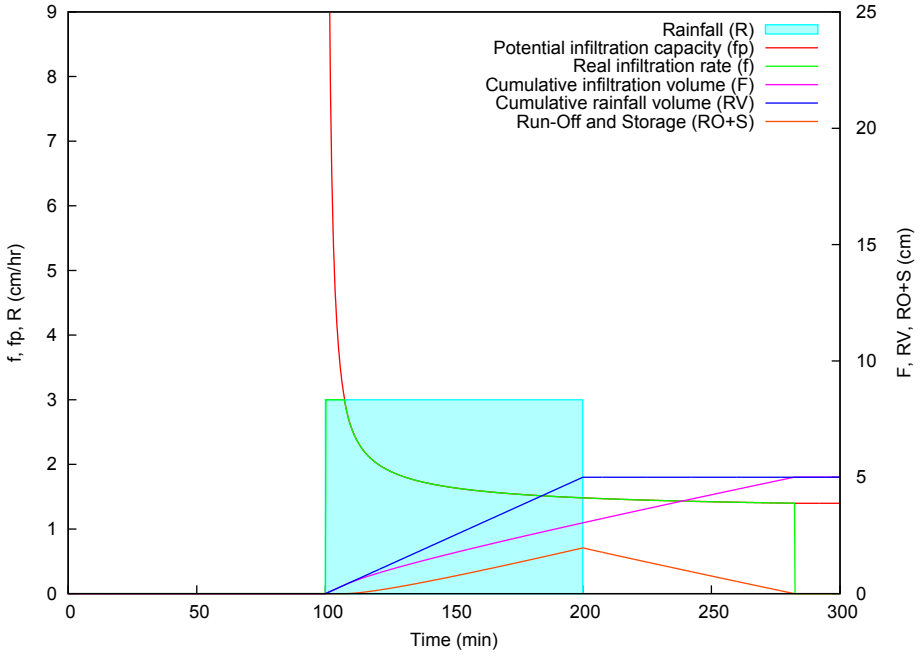

(a) Green-Ampt infiltration case 7

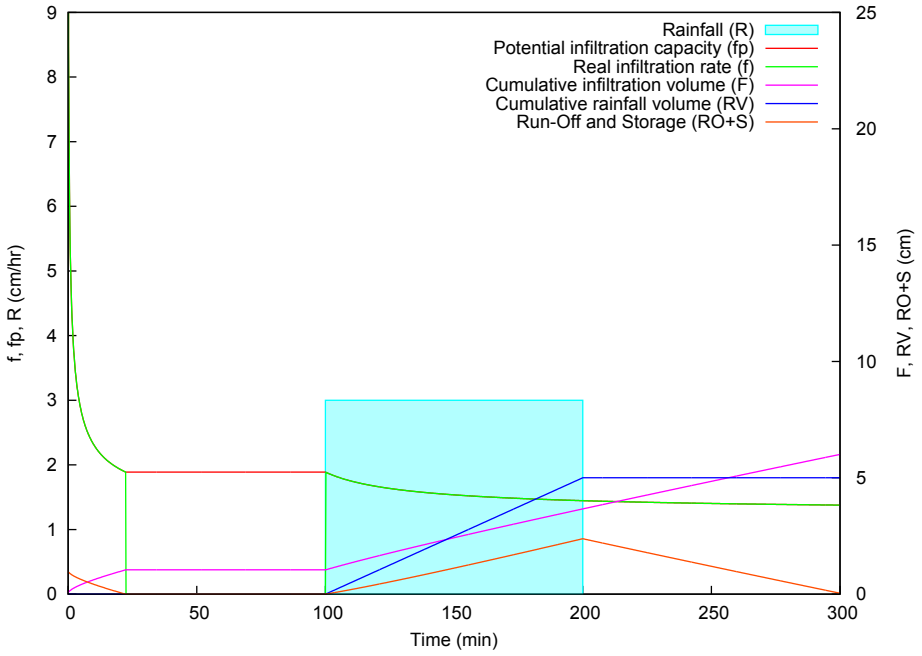

(b) Green-Ampt infiltration case 8

Figure 4.9: Green-Ampt model test cases 7 and 8.

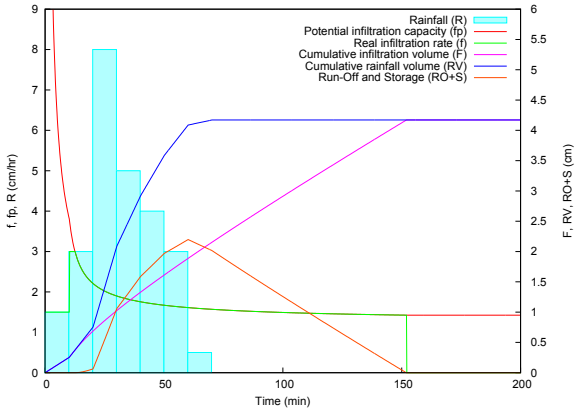

(a) Green-Ampt infiltration case 9

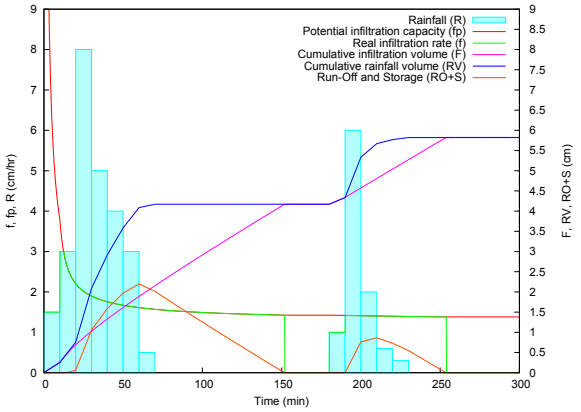

(b) Green-Ampt infiltration case 10

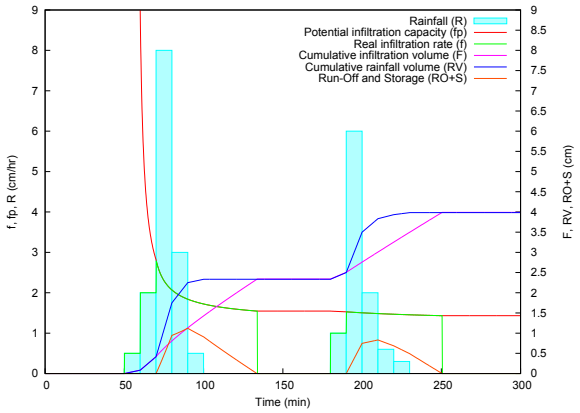

(c) Green-Ampt infiltration case 11

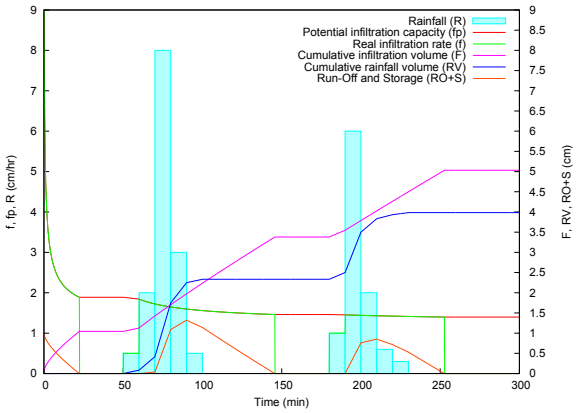

(d) Green-Ampt infiltration case 12

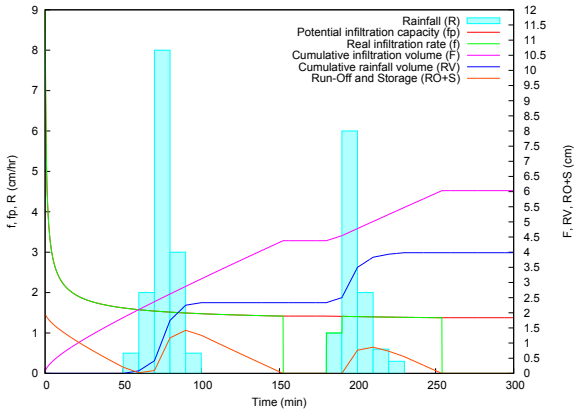

(e) Green-Ampt infiltration case 13

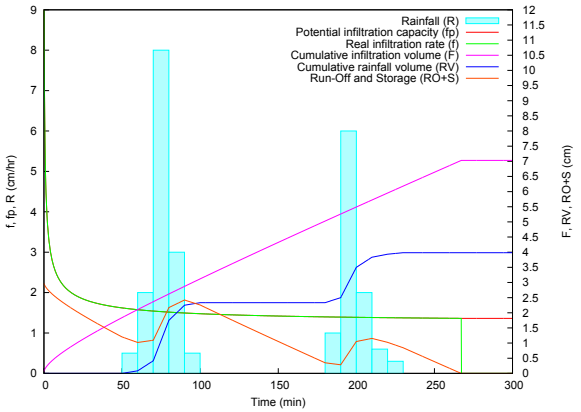

(f) Green-Ampt infiltration case 14

Figure 4.10: Green-Ampt model test cases 9 to 14.

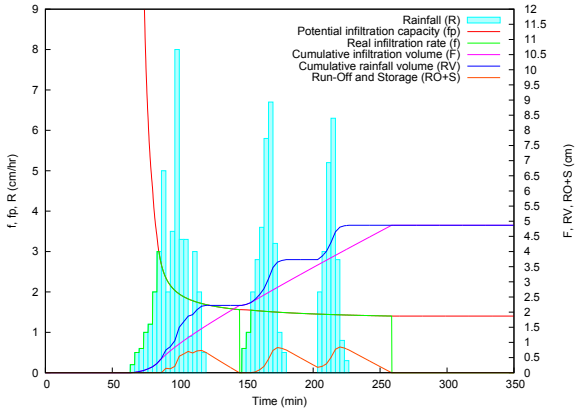

(a) Green-Ampt infiltration case 15

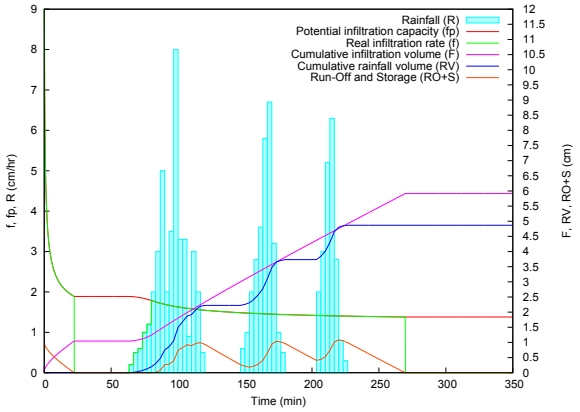

(b) Green-Ampt infiltration case 16

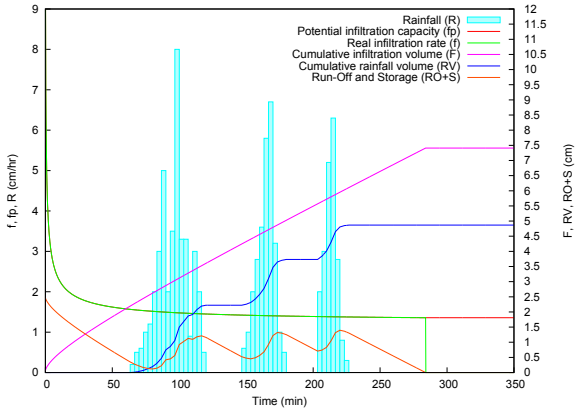

(c) Green-Ampt infiltration case 17

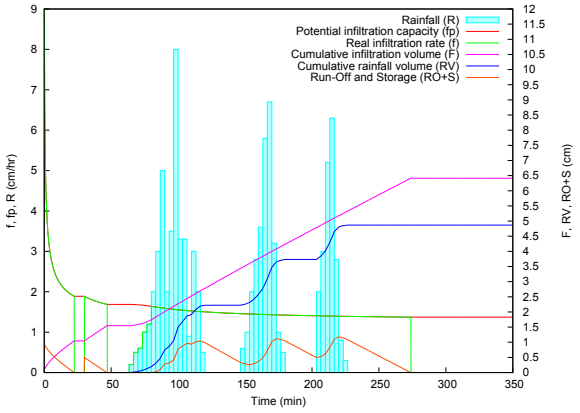

(d) Green-Ampt infiltration case 18

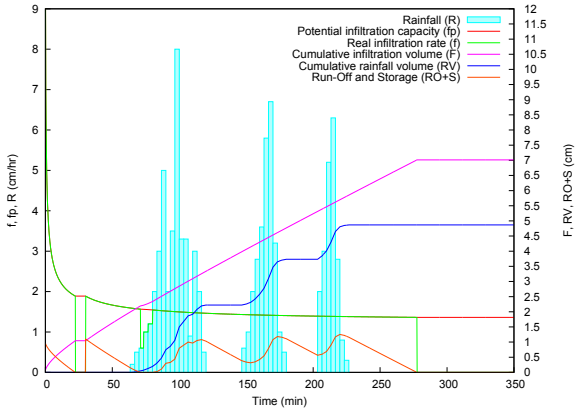

(e) Green-Ampt infiltration case 19

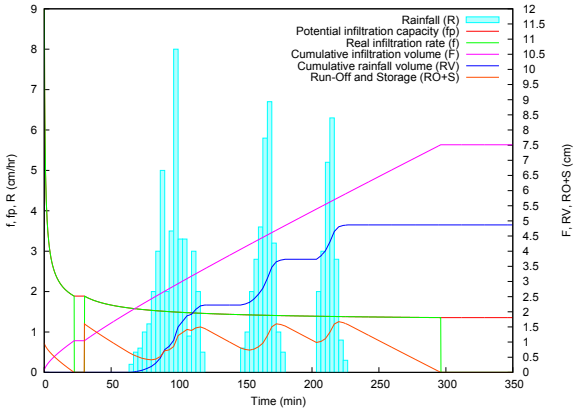

(f) Green-Ampt infiltration case 20

Figure 4.11: Green-Ampt model test cases 15 to 20.

4.1.4 Fractional-Order Green-Ampt model

A horizontal soil with closed walls is assumed with unsteady rainfall pattern for the generation of the surface water ($h = 0, u = v = 0, R \neq 0$ at $t = 0$) in order to examine the influence of the order α of the Caputo fractional derivative on the infiltration curves. The parameters for the FOGA model ar: $K_\alpha = 3.53 \cdot 10^{-6} m^\alpha/s$, $\Psi = 0.0254m$, $\Delta\theta = 0.2m^3/m^3$. This numerical experiment represents a starting point for the application of the FOGA infiltration method to natural storms in real catchments. In this experiment the total rainfall volume RV is defined by

$$RV(t) = \int_{\xi=0}^{t} R(\xi) d\xi \tag{4.5}$$

Figure 4.12 shows the temporal evolution of all the variables of interest: rainfall, infiltration capacity, infiltration rate, infiltration volume, rainfall volume and surface water. For illustration purposes, two choices of α have been considered: $\alpha = 1$ and $\alpha = 0.7$.

By comparing the plots corresponding to $\alpha = 1$ and $\alpha = 0.7$ in Figure 4.12, it is observed that when lowering the value of α, the infiltration rate globally decreases for all times. This conclusion is consistent with the results obtained in [96] for a continuously ponded soil.

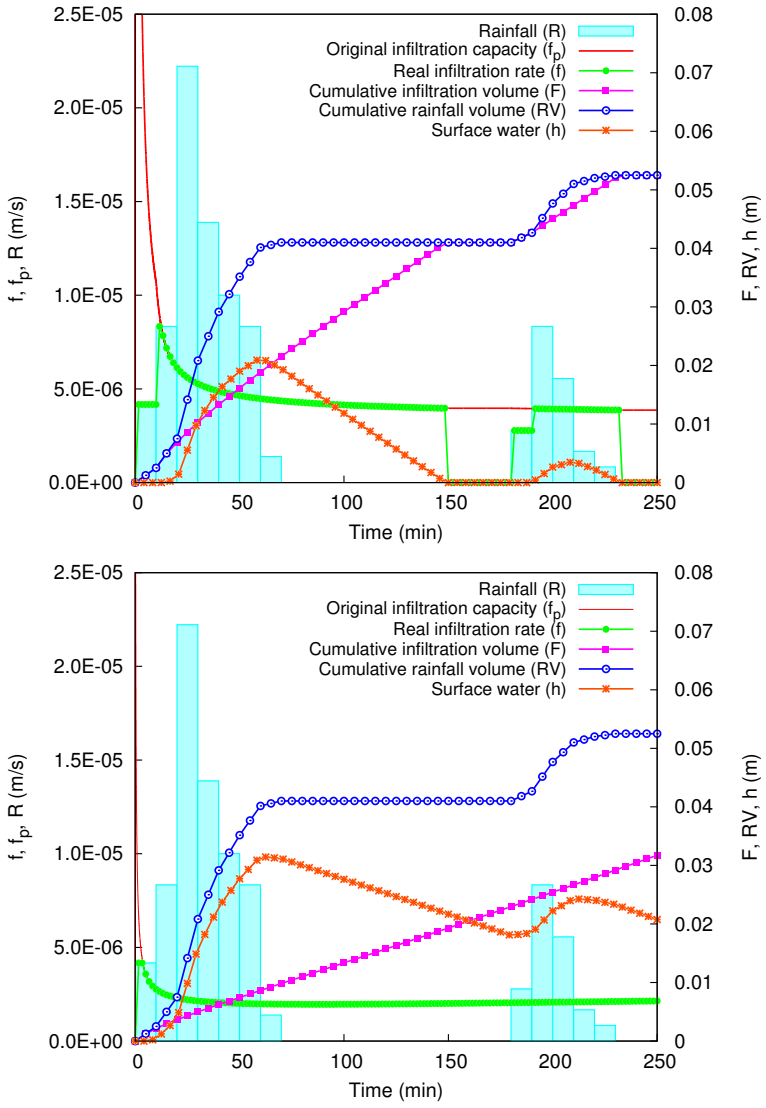

Figure 4.12: Unsteady rainfall: Temporal evolution the hydrological variables for $\alpha = 1$ (upper) and $\alpha = 0.7$ (lower).

4.1.5 Conclusions

In this section, several test cases have been presented with the main goal of understanding the behaviour of all the infiltration laws considered in this thesis under different assumptions for rainfall and initial conditions. The main conclusions can be summarized as follows:

- SCS model is not able to account for the infiltration of ponded areas when the rainfall intensity is null. This fact limits the applicabilty of the method within a distributed surface flow model.
- Both Horton and Green-Ampt infiltration laws show similar behaviours under all the presented cases, including those with complex storm patterns and independently of the surface initial conditions. Therefore, the choice of the infiltration model could depend mainly on the availability of the soil parameters.

4.2 1D Shallow Water equations for drainage modeling

In this section, a set of test cases for 1D SW model is presented. Due to the most of situations are strongly transient, an explicit scheme ($\theta = 0$) is chosen in all cases.

4.2.1 Steady state over a bump

Following [62] a frictionless rectangular $25m \times 1m$ prismatic channel is considered. The variable bed level is given by:

$$z\,(8 \leq x \leq 12) = 0.2 - 0.05(x - 10)^2 \tag{4.6}$$

and the initial conditions for the water depth and discharge:

$$h(x, 0) = 0.5 - z(x), \qquad Q(x, 0) = 0 \tag{4.7}$$

The different boundary conditions for the test cases simulated are summarized in Table 4.6.

Test	Upstream $Q\,(m^3/s)$	Downstream $h\,(m)$
1	0.18	0.33
2	1.53	0.66 (sub)

Table 4.6: Steady state over a bump.

Figure 4.13 (left) shows the generation of hydraulic jump that connects both subcritical and supercritical regimes. In the second test case, shown in Figure 4.13 (rihgt) the connection is made without any shock wave and it can be mathematically proved (and numerically checked) that this transition takes place in the highest part of the bump. The solutions have been calculated by means of the explicit configuration of the numerical scheme ($\theta = 0$)

4.2.2 Dam-break

Dam-break is a classical example of non-linear flow with shocks. It has been widely used to test the accuracy and conservation of the numerical scheme, as the exact

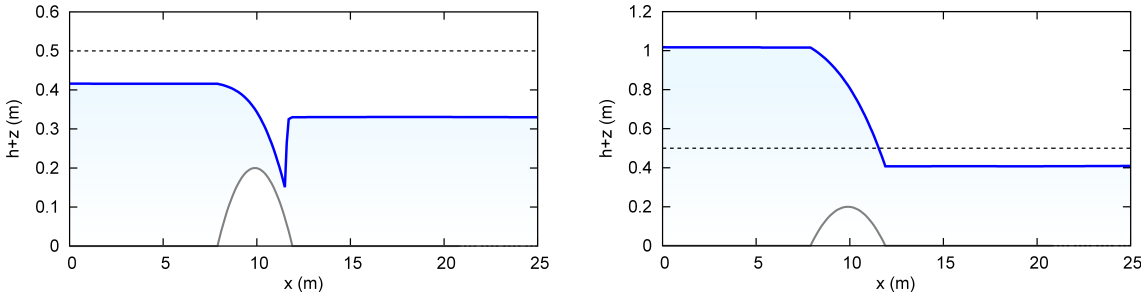

Figure 4.13: Steady state over a bump (Test 1 (left) and Test 2 (right)). Initial state (dashed line). Bed level (grey). Numerical solution (blue)

solution can be computed. In the case presented, an initial discontinuity of $1m$: $0.5m$ ratio with no friction was considered. Figure 4.14 shows the good agreement between numerical and analytical solution at the given time.

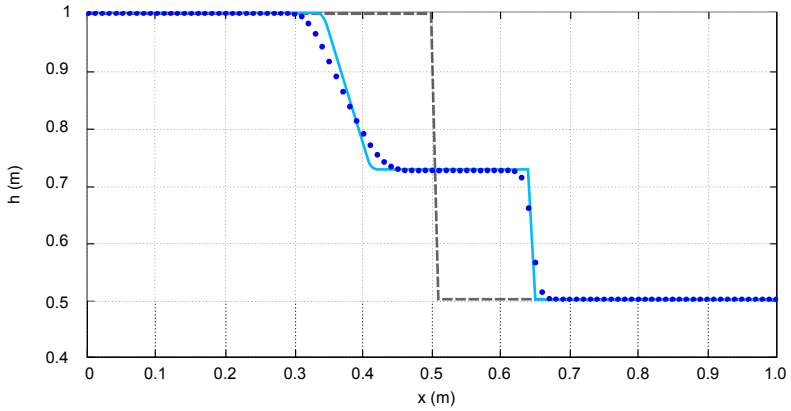

Figure 4.14: Dam-break test case. Initial state (dashed line). Numerical results (blue dots). Analytical solution (cyan line).

4.2.3 Wiggert test case for local pressurization

The experimental case designed by Wiggert [103] and widely numerically reproduced (e.g. [35], [10]) consists of a horizontal 30 m long and 0.51 m wide flume. A 10 m roof is placed in the middle section, setting up a closed rectangular pipe 0.148 m in height (see Figure 4.15). A $0.01sm^{-1/3}$ Manning roughness coefficient is assumed. As initial conditions, a water level of 0.128 m and zero discharge are considered. Then a wave coming from the left causes the pressurization of the pipe. The imposed downstream boundary conditions are the same values measured by Wiggert (Figure 4.16).

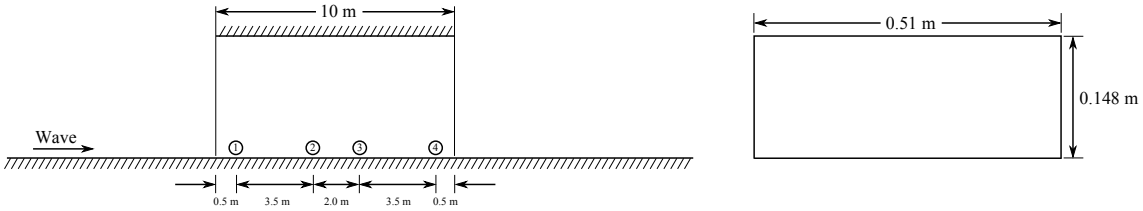

Figure 4.15: Wiggert experimental setup.

Figure 4.17 shows the numerical results for the four gauges. The experimental comparison is done only for the second one, due to data availability issues. An overall good agreement is observed with only small numerical oscillations presented.

4.2.4 Transient mixed flow

The aim of the next test case is to prove the model in the simulation of large-scale strong transients. It considers a uniform slope (0.1%) rectangular pipe connected to a downstream valve ([45] and [46]). The lenght, width and height are $10km$, $10m$ and 9.5m, respectively, and the chosen Manning roughness is $0.015sm^{1/3}$.

As initial condition, a uniform water depth ($8.57m$) and discharge ($Q = 240m^3/s$) are assumed. From this state, the downstream valve is closed, generating a shock wave moving upstream and pressurizing the pipe. Figure 4.18 shows the numerical results obtained for the pressure head at three different times. For this simulation, a 500 cell mesh and a timestep given by CFL=0.5 have beed used. It is clearly observed that the pipe pressure raises gradually with the upwards shockwave movement.

4.2.5 Transient flow in a 7-pipe looped network

In this section a simple looped pipe network (see Figure 4.20) is presented [105]. Each pipe is closed, rectangular cross-section, 1 m wide and 100 m long. The bed slopes are $S_{0,1} = 0.002$, $S_{0,2} = S_{0,3} = 0.001$, $S_{0,4} = 0.0$, $S_{0,5} = S_{0,6} = 0.001$, $S_{0,7} = 0.002$ and a $0.01m^{-1/3}s$ Manning friction coefficient is considered. A first calculation provided the steady state from the following initial conditions:

$$Q_1(i,0) = Q_7(i,0) = 0.1m^3/s$$

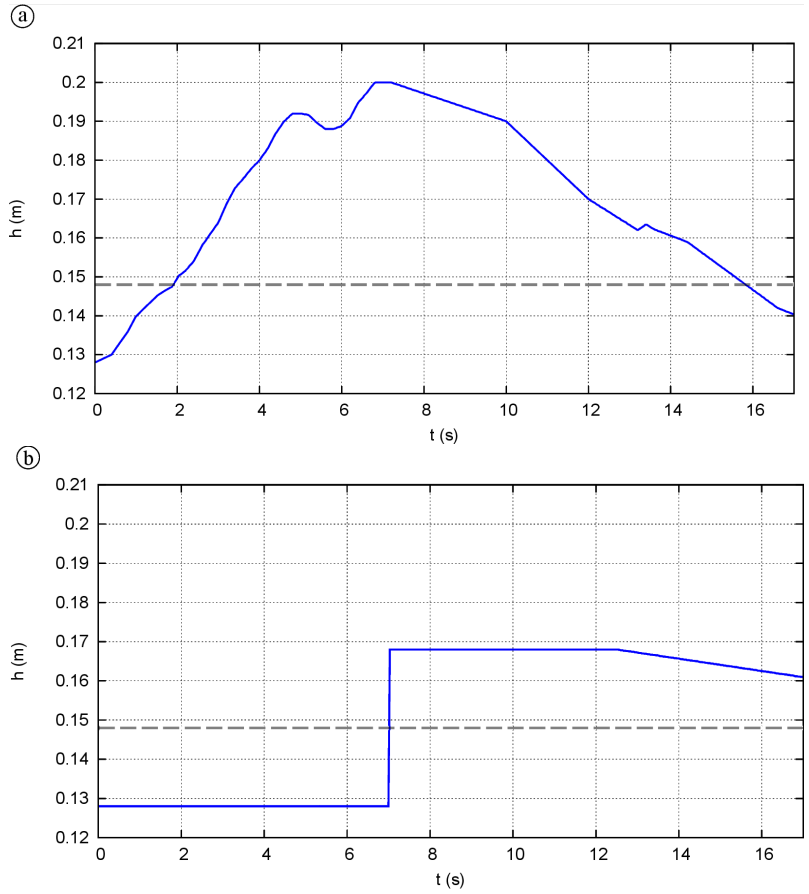

Figure 4.16: Upstream (a) and downstream (b) pressured head level.

$$Q_2(i,0) = Q_3(i,0) = Q_5(i,0) = Q_6(i,0) = 0.05m^3/s$$

$$Q_4(i,0) = 0$$

$$h_j(i,0) = 0.2m, \qquad (j = 1, \cdots, 7)$$

and the upstream boundary condition:

$$Q_1(1,t) = 0.1m^3/s$$

Free outflow downwards boundary condition has been imposed.

Junctions J_1 and J_2 are treated as normal confluences and a storage well of $5m^2$ top surface is assumed in junctions W_1 and W_2. The previously computed steady state is now used as an initial condition for a second calculation. A triangular function of peak discharge Q_{MAX} and a period of 600 s (Figure 4.19) is imposed at

the beginning of the pipe 1. The minimum discharge is $0.1m^3/s$:

Two different situations were studied. In the first one the peak discharge is fixed to $Q_{MAX} = 2.0m^3/s$ and the flow remains unpressurized all over the pipe system. In the second case, the maximum discharge is increased to $Q_{MAX} = 3.0m^3/s$, so pressurization occurs in some points of pipe 1. Figures 4.21 and 4.22 show the results for the pressurized case. The results in pipes 3 and 6 have been omitted because of symmetry reasons. The discharge at the center of the pipe 4 is constantly zero and equal in magnitude but opposite in sign in the symmetric points, which verify the simmetric character of the pipe network.

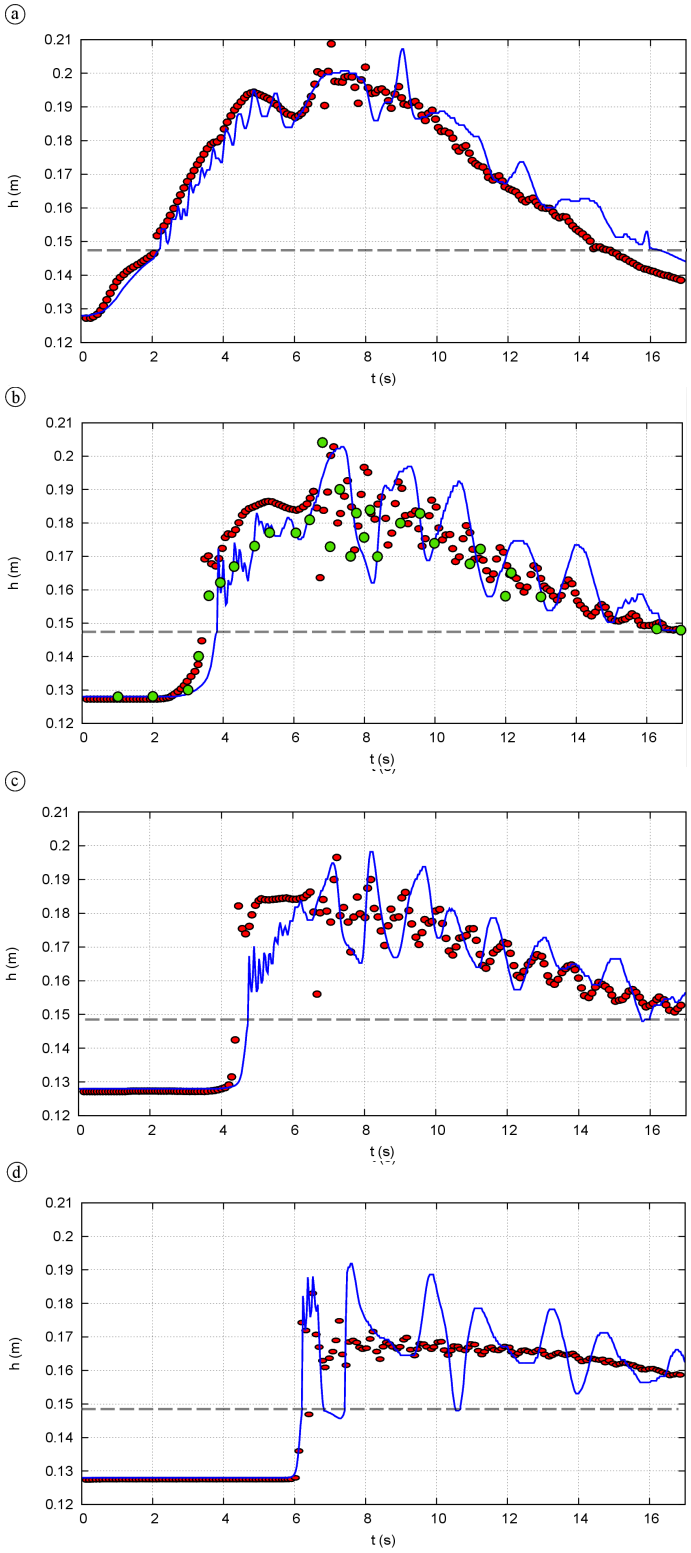

Figure 4.17: Comparision between numerical results (blue), experimental data (green dots) and numerical results from [35] (red dots) for the four gauges of the Wiggert test case setup.

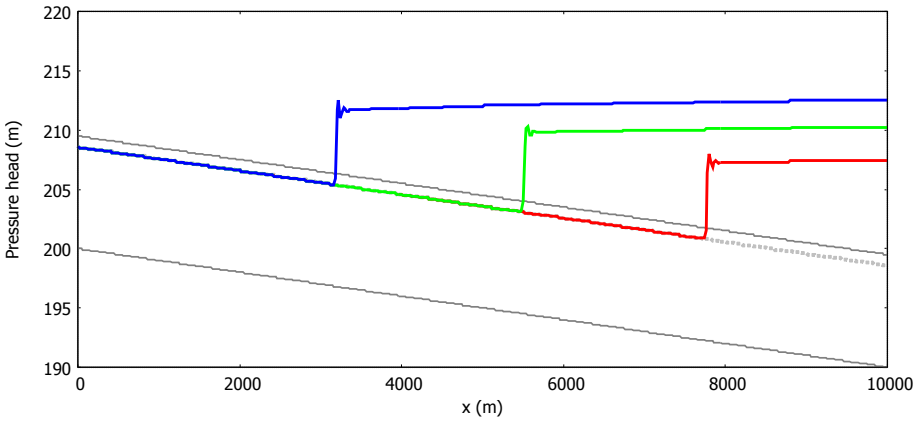

Figure 4.18: Shockwave propagation in transient mixed flow at $t = 100s$ (red), $t = 200s$ (green) and $t = 300s$ (blue).

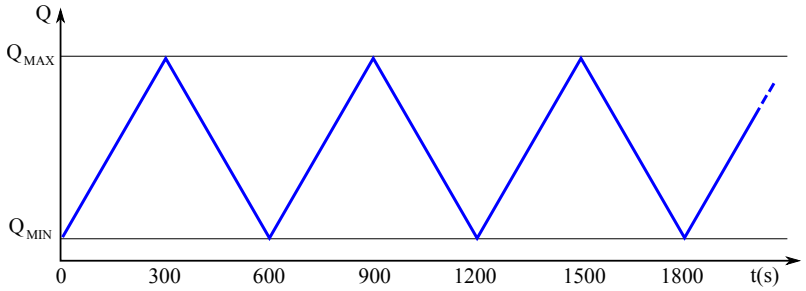

Figure 4.19: Triangular inlet hydrograph in the pipe 1.

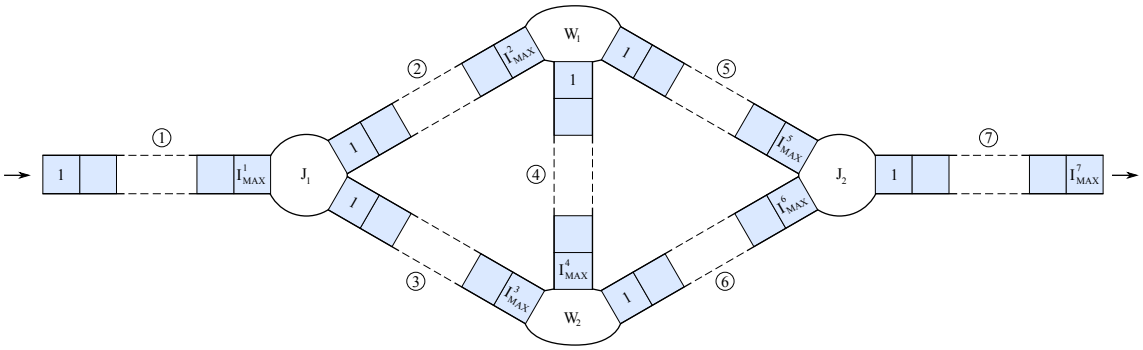

Figure 4.20: Scheme of the looped pipe network.

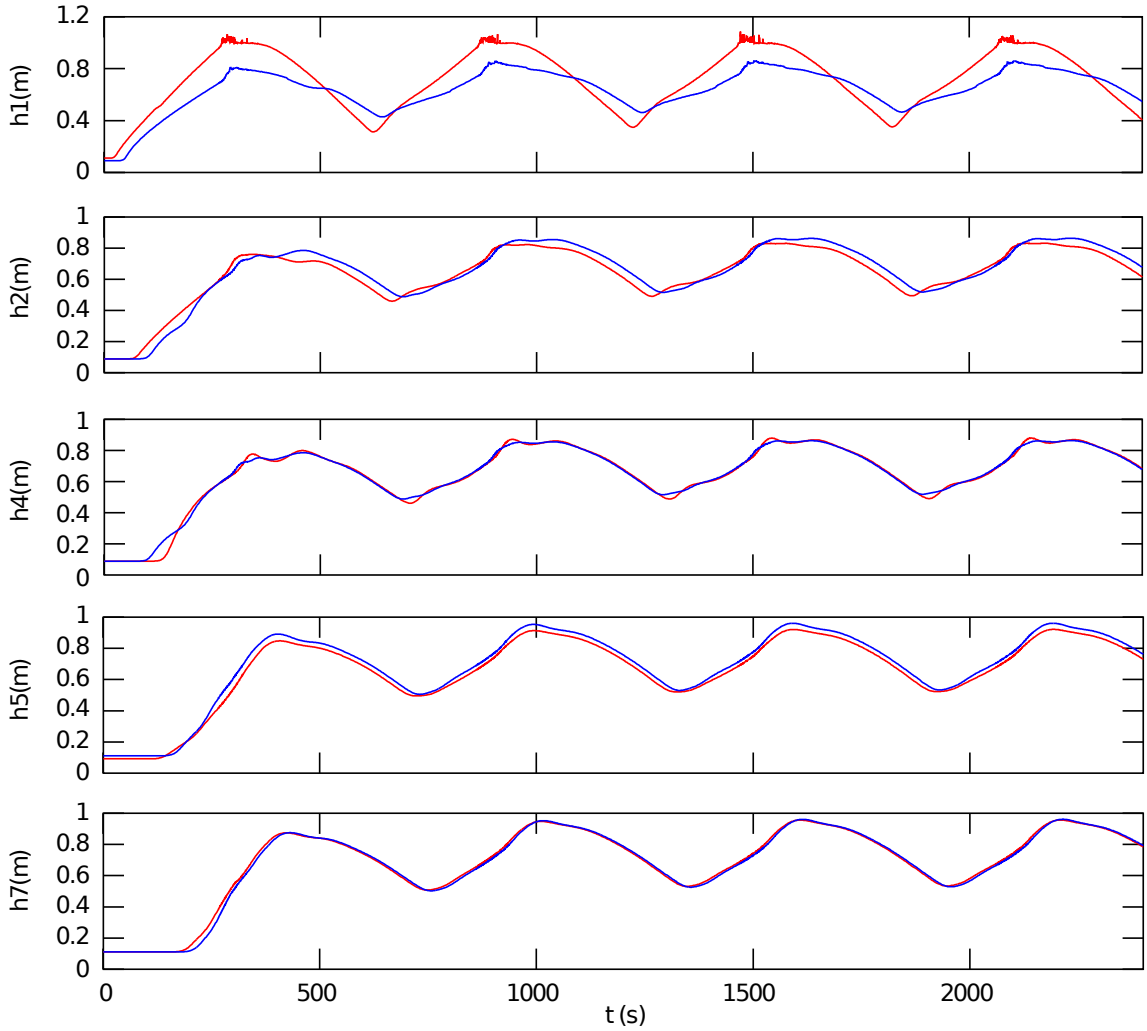

Figure 4.21: Water depth time histories at grid points $i = N/2$ (red) and $i = N$ (blue) for punctually pressurized flow.

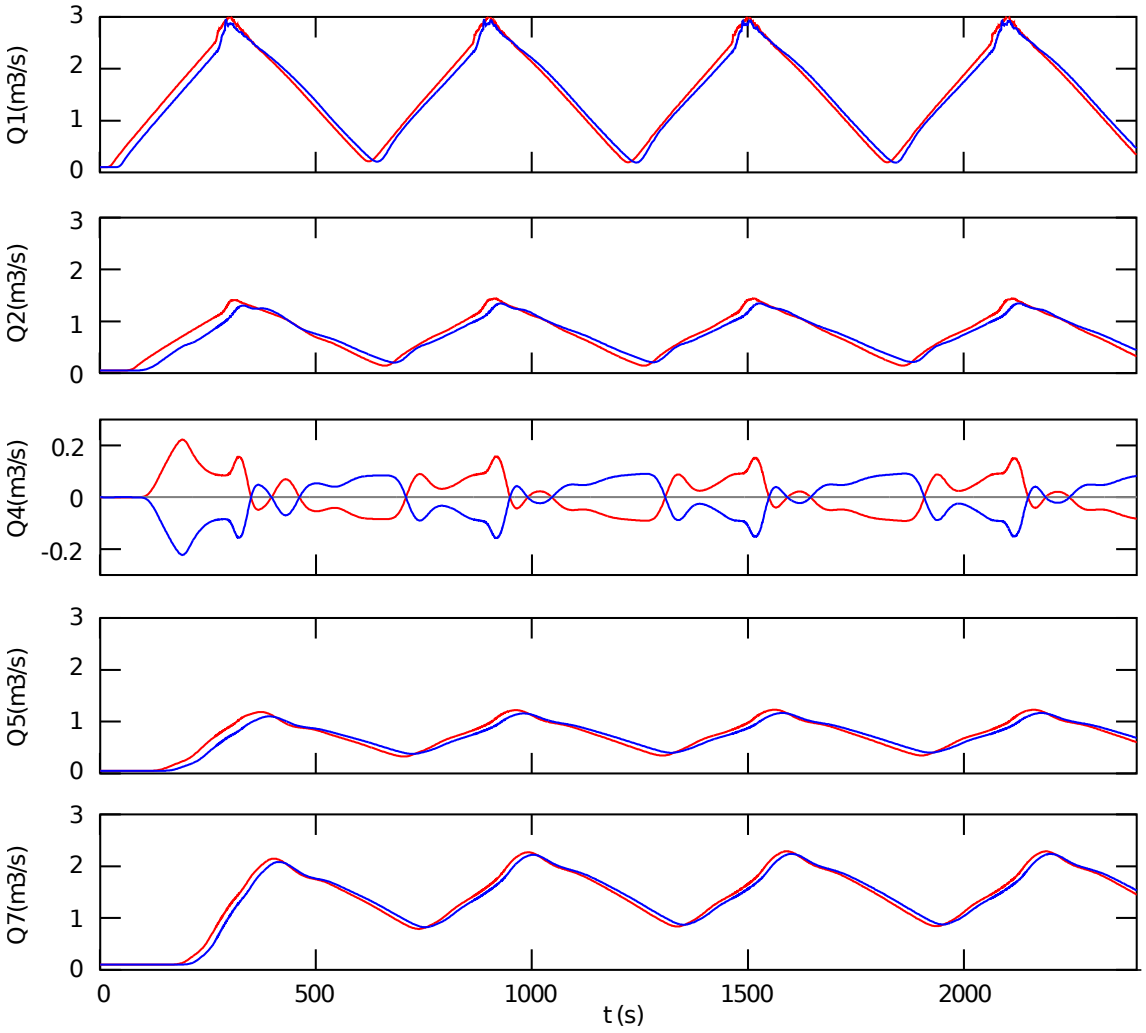

Figure 4.22: Discharge time histories at grid points $i = N/2$ (red) and $i = N$ (blue) for punctually pressurized flow: The discharge for pipe 4 is recorded at locations $i = 1$ (red), $i = N/2$ (grey) and $i = N$ (blue).

4.2.6 Conclusions

This section leads to the conclusion of the reasonably good applicability of the Preissmann slot model for an estimation of the pressure values in unsteady situations between both shallow and pressurized flows. This method takes advantage of the similarity of both equation systems shallow water and pressurized flow) and provides a simple way to simulate occasionally pressurized pipes, treating the system as an open channel in the Preissmann slot. This results in an easier implementation of the model because it avoids the managing of two separate systems of equations (shallow water and water hammer) in order to model separately the pressurized and the free surface flows. The use of an explicit scheme ($\theta = 0$) implies a limitation on the computational time step but allows to capture more adequately the transient phenomelogy, specially when the pipes are pressurized. It is also remarkable the possibility of adapting the method to more realistic systems, like pipe networks which can be punctually pressurized. Some additional internal boundary conditions are necessary in these cases, in order to represent pipe junctions and storage wells.

4.3 2D Shallow Water equations

4.3.1 Mesh sensitivity analysis

In this section, a simple test case is presented in order to show the benefits of triangular unstructured meshes (TU), in terms of its adaptability to irregular topography, which is the most usual in natural environments, as river catchments.

This test presents a comparison between TU and rectangular structured (RS) meshes with approximately the same number of cells ($\sim$ 1500) in a $50m \times 30m$ domain with three bed irregularities, a square obstacle and two spherical humps (see Figure 4.23). Both computational meshes are shown in Figure 4.24. A constant Manning's roughness value of $0.03sm^{-1/3}$ and dry initial conditions ($h = 0m$) are assumed for the entire domain. All the boundaries are closed except the left one in which a constant water depth of $h = 0.3m$ is imposed. It should be noted that the TU mesh offers the possibility of performing a local refinement in the areas of interest. In this test case, the refinement is done on the spherical humps in order to obtain a good discretization of the topography.

Figure 4.25 shows the evolution of the water depth h at $t = 3s$, $t = 9s$ and $t = 600s$ for both RS and TU meshes. The unstructured and locally-refined mesh shows a better fit to the rounded topography with the same number of cells in both transient and steady states. Hence, it is the most suitable choice when dealing with irregular beds. In this numerical example, the good behaviour of the implicit scheme under both transient and steady wet/dry fronts is also verified (Figure 4.25). The numerical scheme is capable of solving this phenomenology without noticing any issues in both implicit and explicit versions.

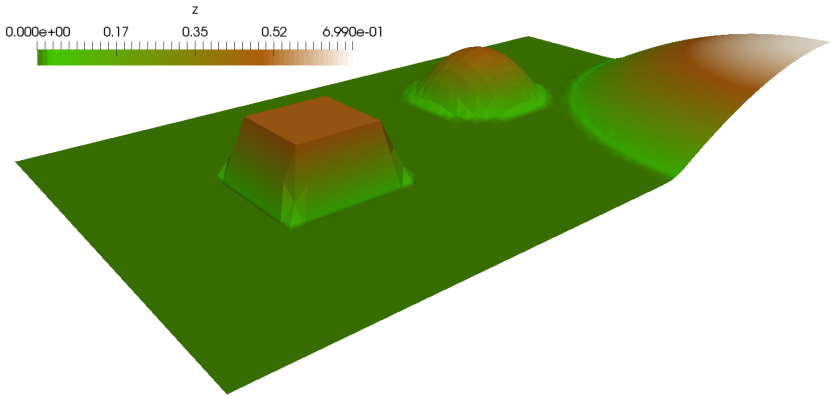

Figure 4.23: 3D representation of the domain (bed elevation is exaggerated 2 times).

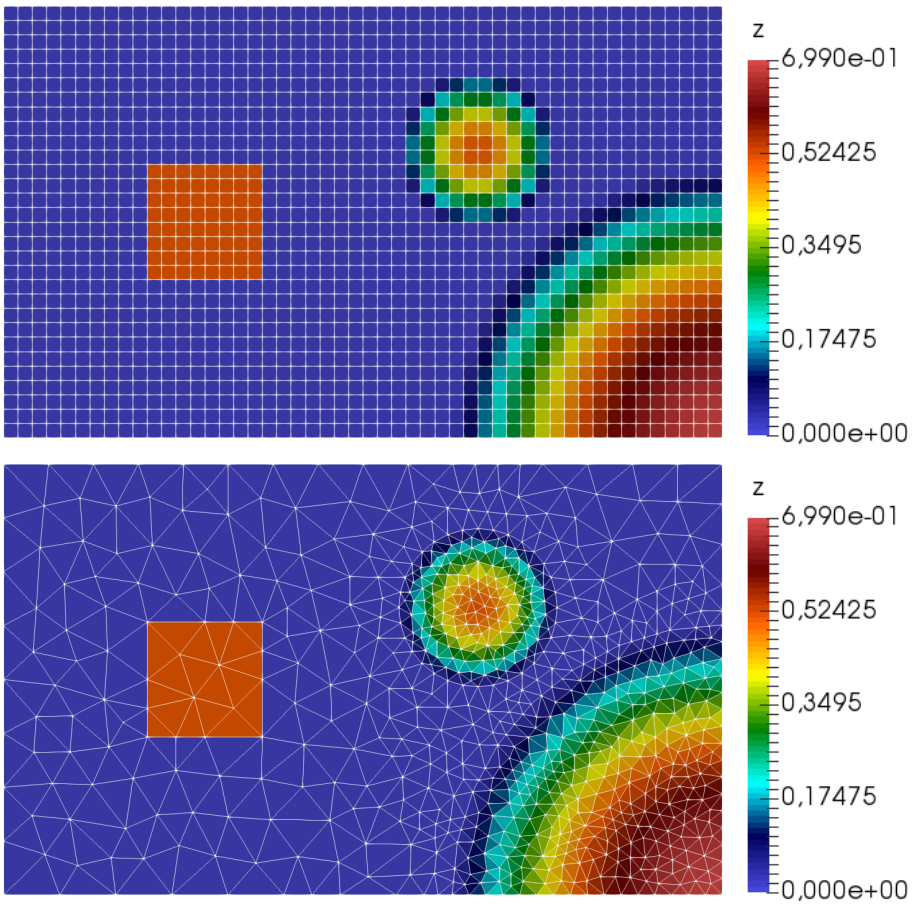

Figure 4.24: Rectangular structured (left) and triangular unstructured (right) meshes.

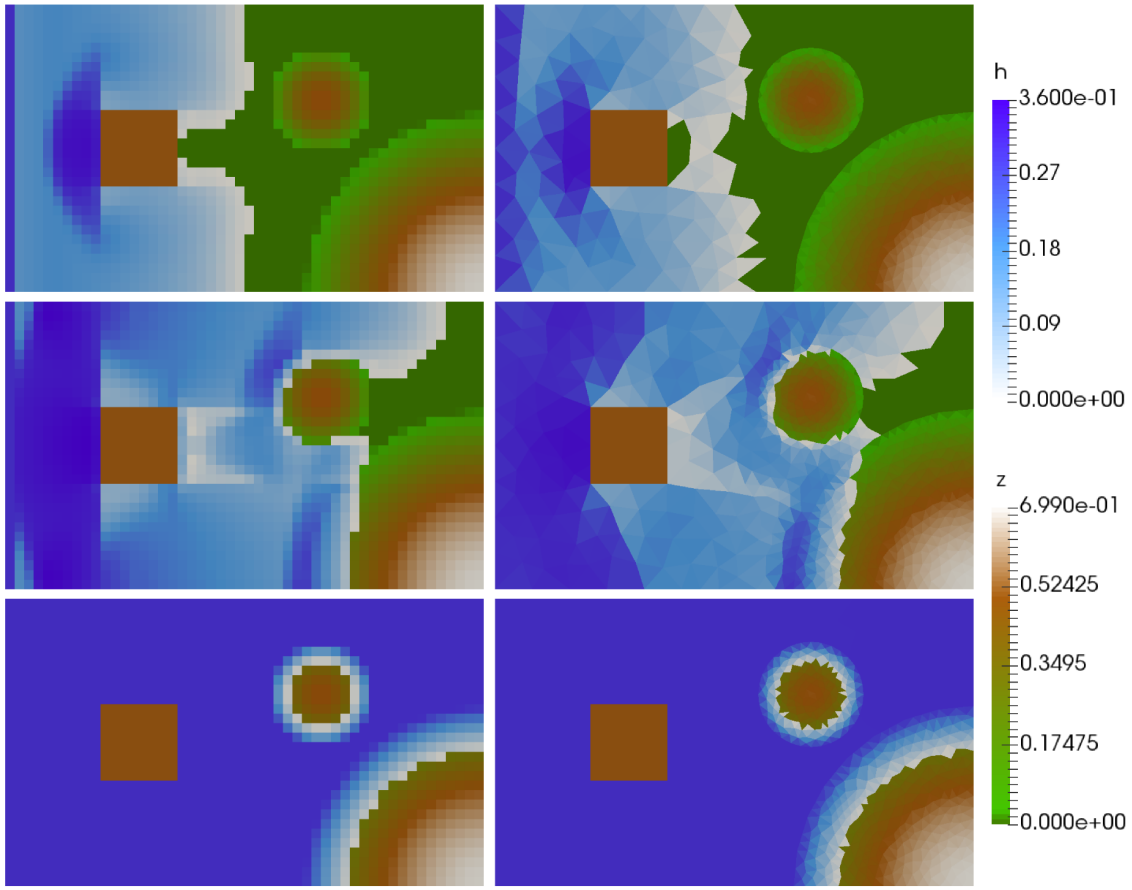

Figure 4.25: Numerical results for the mesh adaptability study. Structured rectangular mesh (left) vs. Unstructured triangular mesh (right). Water depth at $t = 3s$ (upper), $t = 9s$ (middle) and $t = 600s$ (lower).

4.3.2 Water at rest

The motivation for this test case is to check the preservation of the C-property of the model and thence if the source terms are well-balanced in still water situations. The bed level is given by:

$$z(x,y) = \max\left\{0, 2000 - 0.00032\left[(x-4000)^2 + (y-4000)^2\right]\right\} \tag{4.8}$$

The initial quiescent water level is set in $1000m$. The $8000m \times 8000m$ domain has been discretized by means of a 5000 cells unstructured triangular mesh. The simulation has been run for $600s$ with CFL numbers of 2 and 50, leading to time steps of $1.05s$ and $26.2s$, respectively, without observing significant differences. Figure 4.26 shows the three-dimensional representation of the steady state and the cross-sectional plot of the solution at the final time.

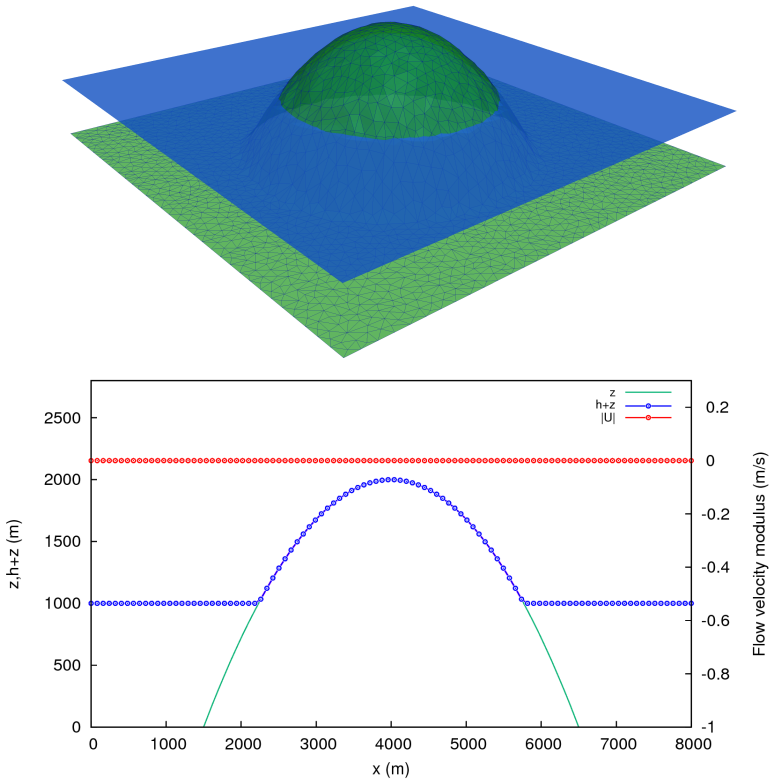

Figure 4.26: 3D representation of the steady state (left) and cross-sectional plot of the solution at the final time (right).

4.3.3 Transcritical steady state over a bump

This test case leads to a final steady state by which the implicit method accuracy can be evaluated [63]. The case setup consists of a horizontal bed level with a bump given by $z(8 \leq x \leq 12) = 0.2 - 0.05(x - 10)^2$. The channel length and width are 25 m and 1.5 m, respectively. As initial condition, a uniform water level of 0.5 m is imposed. The boundary conditions are a fixed water input discharge upstream ($hu = 1.53m^2/s$) and free flow downstream. CFL numbers up to 75 can be chosen for reaching the steady state. Figure 4.27 shows the comparison between numerical and exact solution for this case with CFL=50. Figure 4.28 shows the temporal evolution of the numerical results for different times until the steady state with CFL=2.

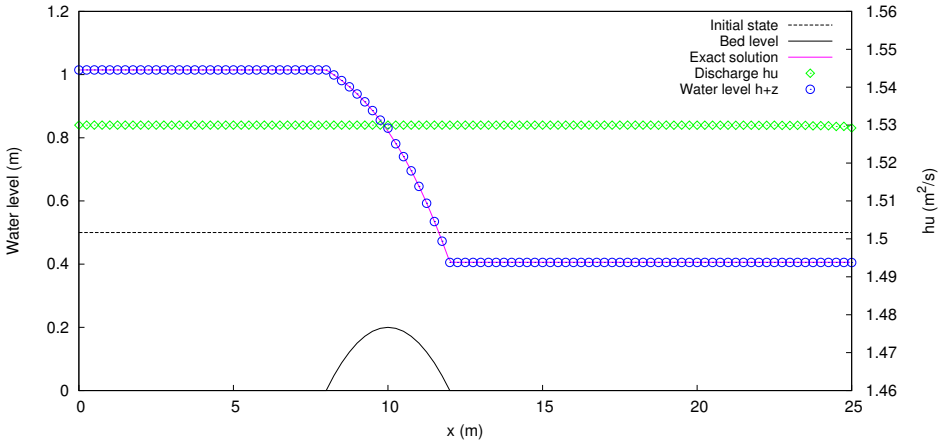

Figure 4.27: Numerical vs. exact solution for the steady state.

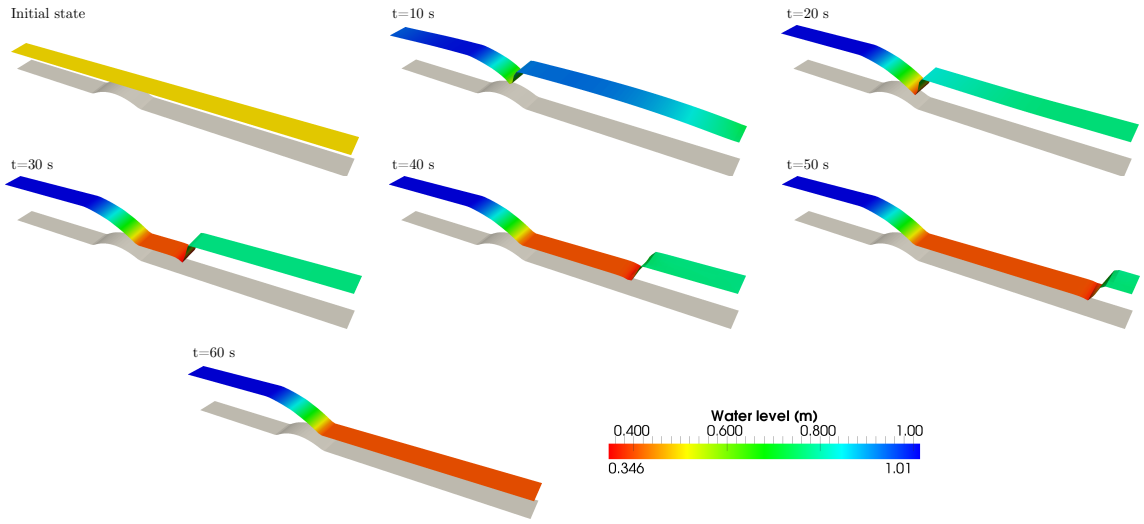

Figure 4.28: Convergence to the transcritical steady state over a bump.

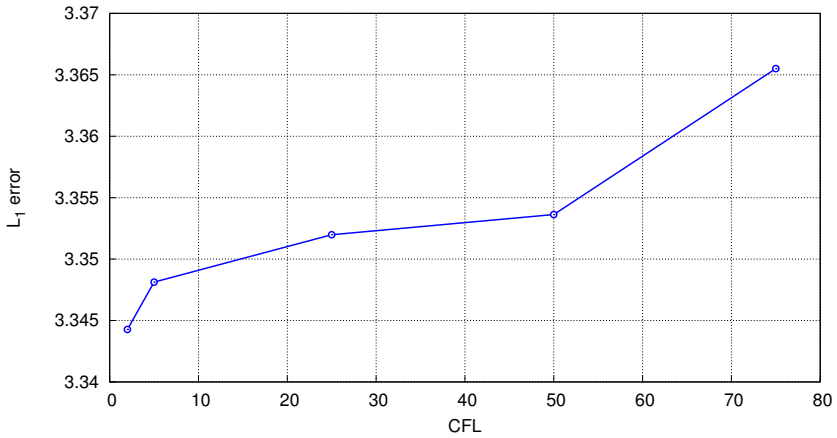

Figure 4.29: L_1 error vs. CFL number.

In order to evaluate the quality of the steady numerical solutions, the L_1 error with respect to the exact solution is computed for several CFL numbers:

$$Error(L_1) = \sum_{i=1}^{N} \left| h_i^{num} - h_i^{exact} \right| \tag{4.9}$$

Table 4.7 and Figure 4.29 show the error values in terms of the CFL. In the light of the results, it is clear that the implicit scheme provides a very good steady solution for high CFL numbers.

Scheme	CFL	L_1 error
Implicit	2	3.344
Implicit	5	3.348
Implicit	25	3.352
Implicit	50	3.354
Implicit	75	3.366

Table 4.7: Transcritical test case L_1 errors in terms of the CFL number.

4.3.4 MacDonald test case

This case was proposed by MacDonald in [51] and [52]. It represents a 1D configuration for open channel flow in which an analytical solution can be obtained for the steady state. The test consists of a rectangular channel $150m$ long with an irregular bed level. A constant Manning friction coefficient of $0.03 s/m^{1/3}$ is set all over the

channel. A constant discharge of $20m^3/s$ is imposed as inlet boundary condition and a fixed water depth of $0.800054m$ is set at the outlet. The analytical solution for the water depth along the channel is given by:

$$h(x) = 0.71 + 0.25 \sin^2\left(\frac{3\pi x}{300}\right) \tag{4.10}$$

Although this case was designed for testing 1D numerical solutions, a 2D configuration is assumed in the present work starting from dry bed initial conditions in order to check the wet/dry algorithm in both transient and steady situations.

Figure 4.30 shows the comparison between numerical and analytical solutions. A CFL number up to 300 can be reached without observing noticeable changes in the steady solution. As in the previous test case, the L_1 errors are provided, together with the CPU time and the speed-up values, defined as the ratio between the CPU times corresponding to implicit and explicit schemes (Table 4.8). Figure 4.31 shows the representation of the CPU computational times and speed-up values, defined as the ratio between the CPU time corresponding to explicit (t^{exp}_{CPU}) and implicit (t^{imp}_{CPU}) schemes, as follows:

$$\text{speed-up} = \frac{t^{exp}_{CPU}}{t^{imp}_{CPU}} \tag{4.11}$$

The implicit scheme shows a high efficiency in this case by reaching the steady solution up to 12 times faster than the explicit version of the numerical scheme, which requires $100.9s$ to complete the simulation. For the sake of completeness, the graphical representation of the L_1 error is also shown in Figure 4.32.

Scheme	CFL	t_{CPU}	speed-up	L_1 error
Explicit	0.9	100.9	-	0.545
Implicit	10	188.6	0.53	0.574
Implicit	35	58.1	1.74	0.573
Implicit	50	40.9	2.47	0.570
Implicit	75	28.4	3.55	0.565
Implicit	150	15.6	6.47	0.560
Implicit	200	11.9	8.48	0.577
Implicit	300	8.65	11.66	0.638

Table 4.8: MacDonald test case. CPU time, speed-up and L_1 error.

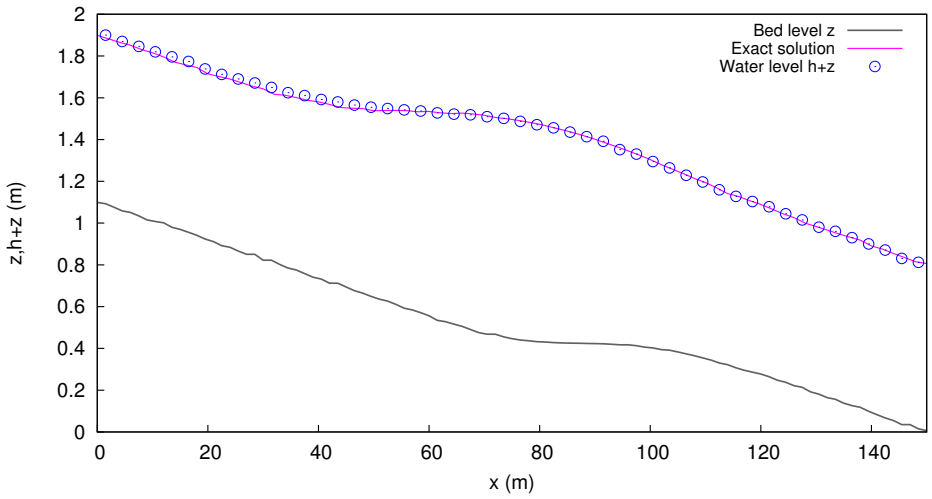

Figure 4.30: Comparison between numerical and exact solution for the MacDonald test case (CFL=300).

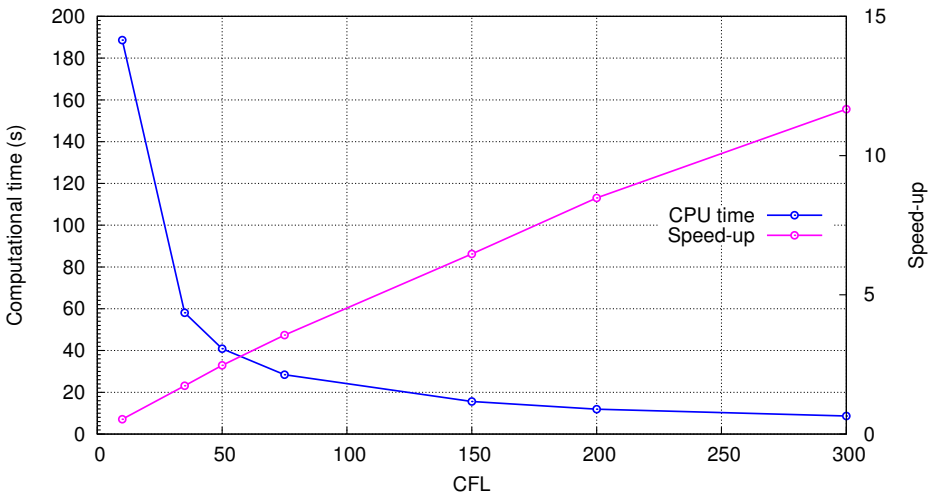

Figure 4.31: CPU times and speed-up values for the MacDonald test case.

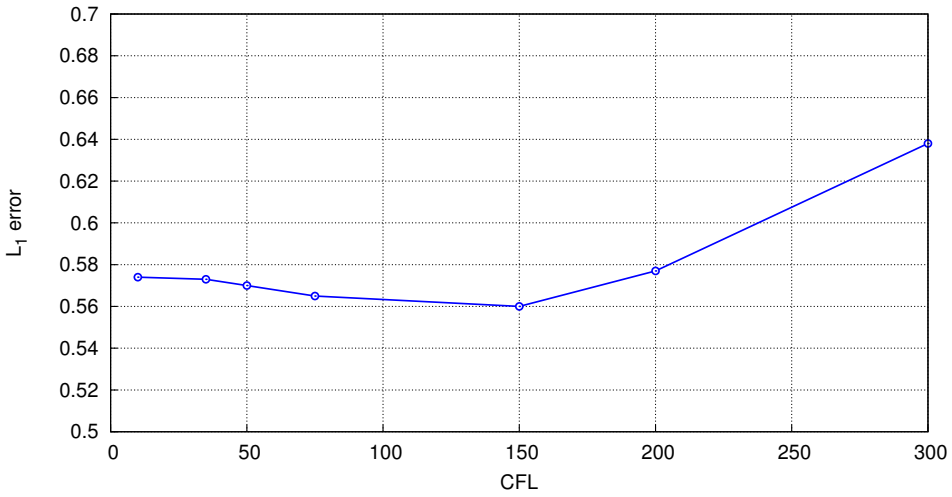

Figure 4.32: L_1 error vs. CFL number.

4.3.5 Circular dam-break

In order to test the behaviour of the SW implicit scheme under transient conditions, a circular dam-break test is considered in this section. A square frictionless domain of $200m \times 200m$ with no slope is considered. All the boundaries are closed and the initial state for the water depth is given by (see Figure 4.33):

$$h(x, y, 0) = \begin{cases} 4.0 & \text{if } \sqrt{x^2 + y^2} \leq 100m \\ 1.0 & \text{otherwise} \end{cases} \tag{4.12}$$

Figure 4.33 also shows the line that will be used to extract a longitudinal plot in where the numerical solutions for several CFL numbers are compared to the exact solution, computed as a 1D solution on the radial direction using a high resolution grid (see Figure 4.34).

A 10363 cell unstructured triangular mesh is used for the spatial discretization. Figure 4.34 shows the comparison between exact and numerical solutions for several CFL values at $t = 12s$. In the light of the results, a good agreement between numerical and exact solution is observed. As expected in a transient case, the larger the CFL value the more diffusive the numerical solution becomes. Nevertheless, in this particular case, an acceptable solution is found up to CFL=25. Figure 4.35 shows the comparison for the water depth values among several CFL numbers at

$t = 12s$. As in the longitudinal profile, this 2D view shows the diffusion of the solution as the CFL increases, specially noticeable with CFL=50.

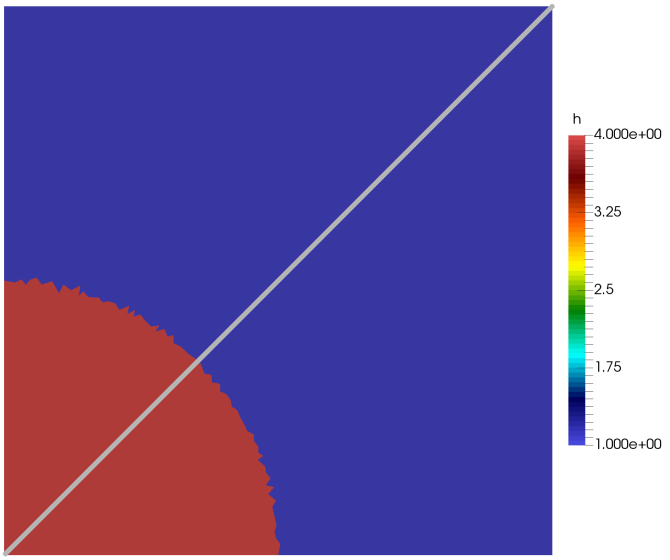

Figure 4.33: Initial conditions for the dam break test case and plotting line.

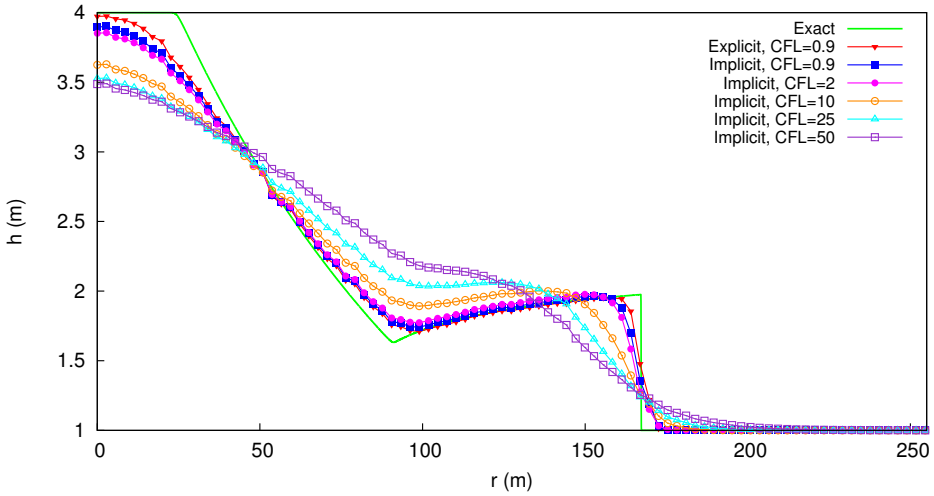

Figure 4.34: Numerical vs. exact solution for the dam break test case at $t = 12s$ (10363 cell mesh).

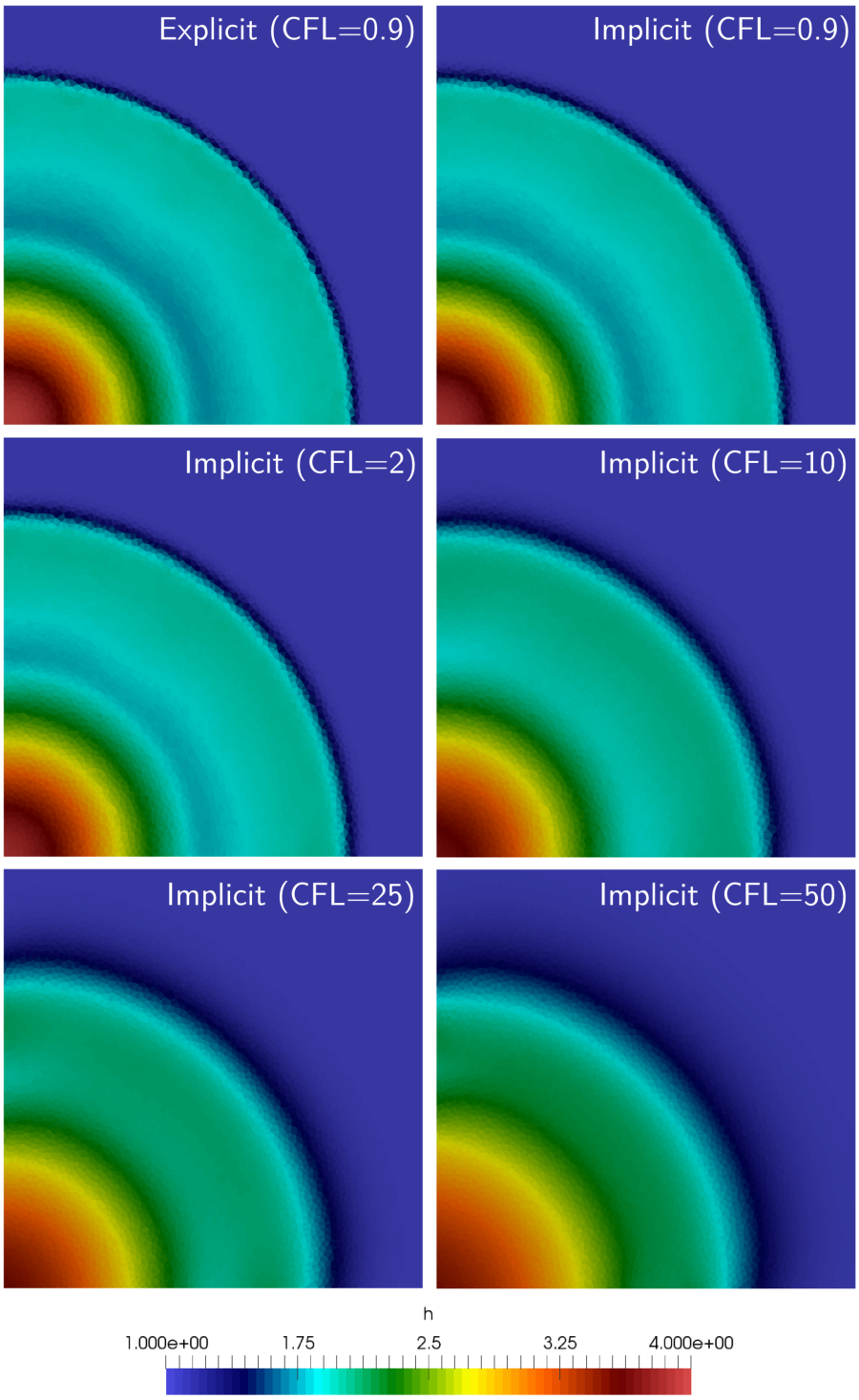

Figure 4.35: Transient solution for the circular dam break test case at $t = 12s$ for several CFL numbers (10363 cell mesh).

The computational times and the speed-up values for this test case are shown in Figure 4.36. In this particular case, the implicit scheme needs a CFL of 50 in order to reach the solution faster than the explicit one, which took $0.69s$. Therefore, an implicit temporal discretization of the SWE is not the most suitable choice for this transient problem due to the diffusion of the numerical solution associated to the large CFL number required to beat the explicit scheme.

In order to perform a mesh convergence study, the L_1 error is computed for this case for all the CFL values using 5 different computational meshes ranging from 1560 to 19389 cells. Table 4.9 shows the CPU time, speed-up and L_1 error in terms of the CFL number for all the meshes considered for this test case. The CPU times for the first two meshes were negligible and they are not shown. All these data are graphically represented in two ways. Figure 4.37 shows the L_1 error with respect to the CFL number for the 5 meshes. It can be seen that the error asymptotically increases with the CFL value and decreases with the mesh refinement, as expected.

On the other hand, Figure 4.38 shows the results of the mesh convergence study. The L_1 error is plotted against the square root of the number of cells (both axis in log scale) for several CFL values. In all the cases, a convergence of almost order 1 is achieved.

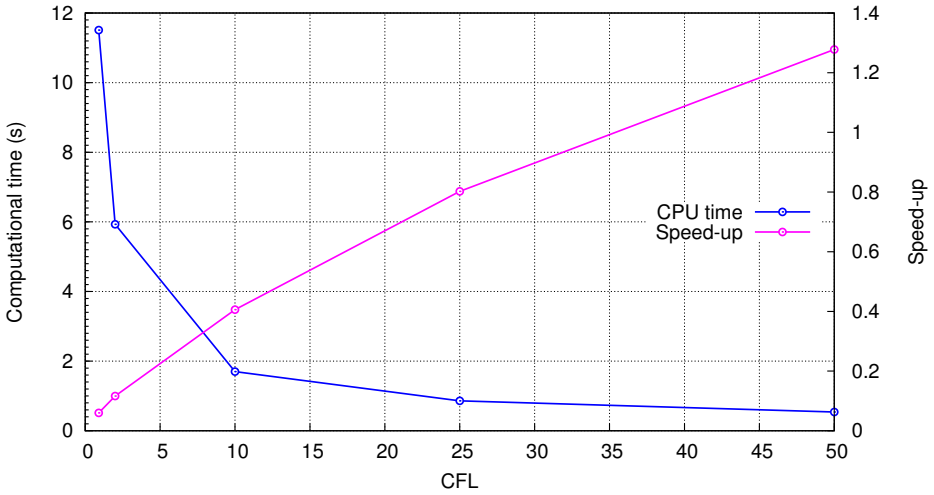

Figure 4.36: CPU times and speed-up values for the circular dam break test case (10363 cell mesh).

Another interesting comparison is performed in this test case. The simulation is repeated by considering an implicit numerical scheme with $\theta = 1/2$. A 10363 cell

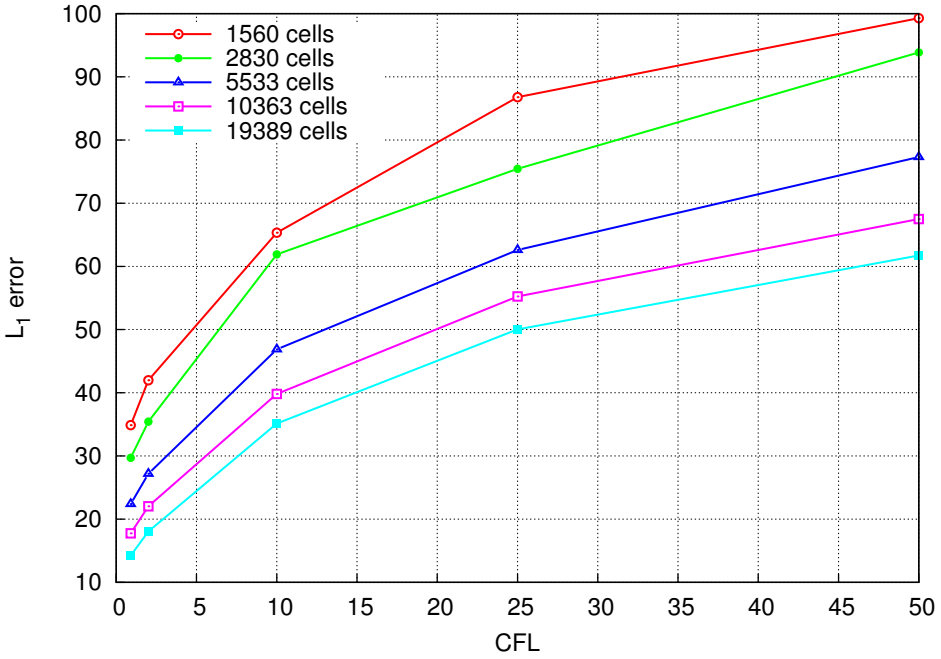

Figure 4.37: L_1 error with respect of CFL number for several meshes.

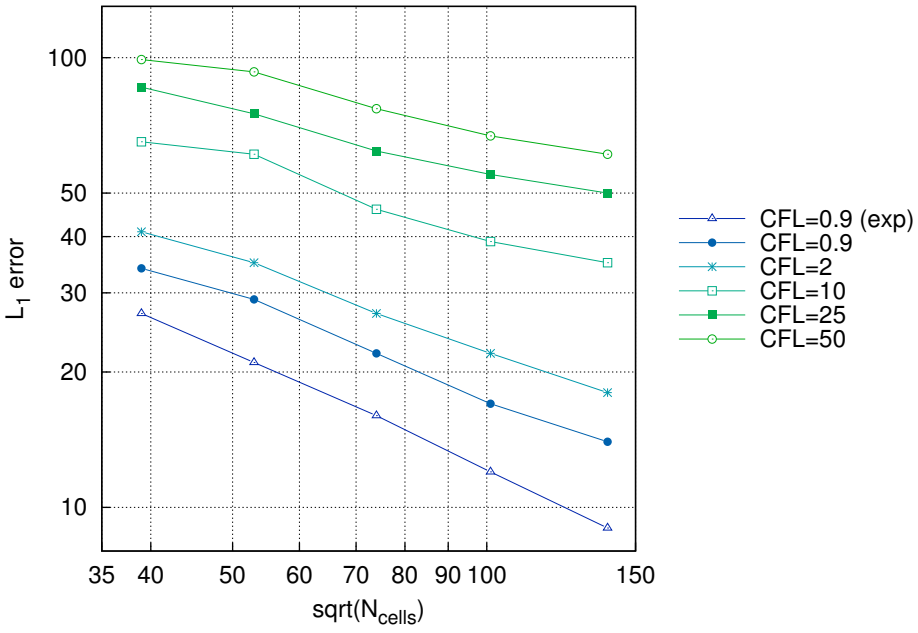

Figure 4.38: L_1 error with respect of the mesh size in logarithmic scale for several CFL numbers.

mesh is used in this case. Figure 4.39 shows the longitudinal profiles of the numerical solutions for several CFL values. It can be seen that the solutions become oscillatory for CFL>2. This behaviour agrees with the non-TVD character of this scheme for high CFL numbers [14].

Figure 4.40 shows the comparison between numerical solutions corresponding to $\theta = 1$ and $\theta = 1/2$ for CFL=2 and CFL=10. As expected, the scheme with $\theta = 1/2$ becomes less diffusive than the full implicit one. This is specially noticeable in the rarefaction wave area.

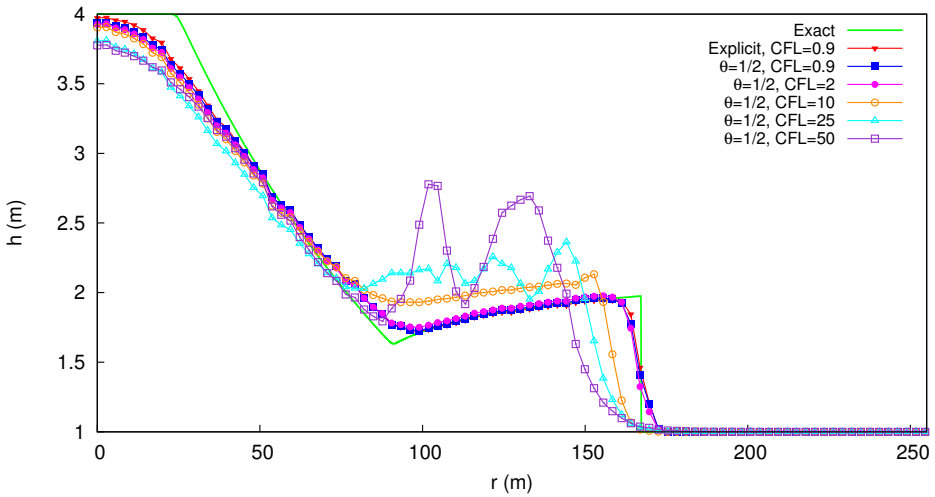

Figure 4.39: Numerical vs. exact solution for the dam break test case at $t = 12s$ using $\theta = 1/2$ (10363 cell mesh).

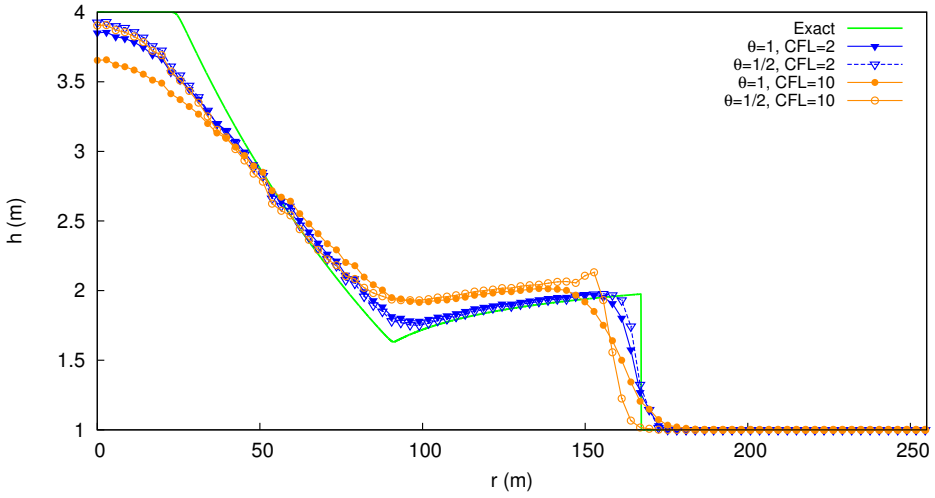

Figure 4.40: Comparison between $\theta = 1$ and $\theta = 1/2$ numerical solutions (10363 cell mesh).

N_{cells}	Scheme	CFL	CPU time	Speed-up	L_1 error
1560	Explicit	0.9	-	-	27.55
	Implicit	0.9	-	-	34.87
	Implicit	2	-	-	41.97
	Implicit	10	-	-	65.34
	Implicit	25	-	-	86.78
	Implicit	50	-	-	99.28
2830	Explicit	0.9	-	-	21.92
	Implicit	0.9	-	-	29.70
	Implicit	2	-	-	35.44
	Implicit	10	-	-	61.89
	Implicit	25	-	-	75.43
	Implicit	50	-	-	93.85
5533	Explicit	0.9	0.31	-	16.91
	Implicit	0.9	4.18	0.07	22.40
	Implicit	2	2.18	0.14	27.18
	Implicit	10	0.57	0.54	46.87
	Implicit	25	0.3	1.03	62.59
	Implicit	50	0.23	1.35	77.30
10363	Explicit	0.9	0.69	-	12.76
	Implicit	0.9	11.51	0.06	17.76
	Implicit	2	5.93	0.12	22.03
	Implicit	10	1.7	0.41	39.82
	Implicit	25	0.86	0.80	55.24
	Implicit	50	0.54	1.28	67.49
19389	Explicit	0.9	3.08	-	9.50
	Implicit	0.9	28.25	0.11	14.23
	Implicit	2	14.29	0.22	18.05
	Implicit	10	4.2	0.73	35.13
	Implicit	25	2.11	1.46	50.03
	Implicit	50	1.33	2.32	61.72

Table 4.9: Circular dam-break test case. CPU time, speed-up and L_1 error.

4.3.6 Tsunami test case

In order to test the implicit scheme in transient conditions with experimental data, a tsunami test case in a 1/400 laboratory scale is carried out in this section [48]. This case was also reproduced by other authors for testing 1D shallow-water schemes [13] or Large Time Step schemes with CFL>1 [60]. Figure 4.41 shows the bed elevation map and the gauging points where experimental data are available. The coordinates for the three gauges are:

$$P1 = (4.52m, 1.196m), \quad P2 = (4.52m, 1.696m), \quad P3 = (4.52m, 2.196m) \quad (4.13)$$

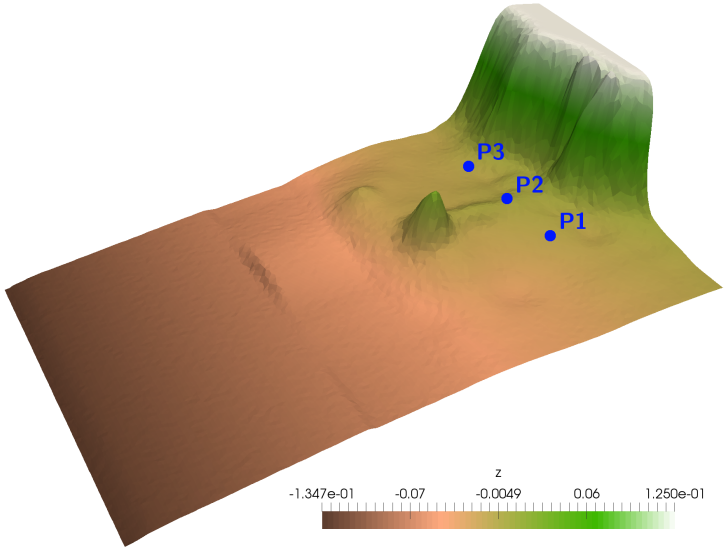

Figure 4.41: Tsunami test case topography and gauge locations.

The domain ($5.488m \times 3.388m$) is discretized by means of an unstructured triangular mesh of 19000 elements. A constant roughness Manning's coefficient of $0.01sm^{-1/3}$ is set and a uniform water level of $h + z = 0.0$ is assumed as initial condition. As in the experimental setup, all the boundaries are closed but the one corresponding to the offshore incoming wave, which is defined as a temporal variation of the water level $(h + z)$, as shown in Figure 4.42.

The numerical simulation has been carried out using several CFL numbers for the implicit scheme in order to establish a comparison between numerical and ex-

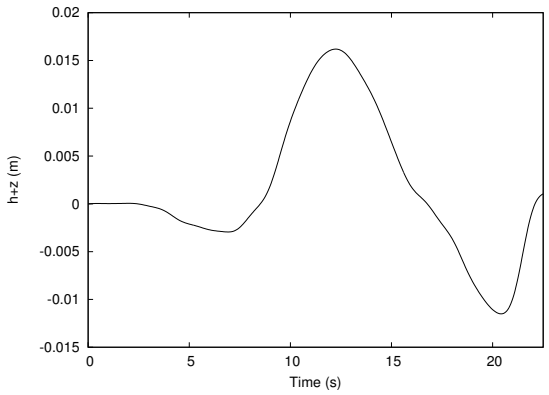

Figure 4.42: Inlet boundary condition.

perimental results. A 3D representation of the numerical results for water depth at $t = 0$, $t = 5s$, $t = 10s$, $t = 13s$, $t = 18s$, $t = 25s$ is shown in Figure 4.43 where a proper solution of all the wet/dry interfaces is reached at any time of the simulation. In order to validate the model, the numerical results for several CFL numbers corresponding to the water level $(h + z)$ are compared with the experimental measures provided by [48] at the $P1$, $P2$ and $P3$ probes (Figure 4.44). The numerical results for the explicit scheme are also shown. A good agreement between numerical and experimental results is observed, even for large CFL numbers. When choosing CFL<1, the implicit scheme produces the same solution as the explicit one, ensuring the consistency of the model. As expected, the larger the CFL the more diffusive the implicit numerical solution is, but acceptable results are achieved until CFL=50 for all the considered gauges. The solution for CFL=200 is also shown in order to remark the stability of the implicit numerical model. In this case, the diffusivity of the solution is also due to the resolution loss of the inlet boundary data when choosing large time steps.

Figure 4.45 shows the CPU times and the speed-up values. In this case, the explicit scheme took $22.26s$ to complete the simulation. An speed-up of 1.14 is obtained when using a CFL of 50 while an speed-up of 2.08 is reached with CFL=200.

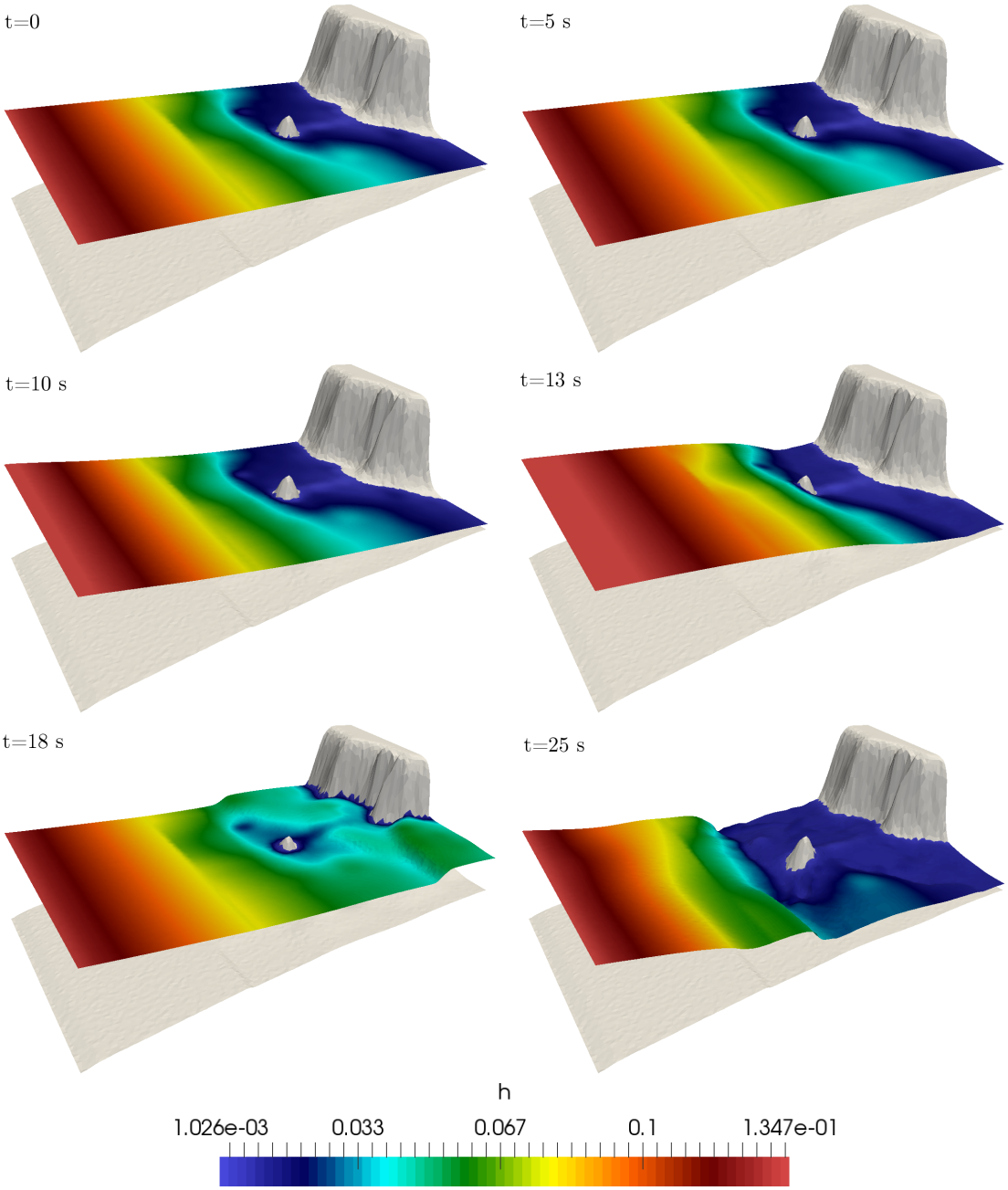

Figure 4.43: 3D representation of the numerical results for water depth at several simulation times.

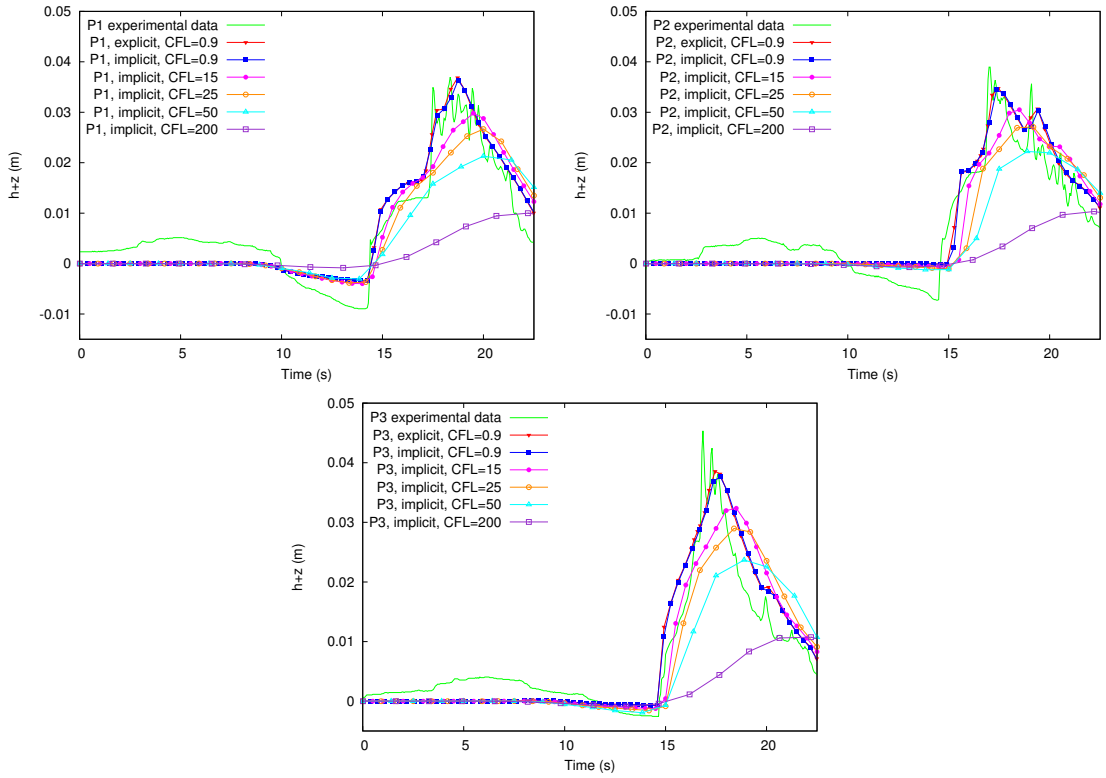

Figure 4.44: Numerical results at the three gauging points.

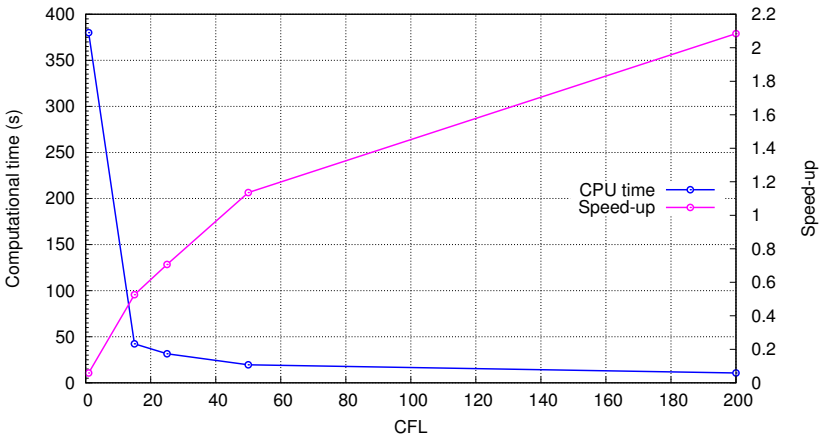

Figure 4.45: CPU times and speed-up values for the tsunami test case.

4.3.7 Conclusions

In general terms, all the results presented in this section show a good agreement with the analytical solution or experimental data, even for large CFL numbers (up to 300 in some cases) when the implicit numerical scheme is used. A quality loss in the transient solution due to the high numerical diffusion is also observed when using large time steps but the steady solution is reached without noticing numerical issues. Hence, in the light of the results presented in this work, the overall conclusions can be summarized in the next points:

- The presented implicit numerical scheme is robust, conservative and preserves well the C-property regardless of the CFL value in quiescent water cases.

- Steady solutions are perfectly reproduced with large CFL numbers, up to 300 in the MacDonald test case presented in Section 4.3.4. The efficiency of the implicit numerical scheme is remarkable in this case, leading to an speed-up value of 12.

- A good agreement between numerical and exact solution is observed in strong transient cases, as the circular dam break presented in Section 4.3.5. As expected, the larger the CFL value the more diffusive is the transient solution but acceptable solutions has been found for CFL up to 25 in this particular case. The tsunami test case presented also shows a good agreement between numerical solutions and experimental data, even for large CFL numbers. Despite the inherent diffusivity of the implicit transient solutions, the unconditional stability of the model is pointed out in this case.

- Despite the fact that an implicit method normally requires less solution steps, each one demands more computational time than the solutions obtained by an explicit scheme. This strongly depends on the number of iterations the matrix solver needs to do for achieving the convergence. Overall, the larger the CFL the more diffusive the implicit numerical solution is. Nevertheless, if the numerical diffusion can be assumable, the possible gain in performance due to the high CFL choice can be a point in favour of using these kind of numerical schemes under transient conditions. On the other hand, the steady solutions

are perfectly reached regardless of the CFL value so the implicit methodology is adequate and recommendable for solving the steady or nearly-steady flows.

- When applied to real catchment, An infiltration map which considers different soil types improves significantly the agreement between numerical and experimental hydrographs in both Horton and Green-Ampt infiltration models. The calibration of the empirical infiltration models studied in this paper, Horton and Green–Ampt methods, present a significant improvements over previous published results corresponding to the Arnás basin. The reason for this good agreement between numerical and experimental data is the careful study concerning the initial state of the catchment, in terms of surface water, and the infiltration mapping.

- The 2D SW model for surface flow calculation allows to improve the hydrograph fitting in two ways. On the one hand, the coupling of Horton and Green–Ampt models with a 2D surface flow model confers the possibility of calculating the soil infiltration rate locally for each cell. On the other hand, it is shown that the possibility of using infiltration maps in order to take into account different soil or vegetation types improves the quality of the results.

4.4 2D Zero-Inertia model

4.4.1 Mesh sensitivity analysis

Some cases are presented in this section to test de 2D Zero-Inertia model with a double motivation. First, a comparison between rectangular structured (RS) and triangular unstructured (TS) meshes is done. Second, the mesh size influence on the implicit scheme performance is studied.

A $8km \times 8km$ domain with the bed level given by:

$$z(x,y) = \max\left\{0, 2.0 - 6.0 \cdot 10^{-7}\left[(x-4000)^2 + (y-4000)^2\right]\right\} \tag{4.14}$$

is discretized by means of the computational meshes presented in Table 4.10. A constant Manning's roughness value of $0.01sm^{-1/3}$ and dry initial conditions ($h = 0m$) are assumed for the entire domain.

Mesh name	Cell type	Cell ordering	Number of cells	Local refining
RS1849	Rectangular	Structured	1849	NO
TU1871	Triangular	Unstructured	1871	YES
TU5674	Triangular	Unstructured	5674	YES

Table 4.10: Mesh characteristics.

In all cases, the implicit scheme efficiency is measured by means of the speed-up factor, defined as in Equation 4.11. The time step chosen for the explicit scheme corresponds to the maximum that guarantees the stability of the numerical scheme. This value is found by following a trial and error procedure.

Transient state

The main purpose of this first case is to check the need to use unstructured triangular meshes in cases where the bed level has an irregular topography. In this test, a propagating-wave front is simulated by setting a fixed-value of $h = 1.0m$ in the lower and right boundaries. Upper and right boundaries are closed. A comparison between two meshes (RS1849) and (TU1871) with approximately the same number

of elements is done (Figure 4.46).

Figure 4.47 shows the transient numerical solution for water depth at $t = 2150s$ with the implicit scheme on both meshes. The RS1849 mesh produces a bad adaptation to the rounded geometry of the problem, contrary to the TU1871 mesh, which allows a perfect fit when using irregular topographies. The dry-wet situation is correctly led by means of the positivity-preserving technique detailed in Section 3.1.3. When the final steady state is reached (Figure 4.48), the good flexibility of the locally refined unstructured triangular mesh allows to calculate an accurate dry-wet border around the bed bump.

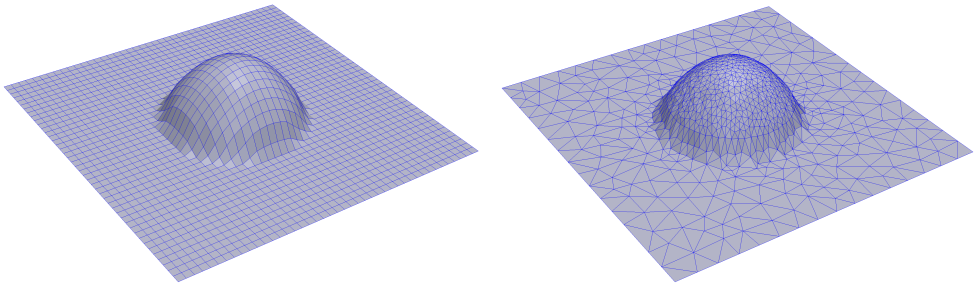

Figure 4.46: Case 1 topography and meshes: RS1849 (left) and TU1871 (right).

Steady state

The previous test showed the benefits of using an unstructured discretization due to the good adaptability to complex geometries. In this second case, the TU1871 mesh is chosen for testing the implicit scheme performance against its explicit version. Additionally, a second finer mesh (TU5674) is used in order to study the influence of the number of mesh elements.

The case geometry and initial conditions are the same as those used in Case 1 (Figure 4.46) where all the boundaries take fixed values: $h = 1.0m$ in the lower and right boundaries and $h = 0.75m$ in the upper and left ones. These initial and boundary conditions lead to a steady state which is reached at $t = 5000s$.

A maximum explicit time step of $0.2s$ was found for this test case. Above this values the numerical solution becomes unstable when using the explicit scheme. Figure 4.49 shows the final steady numerical solution for water depth h and water level $h + z$ for both triangular meshes. Figures 4.50 and 4.51 show the CPU computa-

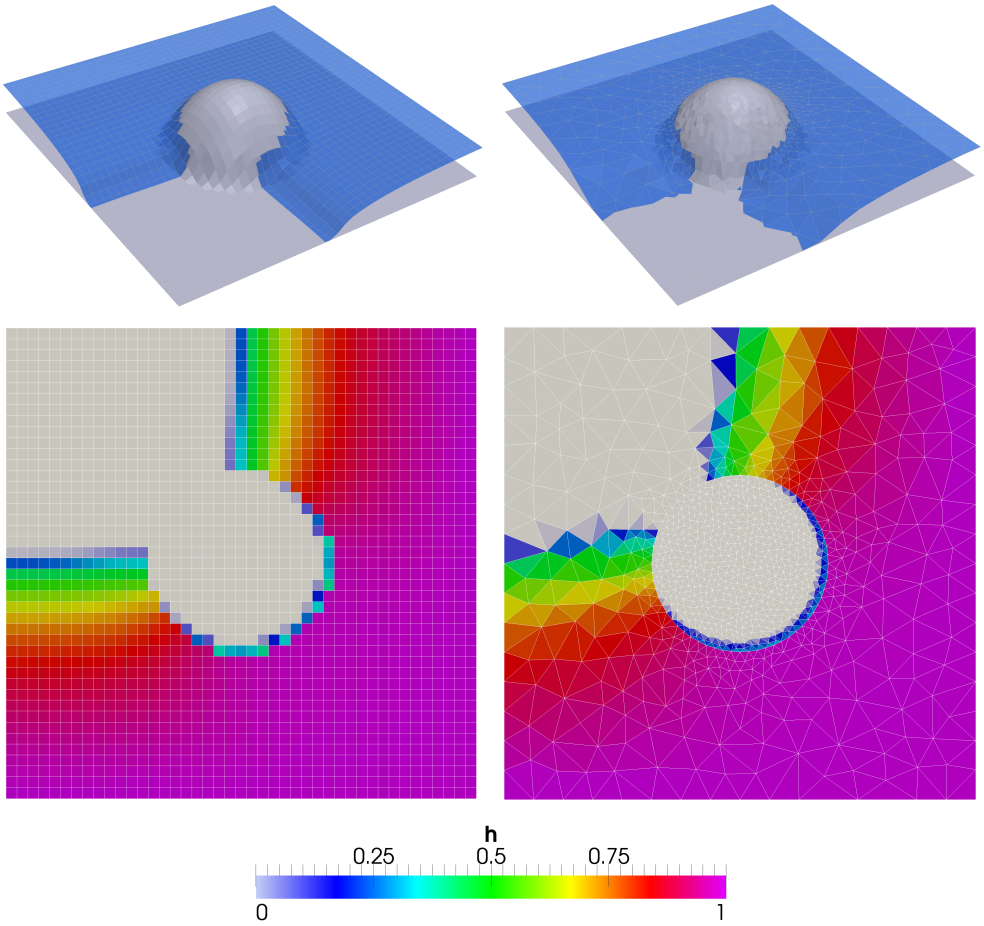

Figure 4.47: Case 1 transient numerical solution at $t = 2150s$: RS1849 mesh (left) and TU1871 mesh (right).

tional costs for an implicit time step selection from $1s$ to $500s$ and the speed-up values for both meshes.

In the light of the results, several conclusions are reached. First, the implicit ZI model is suitable for solving steady states over a complex topography without any restriction in the time step. In this case, a time step selection of $\Delta t = 500s$ allows to complete the simulation 11 times faster than when using the explicit scheme with the maximum time step choice. Secondly, a finer mesh provides a better quality solution but also increases the computational time. This is specially remarkable for the implicit scheme due to the equations system resolution step, which spends most of the computational effort. This is the reason why the speed-up factors are worse in the finer mesh. It is also worth to mention that, for this case, the speed-up factor scales consistently with the time step size, independently of the mesh size.

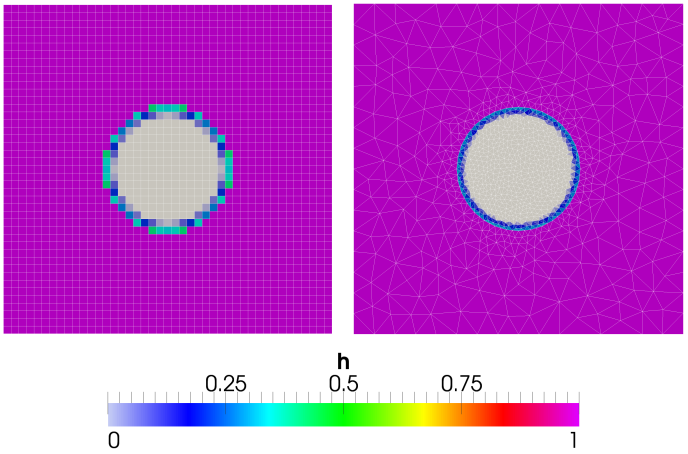

Figure 4.48: Numerical solution for Case 1 at final time: RS1849 mesh (left) and TU1871 mesh (right).

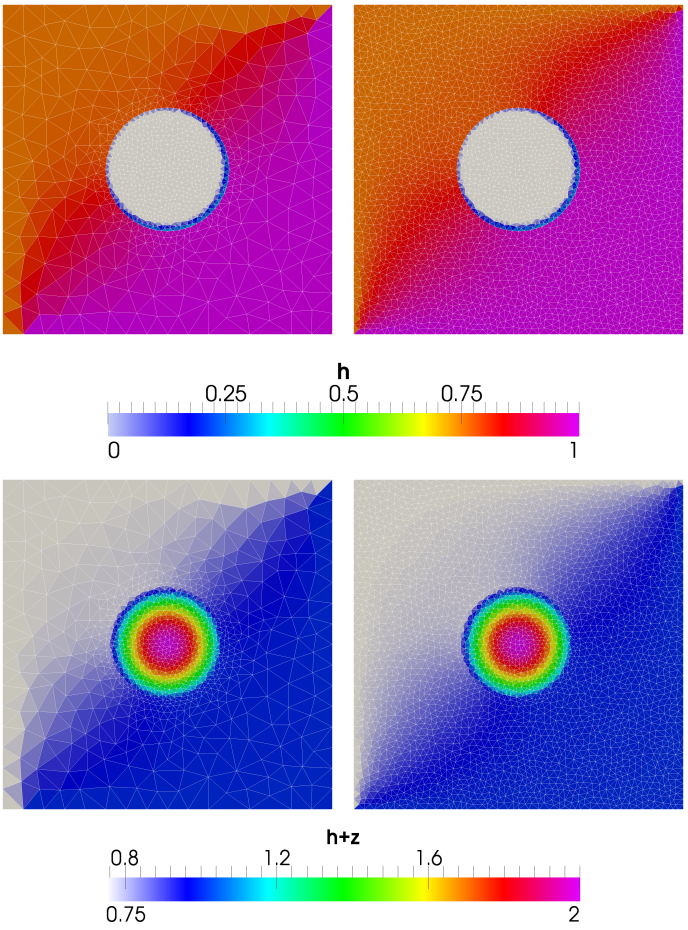

Figure 4.49: Steady state over a hump bed at $t = 5000s$ with TU1871 (left) and TU5674 (right) meshes. Numerical solution for water depth h (above) and water level $h + z$ (below).

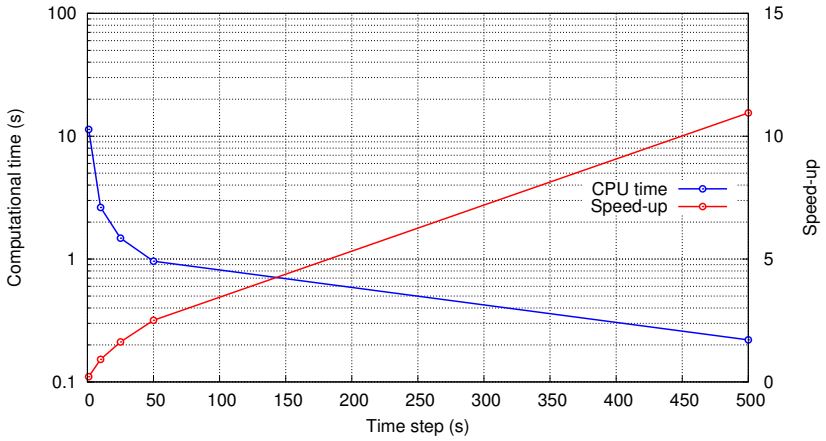

Figure 4.50: CPU time and speed-up for Case 2 with TU1871 mesh.

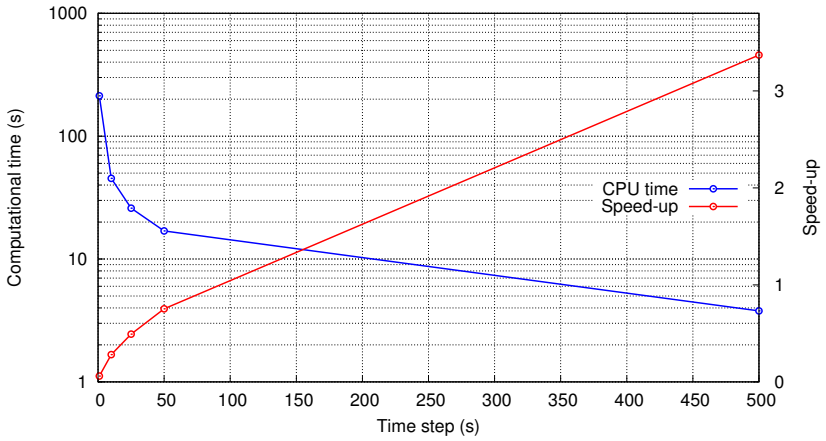

Figure 4.51: CPU time and speed-up for Case 2 with TU5674 mesh.

4.4.2 Tidal flow on a beach slope

An example of smooth-transient state is presented now. In this test case, presented in [98], a tidal flow over a beach is simulated. The topography of the beach is given by

$$z(x) = \begin{cases} 0.001x & (x \leq 300m) \\ 0.01x - 2.7 & (300m < x < 400m) \\ 0.001x + 0.9 & (x \geq 400m) \end{cases} \tag{4.15}$$

The tidal cycle has a period of $3600s$ and the water depth is given by

$$h(t) = 1.0 + 0.75 \cos\left(\pi \frac{t}{1800}\right) \tag{4.16}$$

The case setup consists of a $500m \times 50m$ domain, discretized by a squared uniform mesh of 250 cells. The Manning roughness coefficient is set to $0.03sm^{-1/3}$ and the initial condition consists of a constant water level of $1.75m$ all along the domain. All the boundaries are closed except the one where the tide is imposed.

Figure 4.52 shows the cross-sectional plots of the results for both implicit and explicit ZI model and the percentage difference respect to the explicit solution. The CPU times together with the speed-up values are plotted in Figure 4.53 and the solver iterations required for convergence are shown in Figure 4.54.

The results show a good concordance between implicit and explicit solutions with a maximum relative difference of 6% in the left boundary and less than 1% in the beach area, which would be the region of interest if applied to a real case. A maximum time step of $0.0075s$ was found for this particular case for the explicit scheme.

The first conclusion for this test case arises from the CPU times results (Figure 4.53). The implicit temporal discretization of the numerical scheme provides a freedom for choosing the time step, but a larger time step does not necessarily mean a lower computational cost. This is because a large time step usually means that the system solution process (linearization and matrix inversion) needs a higher number

of iterations for achieving convergence (Figure 4.54). In this particular case, there is an optimal choice of $\Delta t = 30s$ for the time step. Above this value, the solver becomes less efficient. When the optimal time step is chosen, the simulation is completed with a speed-up factor of 157, which means that the implicit scheme is a very efficient way to deal with these kind of smooth-transient problems.

Another interesting conclusion is reached from Figure 4.54. For a given Δt, the number of iterations decreases when the tidal variations are slower, that is, low tide and high tide. This fact supports the conclusion previously reached, regarding the good applicability of the implicit ZI model to smooth-transients quasi-steady and steady cases.

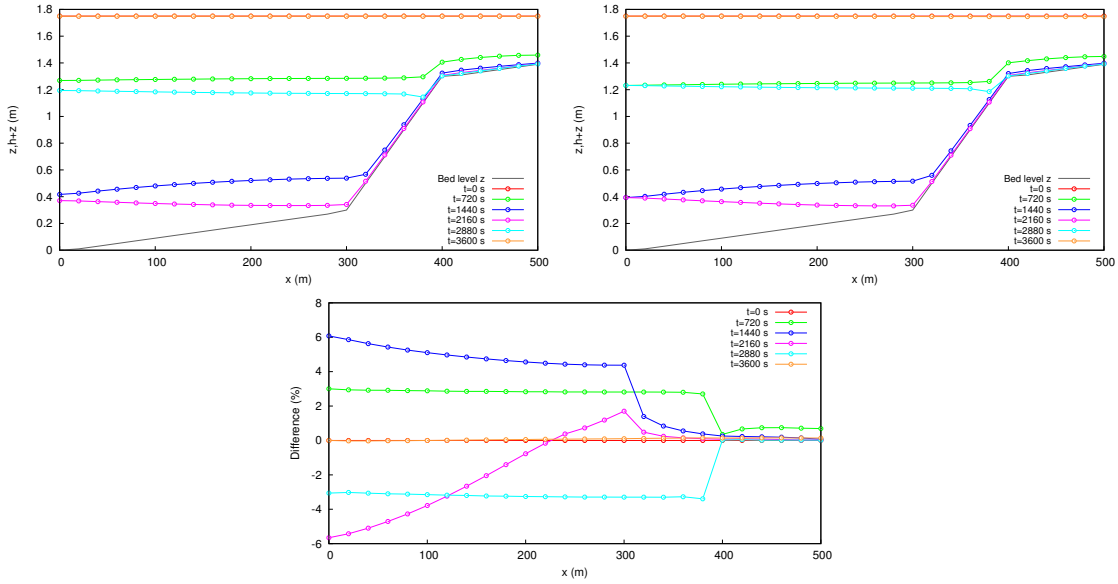

Figure 4.52: Cross-sectional plot of the numerical results for implicit scheme with optimal time step choice (left) and explicit scheme with maximum time step (right) at different times and relative difference between implicit and explicit schemes (below).

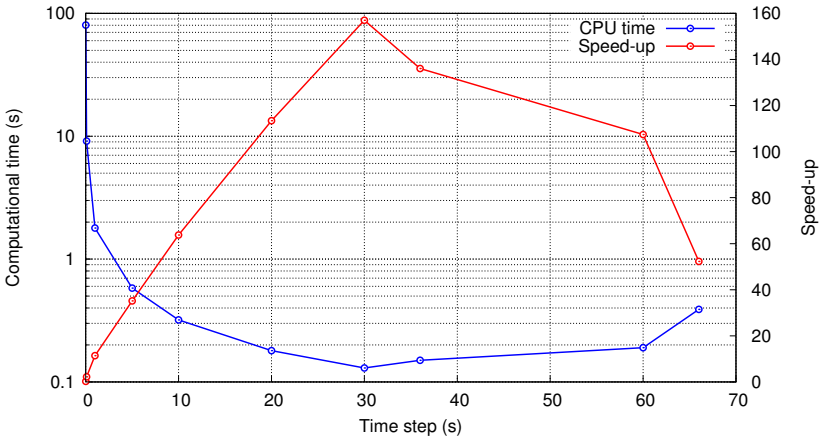

Figure 4.53: CPU time and speed-up for Case 3.

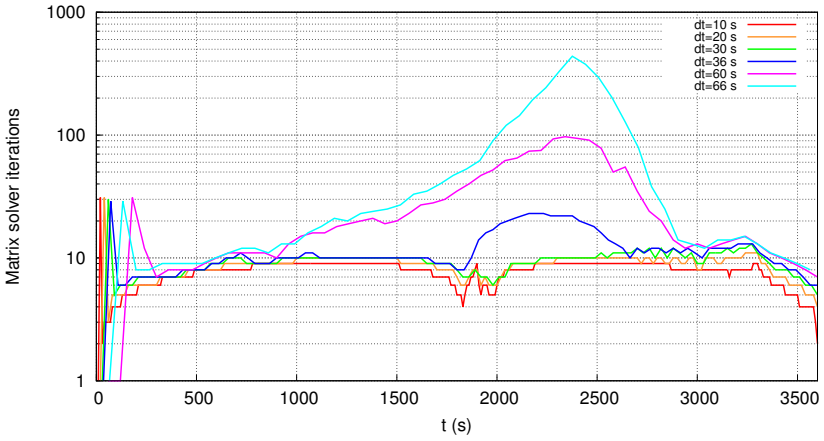

Figure 4.54: Total iterations for a selection of time steps.

4.4.3 Verification with analytical solution

In this section, a verification of the model is presented by means of the comparison of the numerical results with two analytical solutions for steady states. A 2D case with radial symmetry is considered in which a 16296 cell unstructured mesh is used for the spatial discretization (see Figure 4.55).

The first exact solution is built assuming $z(r) = 0$ and a constant Manning's roughness coefficient of $0.03 sm^{-1/3}$. Under these conditions, the analytical solution for Equation (2.28) in r direction is as follows:

$$h(r)^{13/3} = h_R^{13/3} + \frac{13}{3} q^2 n^2 \left(\frac{1}{R} - \frac{1}{r} \right) \tag{4.17}$$

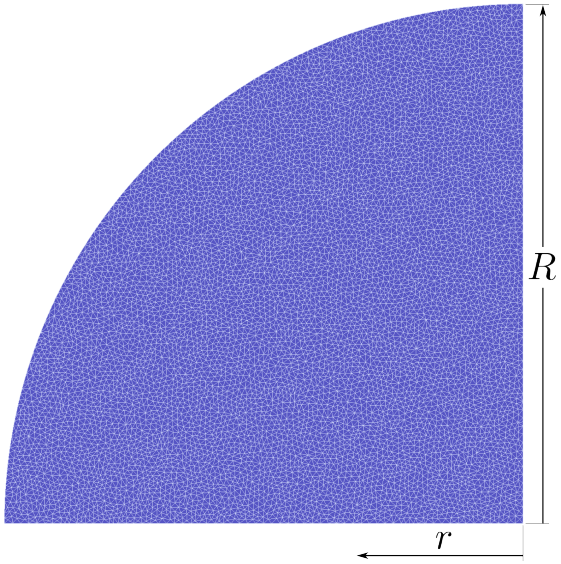

Figure 4.55: Geometry and mesh corresponding to the analytical test cases.

where $R = 200m$ represents the domain limit (see Figure 4.55), $h_R = 0.2m$ is the water depth at $r = R$ and $q = 0.52m^2/s$ is the steady unit discharge.

The second exact solution follows a different philosophy. A constant water depth ($h_0 = 0.15m$) is assumed for the whole domain in steady conditions. The same roughness coefficient as in the previous case is considered. In this case, the spatial derivative of the water depth in (2.28) cancels, so a solution for the bed level z can be found:

$$z(r) = z_R + q^2 \frac{n^2}{h_0^{10/3}} \left(\frac{1}{R} - \frac{1}{r} \right) \tag{4.18}$$

where $z_R = 0.15.$ is the bed level value at $z = R$.

A unit water discharge of $0.5m^2/s$ is set for this second case. Figure 4.56 shows the comparison between numerical and exact solutions for both cases. The implicit version of the numerical scheme is used. Several time step choices have been used without observing significant differences in the steady numerical solution. In the light of the results, a good agreement between numerical and analytical solutions is observed.

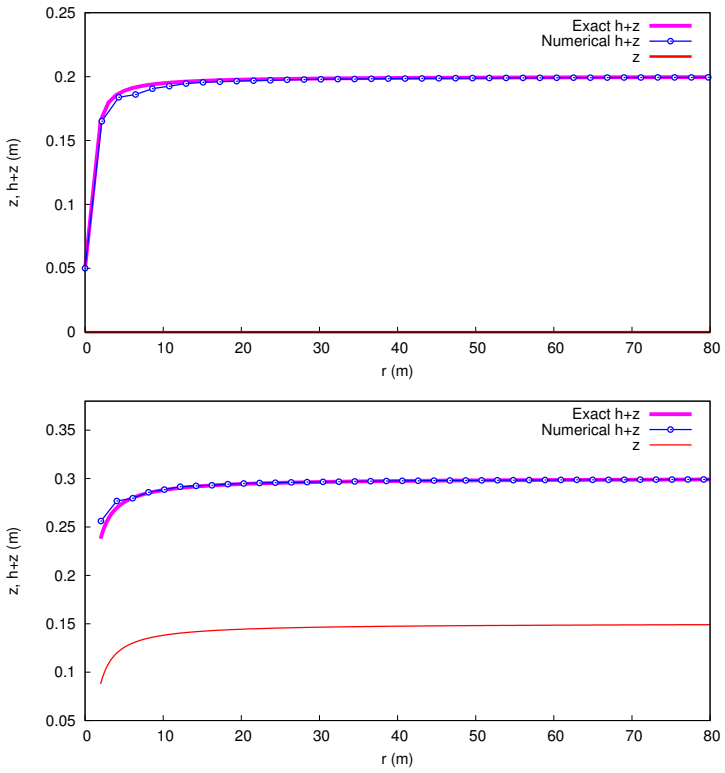

Figure 4.56: Comparison between numerical and exact solutions for the water level.

4.4.4 Validation with experimental test case

The experimental details and setup for this case is presented in [19]. A constant rainfall of $300mm/h$ during $20s$ is assumed all over an impervious domain where several obstacles are placed. The Manning's roughness coefficient is set to $0.016sm^{-1/3}$. The numerical results from implicit ZI model are compared against the experimental data provided in [19]. The obstacles are assumed to be much higher than the previsible water depth, so they are treated as holes in the computational mesh. Figure 4.57 shows the elevation map in a 3D projection, the unstructured triangular computational mesh and the initial dry state. Figure 4.58 shows the temporal evolution of the runoff for six different times.

Figure 4.59 shows the comparison between experimental and numerical outlet hydrographs. The scheme performance analysis with CPU times and speed-up factors is shown in Figure 4.60. Even though the best fit is achieved by means of the explicit scheme, a good agreement is also observed for the implicit scheme when choosing a time step of $0.01s$, that is 100 times larger than the maximum time

step allowed for the explicit scheme ($0.0001s$). This time step selection provides a speed-up of 9.4. The optimal time step choice for this case ($\Delta t = 0.13s$) leads to a speed-up factor of 41.4. When using an implicit scheme together with a large time step (as this one), the solution becomes more diffusive, so the hydrograph peaks may not be well captured, as shown in Figure 4.59.

Figures 4.61 and 4.62 show the spatial differences at a given time ($t = 9s$) for $\Delta t = 0.13s$ (optimal) and $\Delta t = 0.01s$, respectively. In the first case, local maximum differences of 15.5% appear in the wetted perimeter, but the overall average difference is less than 0.5%. On the other hand, when $\Delta t = 0.01s$ is chosen, the local maximum differences reduces to 2.2% and the average difference does not reach the 0.01%.

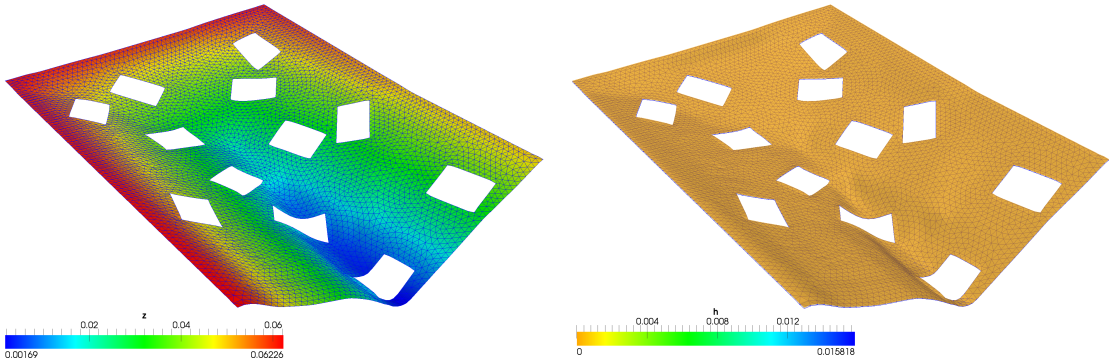

Figure 4.57: Elevation map and computational mesh (left) and initial state (right). Terrain elevation has been exaggerated 10 times.

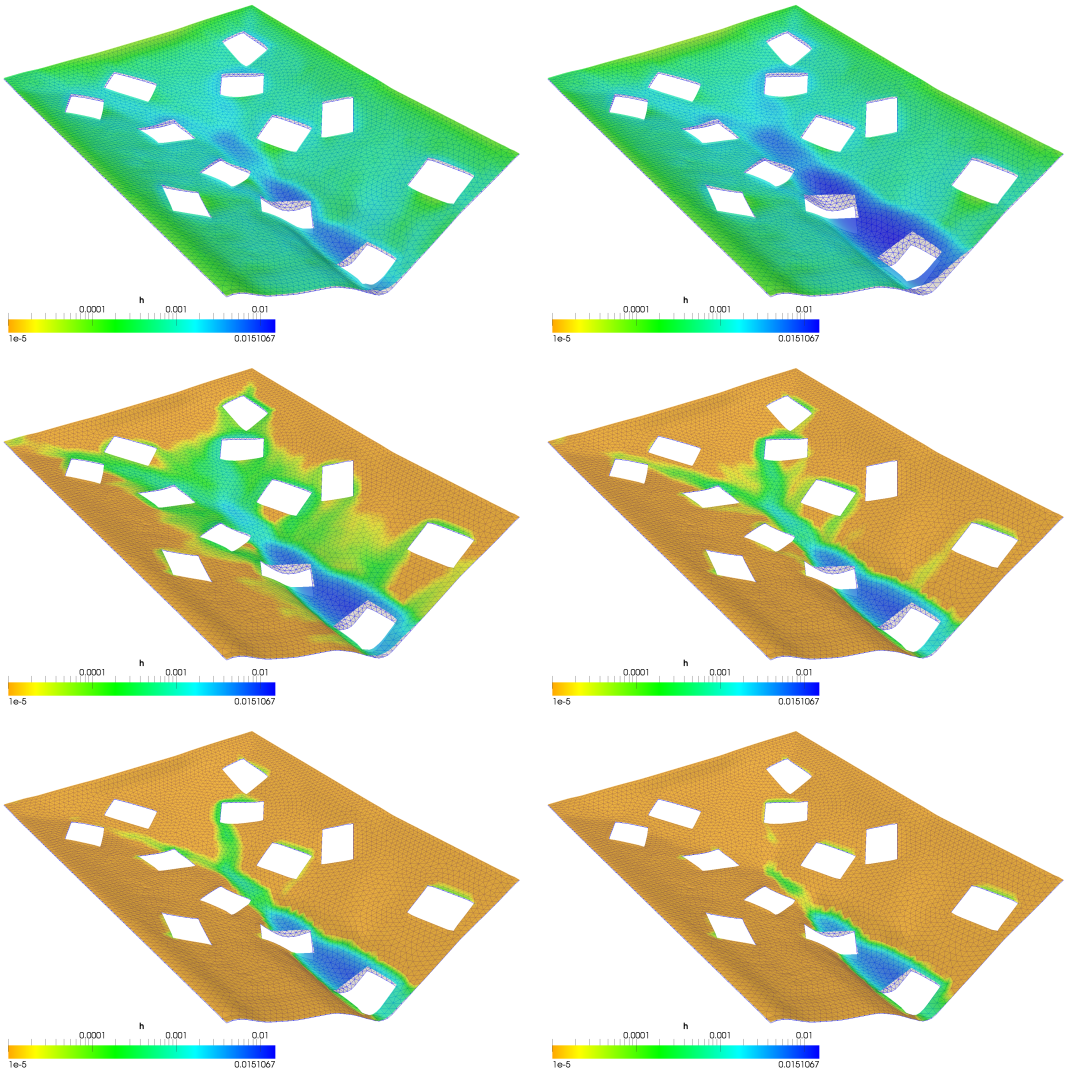

Figure 4.58: Temporal evolution of water depth in logarithmic scale for $t = 10s$, $t = 20s$, $t = 50s$, $t = 75s$, $t = 100s$ and $t = 200s$. ZI model with $dt = 0.1s$

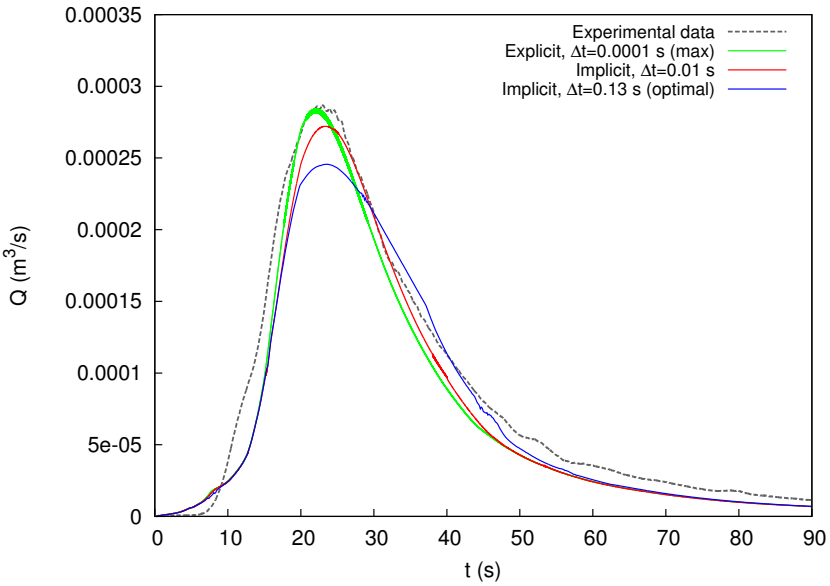

Figure 4.59: Outlet hydrographs for several time step choices.

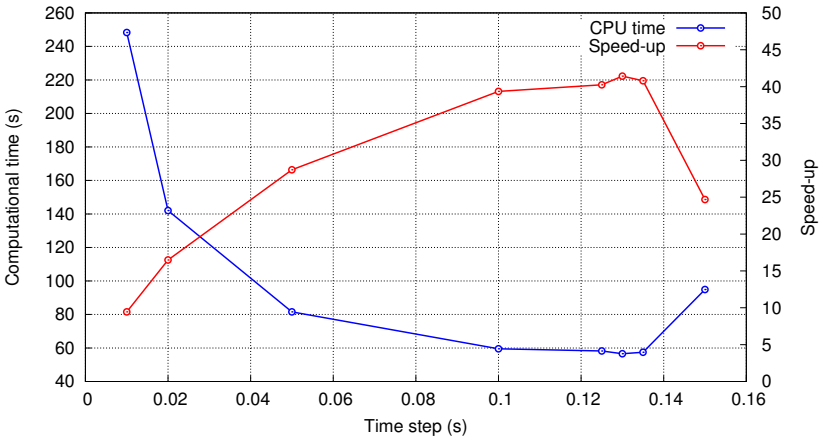

Figure 4.60: CPU computational time and speed-up vs. time step.

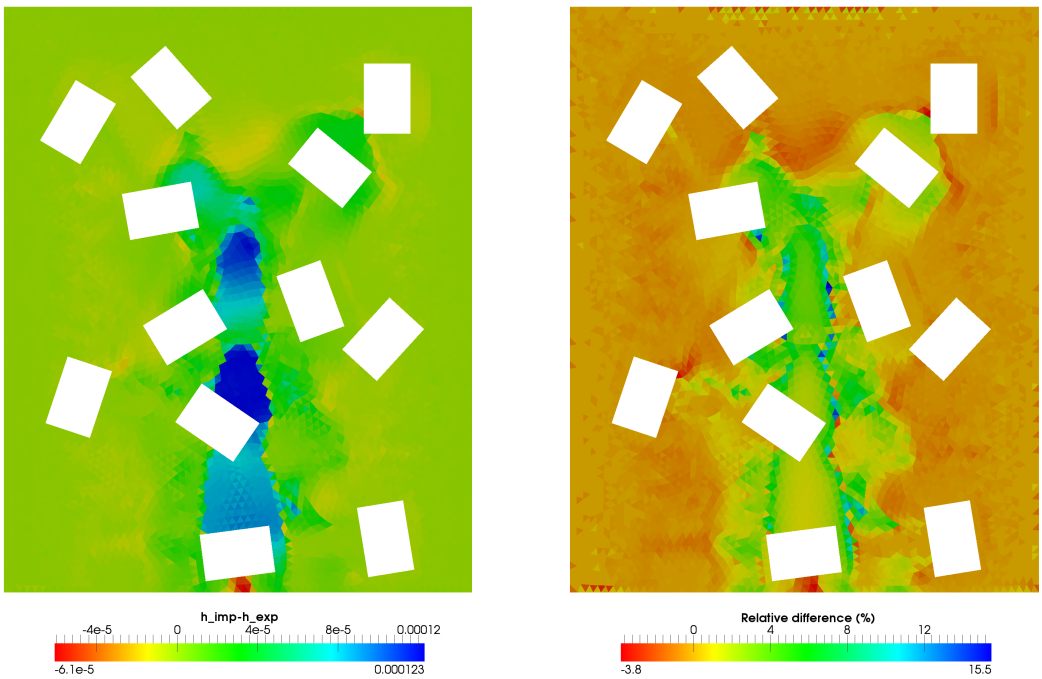

Figure 4.61: Absolute (left) and relative (right) water depth differences between implicit (with optimal Δt) and explicit (with maximum Δt) schemes at $t = 9s$.

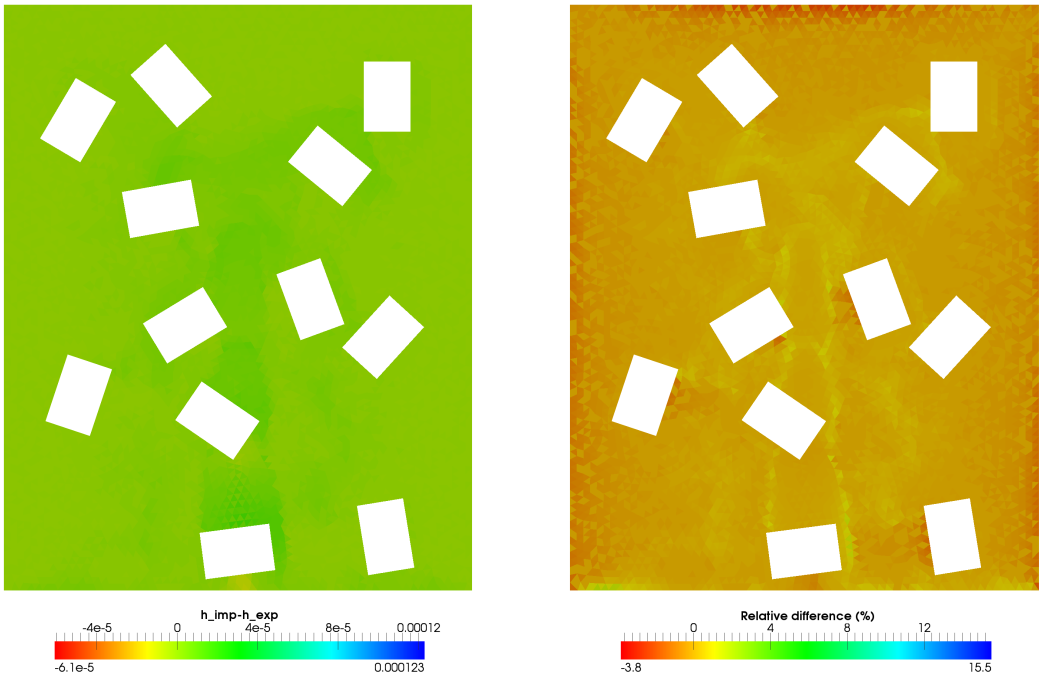

Figure 4.62: Absolute (left) and relative (right) water depth differences between implicit (with $\Delta t = 0.01s$) and explicit (with maximum Δt) schemes at $t = 9s$.

4.4.5 Valley flood simulation

The setup for this test is proposed in [1] to establish a comparison among different simulation models applied to valley flood simulation. Figure 4.63 (left) shows the valley bed elevation map. The domain is discretized by means of an unstructured triangular mesh (7592 cells) (see Figure 4.63 (left)). A uniform Manning's roughness coefficient of $n = 0.04sm^{-1/3}$ is set all over the domain. All the boundaries remain closed except the inlet $\sim 260m$ segment in which a discharge hydrograph is imposed (Figure 4.64) with a peak discharge of $3000m^3/s$. The evolution of the water depth is registered in several gauges located as in Figure 4.65.

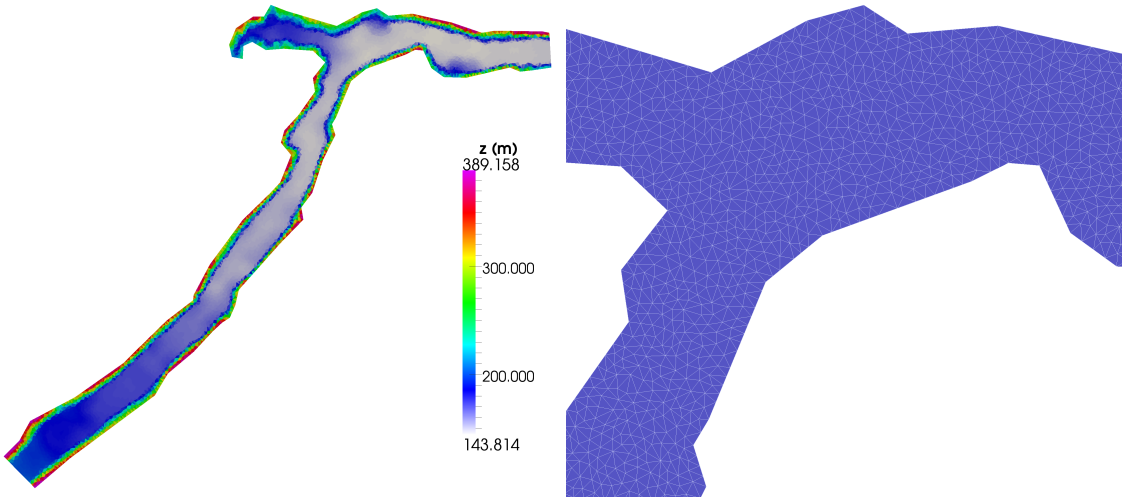

Figure 4.63: Domain bed elevations (left) and detail of the computational mesh (right).

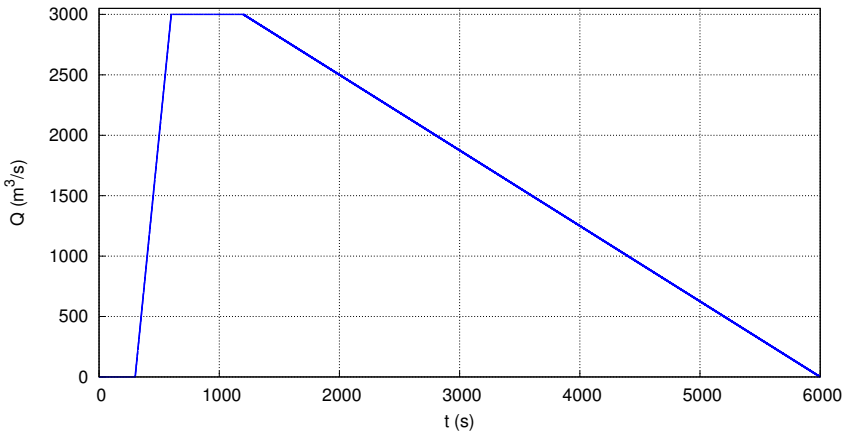

Figure 4.64: Inlet hydrograph.

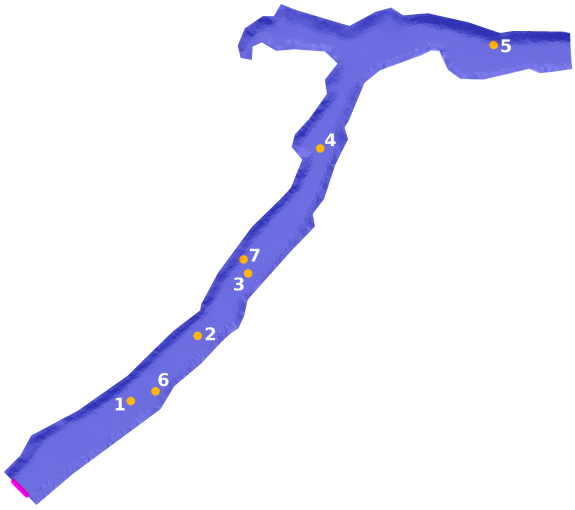

Figure 4.65: Spatial distribution of the gauging points and the inlet segment.

Figure 4.66 shows the initial condition and the temporal evolution of the water depth over the valley for several instants of the simulation. The numerical results given by the seven gauges are plotted in Figure 4.67. The comparison with the 19 numerical models presented in [1] is given in gauges 1, 3, 5 and 7. for the sake of clarity, only the envelope of all these results is plotted. In the light of the numerical results, all the gauges provides limnigraphs contained within the envelope of the rest of the models, taken as reference.

Figure 4.68 shows the contour lines for water depth values equal to $0.5m$. Again, the comparison is made in terms of the envelope of the results of the rest of the numerical models.

Figure 4.69 show the CPU times and speed-up values obtained in this case for a simulation time of $28800s$. The maximum time step allowed by the explicit numerical scheme is $\Delta t = 0.03s$, leading to a simulation time of $903.15s$. In the light of the numerical results, it is observed that the implicit scheme of the zero-inertia model is significantly more efficient that the explicit version for all the chosen time steps. On the other hand, it is observed again that larger time steps do not guaratize faster simulations due to the large number of iterations needed to linearize the equation when large time steps are used. In this particular case, the optimal time step is $\Delta t = 22s$, that is, 733 times larger than the maximum time step allowed by the explicit scheme, for stability reasons.

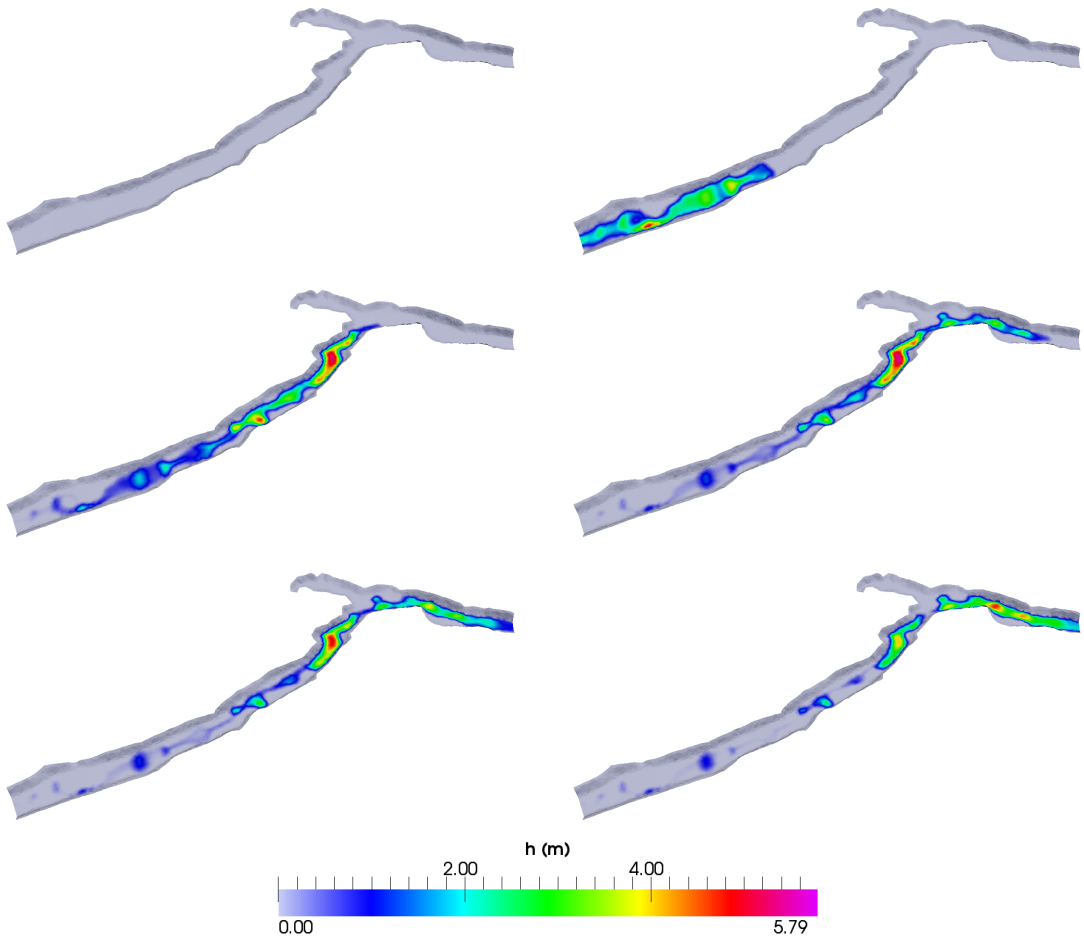

Figure 4.66: Water depth values for $t = 0s$, $t = 2500s$, $t = 7500s$, $t = 12500s$, $t = 17500s$ y $t = 108000s$.

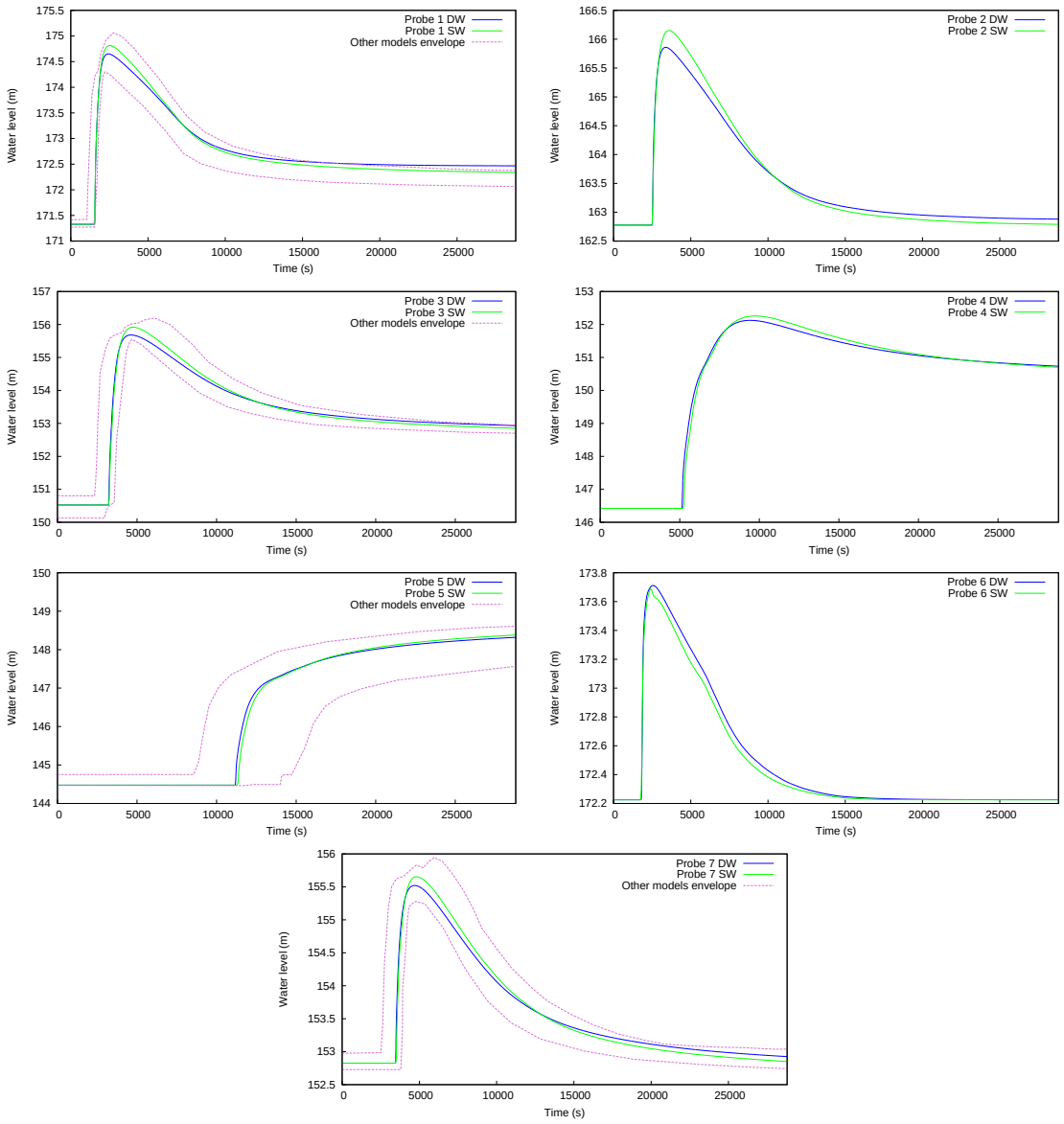

Figure 4.67: Water levels registered by the seven gauges and comparison with the results provided in [1].

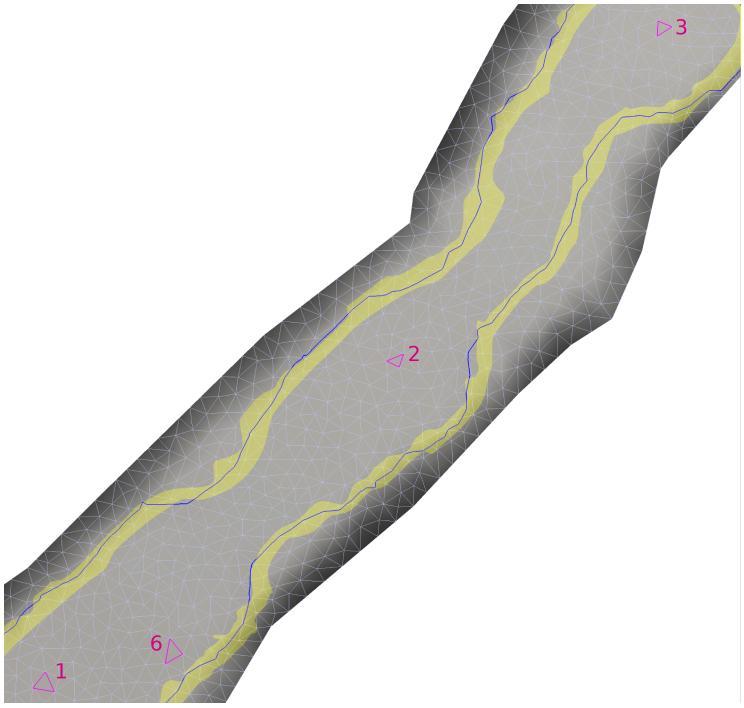

Figure 4.68: Contour values corresponding to water depth values equal to $0.5m$ (blue) and comparison with the results of the rest of the numerical models presented in [1] (yellow).

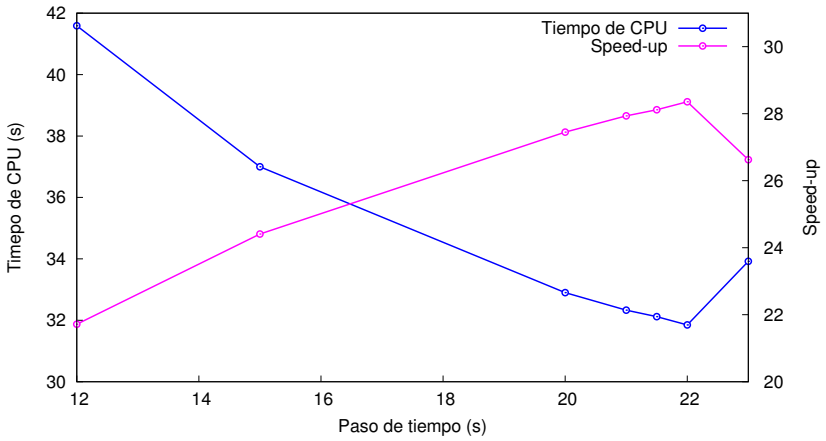

Figure 4.69: Computational time and speed-up value for several choices of time step.

4.4.6 Rainfall/runoff on a real catchment

The Arnás catchment is located in the northern Spanish part of the Pyrenees. The altitude ranges from $900m$ to $1340m$ above sea level (see Figure 4.70, left) and the catchment area is approximately $2.84Km^2$. The domain is discretized by means of the local refinement strategies suggested by [17], resulting in a 6517 cells unstructured triangular mesh (Figure 4.70, right). The Manning roughness coefficient is set to a global value of $0.03sm^{-1/3}$ for the entire domain. The catchment is assumed to be impervious.

Six different simulations have been performed in order to determine the importance of bed slope magnitude and rainfall intensity in the convergence of the implicit scheme and hence in the performance. For the first simulation (AR1), the original altitude map has been considered (Figure 4.70, left). The bed elevation of this map is multiplied by 1/10 and 1/50 factors in the AR2 and AR3 simulations, respectively, in order to reduce the local slopes. A constant rainfall of $25.2mm/h$ during $1000s$ is assumed all over the domain. These three cases are repeated by scaling the rainfall intensity by a 10 factor, that is, $252mm/h$ maintaining the rainfall duration (Cases AR4, AR5 and AR6). Table 4.11 shows a summary of the cases presented. In order to illustrate the spatial distribution of rainfall/runoff process in this catchment, the distribution of water depths for the case AR1 at six different times is shown in Figure 4.71. The outlet numerical hydrographs are presented in Figure 4.72, obtained with the optimal time step for the implicit method and the maximum which allows stability of the solution for the explicit method. The performance study is presented in Figure 4.73 by means of the CPU costs together with the speed-up factors.

In the light of the results of Figure 4.72, very similar hydrographs are observed with both implicit and explicit numerical schemes. Hence, the suitability of the implicit scheme in each case is determined by the speed-up factor. The first case (AR1) presents by far the poorest performance, becoming inefficient in comparison with the explicit method. The reason for this behavior is the high number of iterations required by the implicit scheme for linearizing the ZI equation under conditions of high z gradients and low h values. When increasing the rainfall intensity by 10 (Case AR4), the performance of the implicit scheme increases, even though the speed-up factor does not reach 1.7 value.

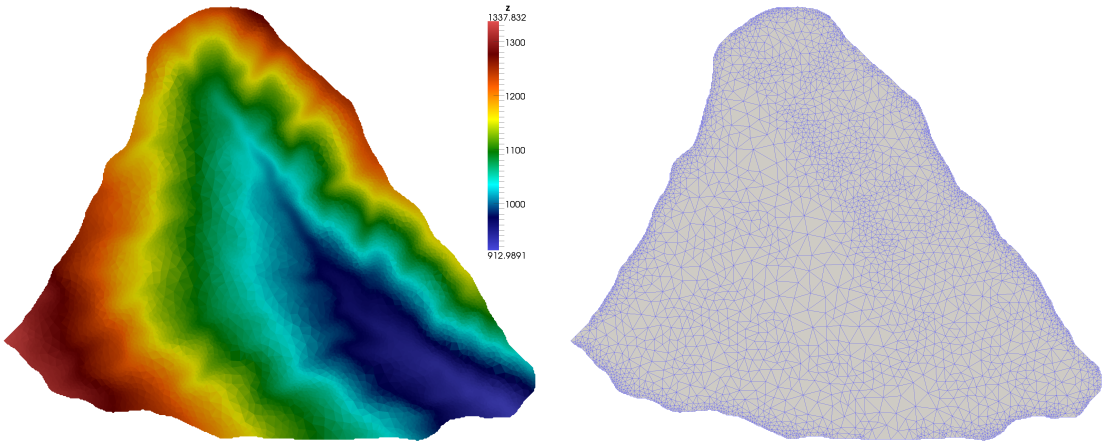

Figure 4.70: Arnás catchment hypsometry map (left) and computational mesh (right).

When scaling the hypsometry map by a 1/10 factor (Case AR2), the z gradients become smoother, so the number of the implicit solver iterations decreases and hence the efficiency of the implicit scheme increases, resulting in a speed-up value of 2.8. If the original terrain is scaled by a 1/50 factor (Case AR3) the speed-up raises again, reaching a value of 3.97. When the rainfall rate is augmented by 10 in these two scaled z-maps (Cases AR5 and AR6), the speed-up values increase again (5.33 and 6.79, respectively), as in Case AR4. Hence, the global conclusion obtained from these cases is that the weakness of the implicit ZI model resides in the combination of high z gradients with low water depths h. When the slope values of the catchments are not so extreme as in the Case AR1, the implicit ZI model becomes efficient in comparison with its explicit version. Additionally, it has been shown that the speed-up factor increases when lowering the z gradients of the catchments and when increasing the rainfall rate, that is, the surface water depth.

Case	z scale factor	R scale factor
AR1	1	1
AR2	1/10	1
AR3	1/50	1
AR4	1	10
AR5	1/10	10
AR6	1/50	10

Table 4.11: Arnás catchment cases summary.

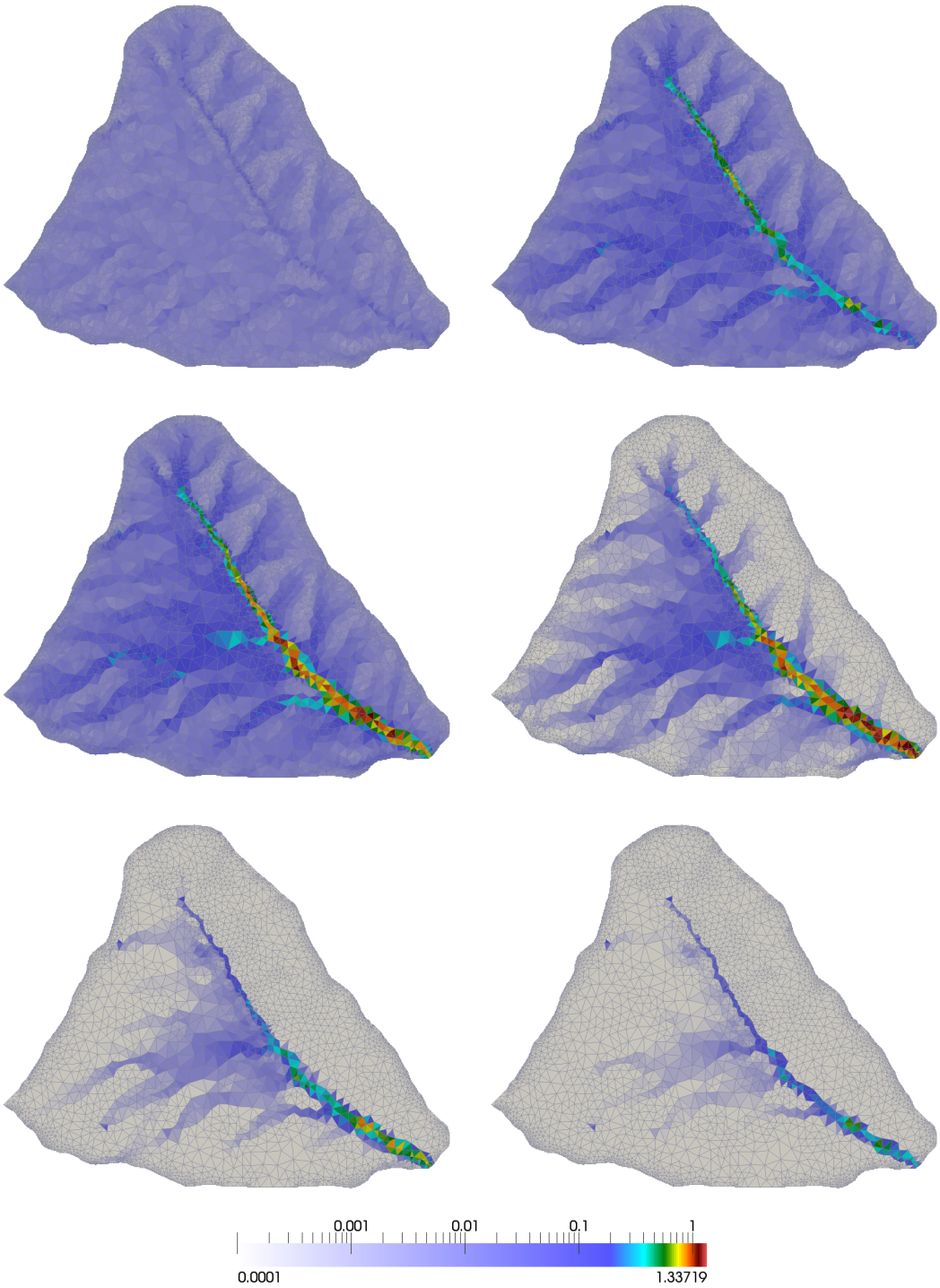

Figure 4.71: Water depth in the Arnás catchment at $t = 100s$, $600s$, $1000s$, $1500s$, $2500s$ and $3600s$.

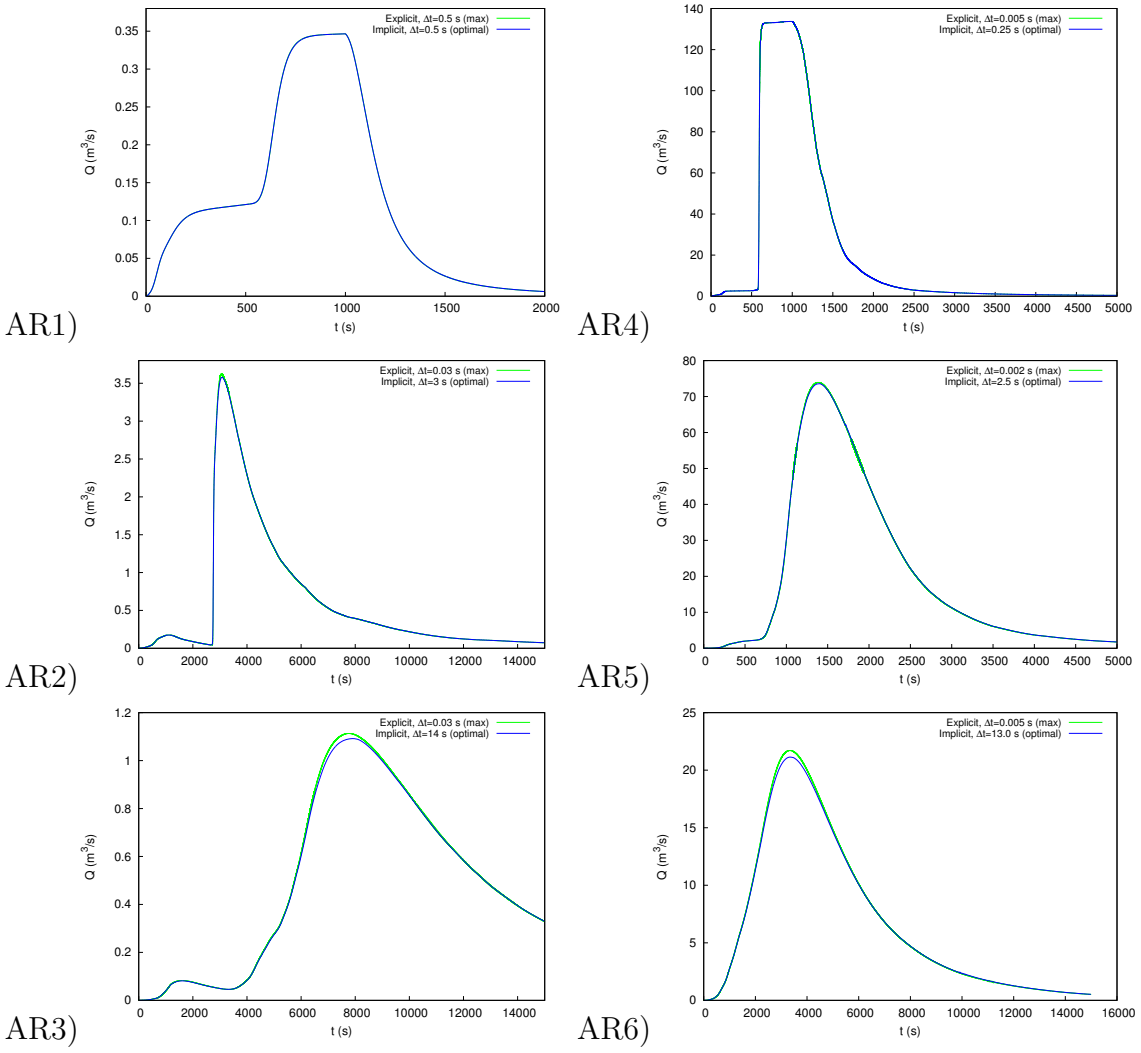

Figure 4.72: Arnás catchment outlet hydrographs with explicit and implicit schemes.

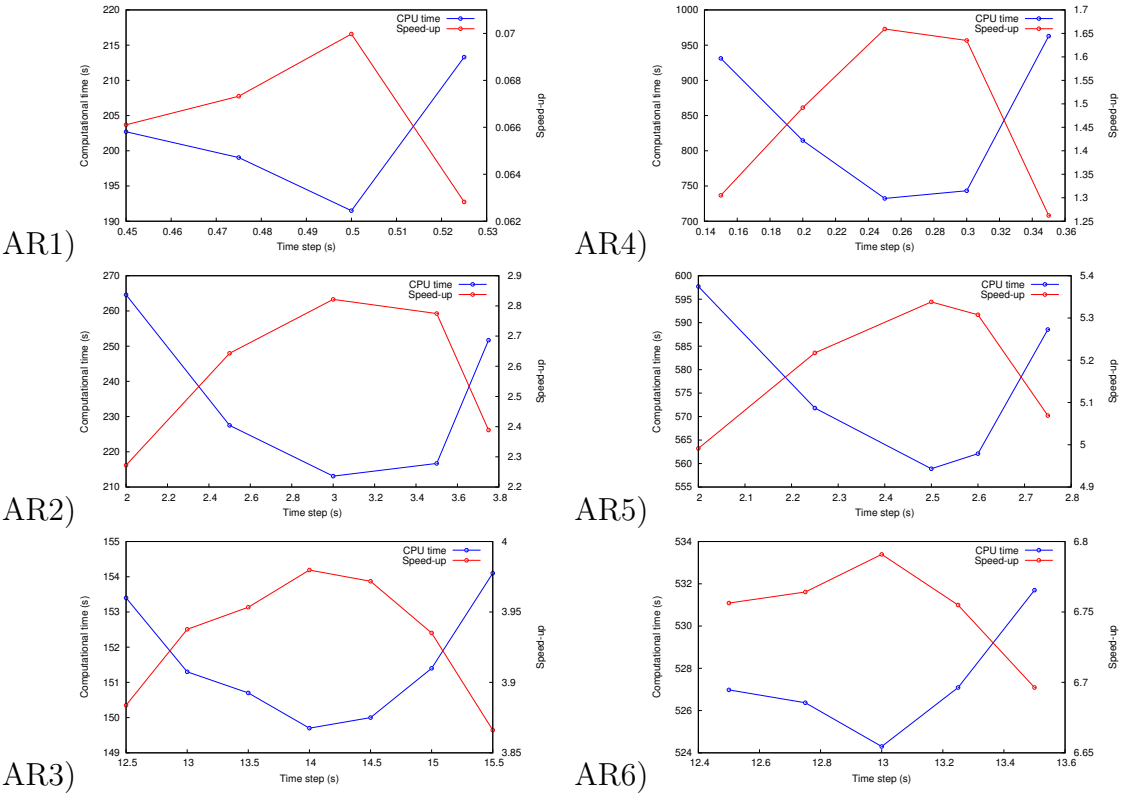

Figure 4.73: Arnás catchment CPU times and speed-ups.

4.4.7 Conclusions

In the light of the results presented, several conclusions have been reached:

- Unstructured triangular meshes provide an efficient way to discretize irregular domains with a moderate number of elements.
- Implicit Zero-Inertia model becomes a very efficient way to simulate steady flows and smooth transients, which include tidal flows over beach-like terrains and rainfall/runoff situations over urban areas. Large speed-up factors (> 150) have been reached, which shows the suitability of the implicit methodology for solving these kind of problems. When the implicit ZI model is applied to a real river catchment, its efficiency is affected by the high z gradients combined with low water depths h.
- In general terms, larger time steps do not necessarily mean lower simulation times when solving a non-linear problem by means of implicit techniques. The optimum time step should be found in order to achieve the fastest simulation.

4.5 2D Groundwater flow

4.5.1 1D test case with analytical solution

Let us consider a porous media with uniform values of saturated hydraulic conductivity ($K = 1.25cm/s$) and porosity ($\eta = 0.4$). A first configuration is set (Setup 1) where a water level of $h_s = 22.2cm$ and $0cm$ are imposed as inlet and outlet boundary conditions, respectively, of a $1m$ lenght domain (see Figure 4.74, upper). A second configuration (Setup 2) is considered by adding a slope to the impervious region frontier. In this case, the imposed inlet water level is $h_s = 35cm$ (Figure 4.74, lower).

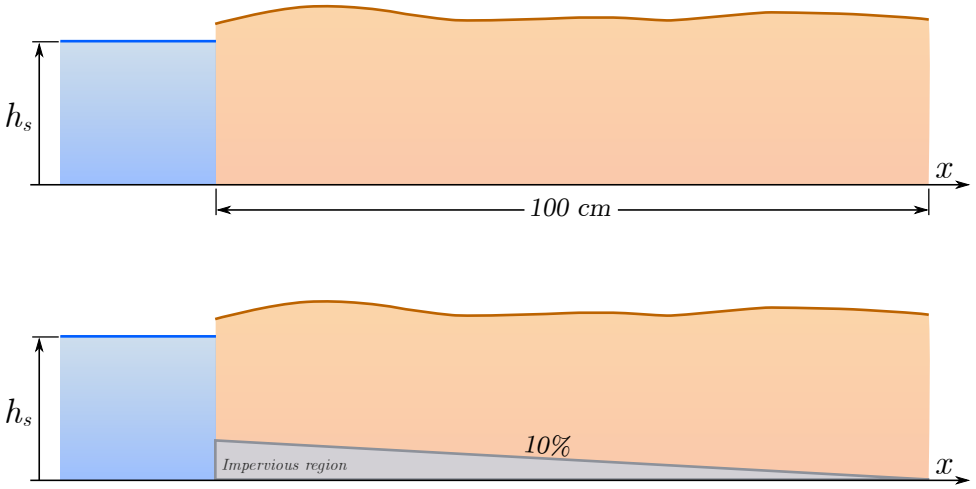

Figure 4.74: Sketch of 1D test case for groundwater flow. Setups 1 (upper) and 2 (lower).

In both cases, the steady analytical solution can be easily found by solving the Darcy's equation with the appropiate boundary values. Equations (4.19) and (4.20) show the exact solutions for $h_s(x)$ in cm for the case setups 1 and 2, respectively:

$$h_s(x) = \sqrt{492.84 - 4.93x} \tag{4.19}$$

$$x + \frac{h_s}{m} + \frac{A}{m^2} ln\left(mh_s - A\right) = B \tag{4.20}$$

where $m = -0.1$ represents the impervious region slope and $A = -4.89\,cm$, $B =$

$-676.78\,cm$ and two constant coefficients.

Figures 4.75 and 4.76 show the convergence of the transient numerical solution to the steady state. In both cases, a perfect fit to the exact solution is achieved. Both explicit and implicit numerical schemes provides exactly the same steady numerical solution.

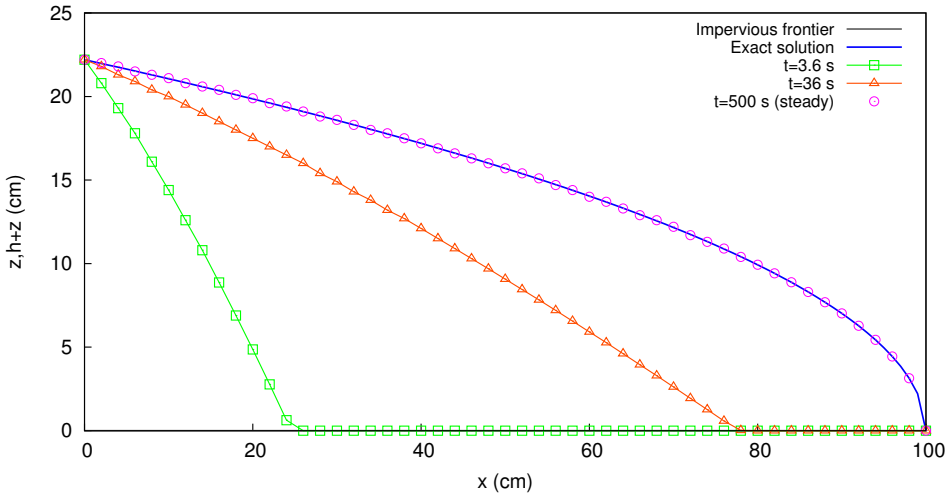

Figure 4.75: Comparison with analytical solution for Setup 1.

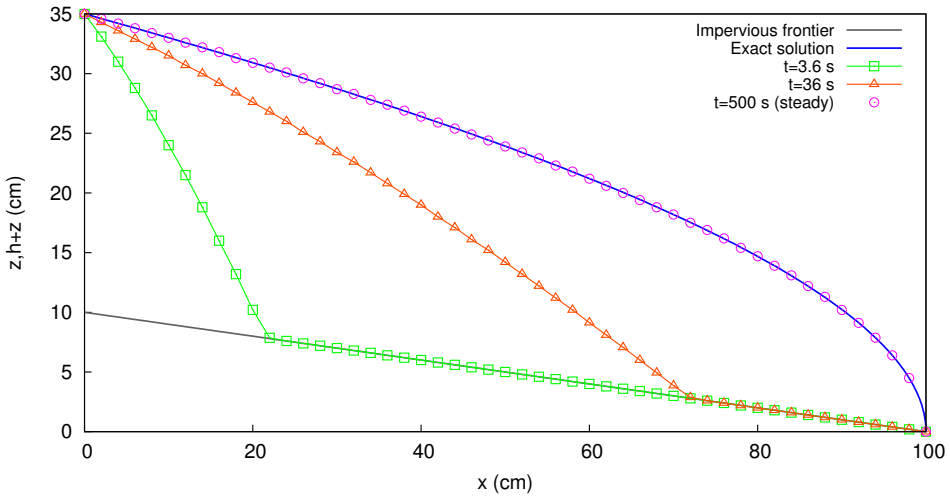

Figure 4.76: Comparison with analytical solution for Setup 2.

4.5.2 2D aquifer modeling with pumping

This test case is proposed in [38] and it consists in a $260m \times 260m$ squared soil ($K = 3.82 \cdot 10^{-5} cm/s$, $\eta = 0.4$) with four symetrical located extractors with the

purpose of lowering the phreatic level of the central $60m \times 60m$ area (see Figure 4.77). Figure 4.78 shows the initial state and the results for some different times. A water level of $h_s = 30m$ is imposed in all the domain boundaries while a constant phreatic level of $h_s = 30m$ is assumed as initial condition. The rate at which the soil water is extracted at each point is $q_{ext} = 1.62 \cdot 10^{-6} m/s$. Figure 4.78 show the full numerical results at several times until the steady state. Note that a rectangular mesh has been chosen due to the symmetric geometry of the problem. Figure 4.79 shows the cross-sectional curves at the position $x = 100m$, where two of the extractors are located.

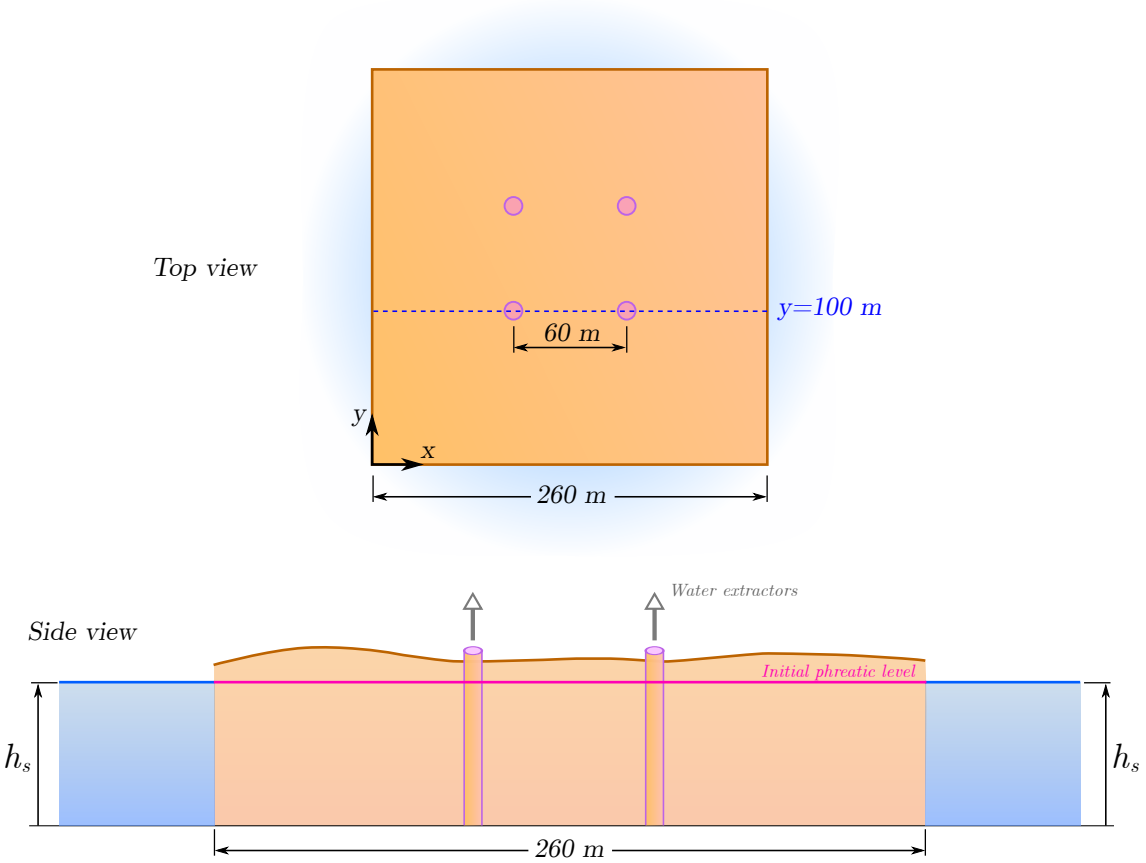

Figure 4.77: Top and side views of the 2D aquifer case setup.

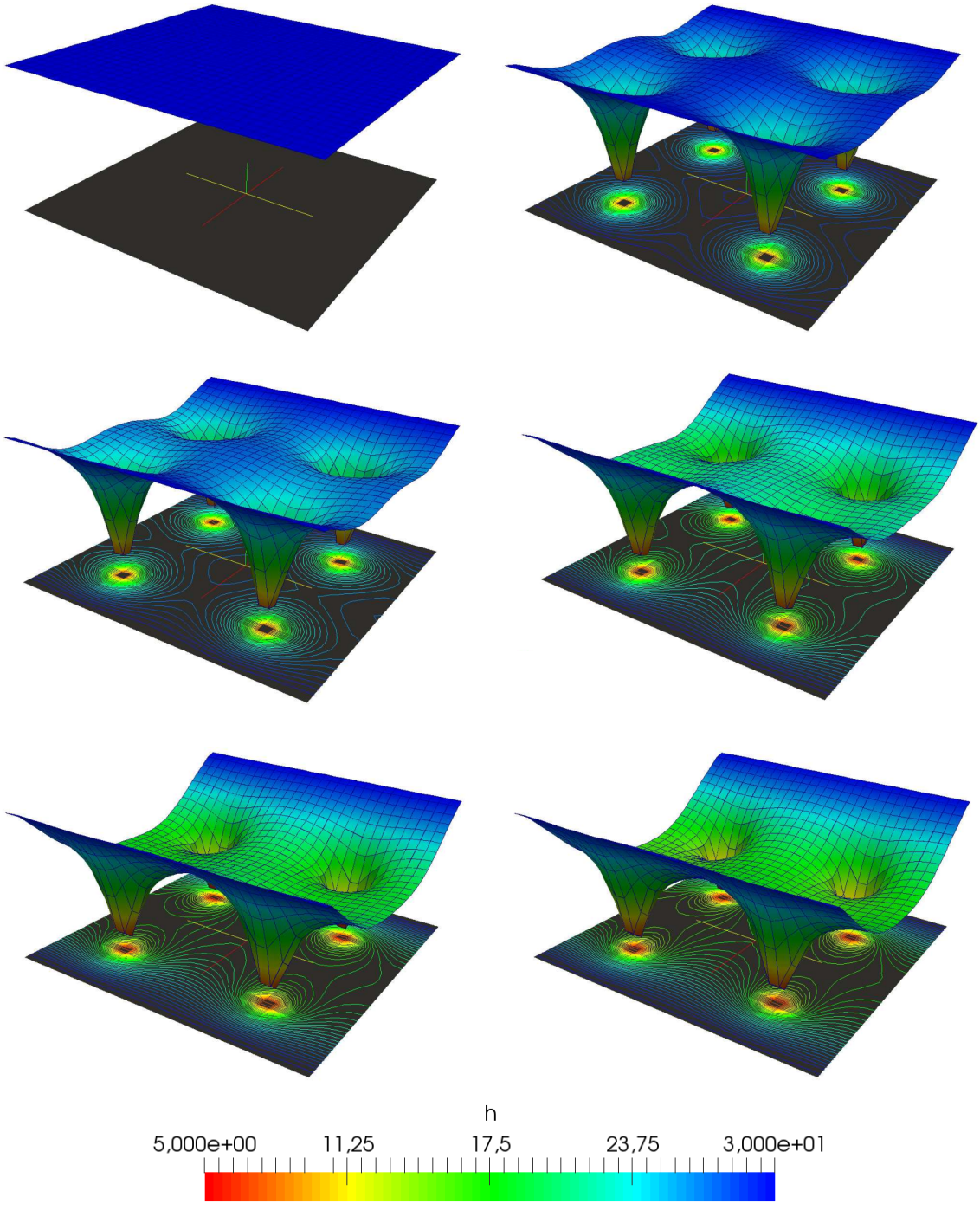

Figure 4.78: Numerical results for the 2D aquifer at $t = 20\,days$, $40\,days$, $240\,days$, $720\,days$, $1200\,days$ and $4800\,days$.

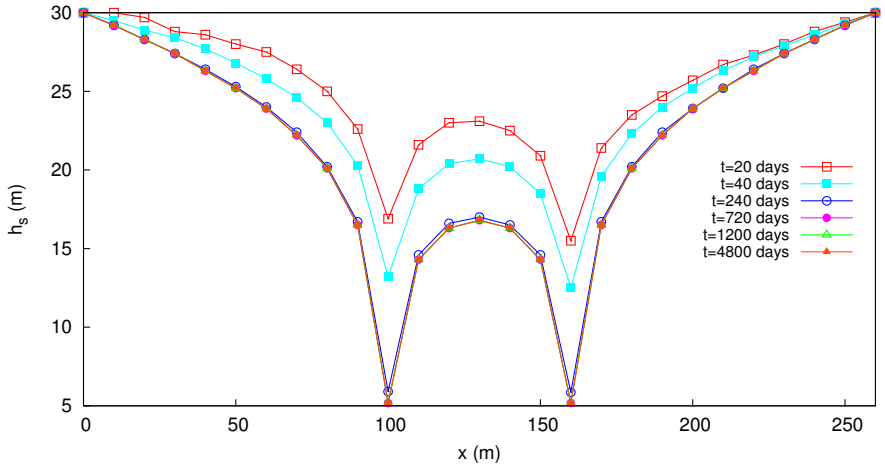

Figure 4.79: Cross-sectional view of the instant phreatic level at several times for $x = 100\,m$.

4.5.3 Conclusions

In the light of the results presented in this section, several conclusions have been reached. On the one hand, the groundwater flow model is able to reproduce the exact solutions in steady conditions, even when the impervious region presents a slope frontier. On the other hand, the aquifer modeling test case points out the ability of the model to update the phreatic level position via local sources/sinks. The results are coherent with the ones presented in [38].

4.6 Matrix solver performance assessment

In numerical linear algebra, the matrix solvers for linear systems $\mathbf{Ax} = \mathbf{b}$, where $\mathbf{A}$ is a nonsingular square matrix with real values, $\mathbf{x}$ is the vector of unknowns and $\mathbf{b}$ is the free right-hand-side vector, can be divided in two main groups: direct and iterative solvers.

Direct methods allow to compute the solution $\mathbf{x}$ within a finite number of operations. Gauss elimination, LU factorization or Thomas algorithm would fall into this group of solvers. In contrast, an iterative method uses an initial guess to generate a sequence of improving approximate solutions, in which the n-th approximation is obtained from the previous ones. This kind of methods should consider a termination

criterion in terms of a given tolerance. An iterative method is called convergent if the corresponding sequence converges for given initial approximations. Some examples of iterative methods are the Jacobi and Gauss-Seidel methods or the solvers within the conjugate gradient family, as the BiConjugate Gradient Stabilized (BiCGStab), considered in this work.

In this section, a performance assessment for two matrix solver (BiCGStab and Thomas algorithm) is presented. The main goal is to find out the applicability of both methods in terms of quality of the implicit numerical solution and efficiency. Several 1D and 2D examples are presented for ZI and SW models.

4.6.1 Thomas algorithm

Classical Thomas algorithm

Thomas algorithm (a.k.a. tridiagonal matrix algorithm or TDMA) is a simplified form of Gaussian elimination to solve tridiagonal system of equations

$$b_i x_{i-1} + d_i x_i + a_i x_{i+1} = c_i \tag{4.21}$$

in where $b_1 = 0$ and $a_N = 0$ [3].

The matrix form of the equation system is

$$\begin{pmatrix} d_1 & a_1 & & & 0 \\ b_2 & d_2 & a_2 & & \\ & b_3 & d_3 & \ddots & \\ & & \ddots & \ddots & a_{N-1} \\ 0 & & & b_N & d_N \end{pmatrix} \begin{pmatrix} x_1 \\ x_2 \\ x_3 \\ \vdots \\ x_N \end{pmatrix} = \begin{pmatrix} c_1 \\ c_2 \\ c_3 \\ \vdots \\ c_N \end{pmatrix} \tag{4.22}$$

The Gaussian elimination for these kind of systems follows a clear patern. By replacing the coefficients of the main diagonal term d_i by:

$$d'_i = d_i - \frac{b_i a_{i-1}}{d'_{i-1}} \qquad (i = 2, 3, \cdots, N) \tag{4.23}$$

and the term on the right hand side of the equation by:

$$c'_i = c_i - \frac{c'_{i-1} b_i}{d'_{i-1}} \qquad (i = 2, 3, \cdots, N) \tag{4.24}$$

This will result into a bidiagonal matrix:

$$\begin{pmatrix} d'_1 & a_1 & & & 0 \\ & d'_2 & a_2 & & \\ & & d'_3 & \ddots & \\ & & & \ddots & a_{N-1} \\ 0 & & & & d'_N \end{pmatrix} \begin{pmatrix} x_1 \\ x_2 \\ x_3 \\ \vdots \\ x_N \end{pmatrix} = \begin{pmatrix} c'_1 \\ c'_2 \\ c'_3 \\ \vdots \\ c'_N \end{pmatrix} \tag{4.25}$$

where $d'_1 = d_1$ and $c'_1 = c_1$.

The last row of the matrix-system (4.25) contains only one unknown x_N. Hence, it can be solved directly:

$$x_N = \frac{c'_N}{d'_N} \tag{4.26}$$

The solution of the remaining unknowns is calculated by sweeping upwards in the system matrix. This result into the next recursion formula:

$$x_i = \frac{c'_i - a_i x_{i+1}}{d'_i} \qquad (i = N-1, N-2, \cdots, 1) \tag{4.27}$$

where x_{i+1} has already been calculated from the previous step. This method requires an ordered sequence of the nodes.

An additional consideration is worthy of mention. When the Thomas algorithm is applied to a numerical problem, boundary conditions are imposed before or after the algorithm, hence they do not participate directly in the calculus. Nevertheless, some of the coefficients can be a function of them. In 1D problems, the most common procedure is to define a grid of N cells ($1 \leq i \leq N$) and set the cells 1 and N as the boundary ones, so the boundary conditions are imposed in these cells. Hence, the system solver acts along the inner cells ($2 \leq i \leq N-1$), so the indices of all the

Algorithm 1 Thomas algorithm for tridiagonal matrices

$d'_1 = d_1$ ▷ Downwards sweep
$c'_1 = c_1$
for $2 \geq i \geq N$ **do**
  $d'_i = d_i - \frac{b_i a_{i-1}}{d'_{i-1}}$
  $c'_i = c_i - \frac{c'_{i-1} b_i}{d'_{i-1}}$
end for
$x_N = \frac{c'_N}{d'_N}$ ▷ Upwards sweep
for $N - 1 \leq i \leq 1$ **do**
  $x_i = \frac{c'_i - a_i x_{i+1}}{d'_i}$
end for

Thomas algorithm formulation need to be adapted. On the contrary, when using iterative solvers, boundary conditions are imposed within the matrix itself and then the matrix is inverted. A typical system-matrix for 1D problems is shown in (4.28) to (4.30):

$$b_i x_{i-1} + d_i x_i + a_i x_{i+1} = c_i \tag{4.28}$$

$$\begin{pmatrix} d_2 & a_2 & & & 0 \\ b_3 & d_3 & a_3 & & \\ & \ddots & \ddots & \ddots & \\ & & \ddots & \ddots & a_{N-2} \\ 0 & & & b_{N-1} & d_{N-1} \end{pmatrix} \begin{pmatrix} x_2 \\ x_3 \\ \vdots \\ \vdots \\ x_{N-1} \end{pmatrix} = \begin{pmatrix} c_2 \\ c_3 \\ \vdots \\ \vdots \\ c_{N-1} \end{pmatrix} \tag{4.29}$$

$$\begin{pmatrix} & & & & & & \\ b_2 & d_2 & a_2 & & & & 0 \\ & b_3 & d_3 & a_3 & & & \\ & & \ddots & \ddots & \ddots & & \\ & & & \ddots & \ddots & a_{N-2} & \\ 0 & & & & b_{N-1} & d_{N-1} & a_{N-1} \\ & & & & & & \end{pmatrix} \begin{pmatrix} x_1 \\ x_2 \\ x_3 \\ \vdots \\ \vdots \\ x_{N-1} \\ x_N \end{pmatrix} = \begin{pmatrix} c_2 \\ c_3 \\ \vdots \\ \vdots \\ c_{N-1} \end{pmatrix} \tag{4.30}$$

$$\begin{pmatrix} d_2 & a_2 & & & 0 \\ b_3 & d_3 & a_3 & & \\ & \ddots & \ddots & \ddots & \\ & & \ddots & \ddots & a_{N-1} \\ 0 & & & b_{N-1} & d_{N-1} \end{pmatrix} \begin{pmatrix} x_2 \\ x_3 \\ \vdots \\ \vdots \\ x_{N-1} \end{pmatrix} = \begin{pmatrix} c_2 - b_2 x_1 \\ c_3 \\ \vdots \\ \vdots \\ c_{N-1} - a_{N-1} x_N \end{pmatrix} \tag{4.31}$$

Thomas algorithm for tridiagonal-block matrices

An extension of the Thomas algorithm for block matrices is presented now:

$$\mathbf{bb}_i \mathbf{x}_{i-1} + \mathbf{dd}_i \mathbf{x}_i + \mathbf{aa}_i \mathbf{x}_{i+1} = \mathbf{k}_i \tag{4.32}$$

$$\begin{pmatrix} \mathbf{dd}_1 & \mathbf{aa}_1 & & & & & \\ \mathbf{bb}_2 & \mathbf{dd}_2 & \mathbf{aa}_2 & & & & \\ & \mathbf{bb}_3 & \mathbf{dd}_3 & \mathbf{aa}_3 & & & \\ & & \ddots & \ddots & \ddots & & \\ & & & \ddots & \ddots & \ddots & \\ & & & & \mathbf{bb}_{N-2} & \mathbf{dd}_{N-2} & \mathbf{aa}_{N-2} \\ & & & & & \mathbf{bb}_{N-1} & \mathbf{dd}_{N-1} & \mathbf{aa}_{N-1} \\ & & & & & & \mathbf{bb}_N & \mathbf{dd}_N \end{pmatrix} \begin{pmatrix} \mathbf{x}_1 \\ \mathbf{x}_2 \\ \mathbf{x}_3 \\ \vdots \\ \vdots \\ \mathbf{x}_{N-2} \\ \mathbf{x}_{N-1} \\ \mathbf{x}_N \end{pmatrix} = \begin{pmatrix} \mathbf{c}_1 \\ \mathbf{c}_2 \\ \mathbf{c}_3 \\ \vdots \\ \vdots \\ \mathbf{c}_{N-2} \\ \mathbf{c}_{N-1} \\ \mathbf{c}_N \end{pmatrix} \tag{4.33}$$

Performing an adaptation of the Gaussian elimination presented previouisly, a similar algorithm is obtained. Note that all the divisions have been replaced by inverse matrices:

Algorithm 2 Thomas algorithm for tridiagonal-block matrices

$\mathbf{dd}'_1 = \mathbf{dd}_1$ ▷ Downwards sweep
$\mathbf{c}'_1 = \mathbf{c}_1$
for $2 \geq i \geq N$ **do**
  $\mathbf{dd}'_i = \mathbf{dd}_i - \mathbf{bb}_i \left(\mathbf{dd}'_{i-1}\right)^{-1} \mathbf{aa}_{i-1}$
  $\mathbf{c}'_i = \mathbf{c}_i - \mathbf{bb}_i \left(\mathbf{dd}'_{i-1}\right)^{-1} \mathbf{c}'_{i-1}$
end for
$\mathbf{x}_N = \left(\mathbf{dd}'_N\right)^{-1} \mathbf{c}'_N$ ▷ Upwards sweep
for $N - 1 \leq i \leq 1$ **do**
  $\mathbf{x}_i = \left(\mathbf{dd}'_i\right)^{-1} \mathbf{c}'_i - \mathbf{aa}_i \left(\mathbf{dd}'_i\right)^{-1} \mathbf{x}_{i+1}$
end for

4.6.2 BiConjugate Gradient Stabilized method

The BiConjugate Gradient Stabilized (BiCGStab) [95, 30] is an iterative method for the numerical solution of non-symmetric linear systems. It represents an evolution of the BiConjugate Gradient Method, leading to a faster and smoother convergence. This method benefits of the use of sparse storage for the system, since the most of the matrix elements have zero value and it is adequate to avoid their storage. It is also common to combine this solver with an efficient precontioning method. A preconditioner **P** of a matrix **A** is another matrix such as **PA** has a lower condition number than **A**. The rate of convergence for most iterative linear solvers increases as the condition number of a matrix decreases. In this work, a strategy that combines the BiCGStab solver using sparse storage with an ILU preconditioner is followed:

- Solver: BiCGStab (BiConjugate Gradient Stabilized).
- Preconditioner: ILU (Incomplete LU factorization).
- Storage: CSR (Compressed Sparse Row).

	1	2	3	4	5	6
1	5	0	3	0	0	0
2	0	4	0	0	0	2
3	0	7	6	9	0	0
4	0	0	0	0	0	1
5	0	0	0	0	3	0
6	0	0	0	6	0	3

→

k	1	2	3	4	5	6	7	8	9	10	11	12	13
ija(k)	8	9	10	12	13	13	14	3	6	2	4	6	4
a(k)	5	4	6	0	3	3		3	2	7	9	1	6

Figure 4.80: Example of a transformation from standard matrix storage to CSR.

The chosen stop criterion consists of a cell-by-cell comparison of the variable of interest between two consecutive solver iterations, as follows:

$$Err = \max\{\left|h_i^{m+1} - h_i^m\right|\} \tag{4.34}$$

The solver performs iterations until the value of the error Err is lower than a given tolerance TOL. The lower the value of the tolerance, the more accurate the solution is.

4.6.3 1D Zero-Inertia equation

Case setup and explicit reference solution

The problem setup consists of a single plane with a 0.05 slope and a uniform Manning roughness coefficient of $0.03sm^{-1/3}$. All the domain is initially dry ($h = 0$) and $h = 2m$ is set as upstream boundary condition while $h = 0.001m$ is imposed downstream. The high slope and water depth values are designed to force the model (and solvers) to work under challenging conditions. This situation should emphasize the differences between both solvers. In order to compare both the Thomas algorithm and the BiCGStab solvers against a reference solution, an explicit numerical solution is computed for three diferent meshes (50, 200 and 500 cells). Figure 4.81 shows the graphical representation of the solution for several simulation times.

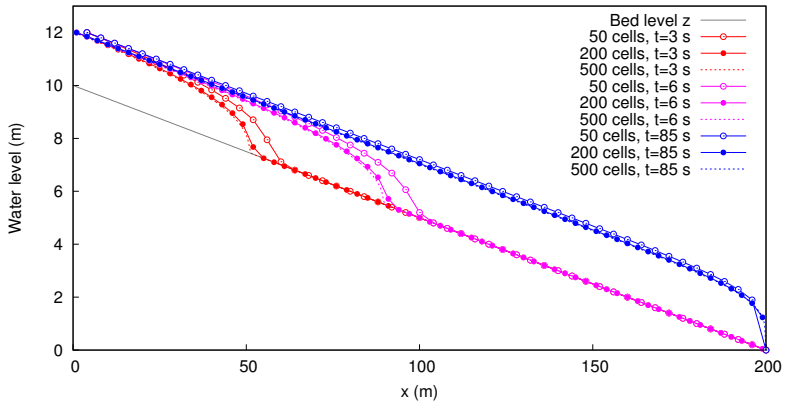

Figure 4.81: Comparison of explicit numerical solutions for 1D ZI model at several times using three different grid resolutions.

BiCGStab tolerance analysis

BiCGStab, as any other iterative method, requires of a termination criterion in terms of a tolerance. The lower the value of the tolerance, the more accurate the solution is. Hence, it is essential to make an estimation of the necessary value of the tolerance in order to perform a fair efficiency comparison among linear matrix solvers. Figures 4.82 and 4.83 show the numerical solutions on a 50 cell and 500 cell mesh, respectively, using tolerances from 10^{-1} (TOL1) to 10^{-9} (TOL9).

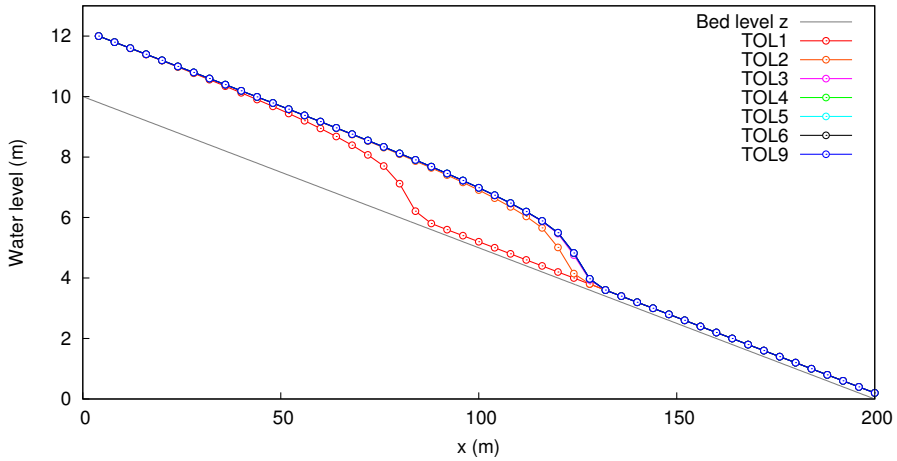

Figure 4.82: Comparison of implicit numerical solutions for 1D ZI model at $t = 9s$ using several BiCGStab solver tolerances as stop criterion in a 50 cell mesh.

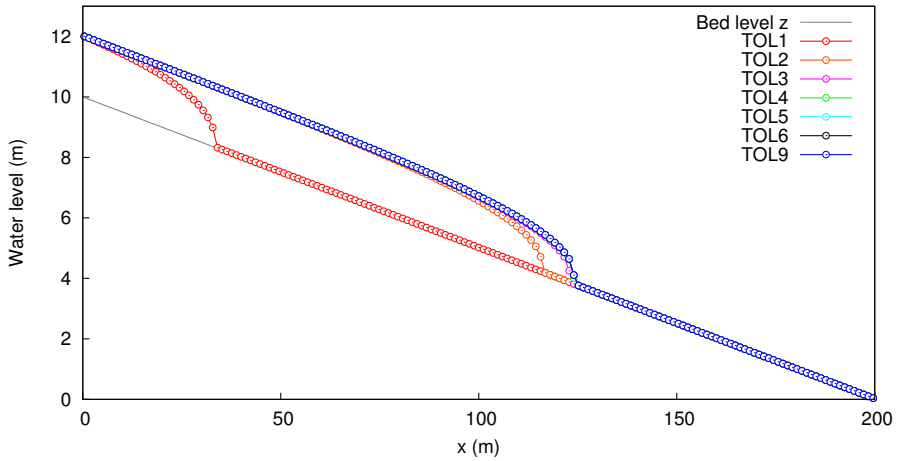

Figure 4.83: Comparison of implicit numerical solutions for 1D ZI model at $t = 9s$ using several BiCGStab solver tolerances as stop criterion in a 500 cell mesh.

Figures 4.84 and 4.85 show the relative error value for 50 and 500 cell meshes, respectively, respect to the explicit reference solution. When the tolerance value is set to $TOL < 10^{-4}$ the maximum relative error values are lower than 2% in both meshes.

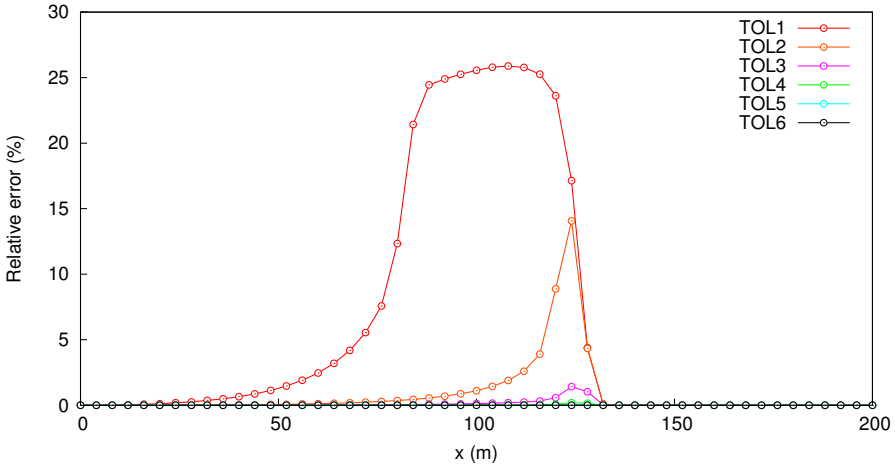

Figure 4.84: Error values for the 50 cell mesh.

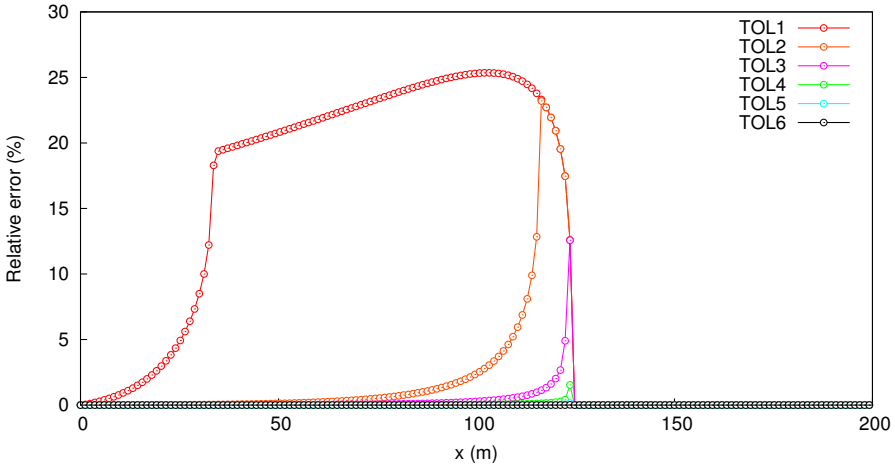

Figure 4.85: Error values for the 500 cell mesh.

Iterative Thomas algorithm tolerance analysis

As the 1D Zero-Inertia equation has a non-linear nature, the Thomas algorithm solver requires to be implemented within a fixed-point iterations loop in order to linearize the equation and achieve a more suitable numerical solution. Hence, it is necessary to perform a tolerance analysis in order to find the optimal value of the tolerance, as in the previous section. Figure 4.86 shows the numerical resuls (left) and the number of iterations performed in the linearization loop (right) on 50 cell (upper), 200 cell (middle) and 500 cell (lower) meshes. In this case, tolerances lower than 10^{-5} produce similar results.

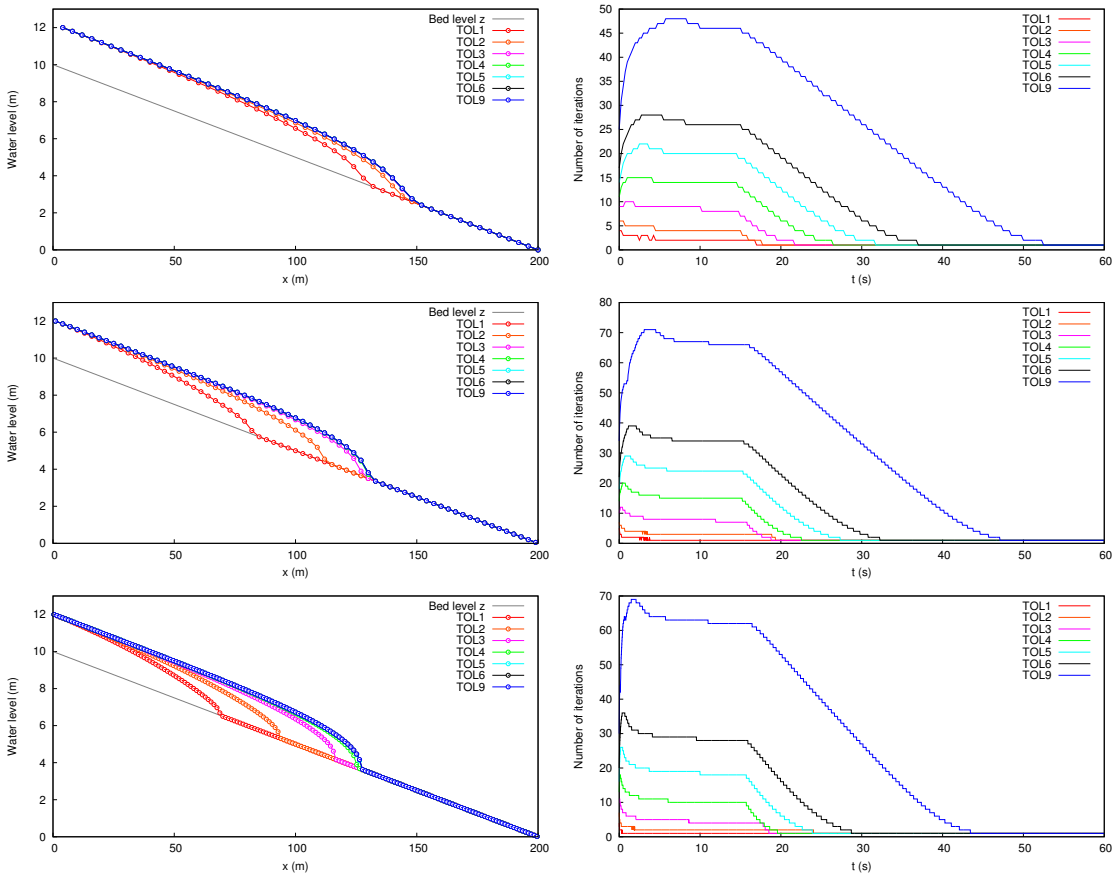

Figure 4.86: Comparison of implicit numerical solutions for 1D ZI model at $t = 9s$ using several Thomas algorithm solver tolerances as stop criterion (left) and number of iterations (right) in 50 cell (upper), 200 cell (middle) and 500 cell (lower) meshes.

Numerical solutions

Once the tolerance values are chosen, the numerical results generated for both models and their comparison are presented in this section in terms of the grid size and the time step selection. As the numerical scheme has an implicit temporal discretization, the numerical instabilities due to large time steps are avoided. Figures 4.87, 4.88 and 4.89 show the numerical results generated by the Thomas algorithm (upper) and BiCGStab (lower) for 50 cell, 200 cell and 500 cell meshes, respectively.

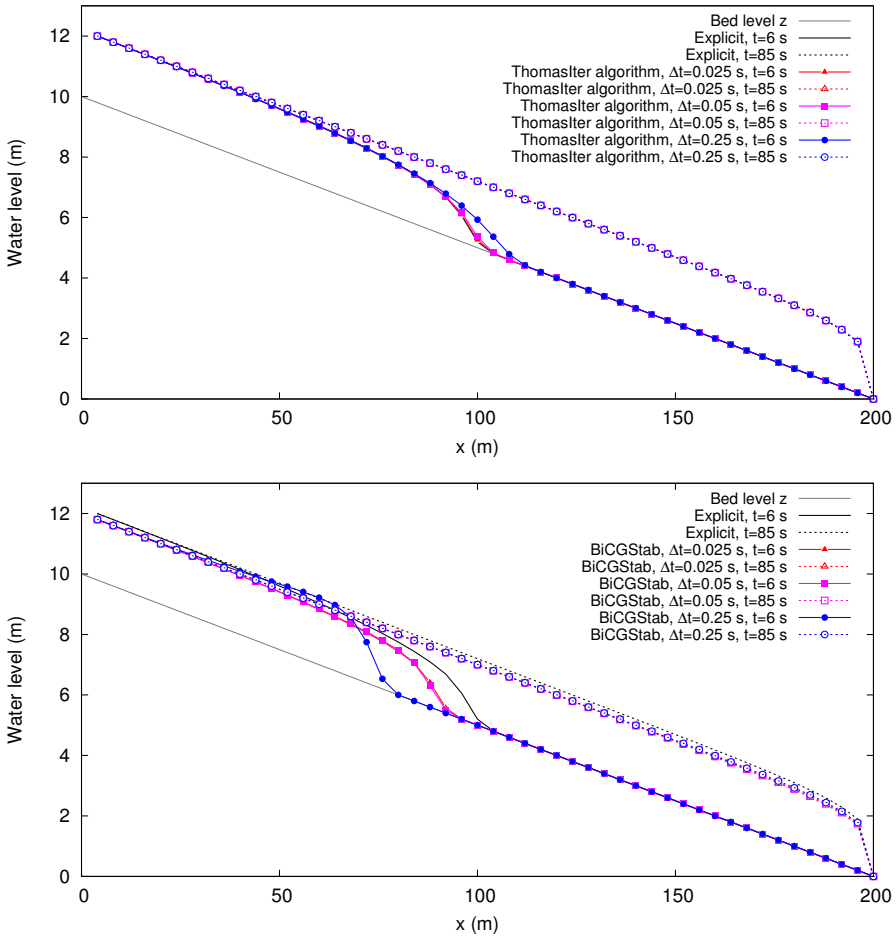

Figure 4.87: Numerical solutions for the Thomas algorithm (upper) and BiCGStab (lower) solvers using a 50 cell mesh.

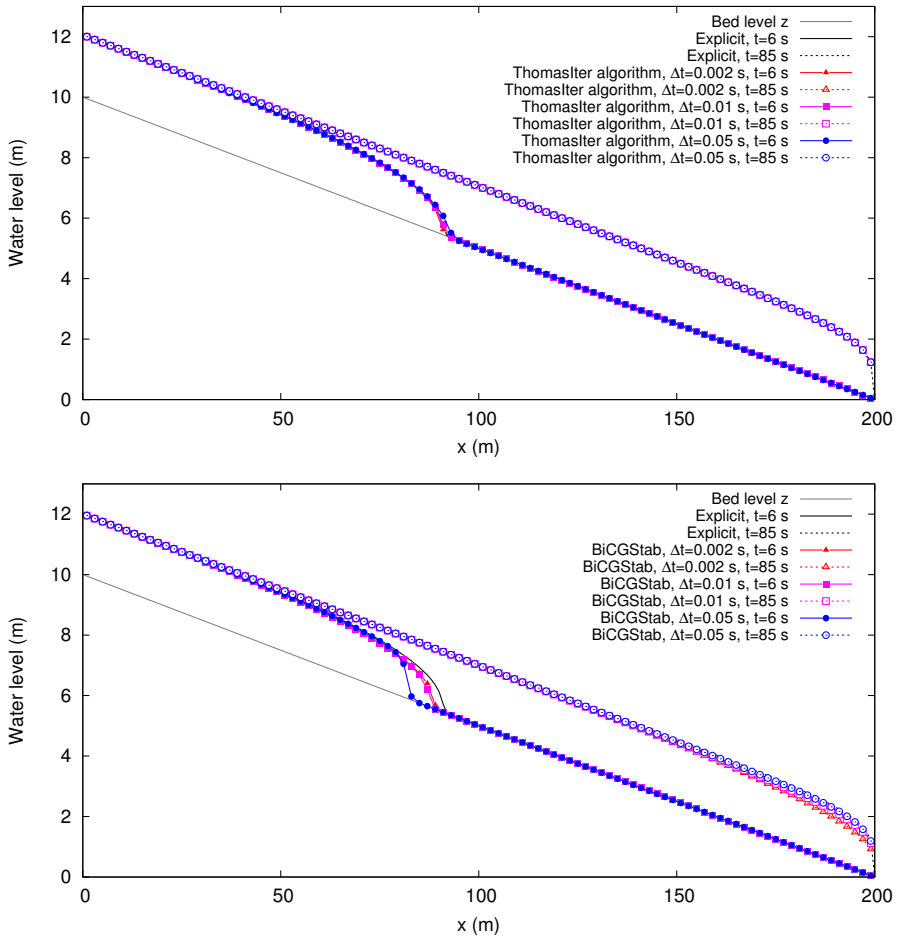

Figure 4.88: Numerical solutions for the Thomas algorithm (upper) and BiCGStab (lower) solvers using a 200 cell mesh.

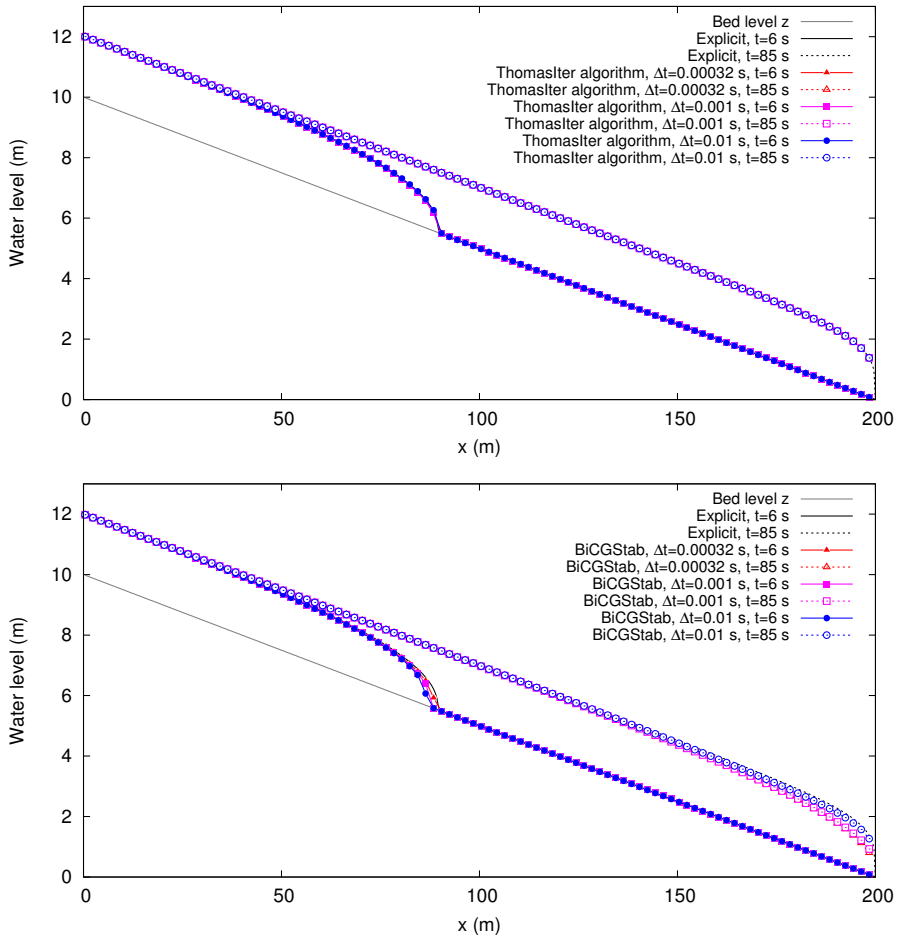

Figure 4.89: Numerical solutions for the Thomas algorithm (upper) and BiCGStab (lower) solvers using a 500 cell mesh.

In order to quantify the quality of the numerical solutions provided by both methods, the maximum and average errors with respect to the reference solution are presented in Figure 4.90. For illustrative purposes, the errors corresponding to the non-iterative version of the Thomas algorithm solver are also depicted in the plots. The numerical values of these errors are also presented in Tables 4.12, 4.13 and 4.14, as well as the computational times (CPU times). The speed-up value shown in Tables 4.13 and 4.14 is computed respect to the BiCGStab CPU time. Figure 4.91 shows the CPU times (upper) and speed-up values for Thomas algorithm (middle) and iterative Thomas algorithm (lower).

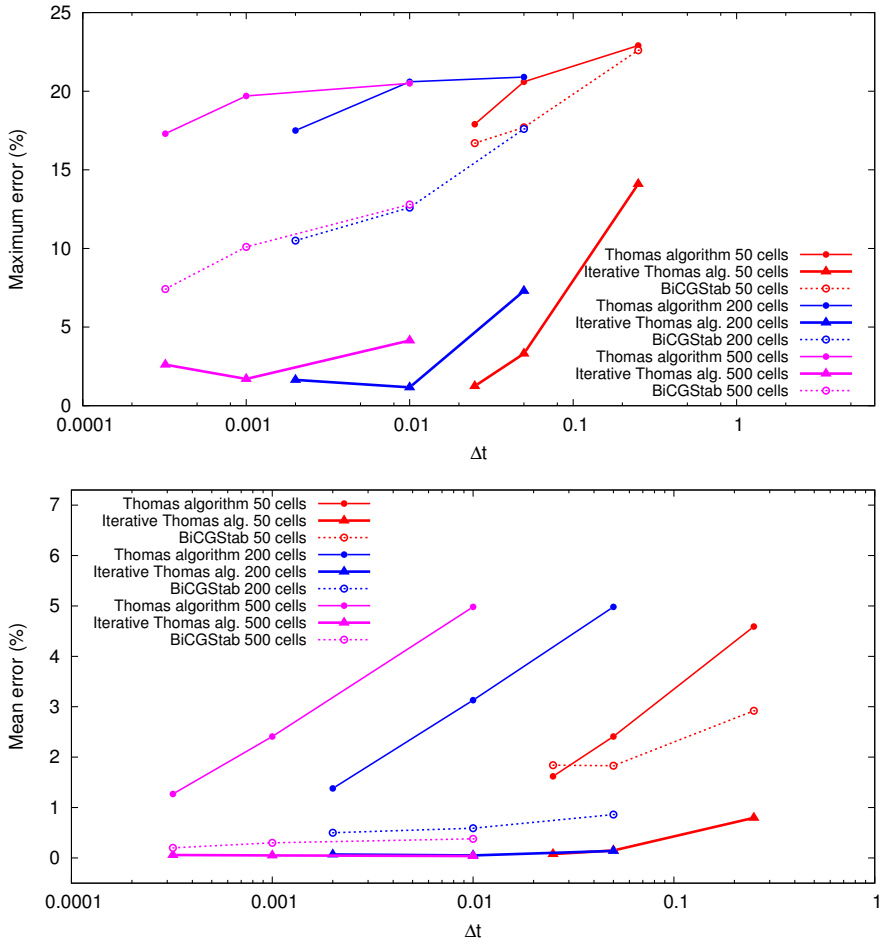

Figure 4.90: Maximum (upper) and mean (lower) error values for both matrix solvers in every mesh at $t = 6s$ (logarithmic scale).

N_{cells}	Δt	CPU time	Maximum error (%)	Average error (%)
50	0.025	0.1	16.7	1.84
	0.05	0.056	17.7	1.83
	0.25	0.02	22.6	2.92
200	0.002	4.3	10.5	0.5
	0.01	0.92	12.6	0.59
	0.05	0.272	17.6	0.86
500	0.00032	67.376	7.42	0.2
	0.001	21.332	10.1	0.3
	0.01	2.724	12.8	0.38

Table 4.12: CPU time, maximum and average errors for BiCGStab algorithm solver.

N_{cells}	Δt	CPU time	Maximum error (%)	Average error (%)	Speed-up
50	0.025	0.064	17.9	1.62	1.56
	0.05	0.036	20.6	2.41	1.56
	0.25	0.015	22.9	4.59	1.33
200	0.002	2.38	17.5	1.38	1.81
	0.01	0.512	20.6	3.13	1.80
	0.05	0.136	20.9	4.98	2.00
500	0.00032	37.5	17.3	1.27	1.80
	0.001	12.9	19.7	2.41	1.65
	0.01	1.3	20.5	4.98	2.10

Table 4.13: CPU time, speed-up and maximum and average errors for Thomas algorithm solver.

N_{cells}	Δt	CPU time	Maximum error (%)	Average error (%)	Speed-up
50	0.025	0.084	1.25	0.077	1.19
	0.05	0.06	3.31	0.148	0.93
	0.25	0.024	14.1	0.797	0.83
200	0.002	3.4	1.64	0.069	1.26
	0.01	1.02	1.17	0.051	0.90
	0.05	0.432	7.3	0.140	0.63
500	0.00032	53.5	2.61	0.059	1.26
	0.001	22.07	1.7	0.051	0.97
	0.01	5.76	4.15	0.038	0.47

Table 4.14: CPU time, speed-up and maximum and average errors for iterative Thomas algorithm solver.

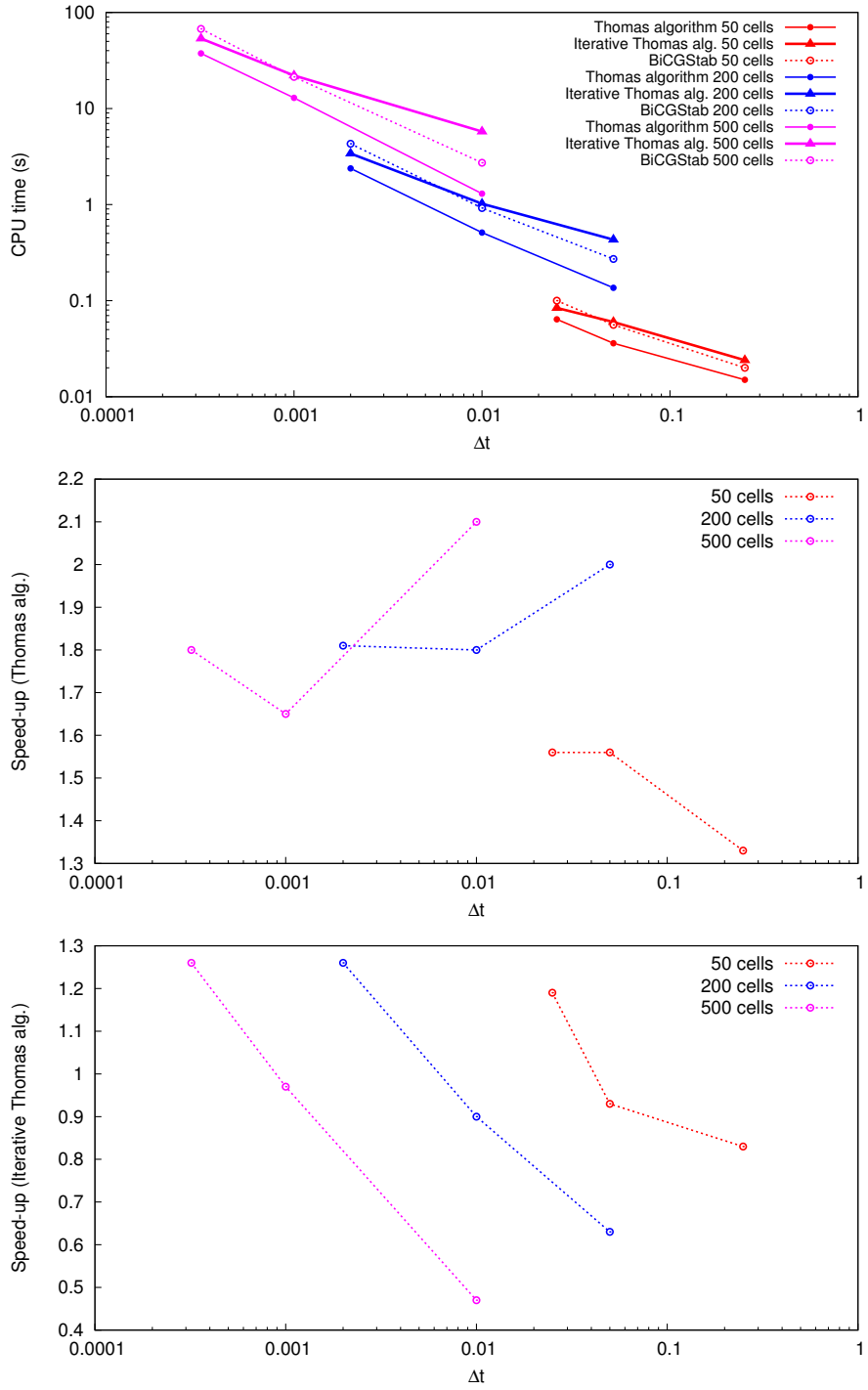

Figure 4.91: CPU times (upper) and speed-up values for Thomas algorithm (middle) and iterative Thomas algorithm (lower).

4.6.4 Conclusions

Several conclusions arise from all the data presented in this section:

- As expected, maximum and average errors decrease as the grid is refined and increase as the time step is increased, for both solvers.
- Maximum and average errors produced by the iterative Thomas algorithm are lower than the ones corresponding to BiCGStab in all the meshes considered in this section.
- Regarding the solver efficiency, the results show that the speed-up values are strongly conditioned by the time step choice and it also depends on the grid size. In the light of the results presented in Table 4.14, BiCGStab becomes more efficient than Thomas algorithm when choosing large time steps and fine meshes.

CHAPTER 5

Multi-model test cases

5.1 Overland flow coupled with infiltration laws: Sensitivity to topography

A set of synthetic test cases is presented now for a better understanding of the infiltration response to rainfall, infiltration parameters and topography variations. Several variations are performed on each case to study the sensitivity to the aforementioned issues.

5.1.1 Case 0: infiltration parameters calibration

First of all, the soil type is the only factor considered. A basic fitting for infiltration parameters is presented. The case consists of infiltration over a horizontal ponded soil. The goal is to get an approximated equivalence between two sets of parameters of Horton (k, f_c, f_0) and Green-Ampt $(K, \Psi, \Delta\theta)$ infiltration models in ideal conditions.

The fitting procedure is summarized as follows:

1. The starting point consists of choosing the Green-Ampt parameters K, $\Delta\theta$ and Ψ so that they are adequate to represent the assumed soil characteristics and initial water content.

2. It is assumed that both the Horton's model final infiltration capacity f_c and the soil hydraulic conductivity K_s reach the same value representing the behavior at large times ($t \to T$).

3. The initial Horton's infiltration rate f_0 is set to the numerical Green-Ampt initial rate $f(t = 0)$.

4. The exponential decay constant k in Horton model is fitted in order to achieve the same final cumulative infiltration volume in both models at a time T.

Following these steps, a set of parameters (Table 5.1) for each infiltration model has been obtained corresponding to a sandy soil type. In order to illustrate the calibration results, Figure 5.1 shows the infiltration rate and cumulative infiltration curves for the infiltration parameters considered.

The relative differences in f and F between infiltration models are also presented in Figure 5.1 in terms of the magnitudes $\Delta f(\%)$ and $\Delta F(\%)$, defined as follows:

$$\Delta f(\%) = 100\frac{f_H - f_{GA}}{f_{GA}}, \qquad \Delta F(\%) = 100\frac{F_H - F_{GA}}{F_{GA}} \tag{5.1}$$

Infiltration model	Parameter 1	Parameter 2	Parameter 3
Horton	$k = 2.43 \cdot 10^{-3} s^{-1}$	$f_c = 3.272 \cdot 10^{-5} m/s$	$f_0 = 1.977 \cdot 10^{-4} m/s$
Green-Ampt	$K = 3.272 \cdot 10^{-5} m/s$	$\Psi = 0.0495 m$	$\Delta\theta = 0.38 m^3/m^3$

Table 5.1: Infiltration parameters sets.

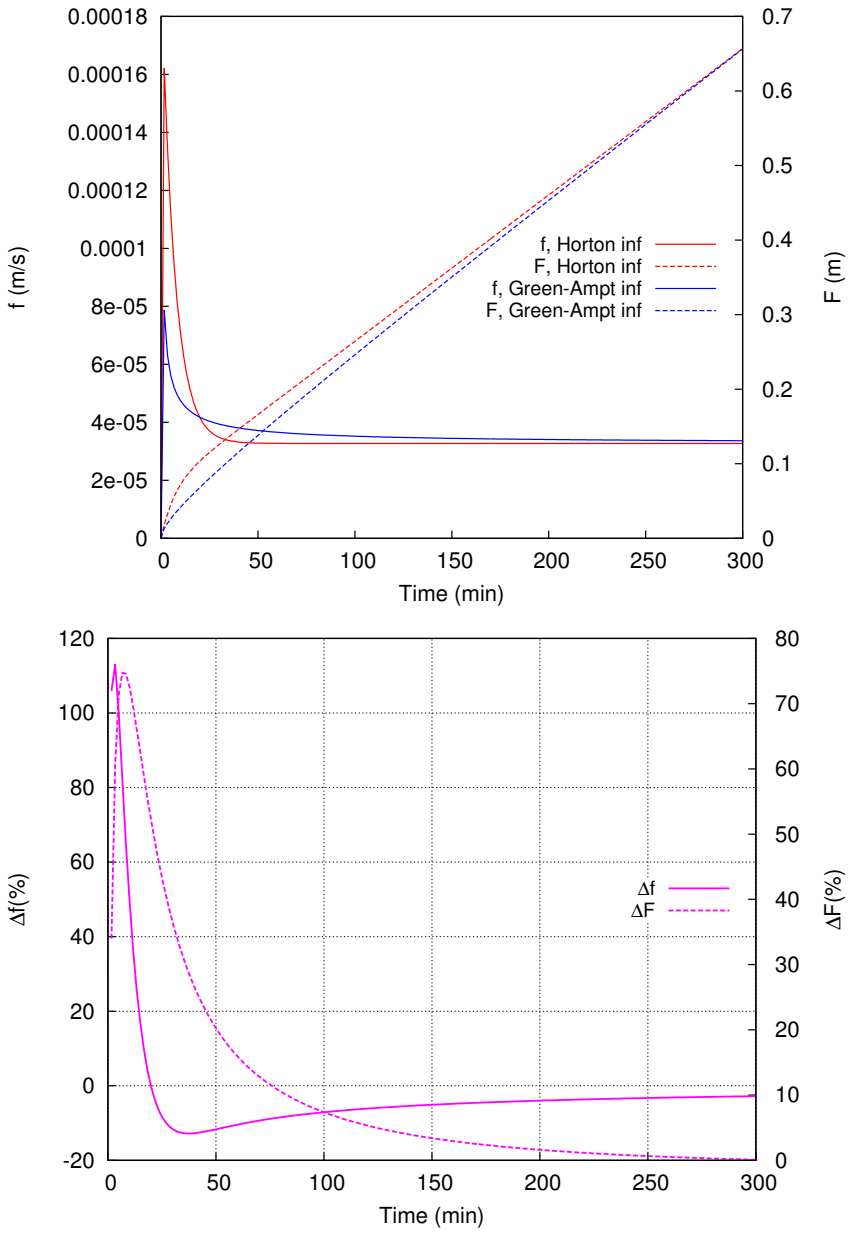

Figure 5.1: Infiltration rate and cumulative infiltration curves (upper) and relative differences between models in f and F (lower) for Case 0.

5.1.2 Case 1: uniform inclined plane

A uniform slope plane of 0.005 is considered in this case (see Figure 5.11). The Manning's roughness coefficient is set to 0.03 $s/m^{1/3}$. The initial conditions for the surface water equations are zero water depth and zero discharge everywhere, that is, dry surface conditions. Water enters the domain only through rainfall, which is assumed to be constant in space, hence there are not inlet boundaries. The only open boundary is at the outlet (downslope) and free outflow is assumed. Two studies are performed with this case: an analysis of the sensitivity to water availability and a study of the effects of slope and roughness variations.

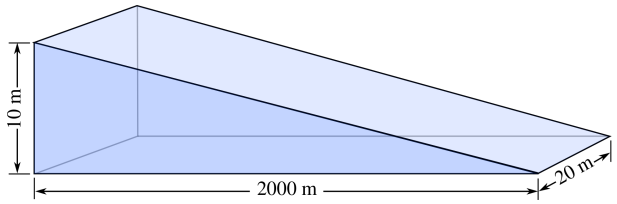

Figure 5.2: Case 1 topography.

Sensitivity to water availability

The motivation for the tests is to check if the response of the two models is the same using the chosen parameters. For this purpose, different rain conditions are considered (see Table 5.2). In Cases 1-1 to 1-3 the rainfall conditions guarantee full water availability at downslope during the period $(0-300min)$, which matches with the period used for calibration in Case 0. This enforces the same conditions of water availability for infiltration as in the calibration process. The results are presented in Figure 5.3. The results for Cases 1-1 to 1-3 show that, while the outlet hydrographs for Horton and Green-Ampt models are slightly different, the same runoff volume (ROV) is achieved. Hence, the calibration of the infiltration parameters performed in a flat ponded soil remains applicable in a mild slope if water is available for infiltration. In addition, neither the storm pattern (Case 1-2, Figure 5.3(b)) nor the rainfall volume (Case 1-3, Figure 5.3(c)) affect the calibration of the infiltration parameters.

On the other hand, it is possible that the rainfall pattern is not adequate for the continuous runoff generation until a time near to the calibration point ($t = 300min$).

This situation can be reached in two ways. The first one consists of a short rainfall duration (Case 1-4, Figure 5.3(d)). In this case, the runoff finishes long before the calibration point. The second possibility corresponds to Case 1-5 and it is shown in Figure 5.3(e). In this case, the storm pattern presents a temporal distribution which generates a discontinuity in the runoff due to a reduction of the water availability for infiltration in the 0-300min period. As shown in Figures 5.3(d) and 5.3(e), both cases present differences in the outlet runoff volumes. The reason for this behavior is that the period of time with available water is less than the one for what the calibration has been performed (Case 0). Hence, the calibration of the infiltration parameters is not valid in this kind of situations.

Figure 5.3(f) shows the evolution in time of the relative difference between the runoff volume for both infiltration models, defined as follows:

$$\Delta(\%) = 100\frac{ROV_{GA} - ROV_H}{ROV_{GA}} \tag{5.2}$$

In the light of these results, it is clear that the greater the difference between water availability time and calibration time, the greater the difference between infiltration models (Cases 1-4 and 1-5). From Figure 5.3(f), it is clearly seen that there are huge differences in outlet hydrographs produced by both models at early times of the simulation. This is due to the fact that the infiltration rates of both models differ at this time, since the fitting time for the models has not been yet reached. When approaching this calibration point ($t = 300min$) the magnitude Δ decreases in general and tends to zero in cases with full water availability during this time (Cases 1-1, 1-2 and 1-3). The difference for Case 1-4 freezes at $t = 100m$ with a value $> 10\%$. The process for Case 1-5 is divided into two stages. First, as in Case 1-4, the difference Δ decreases until the water from the first rainfall period ends. Then, it remains constant between rainfall periods and decreases again during the second rainfall event.

In order to analyze in detail Case 1-5, a probe is set at $x = 1000m$, as a representative point. The temporal evolution of infiltration rate and water depth for this point are plotted in Figures 5.4(a) and 5.4(b) for Horton and Green-Ampt models, respectively. These plots show that, although both infiltration models present very similar behavior, the existence of temporal regions with $f = 0$ implies that the water

is infiltrating for a period of time shorter than the one considered for the calibration process and, hence, the calibration is not correct.

Case	Rainfall pattern	Rain volume (m^3)
1-1	uniform	75000
1-2	non-uniform	75000
1-3	non-uniform	56250
1-4	uniform	35000
1-5	non-uniform	43000

Table 5.2: Cases 1-1 to 1-5 rainfall characteristics and rain volume.

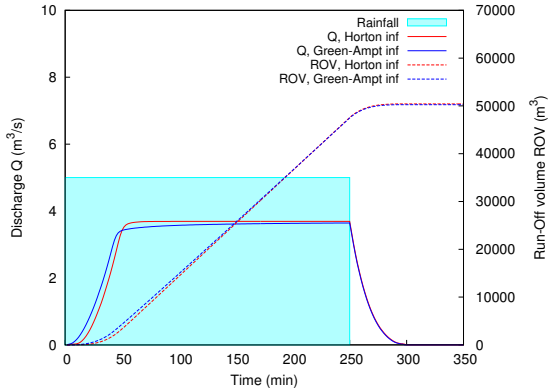

(a) Case 1-1.

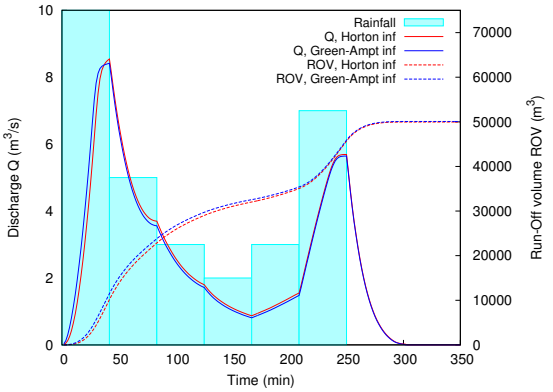

(b) Case 1-2.

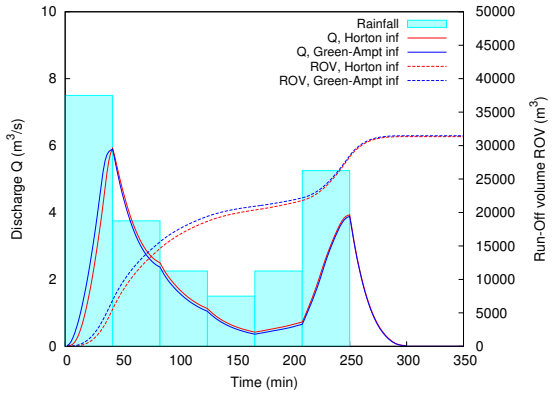

(c) Case 1-3.

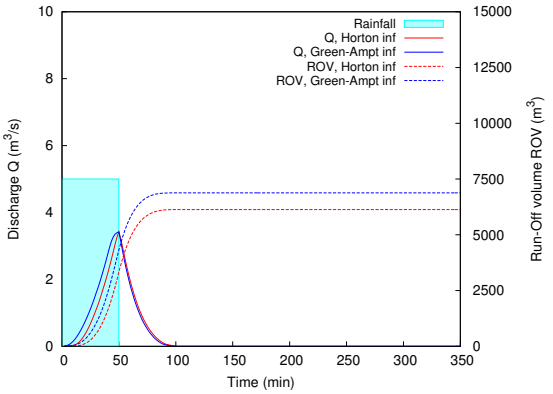

(d) Case 1-4.

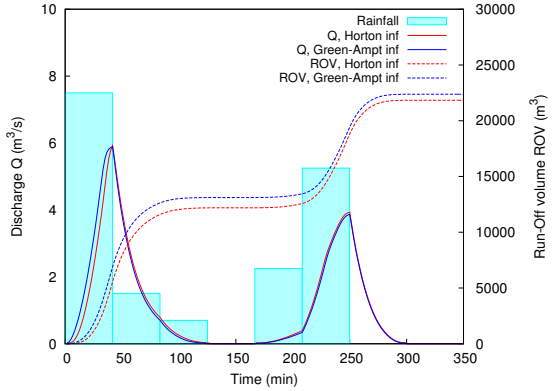

(e) Case 1-5.

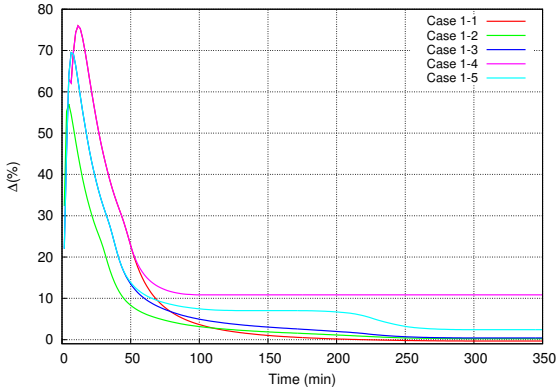

(f) Relative differences.

Figure 5.3: Cases 1-1 to 1-5. Outlet hydrographs for sensitivity to rainfall analysis.

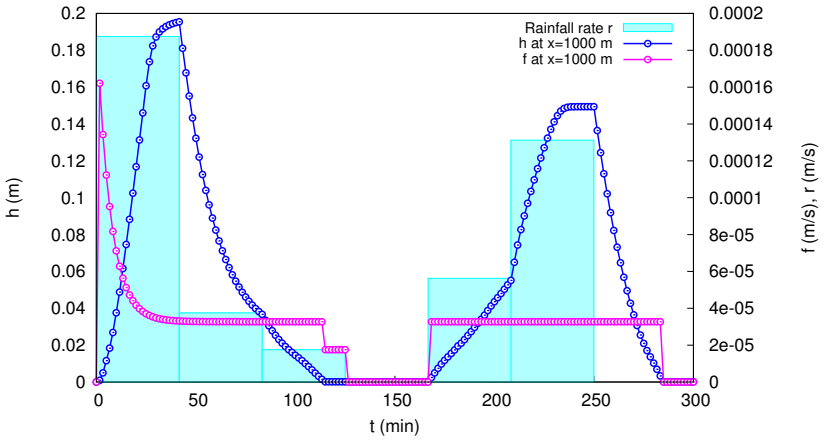

(a) f and h curves for Horton model.

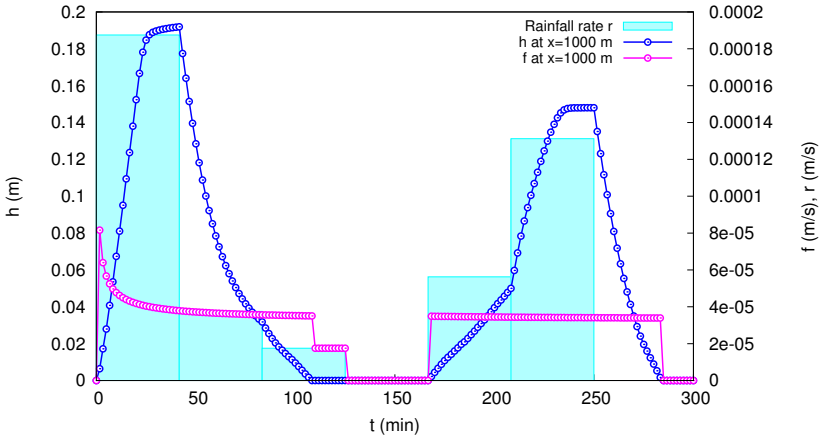

(b) f and h curves for Green-Ampt model.

Figure 5.4: Case 1-5. Water depth and infiltration rate curves for Horton and Green-Ampt models.

Slope and roughness variations

In this section, different slope and roughness combinations are studied in order to determine their influence in the difference between infiltration models. As in the previous section, the calibrated parameters under horizontal ponded soil conditions are used (Table 5.1). The effect of slope and roughness is studied by means of the mildness fraction of the plane, defined as the ratio between normal water depth h_N and critical water depth h_C. A rain discharge of $(5m^3/s)$ and $15000s$ of duration and three different values of h_N/h_C (2.33, 1.40 and 0.61) are set. In all these cases, the rain duration is such that surface water is available between $0 < t < 300min$. Figure 5.5 shows the overall numerical results. Figures 5.5(a) and 5.5(b) clearly show that the outlet hydrographs and the final cumulative volumes for both infiltration models do not differ significantly when changing the mildness fraction. Therefore, in the light of the results, infiltration parameter calibration is not strongly dependent on the mildness fraction under full water supply.

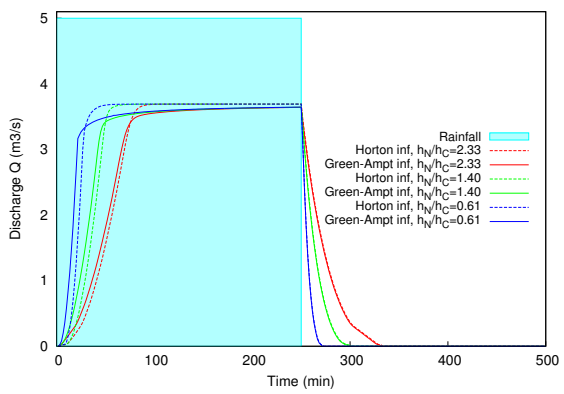

(a) Outlet discharge comparison between Horton and Green-Ampt infiltration models.

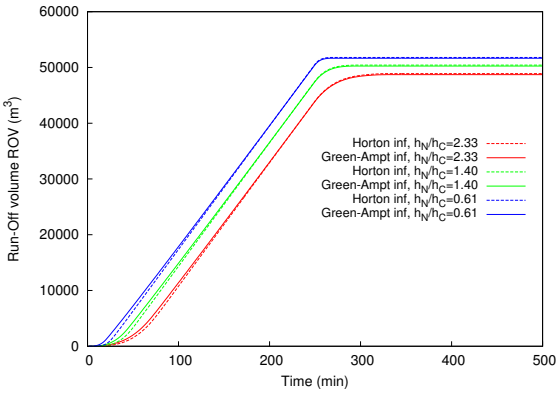

(b) Runoff volume comparison between Horton and Green-Ampt infiltration models.

Figure 5.5: Case 1. Flow profile variations.

5.1.3 Case 2: single storage area

Starting from the same topography used in the previous section, a trapezoidal furrow is added to the plane (see Figure 5.6) acting as a storage depression. The purpose of this case is to check the changes in the outlet hydrographs and runoff volume curves due to the storage under different conditions and to extrapolate them to natural surfaces on real catchments which have depressions (local minima of the surface). The same initial and rainfall setup as in Case 1-1 are assumed in order to establish a comparison with that case of the infiltration calibration and how it is affected by a volume storage of $\approx 1000m^3$.

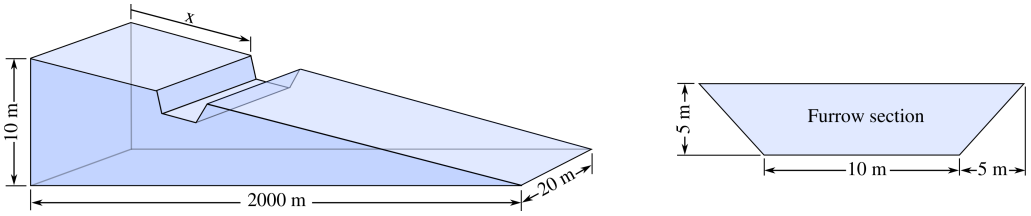

Figure 5.6: Case 2 topography.

Table 5.3 summarizes the numerical cases presented in this section and Figure 5.7 shows the numerical results and the comparison with the no-furrow situation, corresponding to Case 1-1.

Case	Storage area position
2-100	x=100 m
2-1900	x=1900 m

Table 5.3: Case 2 setups.

In view of the results obtained, it is observed that the storage area does not generate significant difference between infiltration models in the outlet runoff volume. On the other hand, the time distribution of the outlet discharge is affected by the position of the furrow, being more significant the difference between infiltration models when the furrow is placed downstream (Case 2-1900, Figure 5.7(d)). Hence, this test shows that the topography features can significantly affect the calibration of the infiltration parameters.

The evolution of the difference between infiltration models changes depending on the position of the furrow. In the case of the downstream furrow, a particular

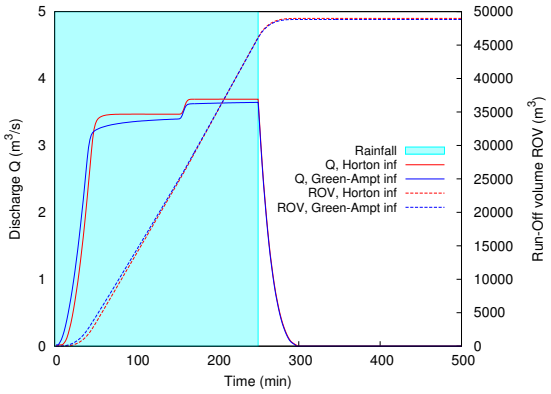

(a) Outlet discharge and runoff for Case 2-100.

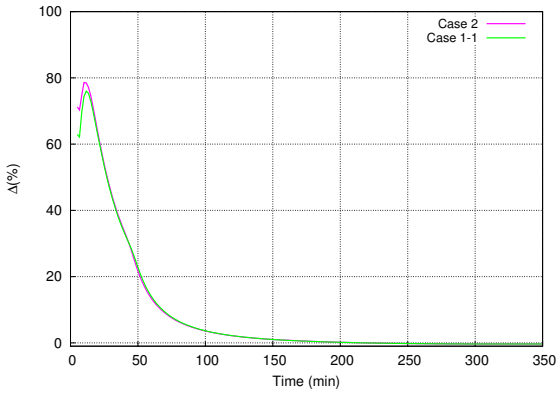

(b) Comparison between differences for Case 2-100.

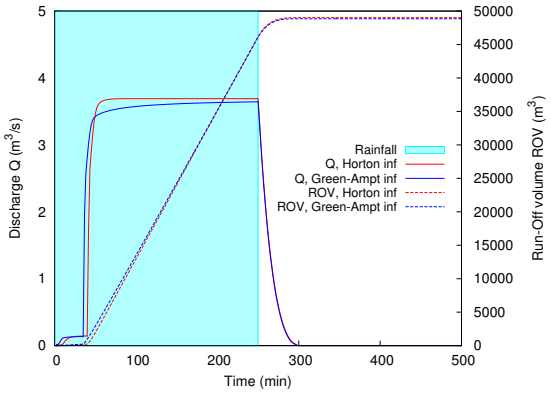

(c) Outlet discharge and runoff for Case 2-1900.

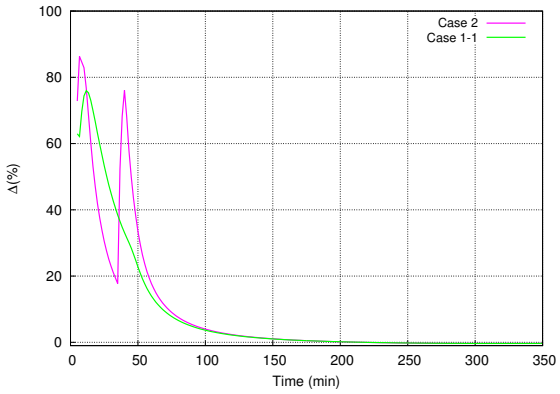

(d) Comparison between differences for Case 2-1900.

Figure 5.7: Hydrographs and differences between infiltration models for Case 2.

behavior is observed. Initially ($t < 40\,s$) the outflow is generated only by rainfall downstream from the furrow, since runoff from upstream areas is stored in the furrow, filling it. The difference between infiltration models during this time behaves as in case 2-100 because it is essentially identical. However, at $t \approx 40\,s$ the Green-Ampt hydrograph shows a sudden rise in outflow, indicating that the furrow has been filled. The Horton hydrograph rises somewhat later. This lag between the sudden increase in outflow generates the increase in difference between both infiltration models seen in figure 5.7(d), which goes almost to 80% (i.e., Green-Ampt produces a large outflow because the furrow has been filled, but Horton is still filling up the furrow). As soon as the Horton hydrograph initiates the rising outflow, both infiltration models are allowing runoff from the entire catchment to flow out, and therefore, as time advances, they tend to be identical.

5.1.4 Case 3: several storage areas

Following from the previous cases and working towards real topography, a case with a very irregular topography is presented and the effect of these terrain irregularities over the infiltration calibration is analyzed. The domain dimensions are presented in Figure 5.8 and the bed level is given by:

$$z = 21.0 + 1.0sin\left(\frac{\pi}{10}x\right) - 0.005x \tag{5.3}$$

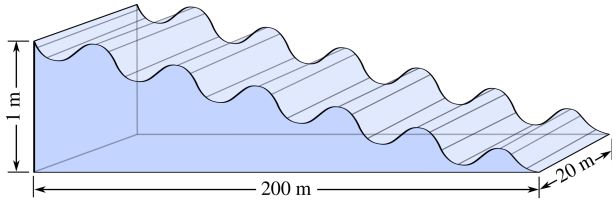

Figure 5.8: Case 3 topography.

This kind of domain provides a large storage capacity for incoming rainfall water in which a study of the influence of an irregular topography on the infiltration models can be carried out. For this particular case, a constant rain pulse of $0.25mm/s$ is assumed over all the domain during $125min$. This particular rain duration guarantees that the local maxima of the domain will not be ponded continuously so the fitting point ($t = 300min$) is not reached (i.e., $F_H \neq F_{GA}$). On the other hand, the local minima are continuously ponded. This allows to observe differences between both regions. The same initial conditions and infiltration parameters (Table 5.1) as in previous cases are considered.

Figure 5.9 shows the longitudinal profiles of the water level $h+z$ and cumulative infiltration F at $t = 125min$, when rainfall stops, $t = 250min$ and $t = 300min$. The relative differences in F between infiltration models are presented in Figure 5.10 in terms of the magnitude $\Delta F(\%)$, defined as in Equation (5.1).

As shown in the Figure 5.9 (upper), surface water is available for infiltration until $t = 125min$, so the relative difference $\Delta F(\%)$ remains constant all along the domain. As stated in the previous cases, this difference is due to the large time lapse for reaching the time for which the parameters have been fitted in Case 0 ($300min$). After this time, rainfall stops and the surface water runs downstream

except for the water stored in the local minima producing ponded and non-ponded regions (Figure 5.9 (middle)). In this situation, differences appear in the cumulative infiltration profile, since water continues infiltrating in the ponded areas but, obviously, no infiltration occurs in non-ponded regions. As shown in Figure 5.10, $\Delta F(\%)$ is minimized for $t = 300min$, leading to a relative difference less than 0.1% in the ponded regions. On the other hand, the water available for infiltration in local maxima has not been enough to reach the fitting point. It is worth to mention that these differences cannot be observed using lumped models, as they do not have a spatial resolution for considering transient ponded conditions. These kind of phenomena show the capabilities and the need for distributed models. These results also bring to light the influence of the topography in the calibration of empirical infiltration models, again highlighting the need for distributed models.

A similar 1D setup was simulated by [91] to study the effects of microtopography in runoff generation and infiltration. Microtopography in [91] is a sinusoidal variation of terrain surface over a background terrain slope, as in the case presented here. [91] found that microtopography (i.e., sinusoidal variations) largely increased infiltration when compared against the slope without microtopography, and such increase was reported as proportional to the amplitude of the microtopography. The results reported in Figure 5.9 are consistent with the observations by [91] and also show the cause of such behavior. There is a clear separation of flow by the maximum elevations which favors long-residence-time ponding (the so-called regime A in [91]). Moreover, in the results shown here it can be seen that there is differential infiltration because of the microtopographic variations which may also be relevant in particular for parameter calibration, specially for mid-intensity rainfall in which ponding times are most relevant.

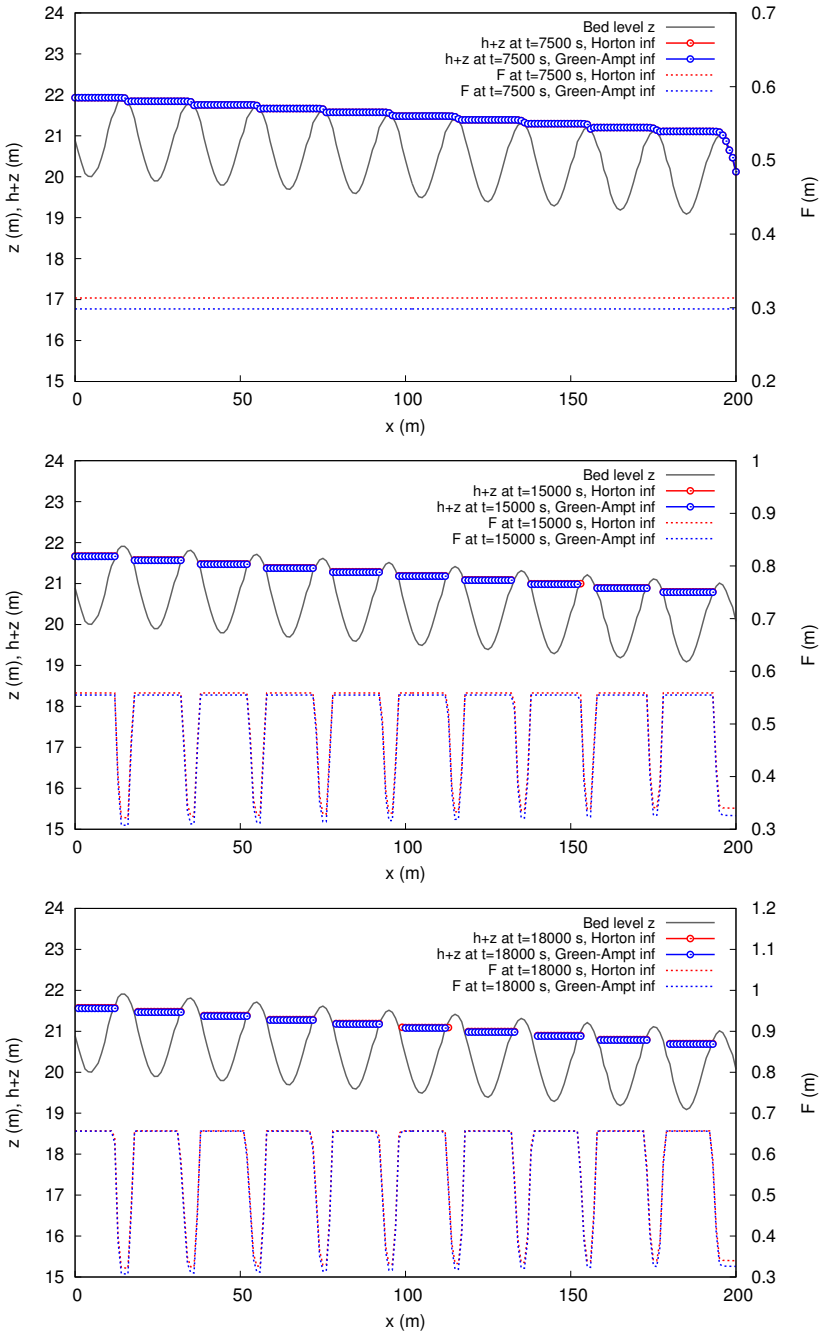

Figure 5.9: Case 3. Longitudinal profiles at $t = 125min$ (upper), $t = 250min$ (middle) and $t = 300min$ (lower).

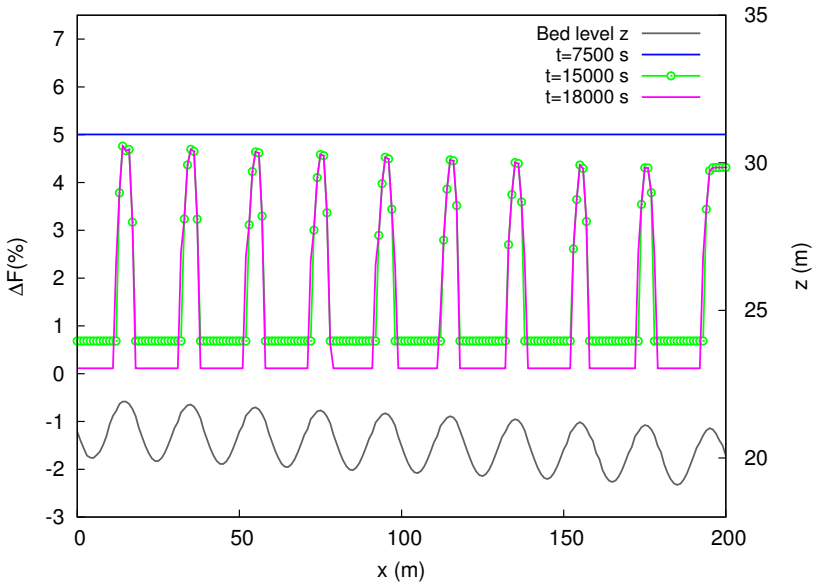

Figure 5.10: Case 3. Relative difference in cumulative infiltration.

5.2 Overland flow coupled with infiltration laws: FOGA model

5.2.1 Rainfall on a slope

A plane with slope 0.005 is considered in this example and the dimensions of the domain are $2000m \times 20m \times 10m$ (see Figure 5.11). The Manning's roughness coefficient is set to $n = 0.02\, sm^{-1/3}$. The initial conditions for the surface water equations are zero water depth and zero discharge everywhere, i.e., dry surface conditions. Water enters the domain only through rainfall, which is assumed to be constant in space, hence there are not inlet boundaries. The only open boundary is at the outlet (downslope) and free outflow is assumed. In order to study how the order of the Caputo fractional derivative affects the shape of the outlet hydrograph, seven test cases have been designed (see Table 5.4). The values of the hydraulic conductivity K_α and the rainfall rate R corresponding to Case 3.1 are taken as reference. In Cases 3.2 and 3.3, the values of K_α and R are multiplied by 10. In all the cases, the simulations are performed for the values of $\alpha = 0.75, 0.8, \ldots, 1$.

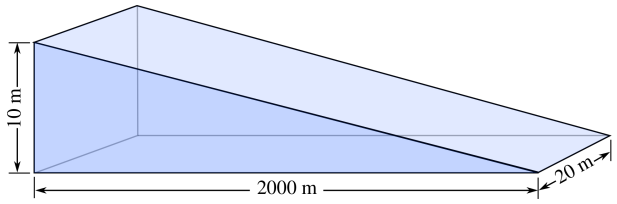

Figure 5.11: Case topography.

Test case	$R(mm/s)$	$K_\alpha(m^\alpha/s)$	$\Psi(m)$	$\Delta\theta(m^3/m^3)$
3.1	0.0825	$3.3 \cdot 10^{-6}$	0.05	0.38
3.2	0.0825	$3.3 \cdot 10^{-5}$	0.05	0.38
3.3	0.825	$3.3 \cdot 10^{-5}$	0.05	0.38
3.4	0.0825	$3.3 \cdot 10^{-6}$	0.005	0.38
3.5	0.0825	$3.3 \cdot 10^{-6}$	0.05	0.038
3.6	Unsteady	$3.3 \cdot 10^{-5}$	0.05	0.38
3.7	Unsteady	$3.3 \cdot 10^{-5}$	0.05	0.38

Table 5.4: Parameter setting.

Figures 5.12-5.14 show the numerical outlet discharge Q for all the proposed cases. This value is computed from the integration of the outlet unit discharges predicted by the surface model at the outlet boundary. In the light of the results,

several conclusions are reached. For Case 3.1, the lower the order α, the lower the soil infiltration rate, since the outlet hydrographs are getting higher peak discharge values. The same conclusion is achieved in Case 3.2, where the value of K_α is increased by a factor of 10. Nevertheless, a change in the trend of the outlet hydrographs is observed for certain values of α, leading to non-monotonic curves. This behavior is a consequence of non-monotonic infiltration rate curves, generated by the FOGA model [96], for certain values of α and the classical parameters set (K_s,Ψ,$\Delta\theta$).

In order to test the influence of the rainfall rate on the infiltration rate recovery predicted by the FOGA model, Case 3.3 is proposed. By maintaining the same K_α value as in Case 3.2, the rainfall rate is increased by a factor of 10. As seen on Figure 5.12 (e,f), the same trend as in Case 3.2 for the outlet hydrographs is reached. This shows that this change on the curves trend depends only on the K_α value, not on the ratio between K_α and R.

The other Green-Ampt parameters, Ψ and $\Delta\theta$ have been also modified in Cases 3.4 and 3.5 observing the same change in the trend, to a lesser extent, in the outlet hydrographs (Figure 5.13).

Figure 5.14 shows the results corresponding to Case 3.6 in which an unsteady rainfall pattern is considered and several values of α have been tested, ranging from 0.35 to 1. As observed in the previous cases, the smaller the value of α, the lower the soil infiltration capacity and, hence, the higher the peak discharges at the outlet. In general terms, it seems that, for this particular case, the order of the fractional derivative has a global effect, rising or lowering the full hydrograph.

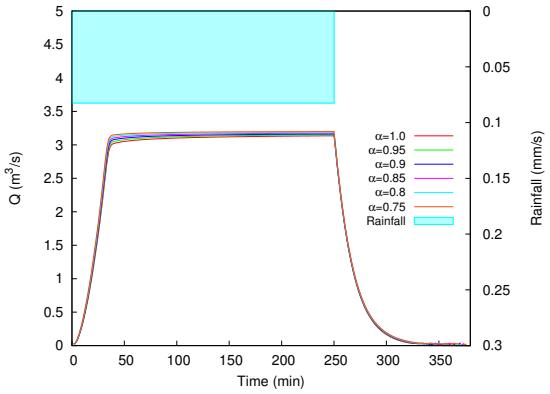

(a) Case 3.1

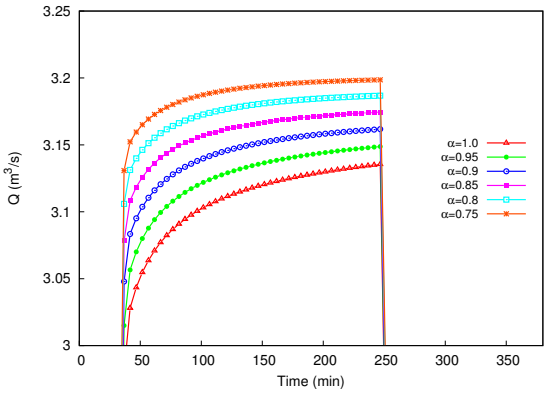

(b) Case 3.1 (close-up)

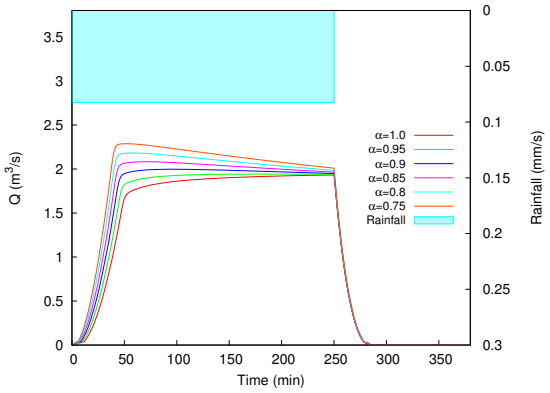

(c) Case 3.2

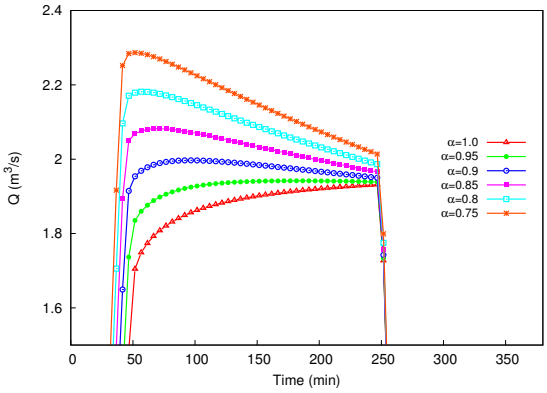

(d) Case 3.2 (close-up)

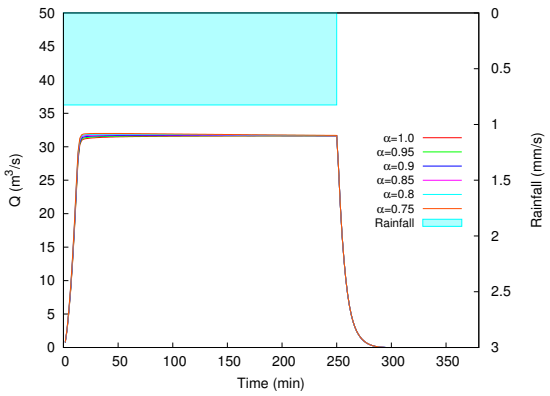

(e) Case 3.3

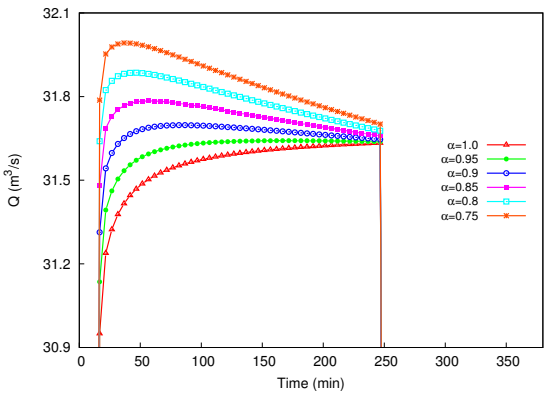

(f) Case 3.3 (close-up)

Figure 5.12: Rainfall on a slope: Outlet hydrographs for the Cases 3.1, 3.2 and 3.3. The figures on the right represent a close-up view.

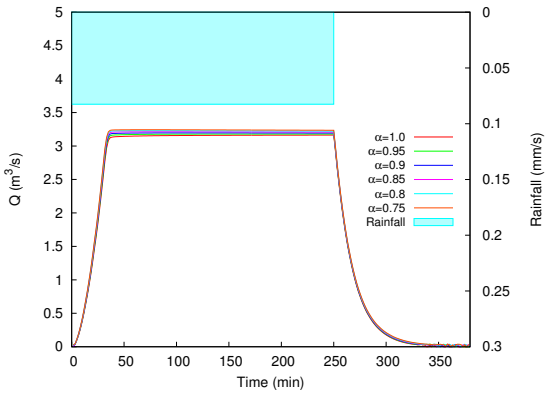

(a) Case 3.4

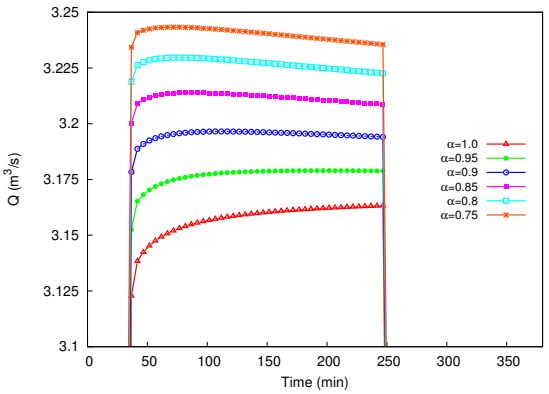

(b) Case 3.4 (close-up)

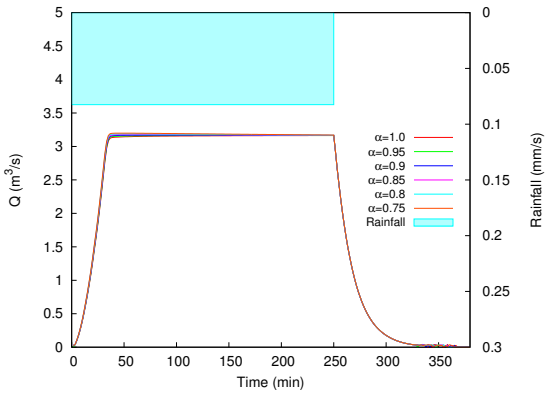

(c) Case 3.5

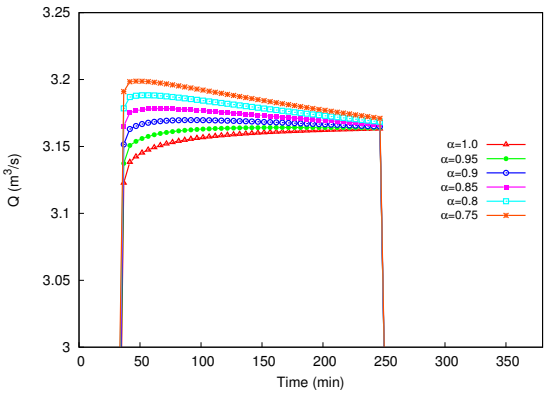

(d) Case 3.5 (close-up)

Figure 5.13: Rainfall on a slope: Outlet hydrographs for the Cases 3.4 and 3.5. The figures on the right represent a close-up view.

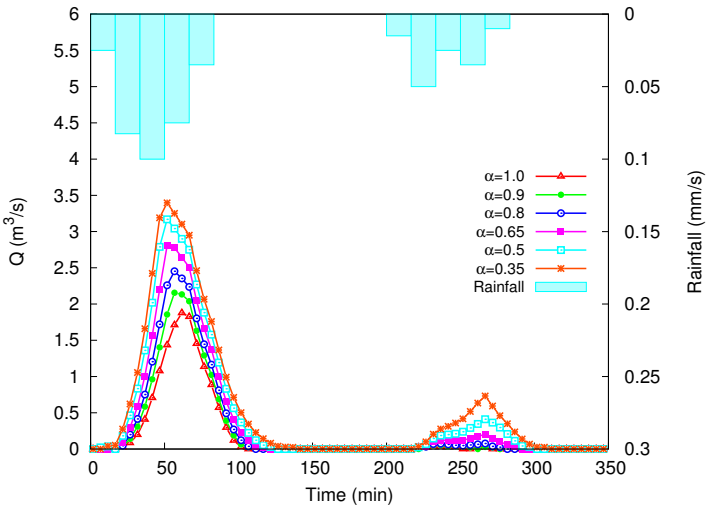

Figure 5.14: Rainfall on a slope: Outlet hydrographs for the Case 3.6.

5.2.2 Application to real catchments I: Araguás basin

The Araguás catchment is located in the Central Pyrenees (Figure 5.15(a)) and it has an extension of $0.45\,Km^2$ [27]. Its altitude ranges from 780 to 1100 m.a.s.l. and the mean slope varies from 20% to 43%. Due to the small size of the basin, a constant Manning's roughness coefficient of $n = 0.025 sm^{-1/3}$ is set. A triangular unstructured mesh of 7728 cells is used for the spatial discretization of the catchment (Figure 5.15(b)).

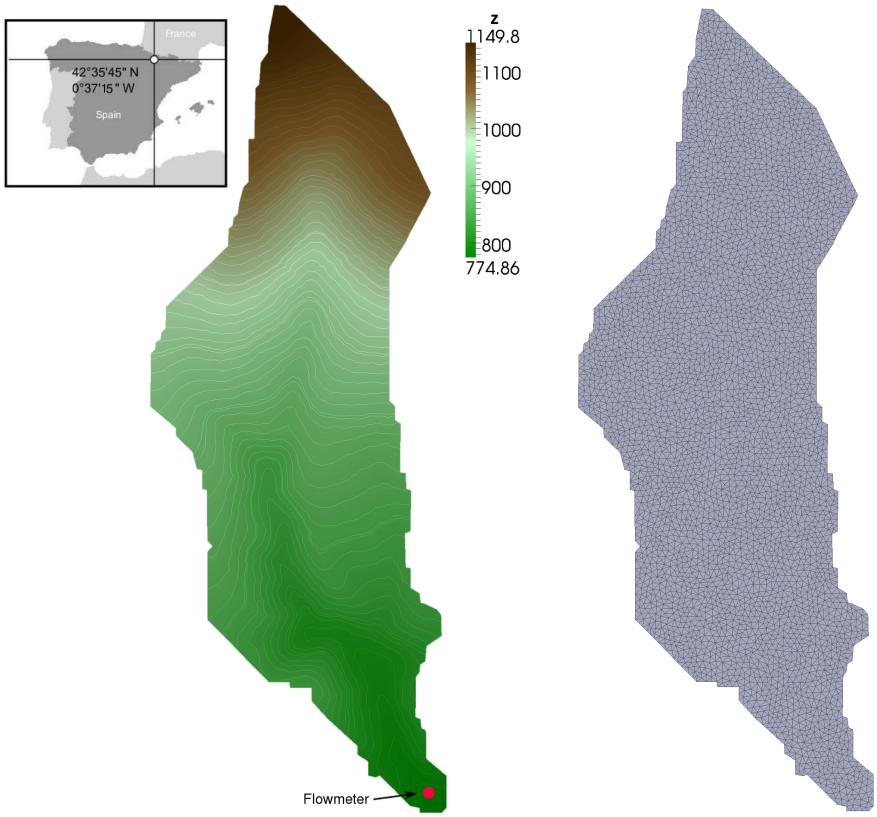

(a) Catchment location and hypsometry map. (b) Computational mesh.

Figure 5.15: Araguás catchment characteristics.

In this catchment, a single event (which is referred to as Event 1) is considered. The flow discharge measurements were acquired at the outlet of the basin (see Figure 5.15(a)) with a 5 minutes frequency. Rainfall was registered by a rain gauge also with the same frequency. Figure 5.16 shows the observed hyetograph and the outlet hydrograph for this particular storm event.

The numerical results obtained for the Araguás catchment are presented now. An

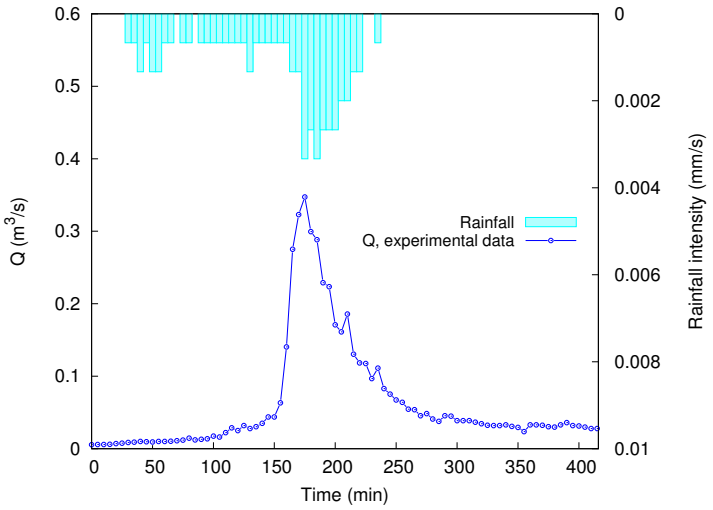

Figure 5.16: Experimental hyetograph and hydrograph for Araguás basin.

explicit 2D SW scheme ($\theta = 0$) is chosen to capture more precisely the water depth variations. In order to highlight the capacities of distributed models, Figure 5.17 shows the spatial distribution of the numerical values of water depth, flow velocity and cumulative infiltration at $t = 13500s$. It can be seen that the main channel cumulative infiltration values are significantly different from the ones computed in the hillsides. This detailed computation of the hydraulic and hydrologic variables leads to a better prediction of the outlet hydrographs and, therefore, to a better fit of the observed data.

Table 5.5 summarizes the simulated cases set with a constant distribution of α. Case 4.1 is considered as the reference case. It corresponds to the parameter set that provides the best fit using the GA model ($\alpha = 1$). Cases 4.2 and 4.3 keep the parameters K, Ψ and $\Delta\theta$ as in Case 4.1 but the order α of the fractional derivative is modified. Figure 5.18 shows the outlet hydrographs corresponding to Cases 4.1, 4.2 and 4.3. The effect of decreasing α corresponds to a global reduction of the soil infiltration capacity predicted by the GA model. Hence, the less the value of α the more the value of the outlet discharge peak.

It is also interesting to explore the possibility of reproducing the same outlet hydrograph of Case 4.1 by means of several combinations of the infiltration parameters with $\alpha \neq 1$. As shown in Figure 5.19, Cases 4.4 to 4.9 generate very similar hydrographs to Case 4.1 by modifying one single parameter each time for two different values of α. In particular, we consider the values of $\alpha = 0.7, 0.9$. Thus, the

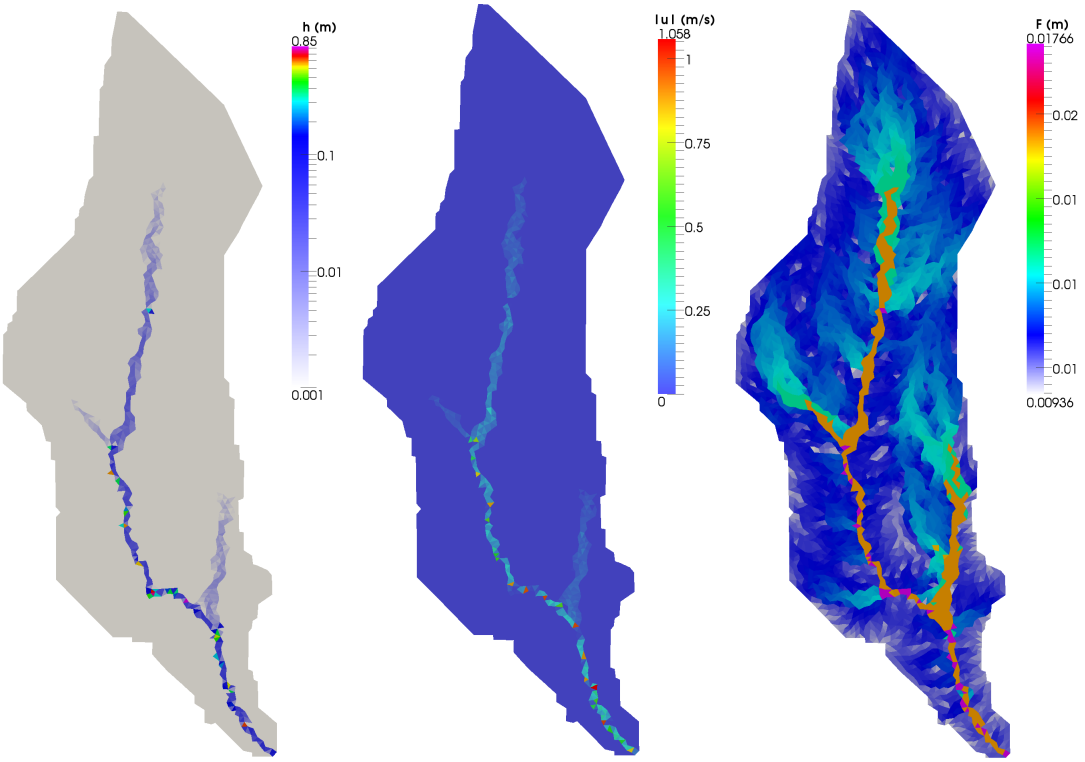

Figure 5.17: Event 1: Spatial distribution of the water depth (h), flow velocity (u) and cumulative infiltration (F) at $t = 13500s$.

numerical results suggest that the fitting cannot be improved in this event using a single value for α.

In the light of the previous numerical results, GA model seems to predict an excessive soil infiltration capacity at the beginning of the storm when the soil is almost dry.

Test case	α	$K_\alpha(m^\alpha/s)$	$\Psi(m)$	$\Delta\theta(m^3/m^3)$
4.1	1	$1.37 \cdot 10^{-7}$	0.02	3.0
4.2	0.95	$1.37 \cdot 10^{-7}$	0.02	3.0
4.3	0.9	$1.37 \cdot 10^{-7}$	0.02	3.0
4.4	0.9	$2.2 \cdot 10^{-7}$	0.02	3.0
4.5	0.7	$7.5 \cdot 10^{-7}$	0.02	3.0
4.6	0.9	$1.37 \cdot 10^{-7}$	0.035	3.0
4.7	0.7	$1.37 \cdot 10^{-7}$	0.12	3.0
4.8	0.9	$1.37 \cdot 10^{-7}$	0.02	6.0
4.9	0.7	$1.37 \cdot 10^{-7}$	0.02	43.0

Table 5.5: Set of cases in Araguás catchment assuming a constant α distribution.

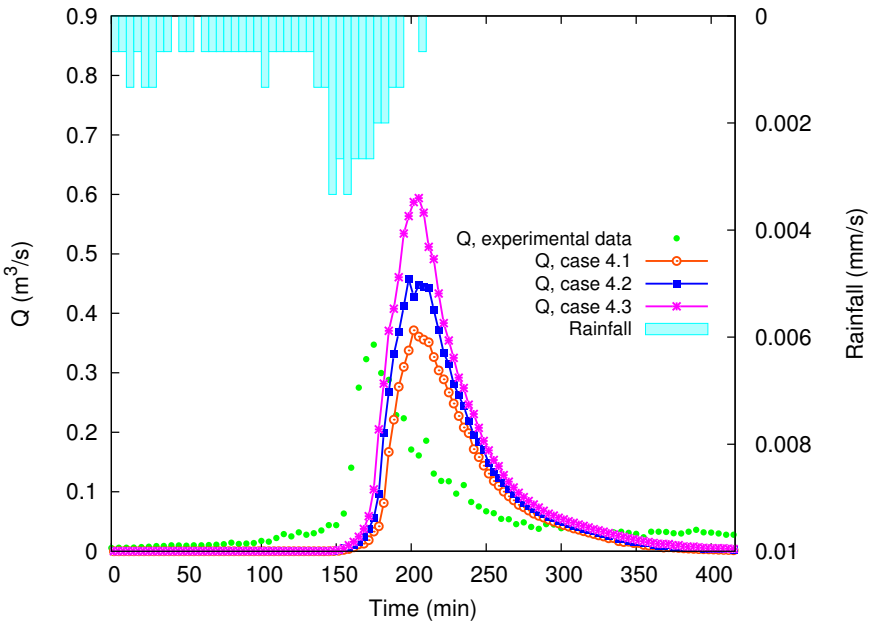

Figure 5.18: Araguás catchment, cases 4.1 to 4.3.

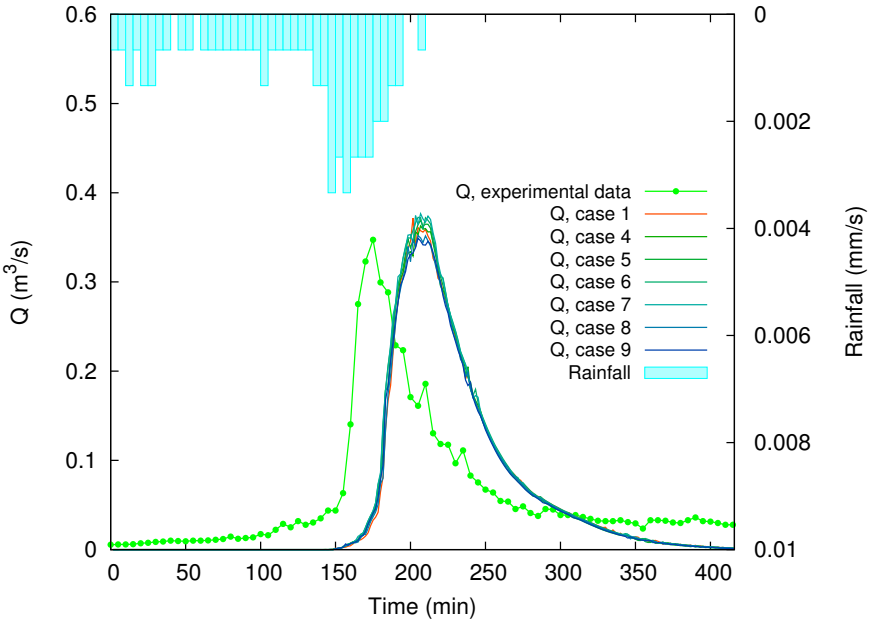

Figure 5.19: Araguás catchment, cases 4.4 to 4.9.

Therefore, we propose to use a variable-order α of the fractional derivative which is given in terms of the cumulative infiltration F and the water depth h. This will lead to an order of the derivative α variable in time and distributed in space (horizontal plane) with a different value for each computational cell. The dependency on h is necessary for long and multiple rainfall events. For this reason, and taking into account that the infiltration rate is also controlled by surface water availability, the variable α is formulated as a combined function of the cumulative infiltration and the available surface water as follows:

$$\alpha(F,h) = \min\{aF + \alpha_{min},\, e^{bh} + \alpha_{min} - 1,\, 1\} \tag{5.4}$$

where a and b are constant values to calibrate and α_{min} is the minimum value that the order of the derivative can reach. Then, it holds that $\alpha_{min} \leq \alpha(F,h) \leq 1$.

The particular function proposed (5.4) discriminates between the presence or absence of surface water but it depends weakly on the surface water depth as it gets quickly truncated (Figure 5.20). The main purpose of this essentially phenomenological fitting model is to provide a way to determine the order of the fractional derivative at the earlier stages of infiltration. Hence, it does not formulate any physical process. Once the infiltration depth (F) and the surface water depth (h) exceed a threshold, the model reduces to the classical GA formulation. Table 5.6 gives the FOGA model parameters obtained for the storm Event 1 considered in this catchment, as well as the classical GA model parameters which provide the best fit. It also presents the L_1^{error} values for both GA and FOGA model, computed as

$$L_1^{error} = \sum_{i=1}^{N} \frac{|Q_i^{num} - Q_i^{exp}|}{N} \tag{5.5}$$

being Q_{num} and Q_{exp} the computed and experimental discharges, respectively, and N the number of discharge curve points. The relative difference $\%_{dif}$ between the error produced by both models is also shown.

For this event, the FOGA model fitting error is 29.3% lower than the one produced by the GA model. Figure 5.21 shows both the numerical hydrograph obtained with the classical GA and FOGA models while the distributed values of h, F and

$\alpha(F, h)$ for this event are given in Figure 5.22. The FOGA model reproduces better the hydrograph. The arrival time is better fitted than with the GA model although the whole physical process is not correctly simulated because the receding part of the curve is lower than the observed one.

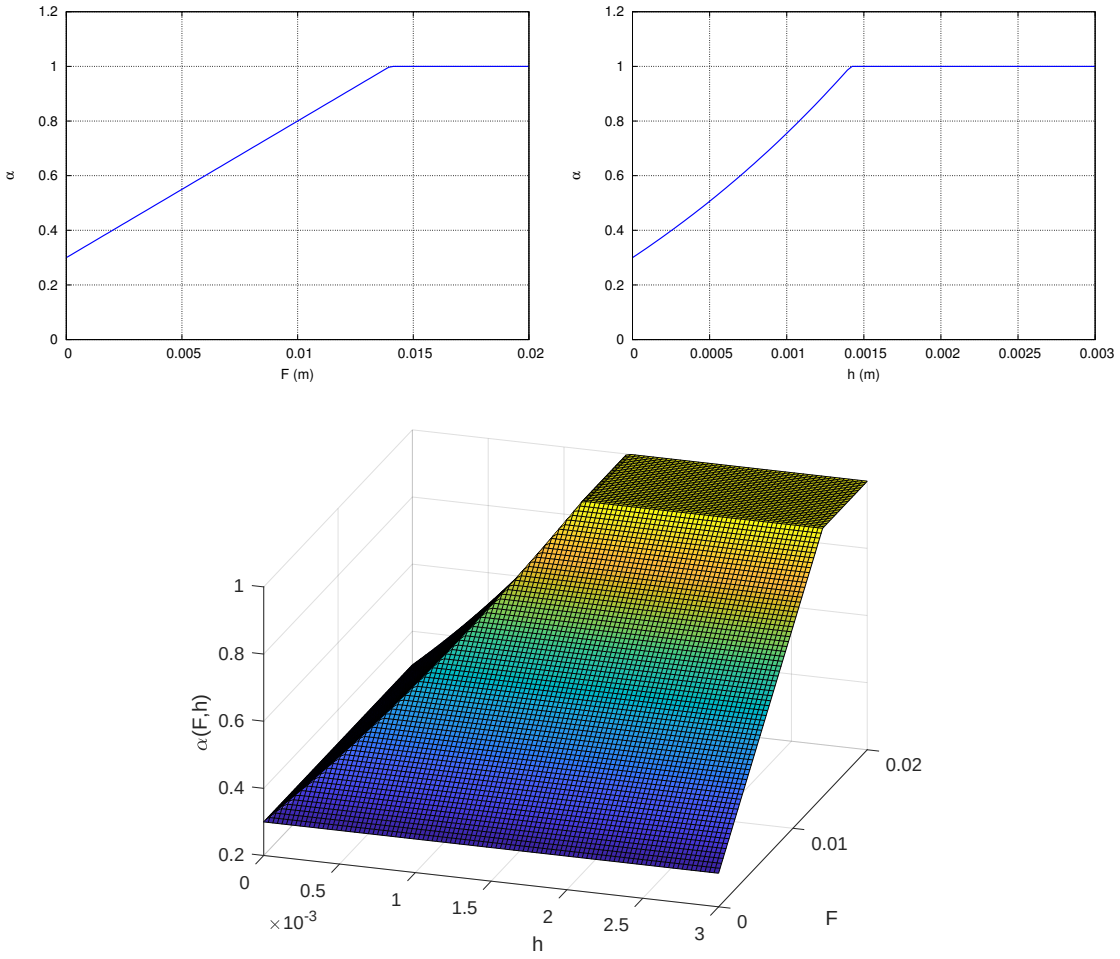

Figure 5.20: Graphical representations of the two terms of Eq. (5.4): $\min\{aF + \alpha_{min}, 1\}$ with $\alpha_{min} = 0.3$, $a = 50$ (left) and $\min\{e^{bh} + \alpha_{min} - 1, 1\}$ with $\alpha_{min} = 0.3$, $b = 375$ (right). 3D representation of Eq. (5.4) (lower).

Model	$K_\alpha(m^\alpha/s)$	$\Psi(m)$	$\Delta\theta(m^3/m^3)$	$a(m^{-1})$	$b(m^{-1})$	α_{min}	L_1^{error}	$\%_{dif}$
GA	$1.37 \cdot 10^{-7}$	0.02	3.0	-	-	-	0.047	-
FOGA	$2.75 \cdot 10^{-7}$	0.02	3.0	68	250	0.5	0.033	-29.3%

Table 5.6: Event 1: Infiltration parameters for the Araguás catchment ($\alpha(h, F)$).

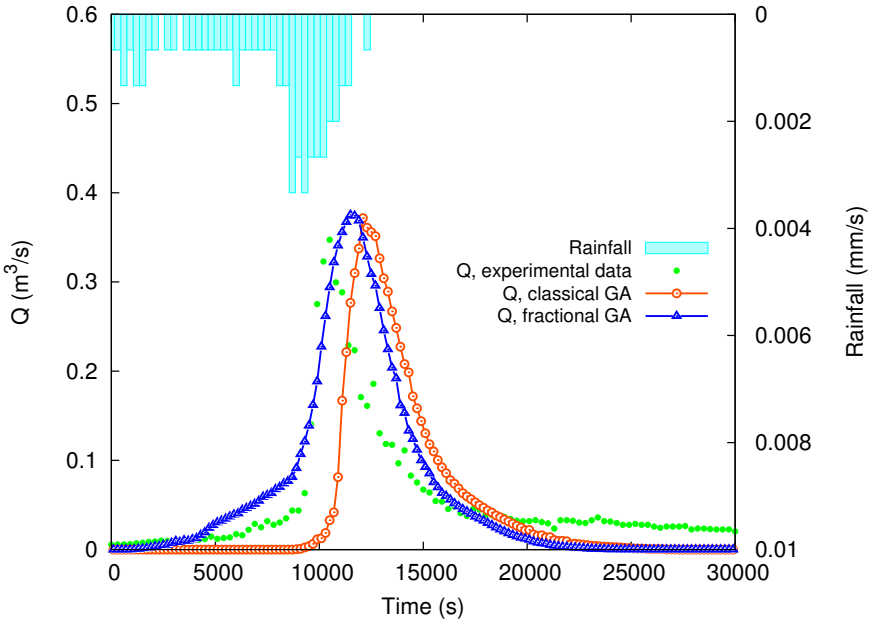

Figure 5.21: Hydrograph fitting for Event 1 ($\alpha(h, F)$).

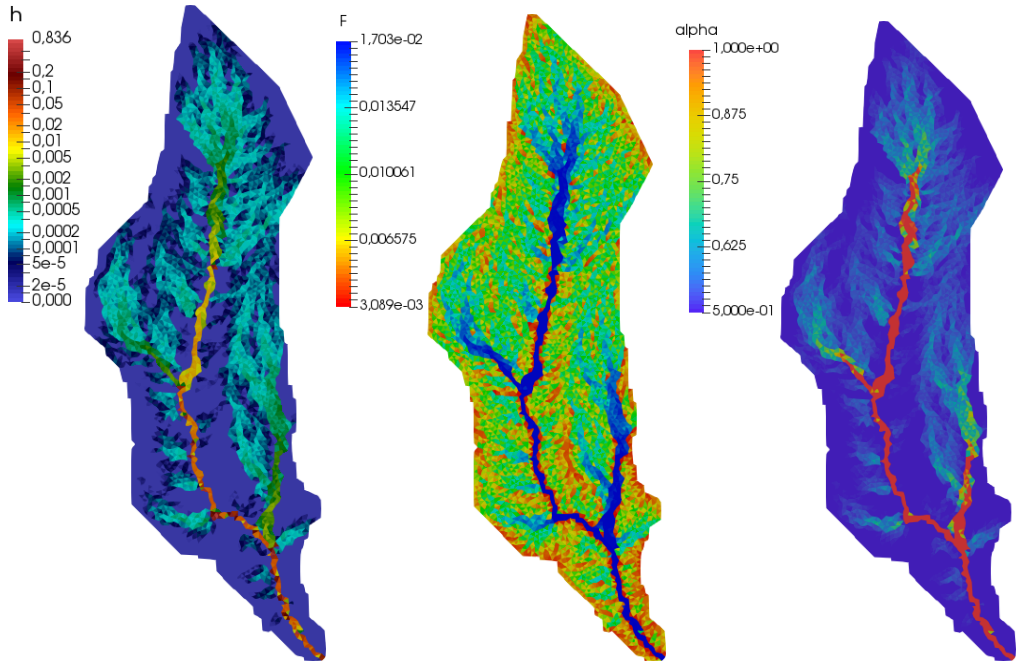

Figure 5.22: Water depth h, cumulative infiltration F and $\alpha(F, h)$ for Event 1 in Araguás catchment at $t = 15000s$.

5.2.3 Application to real catchments II: Arnás basin

The Arnás catchment ($2.84\,Km^2$, 900-1340 m.a.s.l.) is located in the Northern Spanish Pyrenees (see Figure 5.23(a)). Geologically, the catchment and its land use have suffered several changes in recent years which have modified significantly the vegetation cover. This includes patches of forest, grassland meadows, dense bush areas and bare land. The soil types and vegetation mapping have been widely studied in [42, 43, 82]. All these maps conform an accurate hydrological characterization of the Arnás watershed.

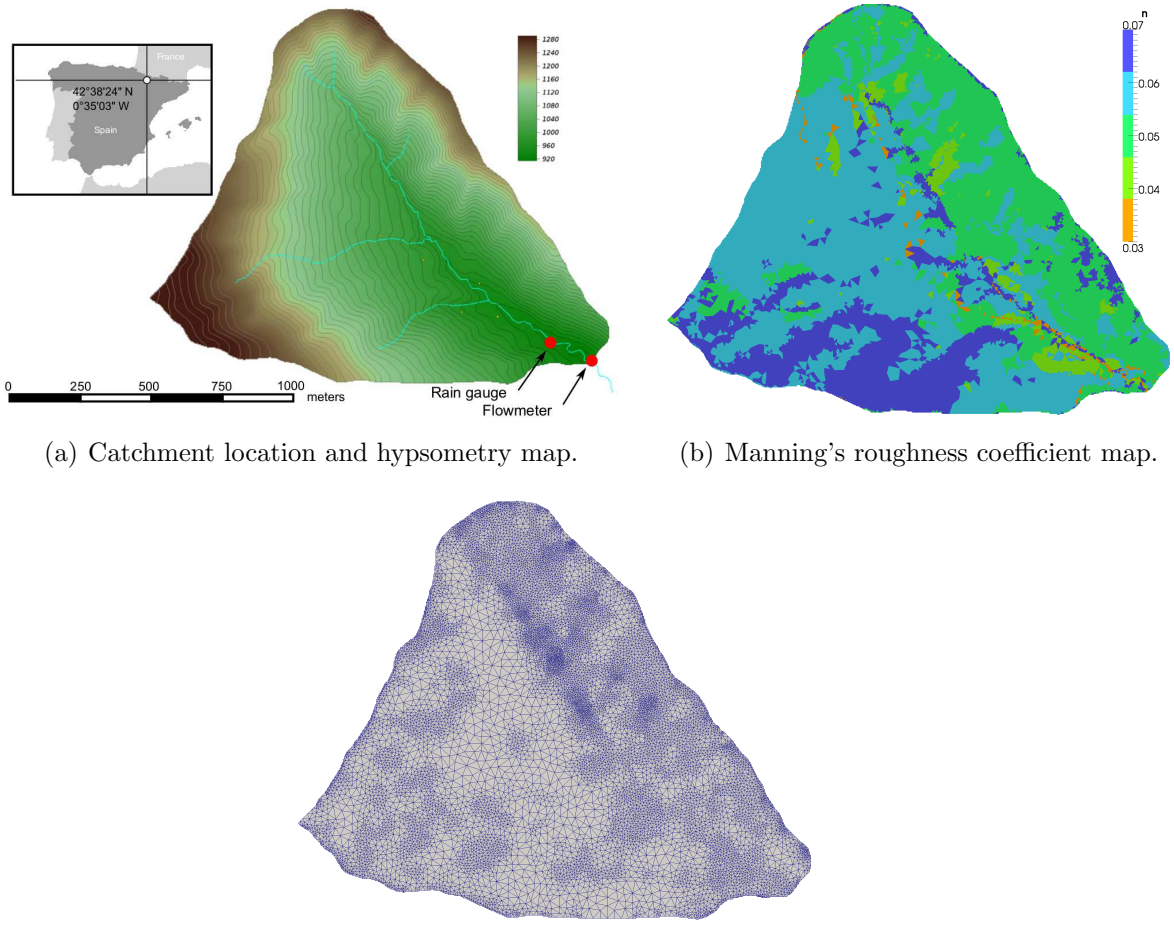

(a) Catchment location and hypsometry map.

(b) Manning's roughness coefficient map.

(c) Catchment refined mesh.

Figure 5.23: Arnás catchment characteristics.

Numerical simulations of the Arnás catchment was carried out in [50] by means of a 2D diffusion wave model for the surface flow and both the Horton and Green-Ampt models for water losses due to infiltration. In [18], a combination of the

2D SWE with SCS-Curve Number model for the precipitation losses was used for rainfall/runoff simulation in this catchment. In both cases, the numerical results showed a poor agreement with the observed data.

In this watershed, the catchment topography meshing has been widely studied in [18], where the authors found the optimal mesh for solving the SW equations in order to minimize the computational time without losing quality in the numerical results. All the simulated events for this catchment use this optimal mesh (see Figure 5.23(c)).

Two events (which are referred to as Event 2 and 3) are simulated and compared with the observed data. In both cases, discharge measurements were taken at the outlet (see Figure 5.23(a)) with a frecuency of 5 minutes. On the other hand, rainfall intensity was registered by a rain gauge with a 5 minute frequency for the Event 2 and 60 minutes for the Event 3. Figure 5.24 shows the observed hyetographs and outlet hydrographs for both storm events.

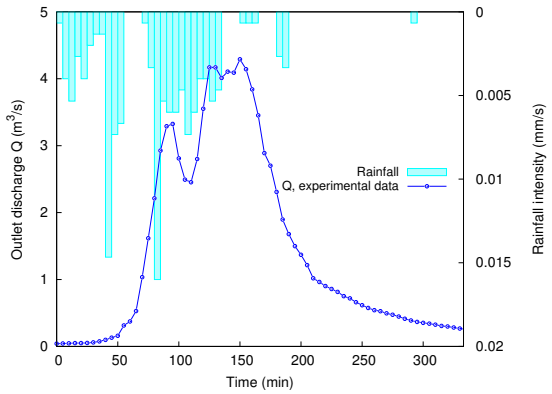

(a) Storm Event 2: Outlet discharge.

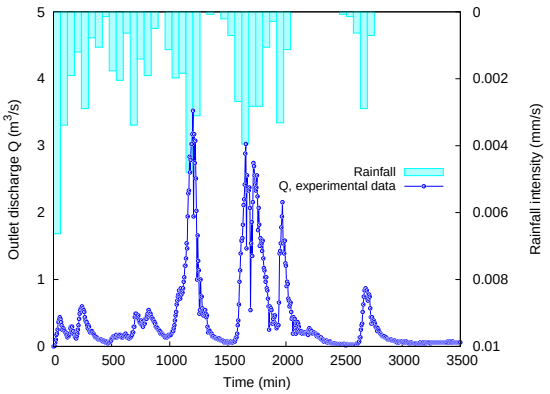

(b) Storm Event 3: Outlet discharge.

Figure 5.24: Observed hyetographs and hydrographs for Arnás basin.

As in the Araguás basin in the previous section, an explicit 2D SW numerical scheme ($\theta = 0$) is used for all the simulations of the Arnás catchment in order to capture more precisely the transient situations of the surface flow and, thence, predict more accurately the infiltration losses. As an illustrative example, Figure 5.25 shows the spatial distribution of the water depth and cumulative infiltration on the whole catchment at three different times for the Event 3. This points out the relevance of using a distributed model for surface flow and infiltration computation, since there are significant differences ($\sim 300\%$ in cumulative infiltration) among catchment re-

gions. Figures 5.26 to 5.29 show the numerical results. Table 5.7 summarizes the infiltration parameters for the two events and both Horton and Green-Ampt models. An overall good agreement between numerical and experimental results is observed for both models. Both reproduce correctly the outflow volume which has been taken as the most relevant property of the catchment's response. In the case of Horton model results, the shape and peak value of the experimental hydrograph are also achieved with a certain delay in time. This is not so noticeable in the Green-Ampt results, but the peak value is not correctly reproduced in this case. Hence, despite the mostly good numerical results, some adjustments seem still to be necessary.

Event	Model	Parameter 1	Parameter 2	Parameter 3
2	Horton	$k = 0.0001s^{-1}$	$f_c = 2.6 \cdot 10^{-6}m/s$	$f_0 = 3.3 \cdot 10^{-6}m/s$
2	Green-Ampt	$K = 8.0 \cdot 10^{-7}m/s$	$\Psi = 0.01m$	$\Delta\theta = 3.5$
3	Horton	$k = 0.0007s^{-1}$	$f_c = 2.0 \cdot 10^{-6}m/s$	$f_0 = 3.5 \cdot 10^{-5}m/s$
3	Green-Ampt	$K = 1.4 \cdot 10^{-6}m/s$	$\Psi = 0.025m$	$\Delta\theta = 2.0$

Table 5.7: Infiltration parameter set.

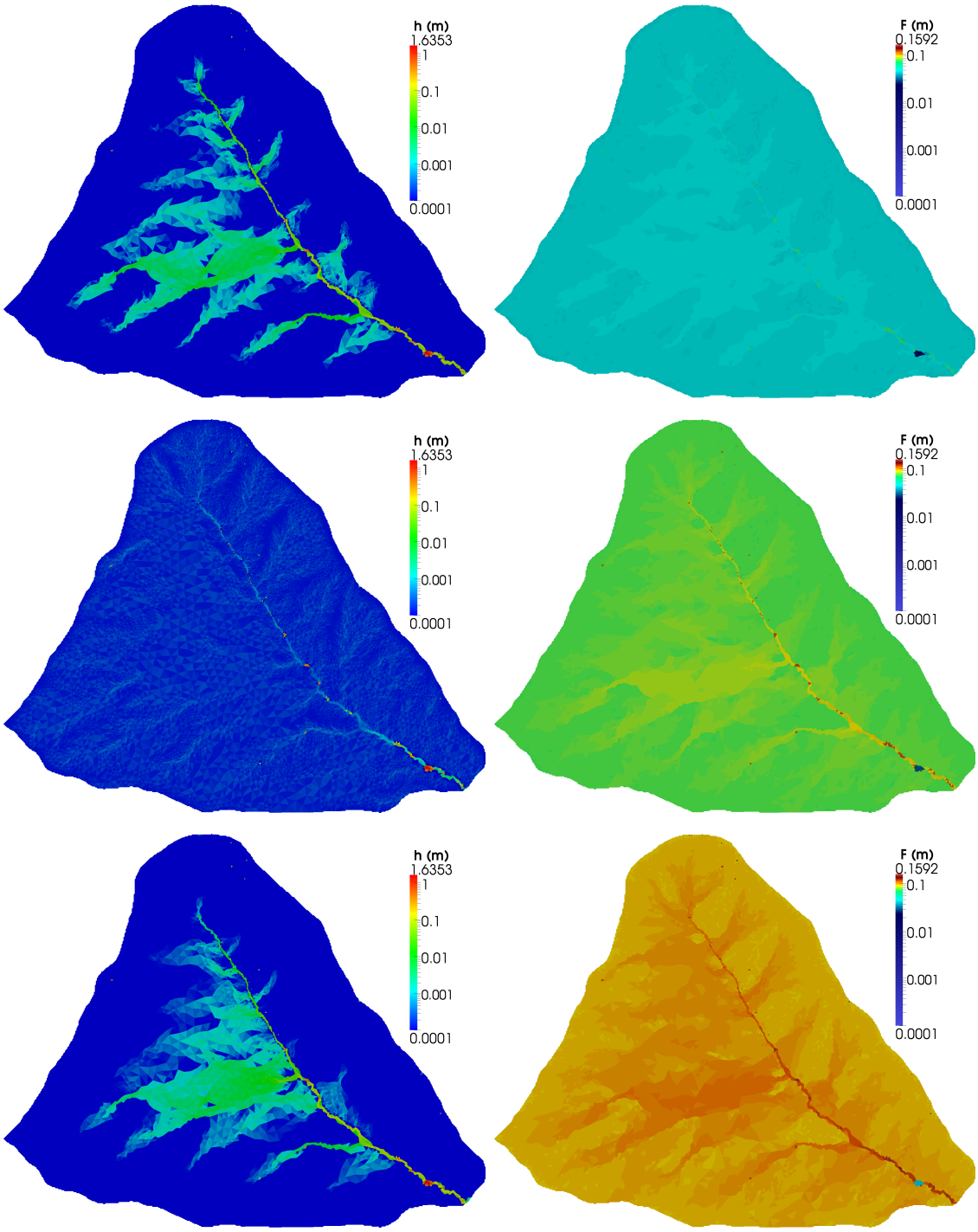

Figure 5.25: Spatial distribution at catchment level of water depth (left) and cumulative infiltration (right) for the Event 3 at $t = 12000s$, $t = 36000s$ and $t = 50000s$.

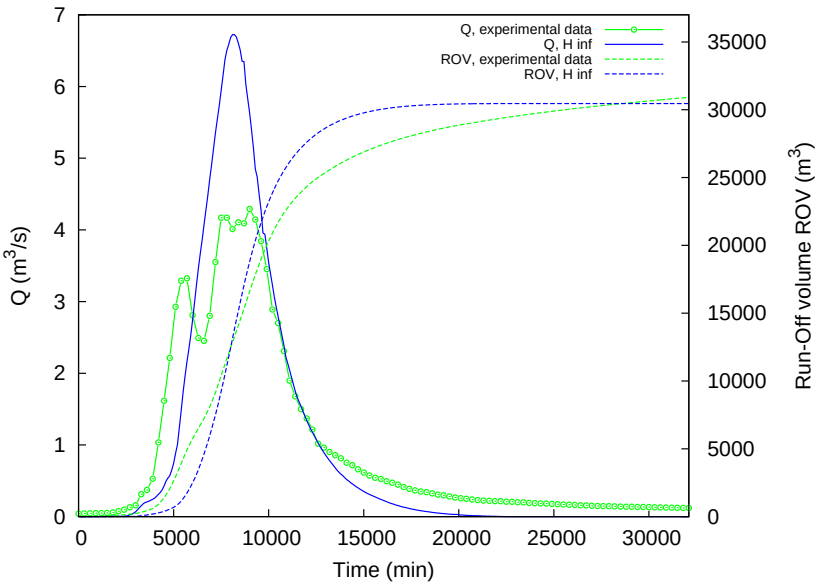

Figure 5.26: Numerical vs. experimental data. Horton infiltration model. Storm event 2.

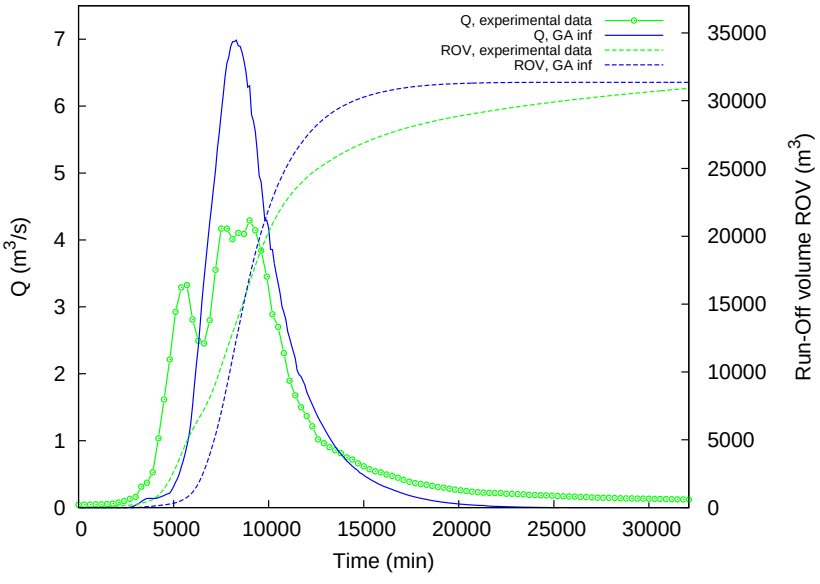

Figure 5.27: Numerical vs. experimental data. Green-Ampt infiltration model. Storm event 2.

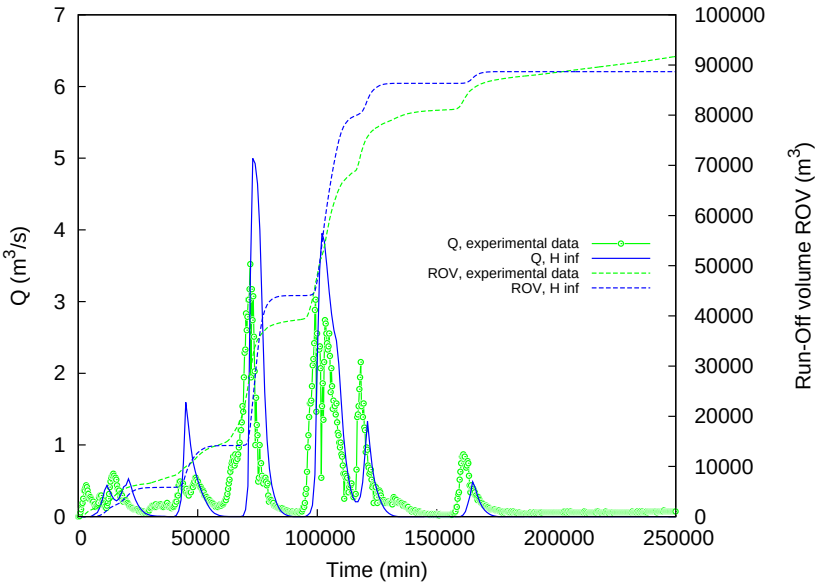

Figure 5.28: Numerical vs. experimental data. Horton infiltration model. Storm event 3.

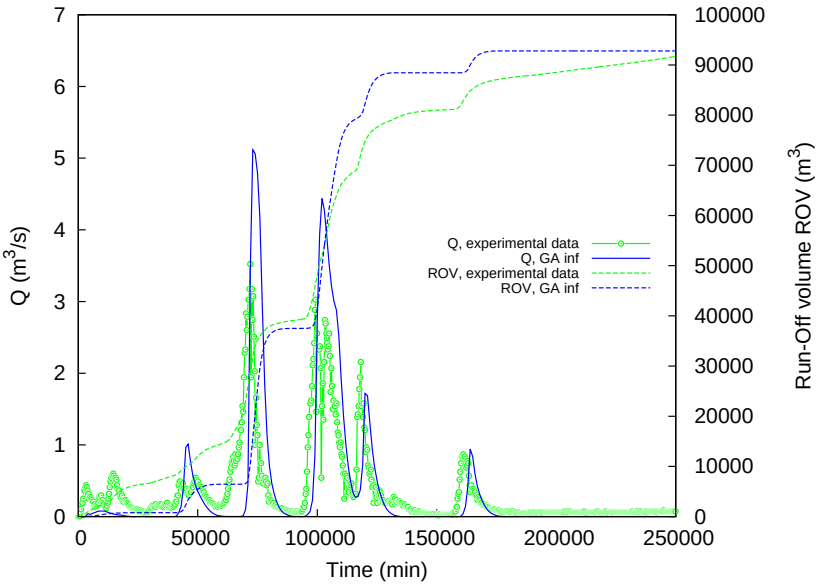

Figure 5.29: Numerical vs. experimental data. Green-Ampt infiltration model. Storm event 3.

Infiltration mapping

The Arnás river catchment has enough soil and vegetation heterogeneity to consider the development of a mapping with several regions with different infiltration parameters. In order to try to improve the agreement between numerical and experimental results and achieve a better experimental fitting, an infiltration map based on the catchment soil types has been designed (see Figure 5.30). Three different regions are considered. The parameters used in the previous section are taken as starting point. This mapping allows to consider several regions infiltrating at different rates, which can be determining if the catchment has clearly different soil types, as in the considered case. Tables 5.8 and 5.9 show the best maps achieved and the infiltration parameters corresponding to each region. Figures 5.31 to 5.34 show the numerical results. A considerable improvement in the shape of the outlet hydrographs is reached by the use of infiltration mapping, specially for the earlier time of the storm. Furthermore, the delay of the peak discharge in Horton model is partially corrected. Green-Ampt model also takes benefit from the infiltration mapping, specially in the storm event 3, in which the first discharge peaks are significantly better reproduced than when a single infiltration zone is used.

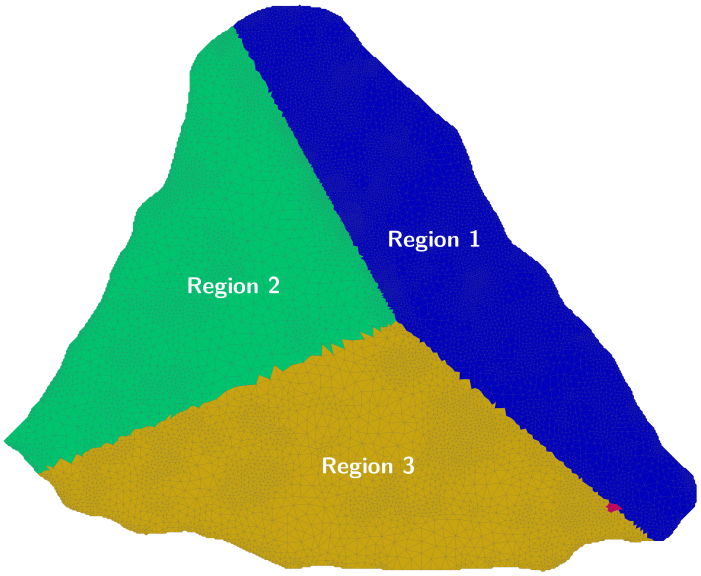

Figure 5.30: Infiltration map based on the soil types.

Area	Model	Parameter 1	Parameter 2	Parameter 3
Map H01 Region 1	H	$k = 0.0001s^{-1}$	$f_c = 1.0 \cdot 10^{-6} m/s$	$f_0 = 3.3 \cdot 10^{-6} m/s$
Map H01 Region 2	H	$k = 0.0001s^{-1}$	$f_c = 4.7 \cdot 10^{-4} m/s$	$f_0 = 5.9 \cdot 10^{-4} m/s$
Map H01 Region 3	H	$k = 0.0001s^{-1}$	$f_c = 1.0 \cdot 10^{-6} m/s$	$f_0 = 1.9 \cdot 10^{-6} m/s$
Map GA01 Region 1	GA	$K = 3.0 \cdot 10^{-7} m/s$	$\Psi = 0.01m$	$\Delta\theta = 3.5$
Map GA01 Region 2	GA	$K = 1.0 \cdot 10^{-6} m/s$	$\Psi = 0.06m$	$\Delta\theta = 3.5$
Map GA01 Region 3	GA	$K = 7.0 \cdot 10^{-7} m/s$	$\Psi = 0.01m$	$\Delta\theta = 3.5$

Table 5.8: Infiltration parameters re-fitting with infiltration map for Event 2.

Area	Model	Parameter 1	Parameter 2	Parameter 3
Map H01 Region 1	H	$k = 0.0007s^{-1}$	$f_c = 2.0 \cdot 10^{-6} m/s$	$f_0 = 3.5 \cdot 10^{-5} m/s$
Map H01 Region 2	H	$k = 0.0007s^{-1}$	$f_c = 2.0 \cdot 10^{-6} m/s$	$f_0 = 3.5 \cdot 10^{-5} m/s$
Map H01 Region 3	H	$k = 0.0007s^{-1}$	$f_c = 2.0 \cdot 10^{-6} m/s$	$f_0 = 2.5 \cdot 10^{-5} m/s$
Map GA01 Region 1	GA	$K = 1.8 \cdot 10^{-6} m/s$	$\Psi = 0.025m$	$\Delta\theta = 2.0$
Map GA01 Region 2	GA	$K = 1.8 \cdot 10^{-6} m/s$	$\Psi = 0.025m$	$\Delta\theta = 2.0$
Map GA01 Region 3	GA	$K = 1.0 \cdot 10^{-6} m/s$	$\Psi = 0.025m$	$\Delta\theta = 2.0$

Table 5.9: Infiltration parameters re-fitting with infiltration map for Event 3.

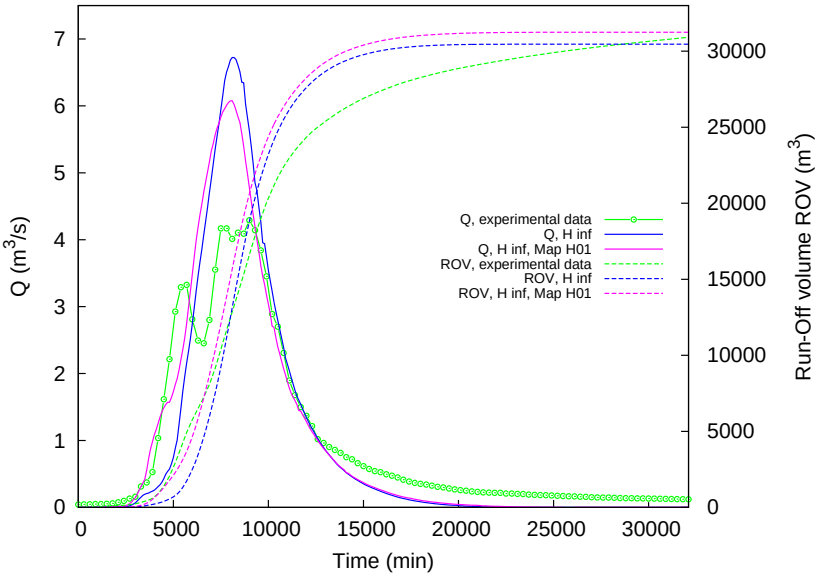

Figure 5.31: Event 2 parameter re-fitting with infiltration map. Horton infiltration model.

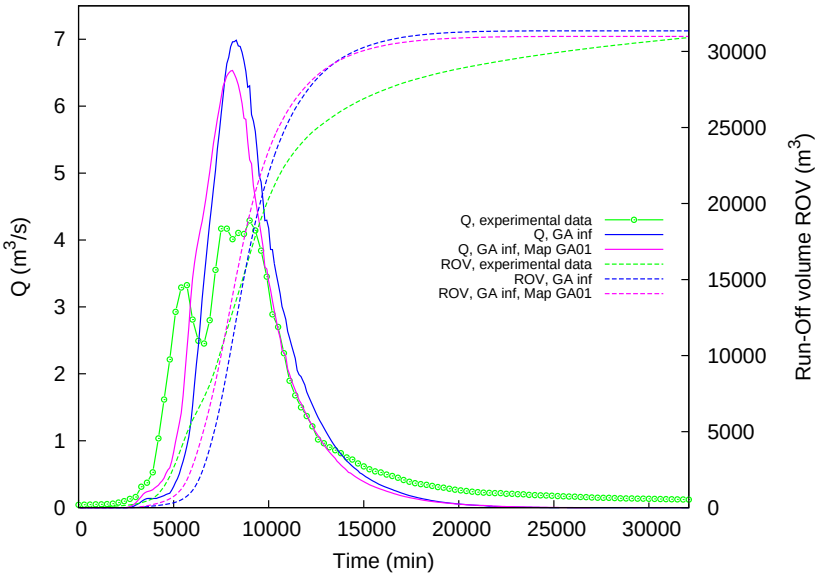

Figure 5.32: Event 2 parameter re-fitting with infiltration map. Green-Ampt infiltration model.

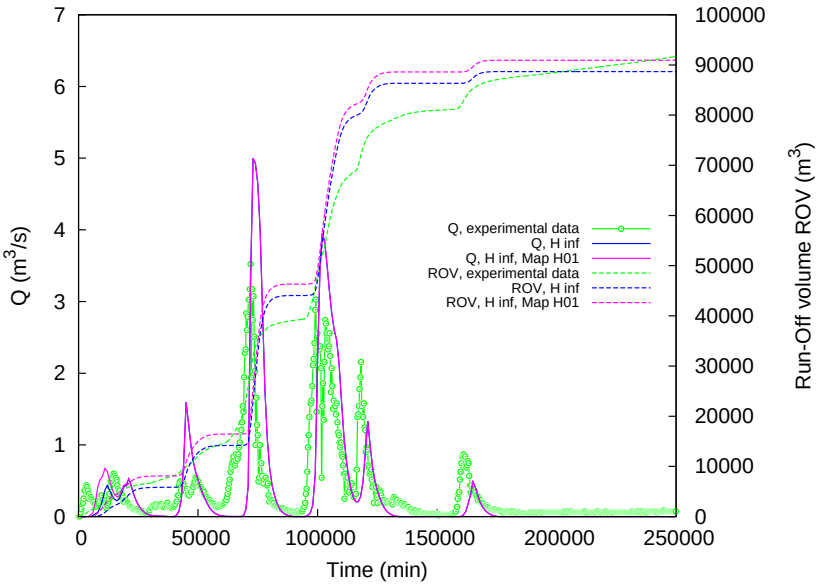

Figure 5.33: Event 3 parameter re-fitting with infiltration map. Horton infiltration model.

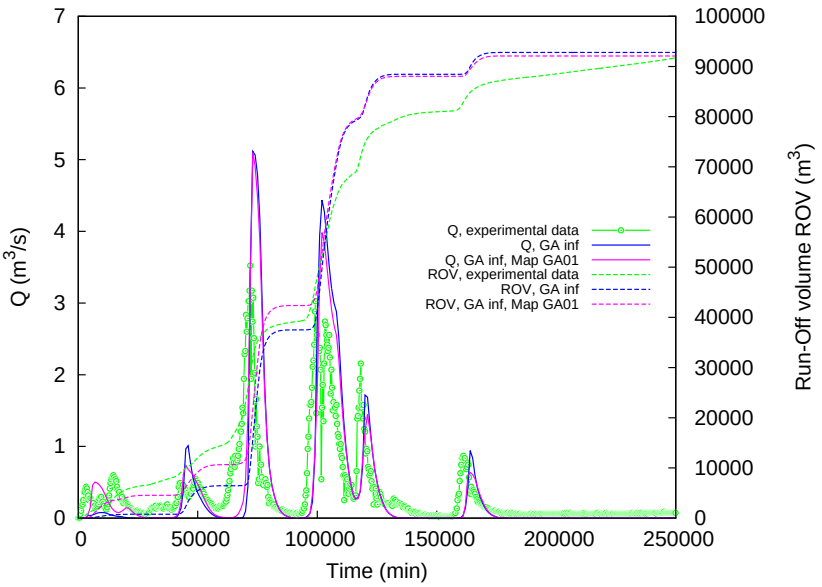

Figure 5.34: Event 3 parameter re-fitting with infiltration map. Green-Ampt infiltration model.

Improvement by means of the FOGA model

The calibrations obtained for Events 2 and 3 using the FOGA are presented in this section. Tables 5.10 and 5.11 summarize the parameters for all the considered events in this catchment using the classical GA model and the FOGA infiltration model based on a variable $\alpha(F, h)$. The hydrograph fittings are shown in Figures 5.35 and 5.36 for Events 2 and 3, respectively. In both cases, significant improvements over the classical GA model are observed. Hydrograph rising limbs show a better adjustment to the observed data in both events. Tables 5.10 and 5.11 also presents the L_1^{error} values for both GA and FOGA model and the relative difference $\%_{dif}$ between the error produced by both models. In this catchment, the FOGA model fitting errors are 16.7% lower than the one produced by the GA model for Event 2 and 25.8% lower for Event 3. The error values obtained for these events (together with the one obtained for the Event 1) quantify the improvement in the hydrograoh fitting by the FOGA model. As in the previous section, spatial distributions of h, F and $\alpha(F, h)$ are presented in Figure 5.37 for Event 2 at $t = 15000s$.

Inf. model	$K_\alpha(m^\alpha/s)$	$\Psi(m)$	$\Delta\theta(m^3/m^3)$	$a(m^{-1})$	$b(m^{-1})$	α_{min}	L_1^{error}	$\%_{dif}$
GA	$1.26 \cdot 10^{-6}$	0.01	3.5	-	-	-	0.447	-
FOGA	$1.8 \cdot 10^{-6}$	0.01	3.5	53	90	0.5	0.371	-16.7%

Table 5.10: Event 2: Infiltration parameters for the Arnás catchment ($\alpha(h, F)$).

Inf. model	$K_\alpha(m^\alpha/s)$	$\Psi(m)$	$\Delta\theta(m^3/m^3)$	$a(m^{-1})$	$b(m^{-1})$	α_{min}	L_1^{error}	$\%_{dif}$
GA	$1.6 \cdot 10^{-6}$	0.025	2.0	-	-	-	0.361	-
FOGA	$2.37 \cdot 10^{-6}$	0.025	2.0	70	150	0.5	0.268	-25.8%

Table 5.11: Event 3: Infiltration parameters for the Arnás catchment ($\alpha(h, F)$).

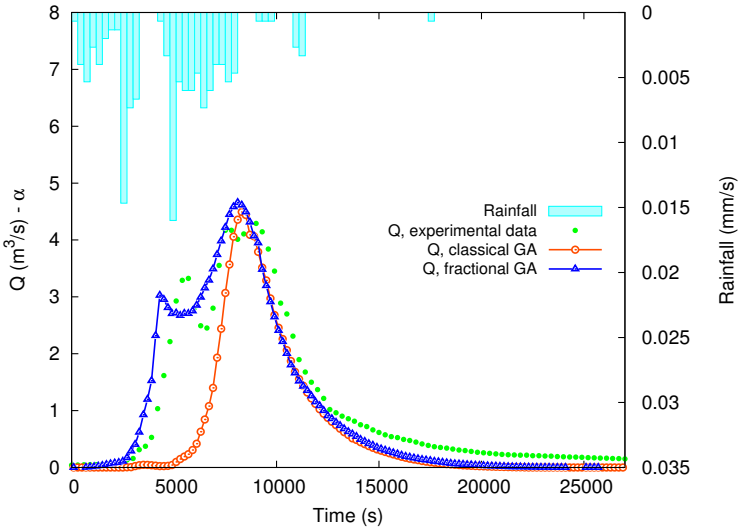

Figure 5.35: Hydrograph fitting for Event 2 ($\alpha(h, F)$).

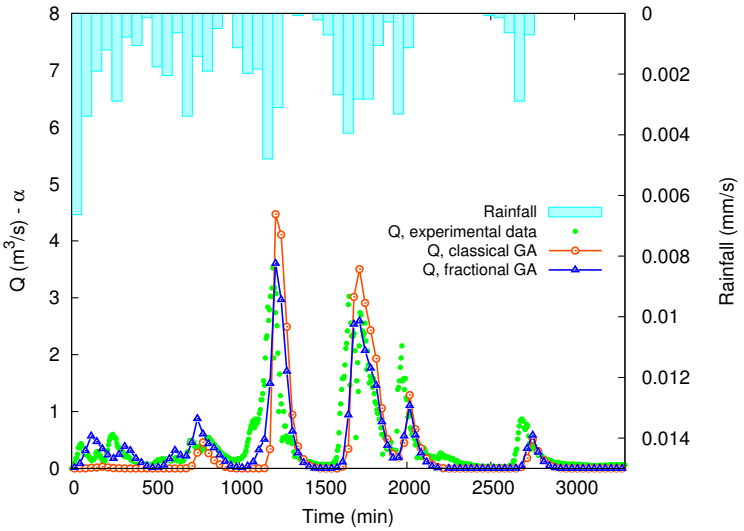

Figure 5.36: Hydrograph fitting for Event 3 ($\alpha(h, F)$).

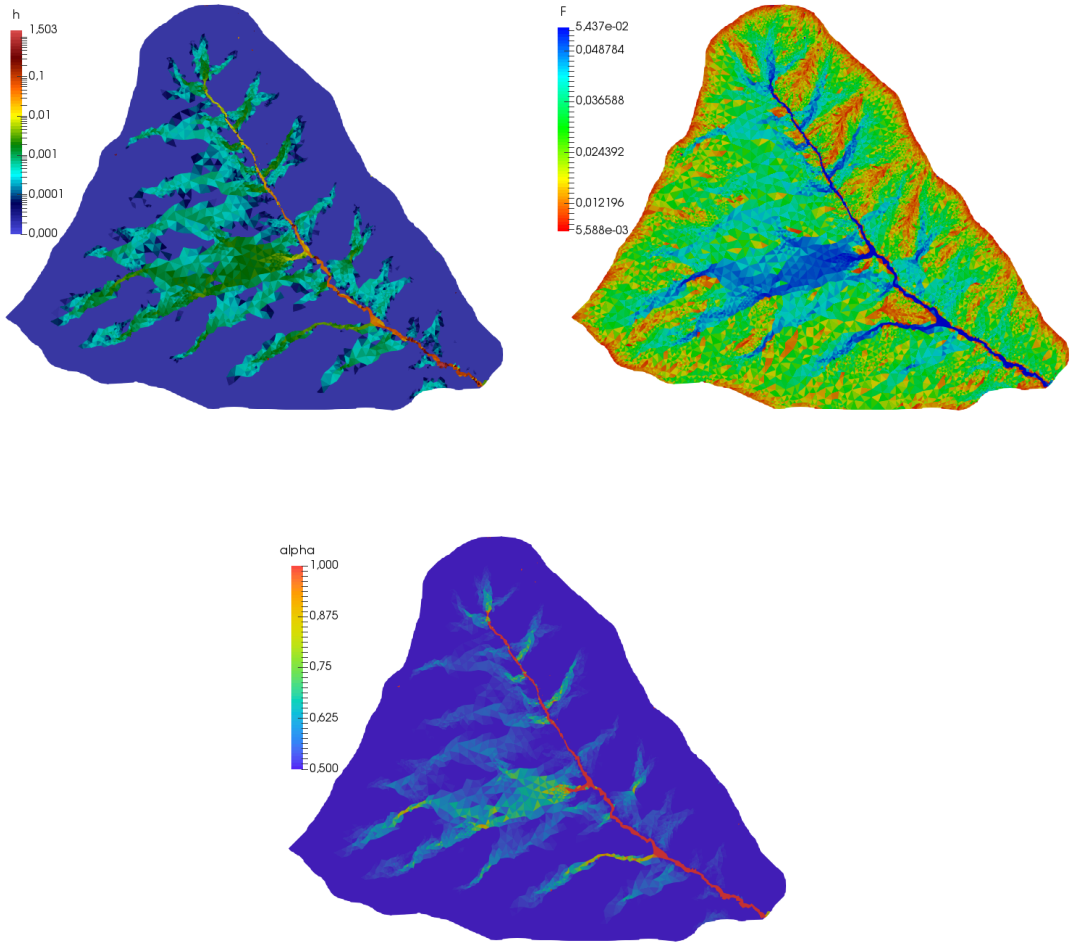

Figure 5.37: Water depth h, cumulative infiltration F and $\alpha(F, h)$ for Event 2 in Arnás catchment at $t = 15000s$.

5.3 Simulation of an oil spill

This section presents the simulation of a real oil pipe leakage that took place in Marshall (Michigan, USA). Figure 5.38 shows the topography of the considered domain (left) and the computational triangular mesh (right). The leak is considered punctual and it occurred in three phases, with the same peak discharge but different temporal distribution (see Figure 5.39). The available data por the crude oil is the density ($\rho = 900.3 Kg/m^3$) and the viscosity ($\mu = 0.0249 Pa\,s$), both at a temperature of $293K$. The oil infiltration is taken into account by means of the Green-Ampt model with the next parameter values: $K = 2.1 \cdot 10^{-8} m/s$, $\Psi = 0.02m$ and $\Delta\theta = 0.2$.

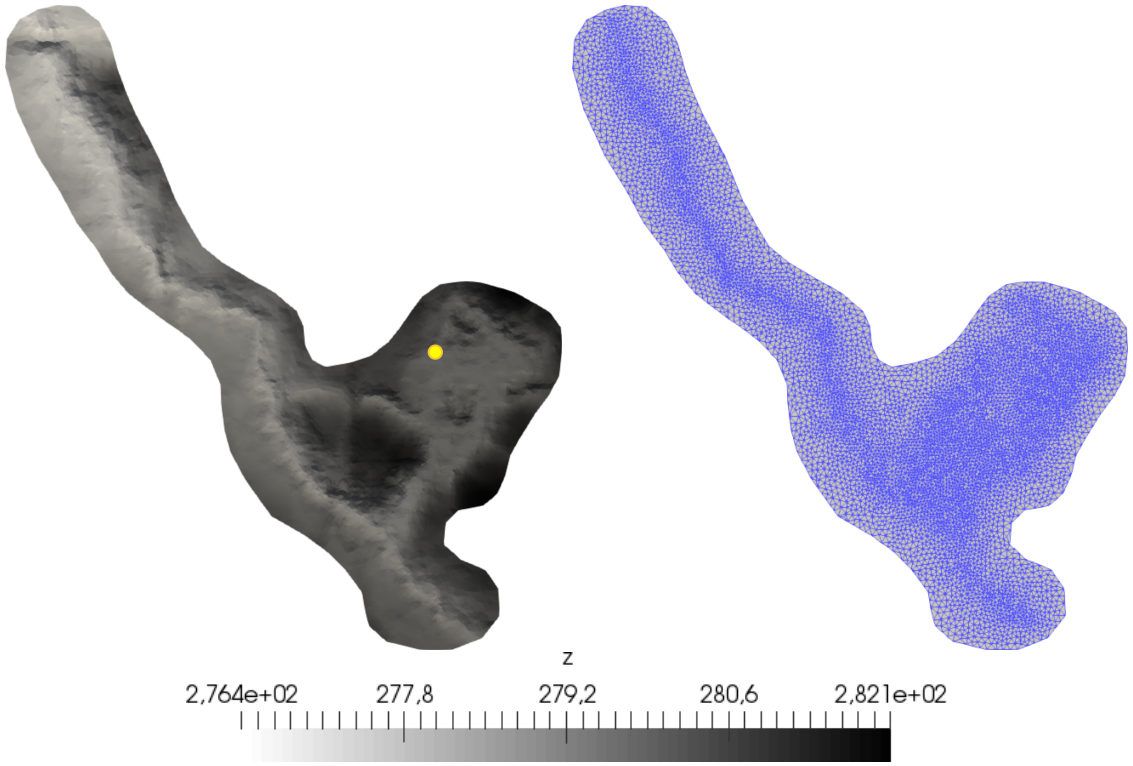

Figure 5.38: Elevation map and rupture point (left) and computational mesh (right) for the oil spill case.

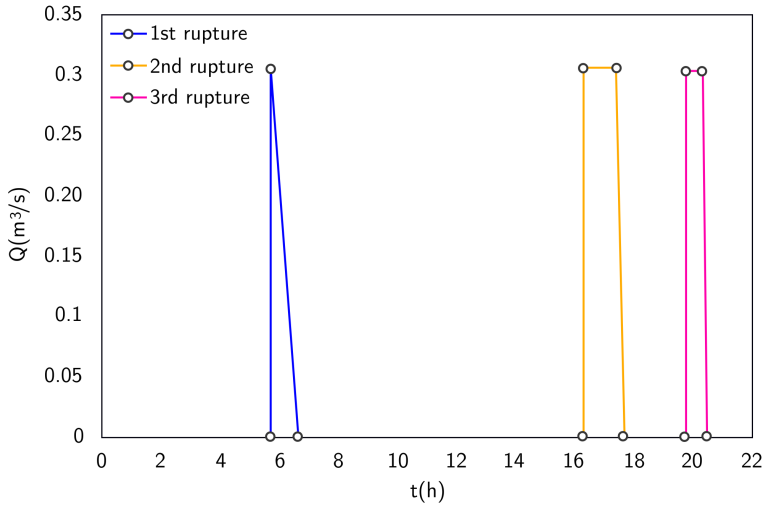

Figure 5.39: Temporal distribution of the oil spill discharge.

Figure 5.40 shows the temporal evolution of the extension of the spill and the oil depth values at $t = 6h$, $t = 9h$, $t = 12h$, $t = 18h$, $t = 24h$ and $t = 30h$. The comparison between numerical and observed oil extensions at $t = 30h$ is also shown (pink line). In the light of the results, the model predicts accurately the final oil extension with a relative difference lower than 5% between numerical and observed spill region area.

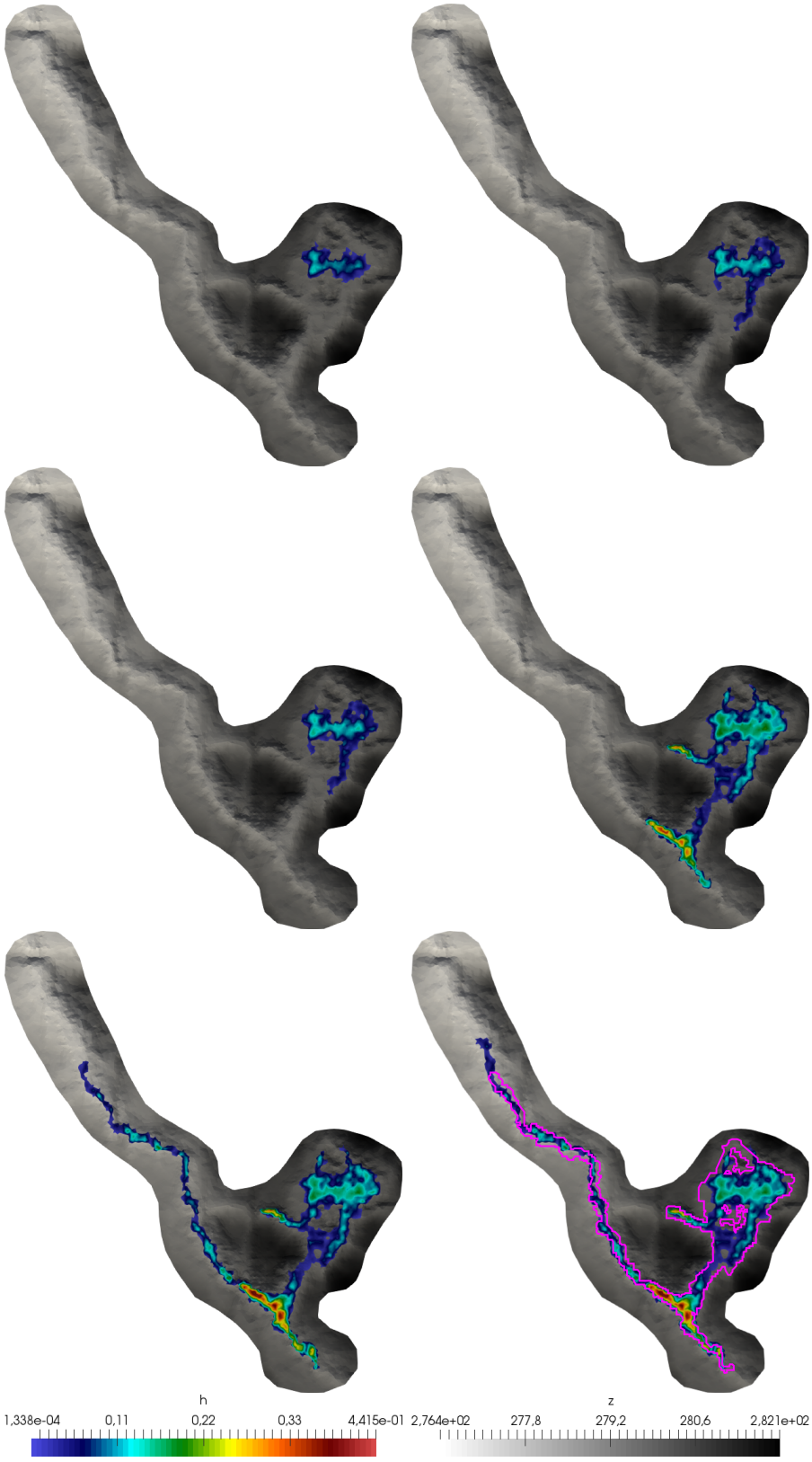

Figure 5.40: Extension of the spill and oil depth at $t = 6h$, $t = 9h$, $t = 12h$, $t = 18h$, $t = 24h$ and $t = 30h$. Observed oil extension at $t = 30h$ is also shown (pink).

5.4 Overland and groundwater coupled flows

5.4.1 Synthetic test cases

Case 0: Still water

The purpose of this case is to check if the C-property is fulfilled when both surface and groundwater flow models are interacting. A $260\,m \times 260\,m$ domain with closed walls is considered. The initial surface water level $h + z$ and phreatic level h_s take a constant value of $5\,m$ in every part of the domain (see Figure 5.41). The initial water discharge is also set to zero. Figure 5.42 shows the initial state (left) and the numerical results after $3600\,s$ of simulation. As expected, both surface water and phreatic level conserve the initial values and the water discharge remains null.

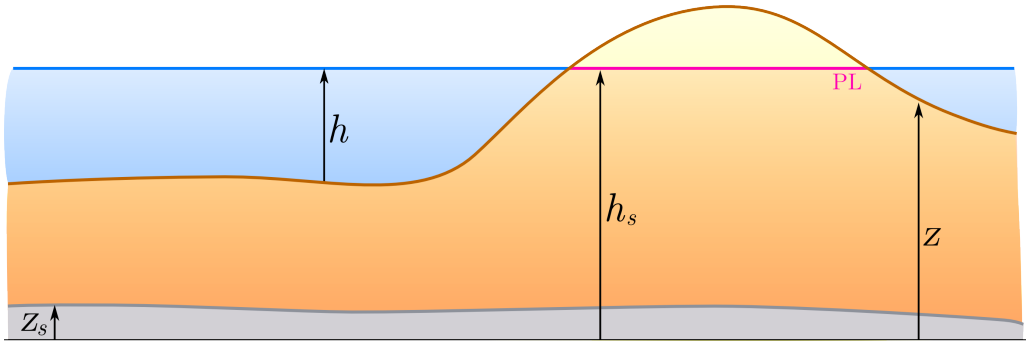

Figure 5.41: Sketch of Case 0.

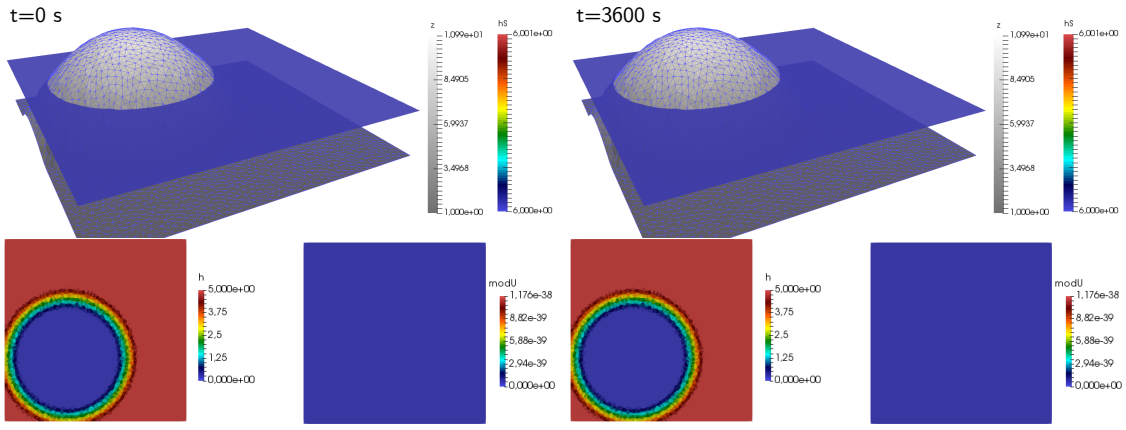

Figure 5.42: Numerical results for Case 0 at $t = 0\,s$ (left) and $t = 3600\,s$ (right).

Case 1: Infiltration+exfiltration

Assuming the same domain as in Case 0, a gradual raising of the surface water level is imposed at the inlet boundary (see Figures 5.43 and 5.44). The rest of the boundaries remain closed. Figures 5.45 to 5.50 show the initial conditions and the numerical results for surface water depth and phreatic level at several times. The results show a smooth evolution of the phreatic surface as the surface water level changes, keeping the continuity between both level during the whole simulation.

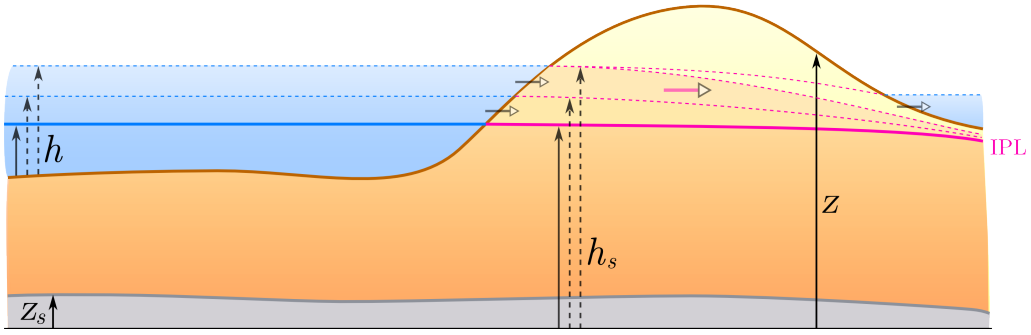

Figure 5.43: Sketch of Case 1.

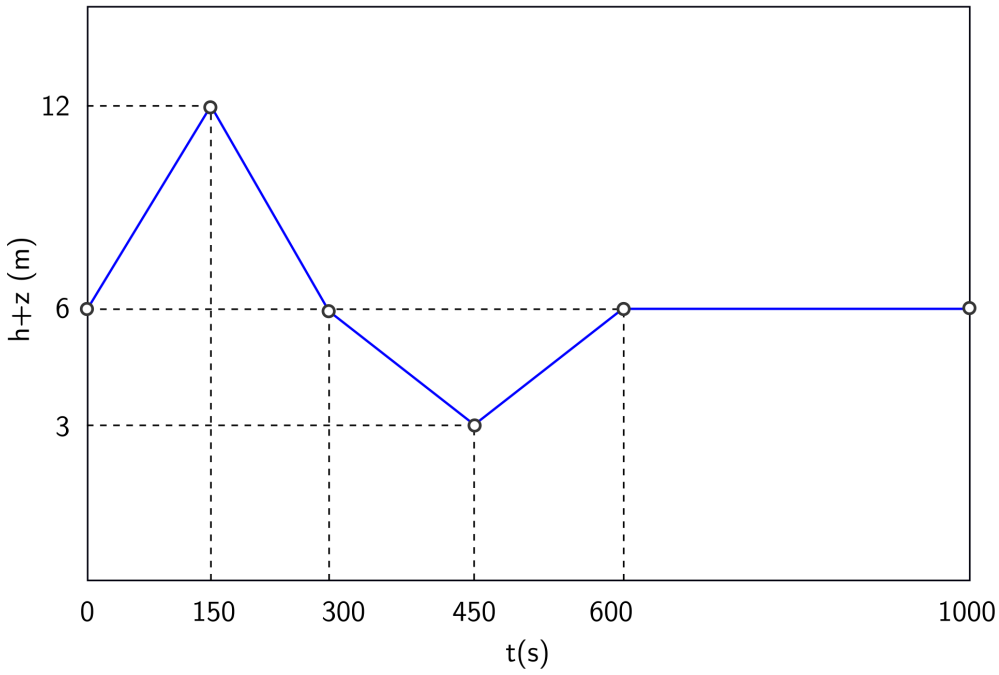

Figure 5.44: Inlet limnigraph for Case 1.

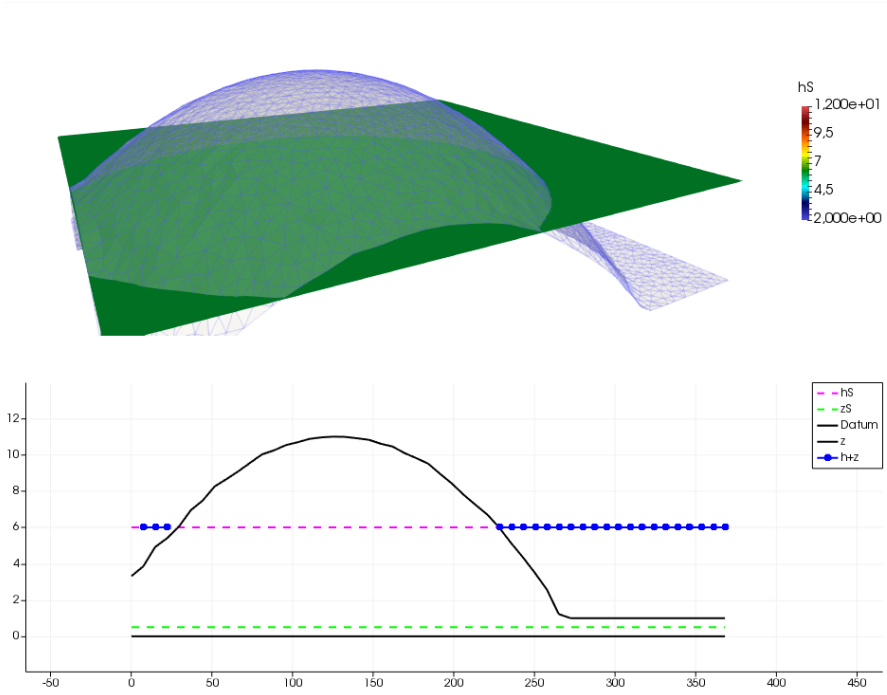

Figure 5.45: Case 1: Initial conditions.

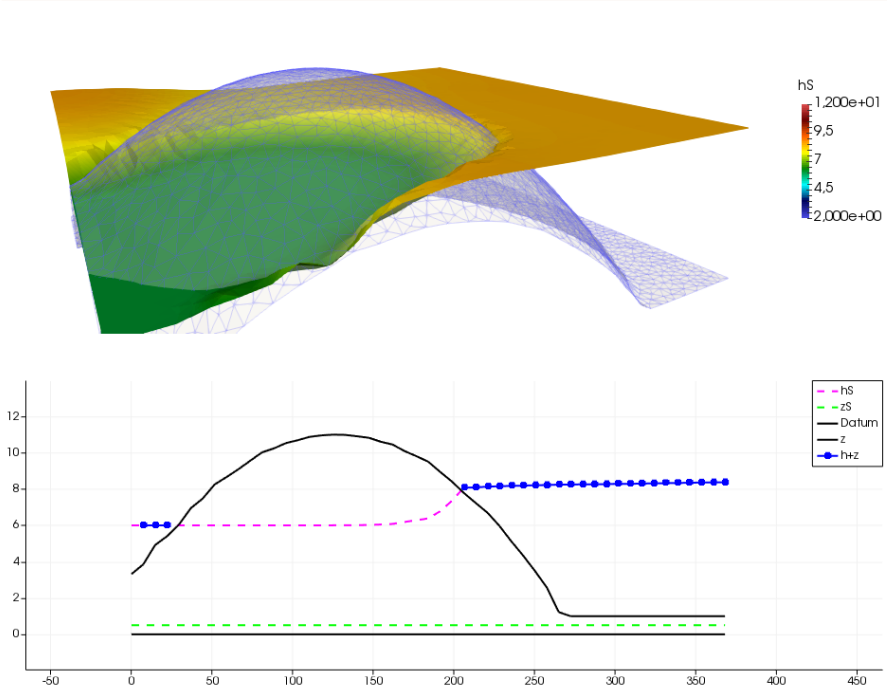

Figure 5.46: Case 1: Numerical results at $t = 60s$.

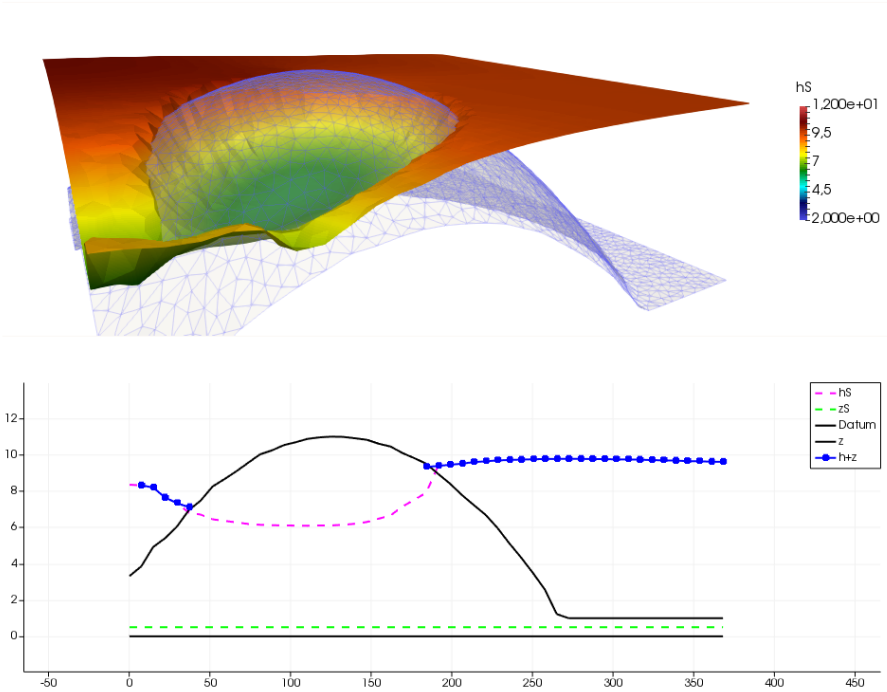

Figure 5.47: Case 1: Numerical results at $t = 90s$.

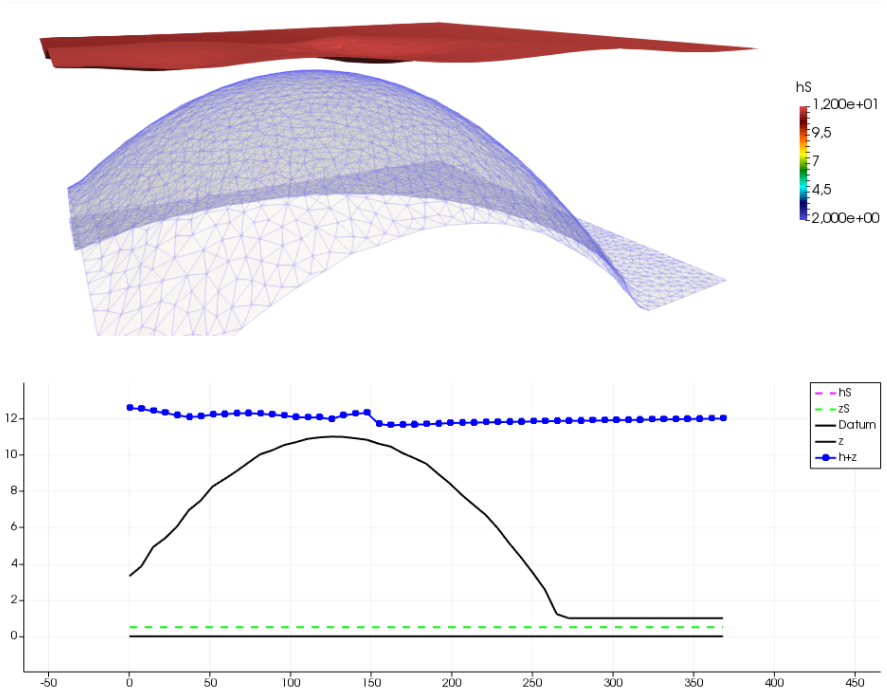

Figure 5.48: Case 1: Numerical results at $t = 150s$.

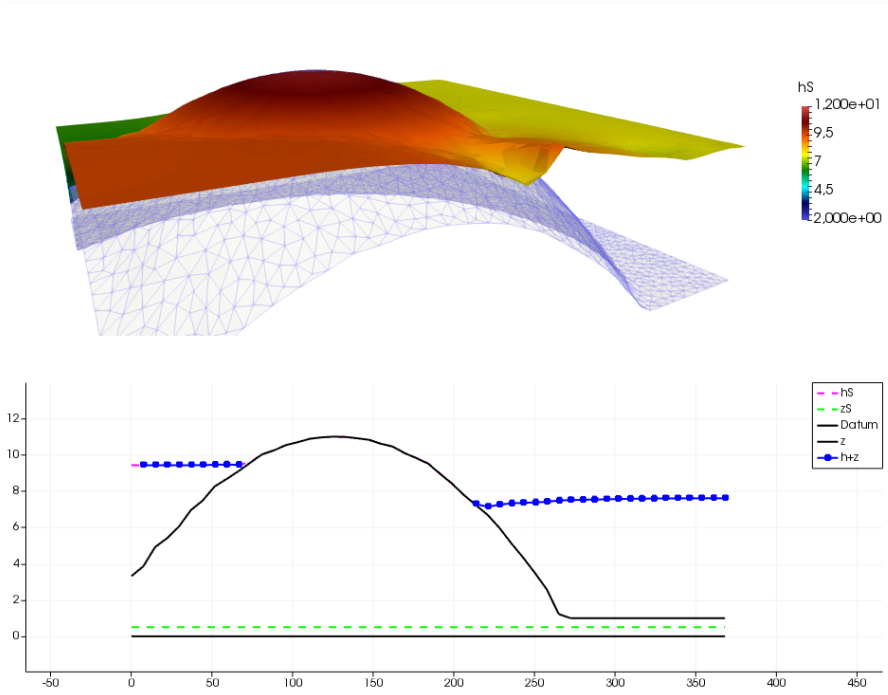

Figure 5.49: Case 1: Numerical results at $t = 260s$.

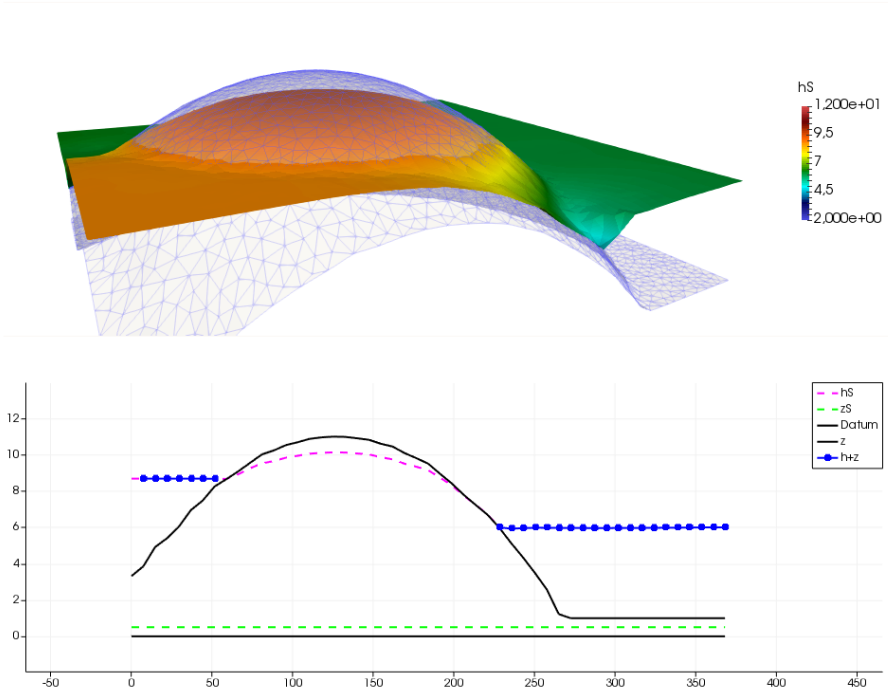

Figure 5.50: Case 1: Numerical results at $t = 300s$.

Case 2: Interaction with impervious zone

The existence of subsurface impervious regions is a common situation when dealing with real world problems. Hence, it is valuable to test the coupled model in this kind of situations. Figure 5.51 shows the case sketch. As in Case 1, a varying limnigraph is imposed at the inlet (Figure 5.52). Figures 5.53 and 5.54 show the initial conditions and the numerical results at $t = 600s$ when the phreatic surface reaches the impervious zone. The model behaves adequately, respecting the impervious zone, where any kind of groundwater flow should appear.

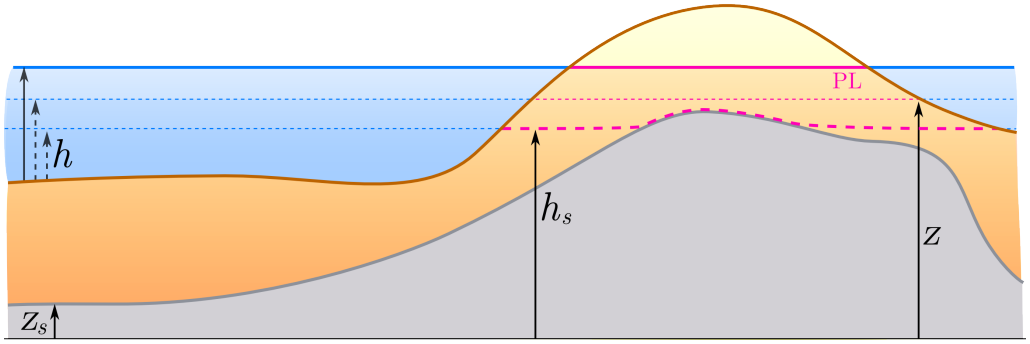

Figure 5.51: Sketch of Case 2.

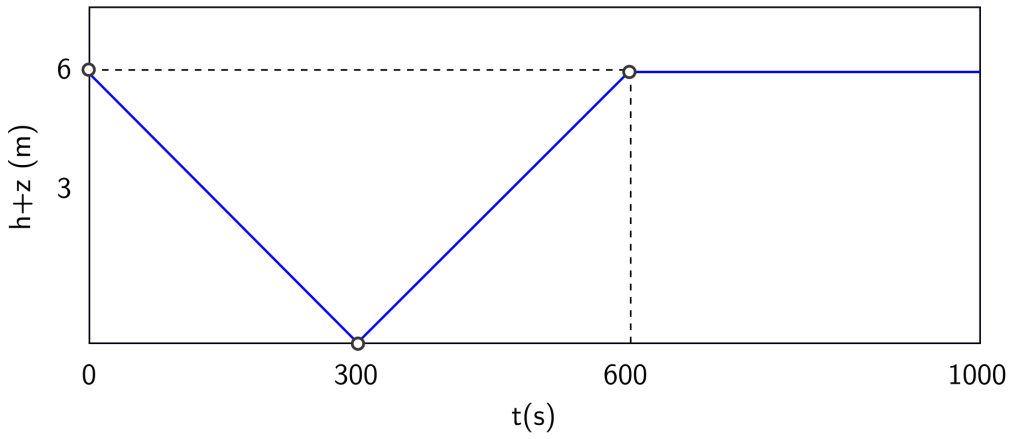

Figure 5.52: Inlet limnigraph for Case 2.

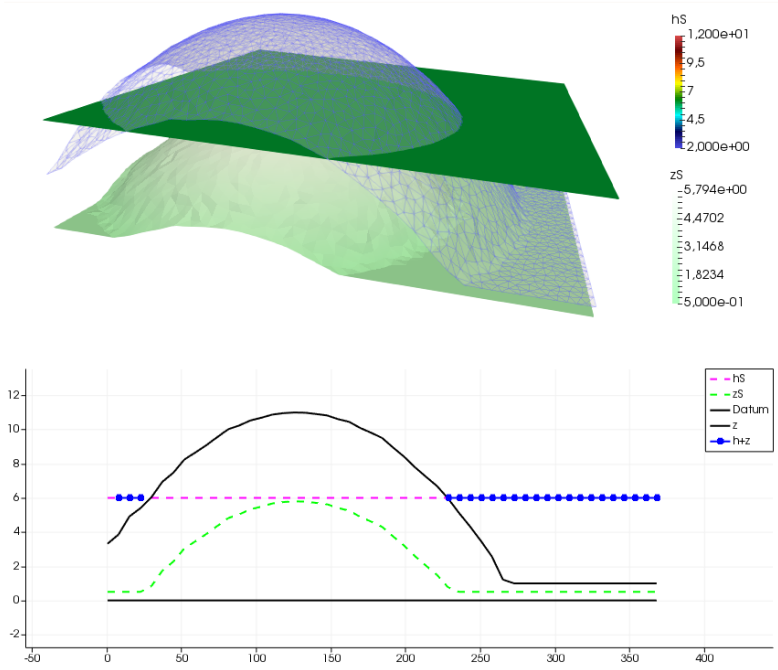

Figure 5.53: Case 2: Initial conditions.

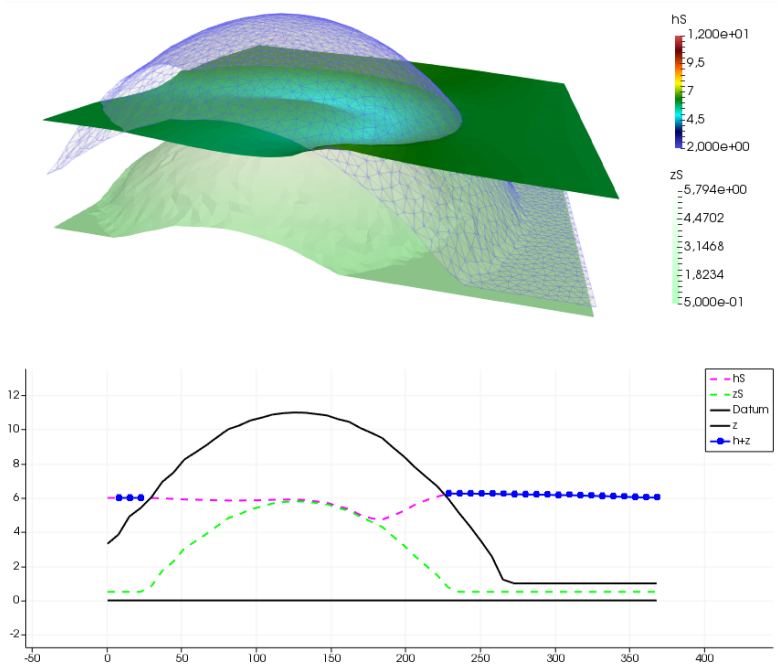

Figure 5.54: Case 2: Numerical results at $t = 600s$.

Case 3: Rainfall+soil infiltration+exfiltration

The purpose for this case is to evaluate the capacity of the coupled model to exfiltrate water which has been previously infiltrated upstream (Figure 5.55). A local unsteady storm is considered in the headwaters of an irregular domain (Figure 5.56). A rainfall intensity of $5mm/s$ is set for $t < 1500s$ and $3000s < t < 5500s$. Figure 5.57 shows the initial conditions for this case, as well as an sketch of the hyetograph together with the current position in time. Figures 5.58 and 5.59 show the numerical results at $t = 1000s$ and $t = 5750s$, respectively.

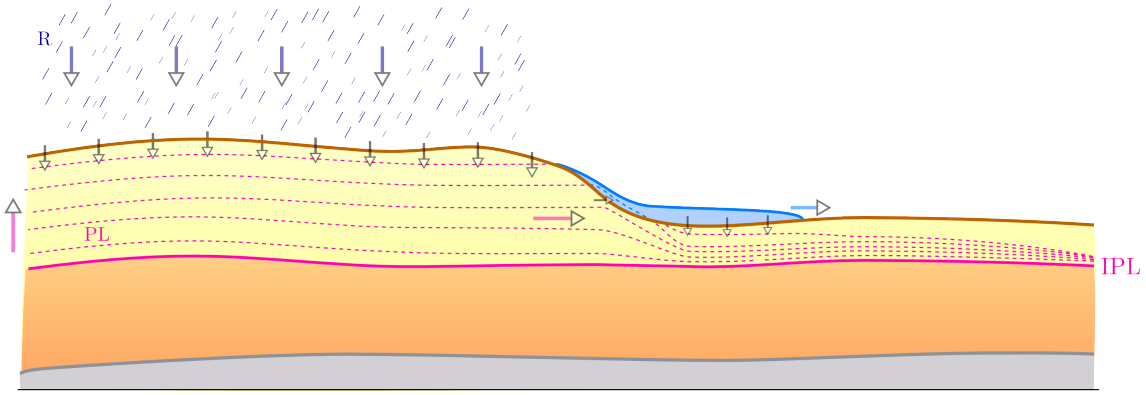

Figure 5.55: Sketch of Case 3.

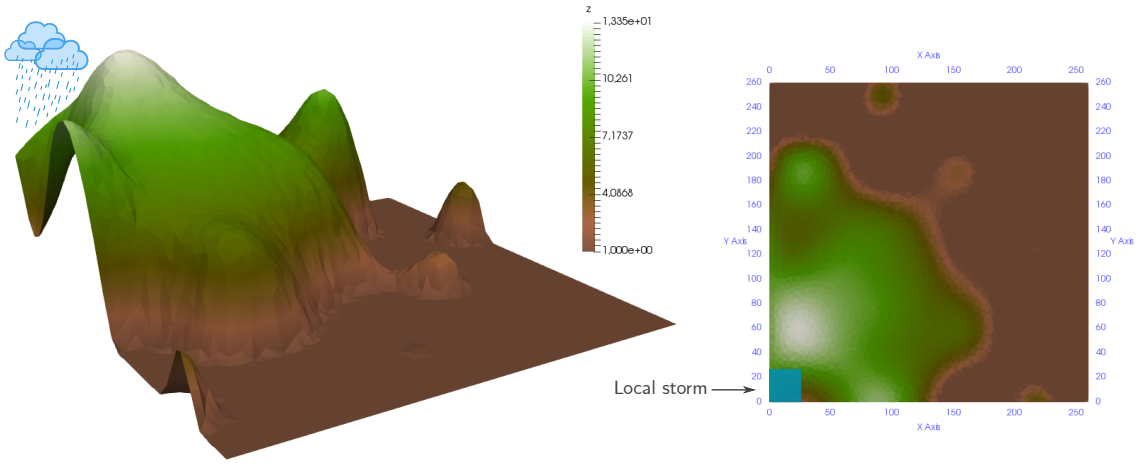

Figure 5.56: Setup of Case 3.

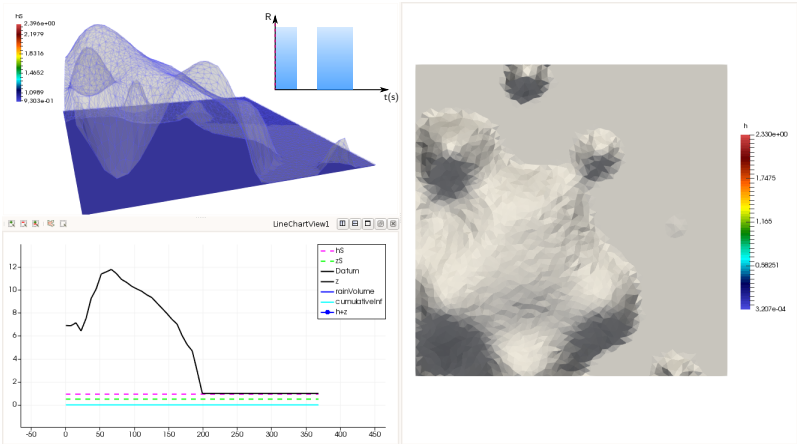

Figure 5.57: Case 3: Initial conditions.

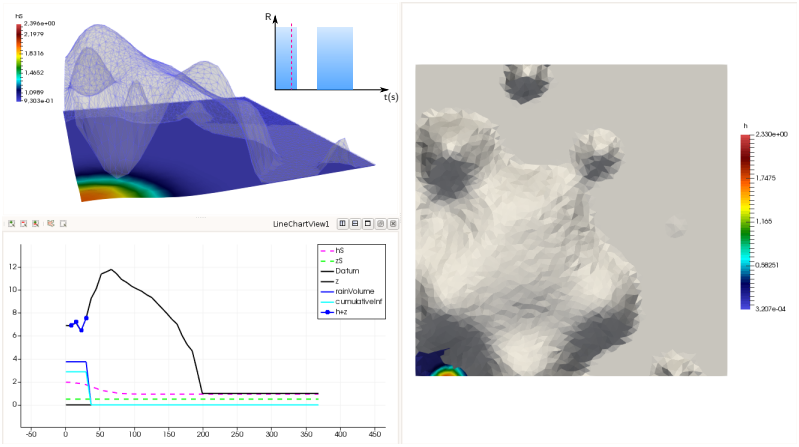

Figure 5.58: Case 3: Numerical results at $t = 1000s$.

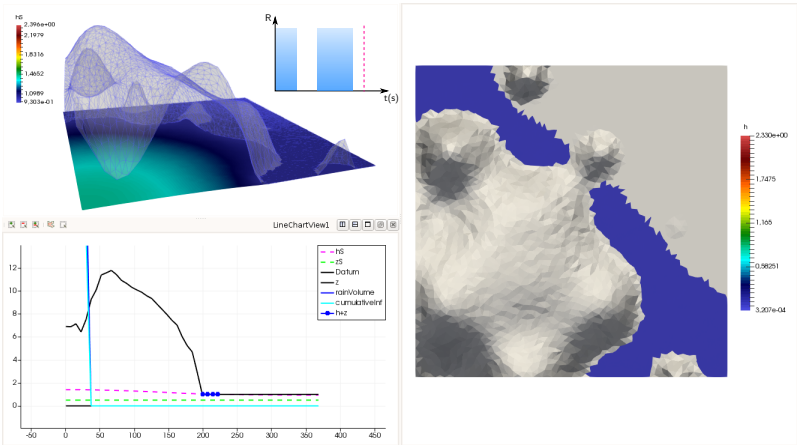

Figure 5.59: Case 3: Numerical results at $t = 5750s$.

5.4.2 Application to real catchment

In this section, the coupled overlan-groundwater flow model is applied to the Arnás basin, described in Section 5.2.3. In this case, a progressive raising of the phreatic level is simulated in two different point of the basin boundary. The purpose is to check the capacity of the coupled model to route this change through the subsurface and generate a streamflow response due to exfiltration in the main channel of the catchment. Figure 5.60 shows the inicial and boundary conditions and the phreatic level evolution at several simulation times. It can be seen an smooth progression and joining of both groundwater fronts. Figure 5.61 shows the temporal evolution of the surface water depth. Exfiltration begins at $t = 4750s$. In order to illustrate more clearly the exfiltration phenomenon, a cross-section view of the catchment soil is presented in Figure 5.62 for the same simulation times as before. The exfiltration starts when the phreatic level reachs the bed level position in the main channel.

It is also interesting to develop a performance analysis in term of the computational cost with several time step values for the groundwater flow model. Table 5.12 and Figure 5.63 shows, for several choices of the groundwater flow model time step, the CPU time and the speed-up factor, being N_{sup} the number of surface model time steps for one single subsurface model time step. The maximum and average errors relative to a simulation performed with $N_{sup} = 1$ are also shown. In the light of this anaysis, acceptable simulations with average errors below 2% can be reached using subsurface time steps 25 times larger than the surface flow model. With this choice, a speed-up value of 8 is reached. As the implicit numerical scheme does not restrict the time step size and the groundwater flow is expected to be much slower than the overland flow, it is shown that larger time steps provide faster simulations.

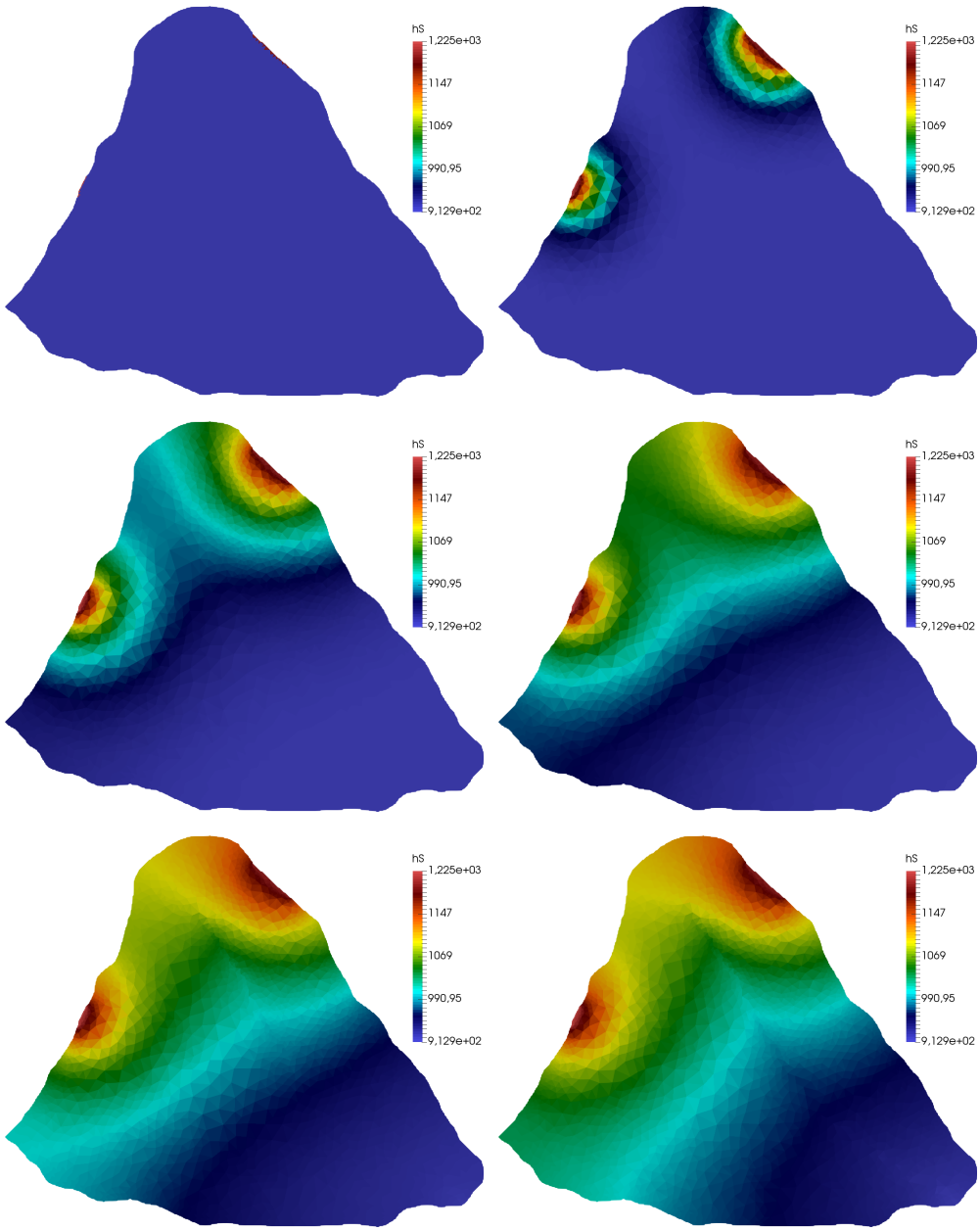

Figure 5.60: Subsurface phreatic level position h_s at $t = 0$, $t = 500s$, $t = 2500s$, $t = 4750s$, $t = 7500s$ and $t = 10000s$.

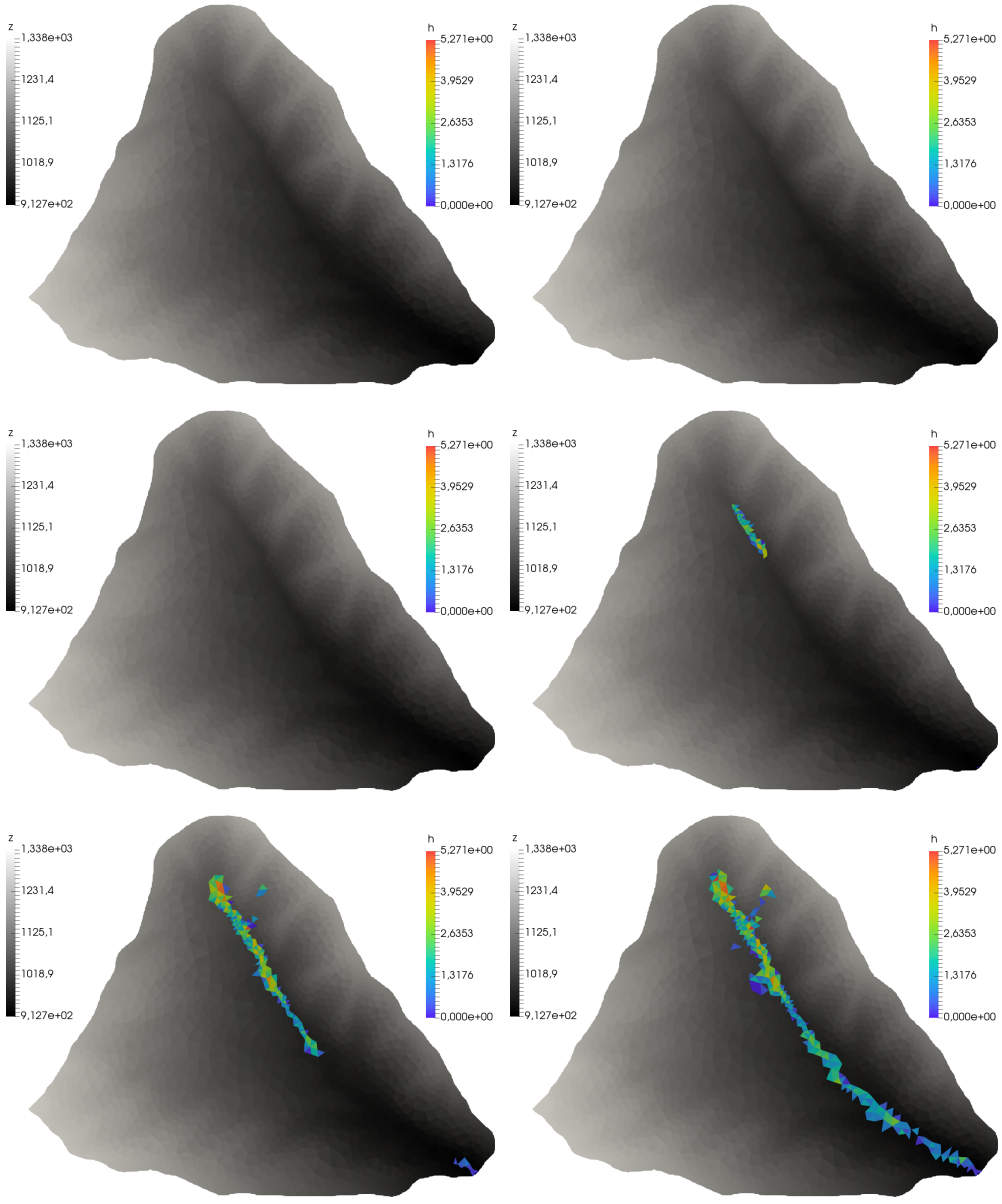

Figure 5.61: Surface water depth h at $t = 0$, $t = 500s$, $t = 2500s$, $t = 4750s$, $t = 7500s$ and $t = 10000s$.

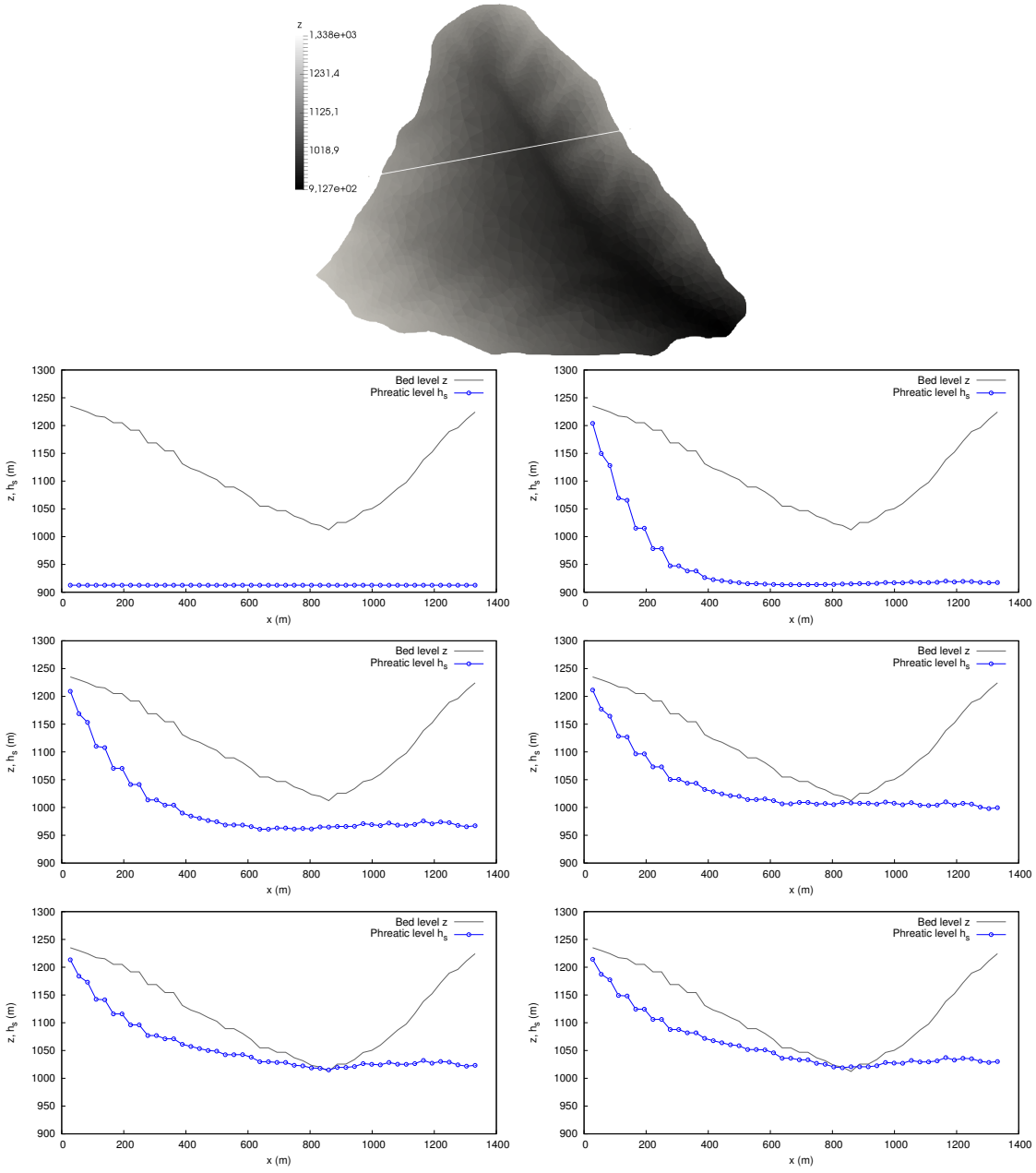

Figure 5.62: Cross-section of the subsurface phreatic level position h_s at $t = 0$, $t = 500s$, $t = 2500s$, $t = 4750s$, $t = 7500s$ and $t = 10000s$.

N_{sup}	CPU time	Speed-up	Maximum error (%)	Average error (%)
1	125	1	0	0
2	71.5	1.7	0.29	0.01
3	49.7	2.5	0.43	0.02
10	22.15	5.6	0.82	0.08
17	19.6	6.4	0.97	0.14
25	15.6	8.0	1.22	0.18

Table 5.12: CPU time, speed-up and maximum and average errors.

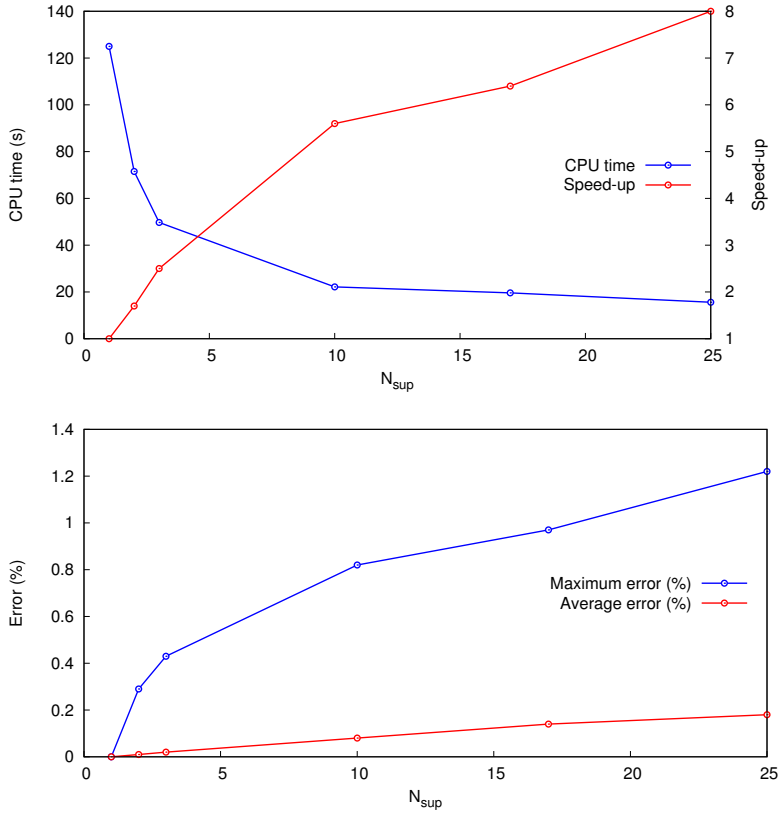

Figure 5.63: CPU time and speed-up values (left). Maximum and average error values all along the spatial domain at final simulation time ($t = 10000s$) (right).

5.5 Overland and drainage system coupled flows

5.5.1 Single sewer/surface flow exchange

This test case was originally presented in [80] where a full range of sewer-to-surface and surface-to-sewer flow conditions at the exchange zone are experimentally analysed and, hence, a complete set of observed data is provided. The experimental facility consists of a physical model of a sewer pipe with no slope connected via a manhole to a shallow flow flume (Figure 5.64). The sewer pipe has an internal width of $b = 75mm$. The flume bed has a slope if $S_0^{1D} = 0.001$ and is aligned with the top of the manhole and is 4 m wide and 8 m long. The bed of the flume is $H = 0.478m$ above the invert level of the pipe. All the facility components (pipe and flume) are constructed from PVC, so the Manning's roughness coefficient is set to $n_{1D} = 0.009$. This facility allows shallow flow over the surface which interacts with the sewer flow via the manhole. The boundary condition consists of a surface inlet discharge $Q_{sup} = 11l/s$ and a sewer inlet discharge Q_{sewer}, which varies depending on the case. The domain is assumed to be dry as initial condition.

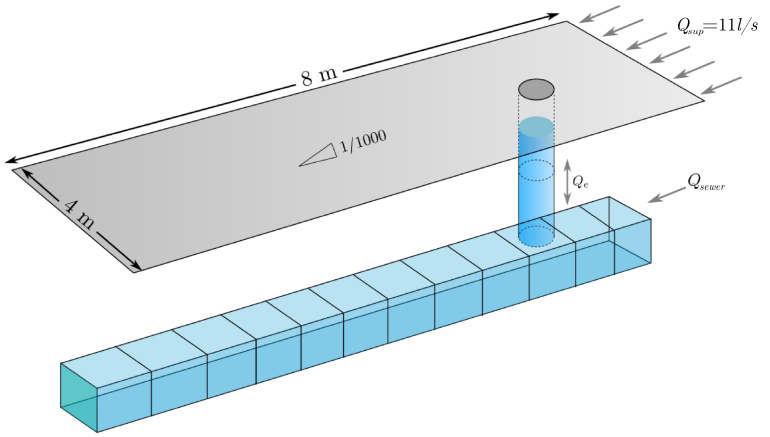

Figure 5.64: Scheme of the laboratory case setup.

Two different cases are considered in this work. They cover all the possible scenarios depicted in Figure 3.30. Case 1 is configured by setting zero discharge at the inlet of the sewer, leading to an inflow from the surface to the sewer during all the case duration. Figure 5.65 (left) shows the comparison between numerical and experimental surface water depth for several values of Q_e, showing a very good overall agreement is observed. The chosen values of Q_e correspond to those in which

data were available [80]. The relative difference between numerical and experimental data is plotted in 5.65 (right), where a maximum error of 5% is observed. The experimental data is measured $460mm$ before the the center of the manhole for the surface water depth and $350mm$ for the pipe pressure head.

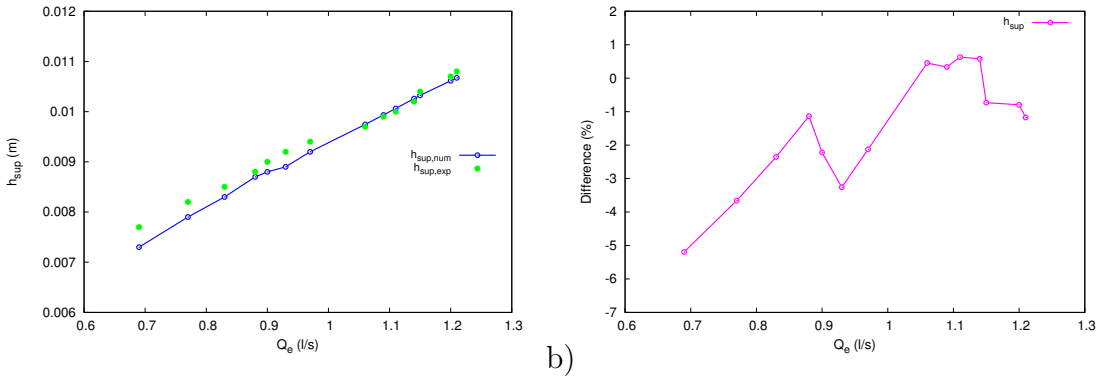

a) b)

Figure 5.65: Case 1.1. Comparison between numerical and experimental data (a) and relative difference (%) (b) for the surface water depth.

For Case 2, $Q_{sewer} = 9.6l/s$ is set at the sewer inlet in order to ease the conduit pressurization. At the beginning of the simulation, water flows from the surface to the sewer (inflow) but, as the pipe pressure increases, the situation reverses (outflow), as shown in the profile view of the numerical results in Figure 5.66. At $t = 30s$, the surface to sewer situation occurs leading to a depression in the surface water level at the manhole position (red line). The conduit is filled progressively and becomes pressurized in a transition situation denoted with a green line in Figure 5.66. When the pressure head in the sewer is enough, the exchange flow discharge changes sign and the water overloads the pipe and arises to the surface (blue line). Figure 5.67 shows the comparison between numerical and experimental data for the surface water depth (left) and pressure head in the sewer (right). The relative differences for both magnitudes are shown in Figure 5.67 (lower) with a maximum of 15% for the surface water depth and 5% for the pressure head. A distributed visualization of the 2D numerical results at three different times is shown in Figure 5.68 with the water depth displayed in grayscale and the velocity vector field in color scale. The transition between inflow and outflow situations is clearly shown.

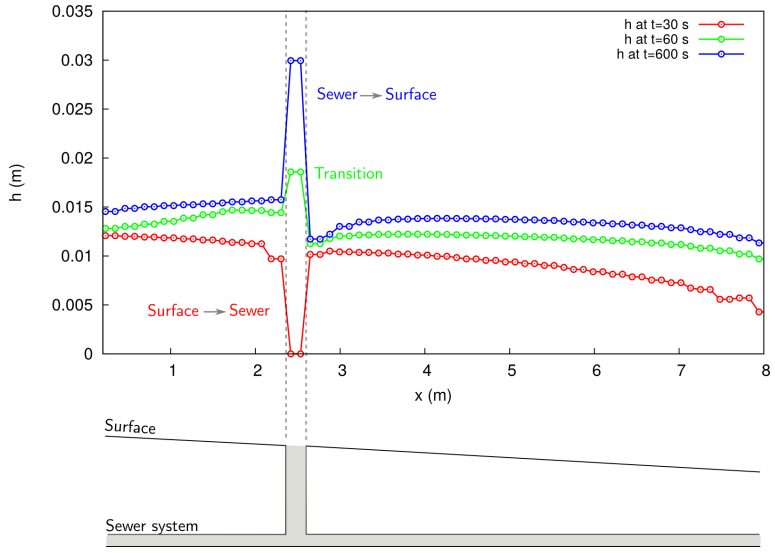

Figure 5.66: Profile view of the numerical results corresponding to 3 different times. Note the sign change of the exchange flow.

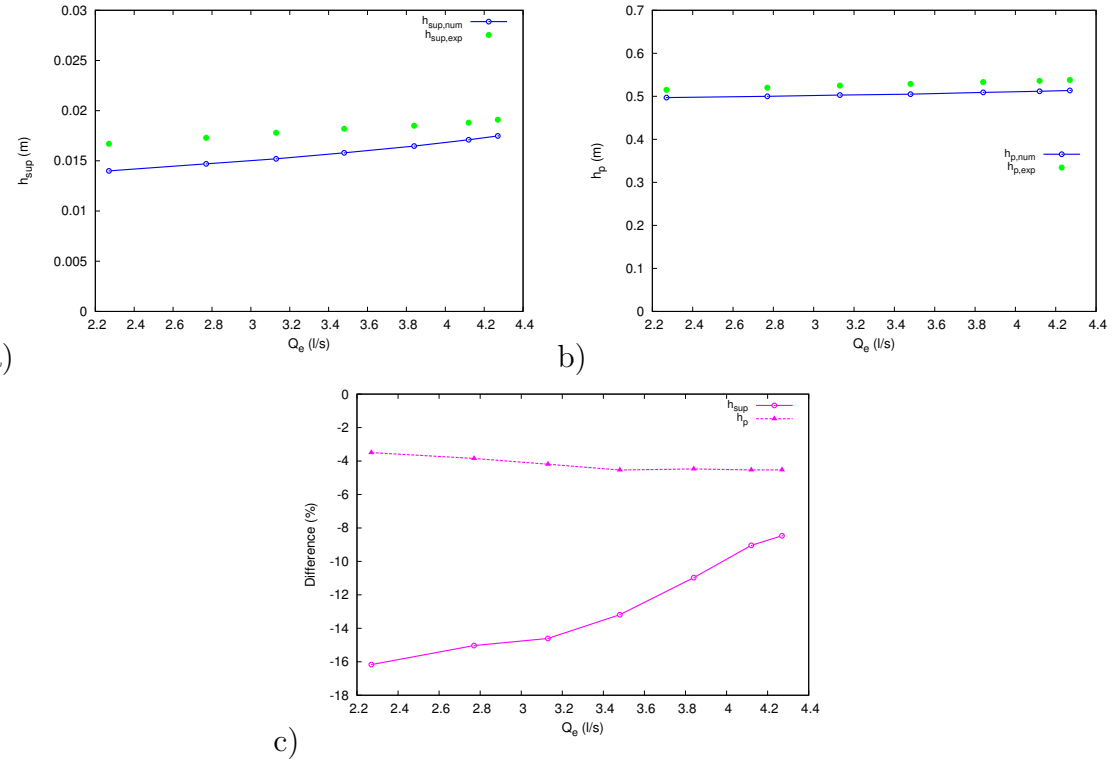

Figure 5.67: Case 1.2. Comparison between numerical and experimental data for the surface water depth (a) and pressure head (b). Relative difference (%) between numerical and experimental data for the surface water depth and pressure head (c).

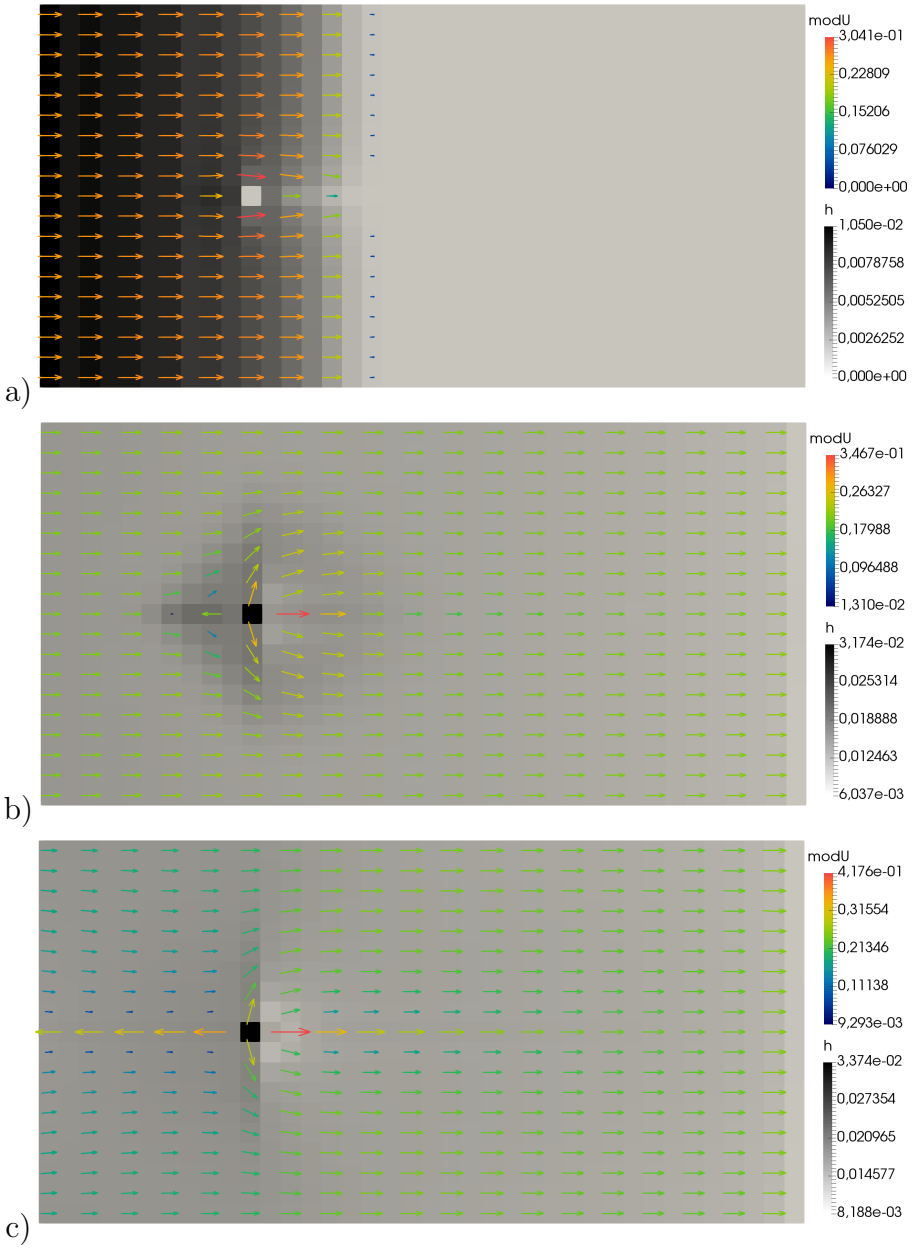

Figure 5.68: Distributed numerical results for the overland flow corresponding to water depth in m (grayscale) and velocity vectors in m/s (colored) at $t = 8s$ (a), $37s$ (b) and $50s$ (c).

5.5.2 Application to a test case on real topography

The Ginel river is a right bank tributary to the Ebro river in Spain. It is a small size ($77.3km^2$) river basin, long and narrow in shape with a length of $17.3km$ and SW-NW oriented. The upstream and downstream bed levels are $328m$ and $165m$ respectively (see 5.69 (left)) hence leading to an average longitudinal slope of 0.9%.

The case study is focused on an approximately $600m$ of the urban reach of the river through the town of Fuentes de Ebro (Zaragoza, Spain). Figure 5.69 (center) shows the spatial distribution of the Manning roughness coefficient used ranging from $n = 0.04sm^{-1/3}$ in the main channel, to $n = 0.016sm^{-1/3}$ in the urban area and assuming $n = 0.05sm^{-1/3}$ on the downstream area where there is more vegetation. The regions used for infiltration parameters can be seen in Figure 5.69 (right). Table 5.13 includes the Horton model parameters used.

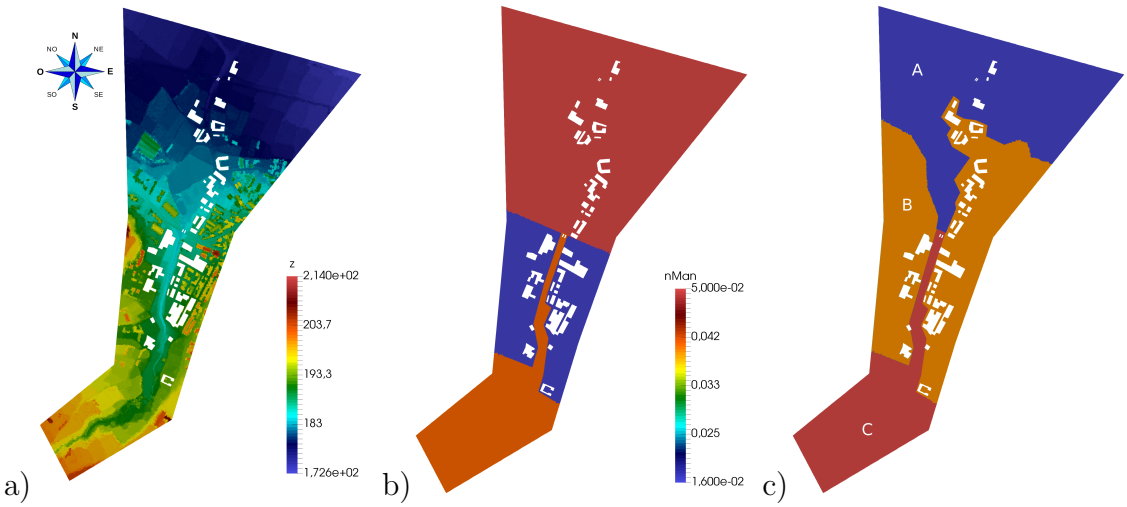

Figure 5.69: Ginel river at Fuentes de Ebro: Elevations map in m (a), Manning roughness coefficients in $sm^{1/3}$ (b) and infiltration regions (c).

Zone	k (s^{-1})	f_0 (m/s)	f_c (m/s)
A	0.0001	$1.9 \cdot 10^{-6}$	$1.0 \cdot 10^{-6}$
B	0.0001	$1.9 \cdot 10^{-8}$	$1.0 \cdot 10^{-8}$
C	0.0001	$1.9 \cdot 10^{-7}$	$1.0 \cdot 10^{-7}$

Table 5.13: Horton infiltration model parameters.

The 2D surface domain was discretized using an unstructured triangular flexible mesh of 29600 cells. The mesh was locally refined near the main channel and in the area between the buildings. Bed elevations where obtained from a $2m \times 2m$

DTM completed with 842 *in situ* topographical data. Figure 5.70 (left) shows the 2D surface computational mesh.

The drainage network geometry is shown in Figure 5.70 (right). It forms the main drainage conduit of the town and is located parallel to the main river channel. The 15 culvert connection positions are also shown in Figure 5.70 (right). The section of the conduit is considered as $0.75m \times 0.75m$ squared. Almost all the network is made of concrete so a Manning roughness coefficient of $0.03sm^{1/3}$ is assumed all along the drainage system. A discretization with a cellsize of $\Delta x = 1m$ is set for all the 1D domain, leading to a 500 cell mesh. As initial condition, a constant water depth of $7mm$ is assumed. A constant discharge of $10l/s$ is set as upstream boundary condition whereas free flow is assumed downstream.

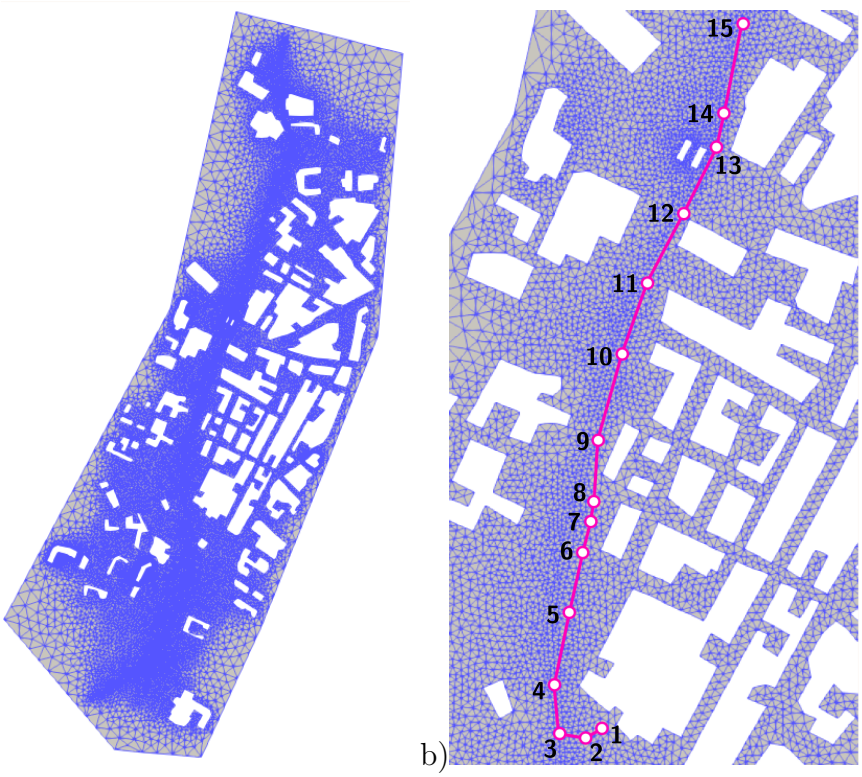

a) b)

Figure 5.70: Flexible mesh used for the 2D model (a) and sewer network scheme together with links locations (b).

Two simulations with different initial conditions are performed. First, a heavy constant rainfall of $0.7mm/s$ with a duration of $600s$ is assumed all over the domain, which is initially dry (Case 2.1). In the second test (Case 2.2), a surface water depth of $2m$ is imposed upstream in order to simulate the peak level of an extraordinary flood situation. The purpose of both tests is to evaluate the sewer system capability

to drain the surface water excess under these two assumptions. The use of a distributed surface flow model allows to calculate every hydraulic/hydrologic variables, as the water depth h, velocities u, v or infiltration rate f, individually for each cell of the computational mesh. Hence the avalaible information is much larger that the results provided by a lumped simulation model.

Figure 5.71 shows the simulated water surface at $t = 150s$ (left), $300s$ (center) and $3000s$ (right) for Case 2.1. The huge intensity and short duration of the storm modelled generates large water depth values (up to $3m$) in the main channel of the river and at several punctual locations. Figure 5.72 shows the water level $(h_p + z)$ within the drainage system and the instant discharge (Q) for 9 instants of the simulation. The bottom and top levels of the sewer are also shown. The contribution from the surface flow through the culverts is clearly seen in the form of water level peaks where the surface-sewer connection is located Figure 5.72. The drainage system is able to absorb the excess of surface water for the entire time of the simulation.

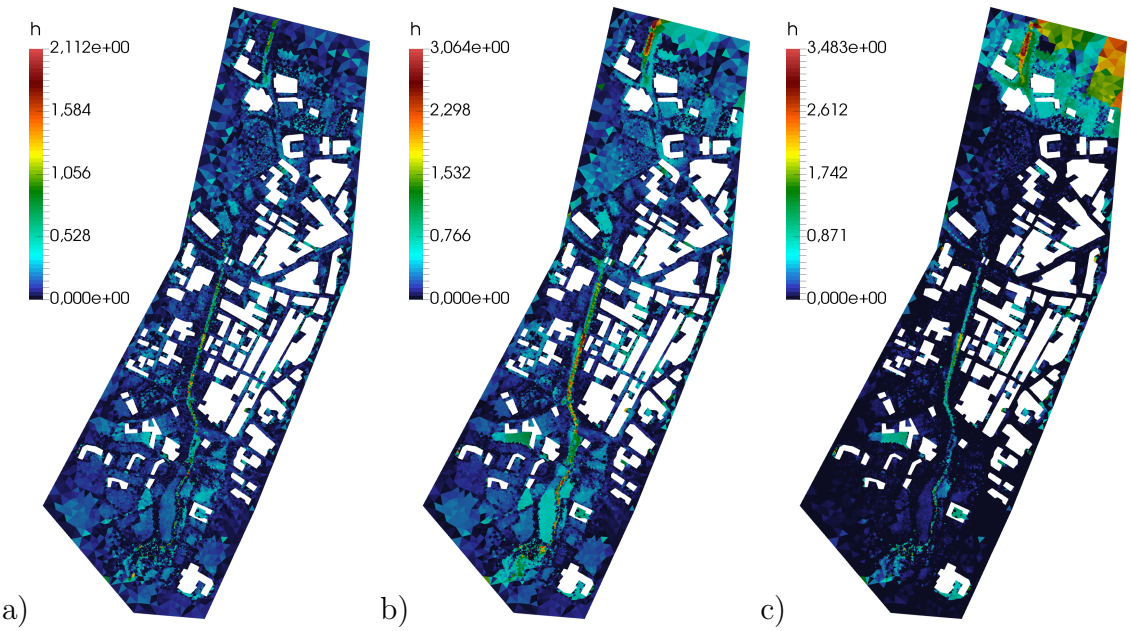

Figure 5.71: Case 2.1. Water depth values h in m at $t = 150s$ (a), $300s$ (b) and $3000s$ (c).

Figure 5.73 shows surface water depth values at $t = 60s$, $150s$, $300s$, $750s$, $1000s$, $2500s$ for Case 2.2. The figures show the progression of the flood wave along the urban area, overflowing the main channel in some points with water depth values of $5m$. Figure 5.74 shows the water level $(h_p + z)$ within the drainage system and

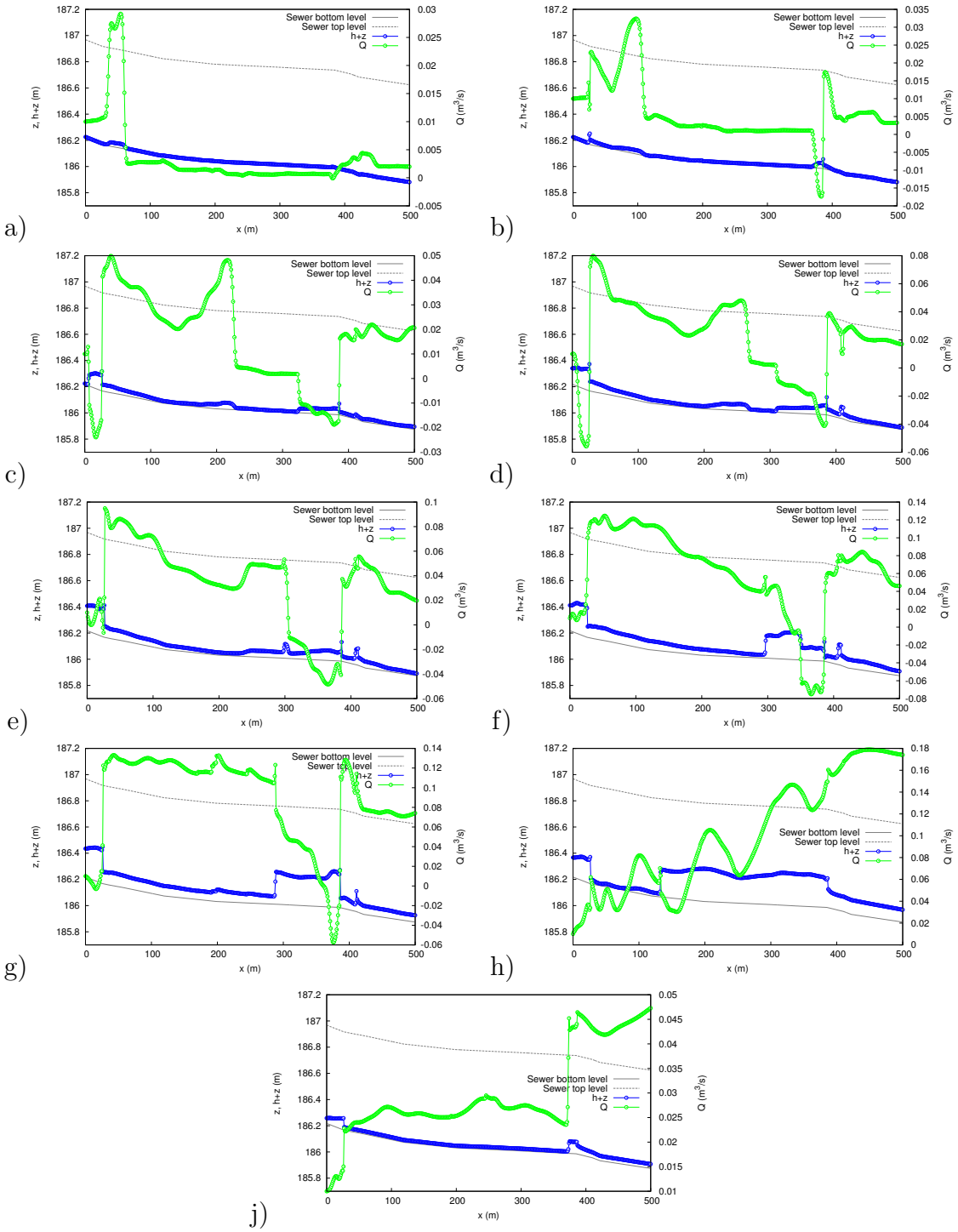

Figure 5.72: Case 2.1. Network profile at $t = 50s$ (a), $80s$ (b), $150s$ (c), $175s$ (d), $200s$ (e), $250s$ (f), $300s$ (g), $1000s$ (h) and $2000s$ (j).

the instant discharge (Q) for 10 simulation times. As in Case 2.1, the surface water contributions are clearly seen along the sewer. In this case, the sewer is puntually pressurized but the coupled model is able to deal with these kind of situation without

any issues. As there is not actual data to validate model results for this test, it is not possible to verify their credibility but the examples are useful to demonstrate that the coupling of the models provides stable tiem evolution of all the the variables including the exchange discharge.

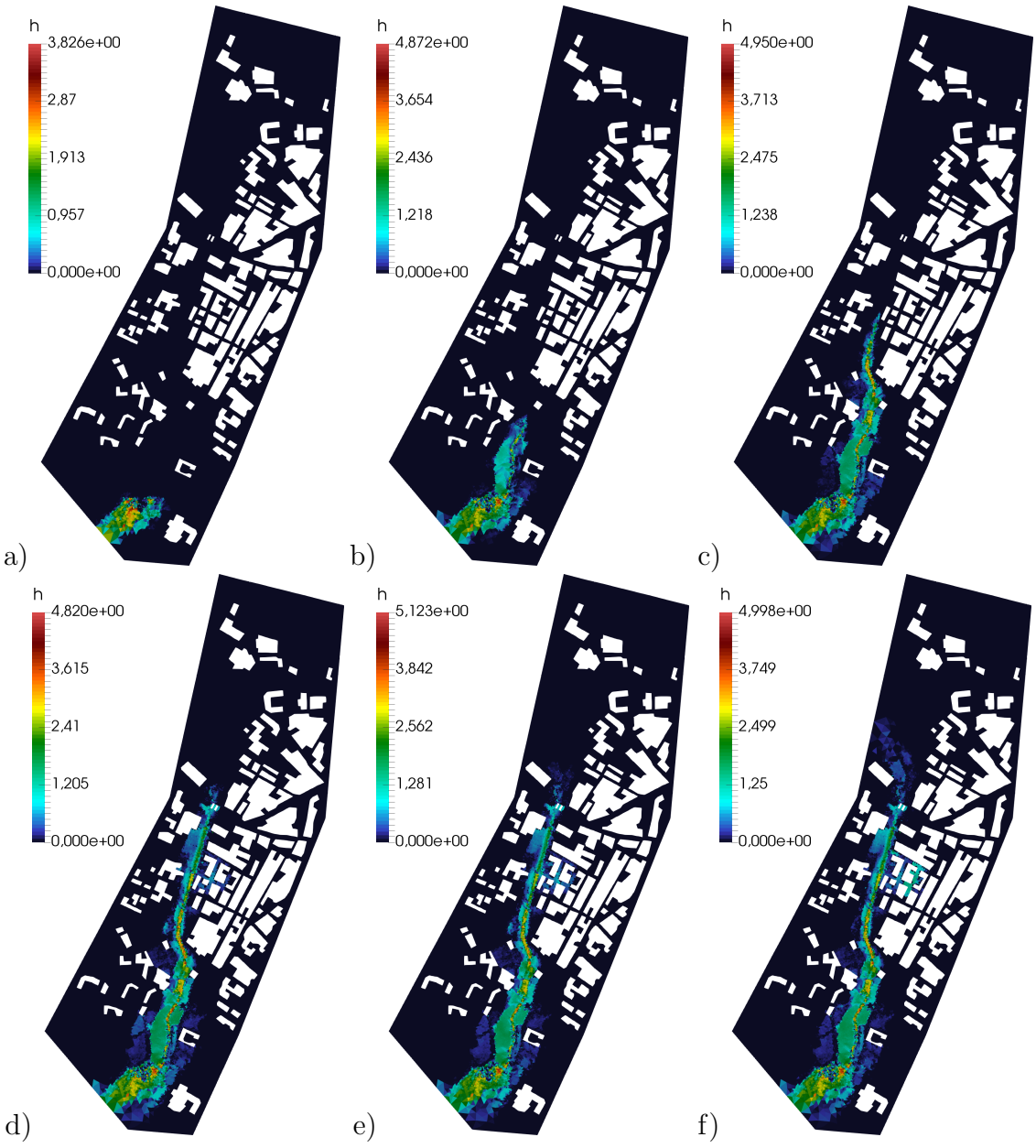

Figure 5.73: Case 2.2. Water depth values h in m at $t = 60s$ (a), $150s$ (b), $300s$ (c), $750s$ (d), $1000s$ (e), $2500s$ (f).

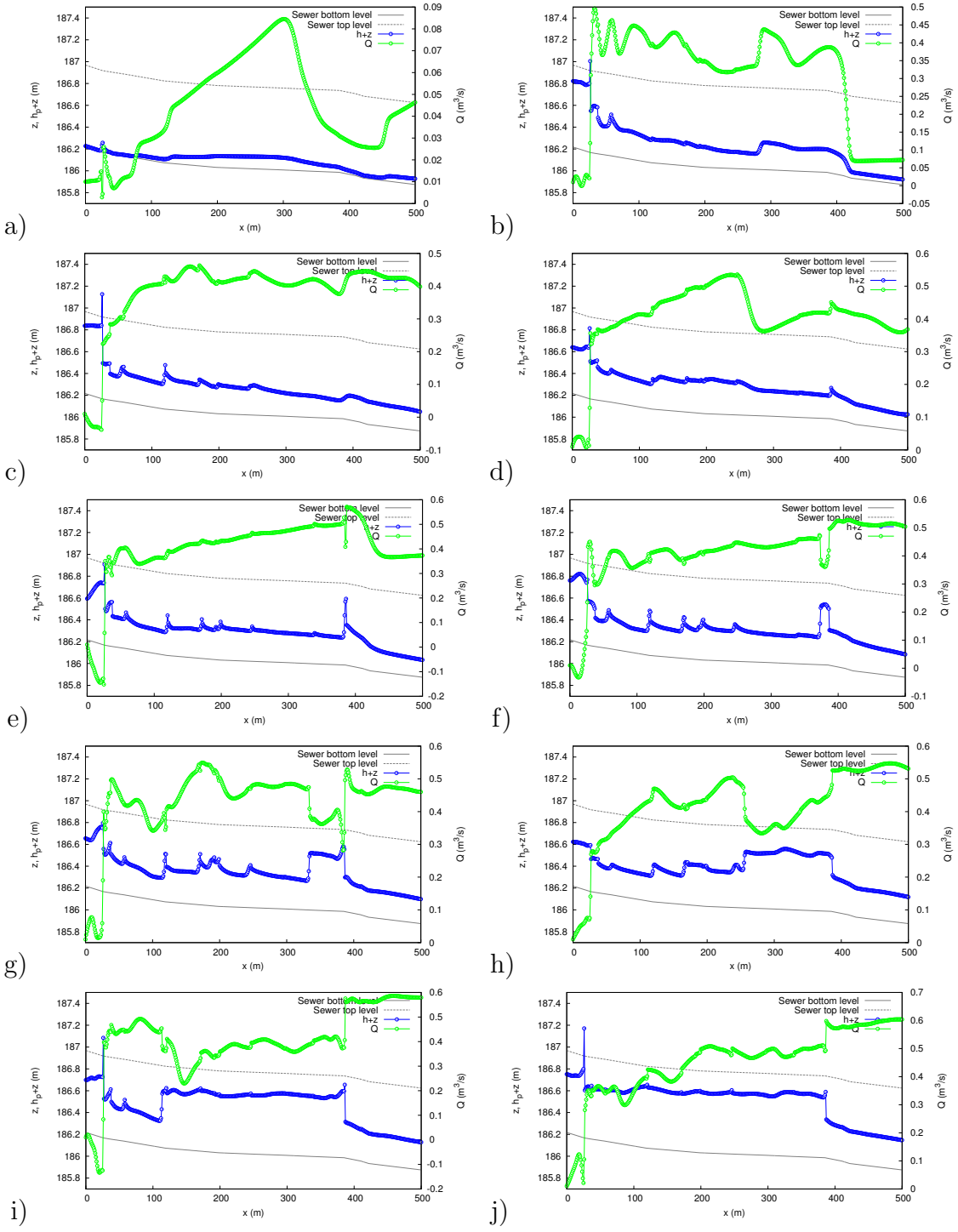

Figure 5.74: Case 2.2. Network profile at $t = 190s$ (a), $350s$ (b), $430s$ (c), $500s$ (d), $540s$ (e), $565s$ (f), $650s$ (g), $800s$ (h), $1000s$ (i) and $2500s$ (j).

CHAPTER 6

Conclusions

6.1 General conclusions

Computational simulation is nowadays an essential tool in many scientific and engineering areas. The constant innovation in numerical techniques combined with the high computation power of modern personal computers has made numerical simulation a reliable and efficient technique to obtain predictive results on a specific problem. It is clear that numerical models need to be widely validated before they can be released for research or commercial purposes. In this point, experimental measurements play an important role in order to provide validation/verification.

In this thesis, the development of a hydraulic/hydrological model have been presented, considering the coupling of surface-subsurface flows, paying special attention to the interactions among submodels. The surface flow is simulated by means of 2D Shallow Water equations and 2D Zero-Inertia model and includes hydrological components as rainfall or infiltration. Both models have been discretized using an hybrid implicit-explicit finite volume scheme. A full comparison is also included, carried out in terms of accuracy and efficiency in several applications, which have been led

to the following concluding remarks. For the sake of clearness, the conclusions are divided in two main groups (single models and coupled models).

6.1.1 Single models

Infiltration laws

The three most common infiltration laws are tested in a set of sinthetic cases which consider all the possible situation of rainfall and surface ponding one can find in a real world situation, specially in mountain river catchments.

- SCS-CN model is not able to account for the infiltration of ponded areas when the rainfall intensity is null. This fact limits the applicabilty of the method within a distributed surface flow model.
- Both Horton and Green-Ampt infiltration laws show similar behaviours in all the presented cases, including those with complex storm patterns and independently of the surface initial conditions. Therefore, the choice of the infiltration model could depend mainly on the availability of the soil parameters.
- The FOGA model allows the infiltration rate curve to have a non-monotonic behavior, leading to a soil infiltration recovery. As reported in previous literature, this can be useful to model infiltration in heterogeneous soils.

Drainage model

A reasonably good applicability of the Preissmann slot model for an estimation of the pressure values in unsteady situations between both shallow and pressurized flows is achieved. This method takes advantage of the similarity of both equation systems (shallow water and pressurized flow) and provides a simple way to simulate occasionally pressurized pipes, treating the system as an open channel in the Preissmann slot. This results in an easier implementation of the model because it avoids the managing of two separate systems of equations (shallow water and water hammer) in order to model separately the pressurized and the free surface flows. The use of an explicit scheme ($\theta = 0$) implies a limitation on the computational time

step but allows to capture more adequately the transient phenomelogy, specially when the pipes are pressurized. It is also remarkable the possibility of adapting the method to more realistic systems, like pipe networks which can be punctually pressurized. Some additional internal boundary conditions are necessary in these cases, in order to represent pipe junctions and storage wells.

2D Shallow Water model

In general terms, all the results presented in this section show a good agreement with the analytical solution or experimental data, even for large CFL numbers (up to 300 in some cases) when the implicit numerical scheme is used. A quality loss in the transient solution due to the high numerical diffusion is also observed when using large time steps but the steady solution is reached without noticing numerical issues. Hence, in the light of the results obtained, the overall conclusions can be summarized in the next points:

- The presented implicit numerical scheme is robust, conservative and preserves well the C-property regardless of the CFL value in quiescent water cases.
- Steady solutions are perfectly reproduced with large CFL numbers, up to 300 in the MacDonald test case presented in Section 4.3.4. The efficiency of the implicit numerical scheme is remarkable in this case, leading to an speed-up value of 12.
- A good agreement between numerical and exact solution is observed in strong transient cases, as the circular dam break presented in Section 4.3.5. As expected, the larger the CFL value the more diffusive is the transient solution but acceptable solutions has been found for CFL up to 25 in this particular case. The tsunami test case presented also shows a good agreement between numerical solutions and experimental data, even for large CFL numbers. Despite the inherent diffusivity of the implicit transient solutions, the unconditional stability of the model is pointed out in this case.
- Despite the fact that an implicit method normally requires less solution steps, each one demands more computational time than the solutions obtained by an explicit scheme. This strongly depends on the number of iterations the

matrix solver needs to do for achieving the convergence. Overall, the larger the CFL the more diffusive the implicit numerical solution is. Nevertheless, if the numerical diffusion can be assumable, the possible gain in performance due to the high CFL choice can be a point in favour of using these kind of numerical schemes under transient conditions. On the other hand, the steady solutions are perfectly reached regardless of the CFL value so the implicit methodology is adequate and recommendable for solving the steady or nearly-steady flows.

2D Zero-Inertia model

The 2D Zero-Inertia scalar equation for surface flow modeling has been applied to several synthetic test cases, a laboratory experiment for validation and a river catchment in order to test the performance of the implicit scheme in a real situation. In the light of the results, several conclusions have been reached:

- Unstructured triangular meshes provide an efficient way to discretize irregular domains with a moderate number of elements.
- Implicit Zero-Inertia model becomes a very efficient way to simulate steady flows and smooth transients, which include tidal flows over beach-like terrains and rainfall/runoff situations over urban areas. Large speed-up factors (> 150) have been reached, which shows the suitability of the implicit methodology for solving these kind of problems. When the implicit ZI model is applied to a real river catchment, its efficiency is affected by the high z gradients combined with low water depths h.
- In general terms, larger time steps do not necessarily mean lower simulation times when solving a non-linear problem by means of implicit techniques. The optimum time step should be found in order to achieve the fastest simulation.

2D Groundwater flow model

The groundwater flow model is able to reproduce the exact solutions in steady conditions, even when the impervious region presents a slope frontier. On the other hand, the aquifer modeling test case points out the ability of the model to update

the phreatic level position via local sources/sinks. The results are coherent with the ones presented in [38].

Matrix solver performance assessment

An exhaustive analysis of the BiCGStab matrix solver and Thomas algorithm performance has been presented in Section 4.6. The following conclusions have been reached:

- As expected, maximum and average errors decrease as the grid is refined and increase as the time step is increased, for both solvers.
- Maximum and average errors produced by the iterative Thomas algorithm are lower than the ones corresponding to BiCGStab in all the meshes considered in this section.
- Regarding the solver efficiency, the results show that the speed-up values are strongly conditioned by the time step choice and it also depends on the grid size. In the light of the results presented in Table 4.14, BiCGStab becomes more efficient than Thomas algorithm when choosing large time steps and fine meshes.

6.1.2 Coupled models

2D surface flow + Infiltration laws

Regarding the simulation of real catchments and the experimental outlet hydrograph fitting, two examples have been shown, Arnás and Araguás rivers. In both cases, the infiltration losses have been characterized by the classical Horton and Green-Ampt laws, using a single infiltration region for the whole catchments and a multi-region map in the case of the Arnás basin, leading to good but improvable hydrograph fittings. In particular, a considerable delay in raising limbs of the numerical hydrographs with respect to the experimental data is observed when classical laws are used for estimating the infiltration losses. The 2D Shallow Water equations have been also combined with a Fractional-Order Green-Ampt infiltration model (FOGA)

for a better modeling of the infiltration process in these complex real catchments. In the light of the results, it have been proved that the modification of the infiltration Green-Ampt method by means of fractional calculus significantly improves both rising and falling limbs.

2D surface flow + Drainage model

The implementation of a finite volume upwind scheme to solve the 2D shallow water equations and the 1D shallow water equations as well as their coupling has been presented in this part of the thesis. The leading interest is the possibility to provide dynamic simulations of the interaction between free surface flow on the surface and drainage flow in urban systems.

The coupled model has been validated in both smooth-transient and steady situations through a test case with laboratory measured data in several configurations for the inlet discharge. An overall good coincidence with experimental results is obtained with maximum differences of approximately 5% for the water depth in the unpressurized case and 5% and 15% in the pressurized situation for the water depth values and pressured head, respectively.

A real world application has been shown in the last part of this section. An intense and short pulse of rainfall is simulated over the detailed topography of Fuentes de Ebro (Zaragoza, Spain) in where the main sewer conduit together with 15 manholes is also modeled. Several infiltration and roughness regions have been considered mainly depending on the soil characteristics. A locally-refined triangular mesh allowed a precise discretization of the surface domain with the optimal number of cells. The use of a complete 2D dynamic surface distributed model allows the access to detailed information concerning the spatial distributions and time evolution of water depth, velocity, infiltration rate or any other hydraulic/hydrologic variable. Under two different assumptions for the initial conditions (heavy rainfall and flood event), both surface and sewer flow models predict the instant evolution of the water depth in both domains (surface and sewer). The overall conclusion from this part of the thesis is that it is possible to adapt 2D surface flow models to drainage networks which can become locally pressurized.

2D surface flow + 2D groundwater flow model

A set of synthetic tests have been presented, collecting all the challenging situations that can be present in real world applications, including infiltration, exfiltration or phreatic level updating by means of soil infiltration. A couple of applications in a river catchment have been also shown. In all the cases, both surface and groundwater flow submodels behave correctly and the interaction between them is smooth and coherent.

Overall, the full model presented in this work is able to simulate accurately and efficiently coupled hydraulic flows, taking into consideration a great variety of hydrological phenomena. This allows to consider this kind of models as powerful and reliable tool for predictive simulations in a wide range of real world applications.

6.2 Conclusiones generales

Hoy en día, la simulación computacional es una herramienta esencial en muchas disciplinas científicas e ingenieriles. La innovación constante en las técnicas numéricas combinada con la gran potencia de cálculo de los ordenadores personales modernos ha hecho de la simulación numérica una técnica muy eficiente para obtener resultados predictivos en un determinado problema. Resulta evidente que los modelos numéricos necesitan ser validados antes de su lanzamiento con propósitos comerciales o de investigación. En ese aspecto, la disponibilidad de medidas experimentales juega un importante papel a la hora de proveer una validación o verificación.

En esta tesis, se ha presentado el desarrollo de un modelo hidráulico/hidrológico, considerando el acoplamiento de flujos superficiales y sub-superficiales y poniendo especial atención a las interacciones entre modelos. El flujo superficial se ha simulado mediante las ecuaciones de aguas poco profundas (o modelo de onda dinámica) en 2D y el modelo cero-inercia (o modelo de onda difusiva) en 2D. Se han incluido componentes hidrológicos como la lluvia o la infiltración. Ambos modelos has sido discretizados empleando un esquema híbrido explícito-implícito de volúmenes finitos. Se incluye también una comparación entre ambos esquemas, llevada a cabo en términos de precisión y eficiencia en varias aplicaciones. Por claridad, las conclusiones se han dividido en dos grupos principales (modelos sencillos y modelos acoplados).

6.2.1 Modelos sencillos

Leyes de infiltración

Los tres modelos de infiltración más usados comunmente has sido comprobados en una serie de casos sintéticos que consideran todas las posibles situaciones de lluvia y encharcamiento del suelo que se pueden dar en la realidad, especialmente en cuencas de montaña.

- El modelo SCS-CN no puede estimar las pérdidas por infiltración de las zonas encharcadas cuando la intensidad de lluvia es nula. Este hecho limita la aplicabilidad del método dentro de un modelo distribuido de flujo superficial.

- Tanto el modelo de infiltración de Horton como el de Green-Ampt muestran comportamientos similares en todos los casos presentados, incluyendo aquellos con patrones de tormenta complejos e independientemente de las condiciones iniciales en la superficie. Por lo tanto, la elección del modelo de infiltración podría depender principalmente de la disponibilidad de los parámetros del suelo.

- El modelo FOGA permite que la curva de infiltración tenga un carácter no monótono, lo que conlleva a una recuperación de la capacidad de infiltración del suelo. Tal y como se reporta en la literatura, este factor puede ser de utilidad a la hora de modelar la infiltración en suelos heterogéneos.

Modelo de drenaje

Se ha mostrado una buena aplicabilidad del modelo de la rendija de Preissman para la estimación de los valores de presión en situaciones transitorias entre flujo libre y presurizado. Este método se aprovecha de la similaridad entre los sistemas de ecuaciones que gobiernan ambos tipos de flujo y provee una forma sencilla de simular tuberías ocasionalmente presurizadas, tratando el sistema como un canal en lámina libre en la rendija de Preissmann. Esto supone una implementación más sencilla del modelo, ya que evita la implementación y la gestión de dos sistemas de ecuaciones diferentes. El uso de un esquema explícito ($\theta = 0$) implica una limitación en el paso de tiempo computacional pero permite capturar de manera más adecuada todo la fenomenología transitoria, especialmente cuando las tuberías están presurizadas. También es remarcable la posibilidad de adaptar el método a sistemas más realistas, como redes de tuberías que pueden verse puntualmente presurizadas. En estos casos, se necesitan algunas condiciones de contorno internas para poder representar de forma adecuada elementos como bifurcaciones o uniones de tuberías.

Modelo 2D de aguas poco profundas

En términos generales, todos los resultados numéricos generados por el esquema implícito presentados en esta sección muestran una gran concordancia con las soluciones analíticas o con los datos experimentales, incluso para valores altos de CFL

(hasta 300 en algunos casos). Se observa una pérdida de calidad en soluciones transitorias debidas a la difusión numérica cuando se emplean pasos de tiempo largos pero la solución estacionaria se alcanza sin observar ningún tipo de inestabilidad. Por lo tanto, en base a los resultados obtenidos, las conclusiones de esta parte de la tesis se pueden resumir en los siguientes puntos:

- El esquema implícito presentado es robusto, conserativo y preserva bien la propiedad-C independientemente del valor CFL en casos de agua en reposo.
- Las soluciones estacionarias se reproducen perfectamente con números CFL grandes, hasta 300 en el caso test de MacDonald presentado en las Sección 4.3.4. La eficiencia del esquema implícito es remarcable en este caso, obteniendo valores speed-up de 12.
- Se observa una buena concordancia entre las soluciones numérica y exacta en casos transitorios bruscos, como la rotura de presa circular presentada en las Sección 4.3.5. Como era de esperar, a medida que se aumenta el valor del CFL, la solución transitoria se vuelve más difusiva. No obstante, en este caso concreto, se obtienen soluciones aceptables hasta un valor de CFL de 25. El caso correspondiente al tsumani a escala de laboratorio presentado también muestra resultados satisfactorios, incluyo para valores de CFL altos. A pesar de la difusividad inherente a las soluciones transitorias implícitas, la estabilidad incondicional del modelo se pone de manifiesto en este caso.
- A pesar del hecho de que un esquema implícito normalmente requiere menos pasos de tiempo para obtener la solución, cada uno de ellos requiere un mayor coste computacional que el correspondiente a un esquema explícito. Esto depende del número de iteraciones que el resolvedor lineal de la matriz requiera para converger a una solución. En general, cuanto mayor sea el valor del número CFL, más difusiva será la solución numérica proporcionada por un esquema implícito. Sin embargo, si la difusión numérica puede llegar a considerarse asumible, la posible ganancia en eficiencia debida a un valor alto del CFL puede ser un punto a favor del uso de este tipo de esquemas en situaciones transitorias. Por otro lado, las soluciones estacionarias se obtienen sin ningún problema independientemente del valor del CFL, por lo que la metodología implícita resulta muy recomendable para resolver problemas de flujo estacionario o transitorios suaves.

Modelo 2D Cero-Inercia

En enta tesis, el modelo escalar 2D Cero-Inercia para el flujo en superficie libre se ha aplicado a varios casos test sintéticos, un caso experimental de laboratorio y una cuenca de montaña con el objetivo de validad y comprobar la eficacia del esquema implícito en situaciones reales. En base a los resultados numéricos, se han obtenido las siguientes conclusiones:

- Las mallas triangulares no estructuradas proveen una manera eficiente de discretizar dominios irregulares con un número de elementos moderado.

- El esquema implícito para el modelo Cero-Inercia se muestra como una discretización temporal muy eficiente para la simulación de flujos estacionarios y transitorios suaves, incluyendo oleajes sobre terrenos de tipo playa y situaciones de transformación de lluvia en escorrentía. Se han alcanzado factores de aceleración mayores de 150, lo que muestra la gran aplicabilidad de la metodología implícita para la resolución de este tipo de flujos. Cuando el modelo ZI implícito se aplica a una cuenca real de montaña, su eficiencia se ve afectada por los grandes pendientes locales en combinación con los calados de agua pequeños.

- En términos generales, cuando se resuelven problemas no lineales mediante técnicas implícitas, la elección de un paso de tiempo grande no garantiza necesariamente tiempos de simulación más cortos. Se recomienda la obtención del paso de tiempo óptimo para maximizar la eficiencia de la simulación.

Modelo 2D de flujo subterráneo

El modelo de flujo subterráneo es capaz de reproducir satisfactoriamente soluciones exactas estacionarias, incluso cuando la región impermeable presenta una frontera no horizontal. Por otro lado, el caso test correspondiente al modelado de un acuífero con sistemas de bombeo pone de manifiesto la capacidad del modelo para actualizar la posición del nivel freático vía fuentes o sumideros locales. Los resultados son coherentes con los presentados en [38].

Análisis de la eficiencia de los resolvedores de matrices

En la Sección 4.6 se ha presentado un análisis exhaustivo de la eficiencia y calidad de resultados del método BiCGStab y del algoritmo de Thomas, mediante el cuál se han obtenido las siguientes conclusiones:

- Como era de esperar, para ambos métodos los errores máximos y medios decrecen a medida que se refina la malla de cálculo y aumentan a medida que se eligen pasos de tiempo más largos.
- Los errores máximos y medios producidos por el algoritmo de Thomas iterativo son inferiores a los generados por el método BiCGStab en todas las mallas consideradas.
- Con resoecto a la eficiencia de los métodos, los resultados muestran que los valores de ganancia están fuertemente condicionados por la elección del paso de tiempo y también dependen de la resolución de la malla. En base a los resultados presetnados en la Tabla 4.14, el método BiCGStab resulta más eficiente que el algoritmo de Thomas cuando se eligen pasos de tiempo largos y mallas finas.

6.2.2 Modelos acoplados

Flujo superficial 2D + Modelos de infiltración

Con respecto a la simulación de cuencas reales con suelos permeables, se han mostrado dos aplicaciones (las cuencas de los ríos Arnás y Araguás) en las que se pretende ajustar los hidrogramas numéricos a las medidas experimentales de caudal mediante la calibración de los parámetros del modelo de infiltración. En ambos casos, las pérdidas de infiltración han sido caracterizadas por las leyes clásicas de Horton y Green-Ampt, usando una única región de infiltración y un mapa con distintas regiones en el caso de la cuenca de Arnás. Los resultados obtenidos para el ajuste de los hidrogramas son buenos pero mejorables. En particular, un retraso considerable aparece en los picos de caudal de los hidrogramas numéricos con respecto a los datos experimentales. El modelo SW 2D también ha sido combinado con un

modelo fraccionario de infiltración de green-Ampt (FOGA) para una mejor modelización del proceso de infiltración en estas cuencas complejas. En base a los resultados obtenidos, se ha demostrado que la modificación del método de infiltración de Green-Ampt por medio del cálculo fraccionario mejora significativamente el ajuste de los hidrogramas a la salida de las cuencas.

Flujo superficial 2D + Modelo de drenaje

En esta parte de la tesis, se ha mostrado la implementación de un esquema upwind de volúmenes finitos para resolver las ecuaciones de aguas poco profundas en 2D para el flujo superficial y en 1D para el flujo en tuberías, así como su acoplamiento. El principal interés radica en la posibilidad de proveer simulaciones dinámicas de ka interacción entre el flujo superficial en la superficie y el flujo en una o varias tuberías, correspondientes a un sistema de drenaje urbano.

El modelo acoplado se ha validado en situaciones transitorias suaves y también en situaciones estacionarias mediante un caso test con medidas experimentales en diversas configuraciones para el caudal de entrada. En general, se observa una buena concordancia entre los resultados numéricos y las medidas observadas, con diferencias máximas del 5% para el calado superficial en caso de que el flujo en la tubería permanezca sin presurizar y entre el 5% y 15% en situaciones presurizadas para el calado superficial y la altura de presión, respectivamente.

En la última parte de esta sección, se muestra una aplicación realista mediante la simulación de una tormenta corta pero intensa sobre la topografía de la localidad de Fuentes de Ebro (Zaragoza, España) en la que se considera el conducto principal del sistema de drenaje con 15 alcantarillas. Se han modelizado varias regiones de rozamiento e infiltración, dependiendo de las características del suelo y de la vegetación. Una malla triangular no estructurada y refinada localmente permite una discretización precisa del dominio superficial con el número óptimo de celdas. El uso de un modelo distribuido de onda dinámica permite obtener resultados numéricos muy variados, incluyendo distribuciones espaciales y evoluciones temporales de calados de agua, velocidad, tasas de infiltración y cualquier otra variabe hidráulica/hidrológica. Considerando dos hipótesis diferentes para las condiciones iniciales (lluvia intensa y evento de inundación), ambos submodelos predicen la evolución instantánea del calado de agua en ambos dominios (superficie y tu-

bería). La conclusión fundamental de esta parte de la tesis es el hecho de que es posible acoplar de manera exitosa modelos de flujo superficial a sistemas de drenaje subterráneos que pueden verse localmente presurizados.

Flujo superficial 2D + Flujo subterráneo 2D

Se ha presentado un conjunto de casos tests sintéticos, reuniendo todas las situaciones que se pueden dar en aplicacioens reales, inuyendo infiltración, exfiltración o cambios en el nivel freático a causa de la infiltración en el suelo. También se han mostrado un par de aplicaciones en cuencas de montaña. En todos los casos, ambos modelos, superficial y subsuperficial, se comportan adecuadamente y la interacción entre ello es suave y coherente.

En general, el modelo completo presentado en enta tesis es capaz de simular de forma precisa y eficiente flujos hidráulicos acoplados, teniendo en consideración una gran variedad de fenómenos hidrológicos. Esto permite considerar a este tipo de modelos como herramientas muy útiles para simulaciones predictivas en un amplio rango de aplicaciones.

Bibliography

[1] UK Environment Agency. Benchmarking of 2D hydraulic modelling packages. Environment agency report, UK Environment Agency, 2013.

[2] A.O. Akan. *Urban Stormwater Hydrology: A Guide to Engineering Calculations*. CRC Press, 1993.

[3] J.D. Anderson. *Computational fluid dynamics*. McGraw-Hill, 1995.

[4] J. Bagheri and S.K. Das. Modeling of shallow-water equations by using implicit higher-order compact scheme with application to dam-break problem. *Journal of Applied & Computational Mathematics*, 2(3):132, 2013.

[5] J.J. Barley. A survey of operator splitting applied to upwind differentiating. Numerical Analysis Report 2/88, University of Reading, 1988.

[6] D.A. Benson, M.M. Meerschaert, and J. Revielle. Fractional calculus in hydrologic modeling: A numerical perspective. *Advances in Water Resources*, 51:479 – 497, 2013. 35th Year Anniversary Issue.

[7] A. Bermúdez and M.E. Vázquez-Cendón. Upwind methods for hyperbolic conservation laws with source terms. *Computers & Fluids*, 23:1049–1071, 1994.

[8] H. Berninger, M. Ohlberger, O. Sander, and K. Smetana. Unsaturated subsurface flow with surface water and nonlinear in- and outflow conditions. *Mathematical Models and Methods in Applied Sciences*, 24(05):901–936, 2014.

[9] M.F. Borthwick. *Application of Fractional Calculus to Rainfall-Streamflow Modelling*. PhD thesis, University of Plymouth, 2010.

[10] C. Bourdarias and S. Gerbi. A finite volume scheme for a model coupling free surface and pressurised flows in pipes. *Journal of Computational and Applied Mathematics*, 209:109–131, 2007.

[11] A.R. Brodtkorb, M.L. Sætra, and M. Altinakar. Efficient shallow water simulations on GPUs: Implementation, visualization, verification, and validation. *Computers & Fluids*, 55:1 – 12, 2012.

[12] J. Burguete. *Modelos unidimensionales de flujos de superficie libre y transporte en geometrías irregulares. Aplicación al flujo en ríos*. PhD thesis, Universidad de Zaragoza, 2003.

[13] J. Burguete, P. García-Navarro, and J. Murillo. Friction term discretization and limitation to preserve stability and conservation in the 1D shallow-water model: Application to unsteady irrigation and river flow. *International Journal for Numerical Methods in Fluids*, 58(4):403–425, 2008.

[14] J. Burguete and P. García-Navarro. Implicit schemes with large time step for non-linear equations: application to river flow hydraulics. *International Journal for Numerical Methods in Fluids*, 46(6):607–636, 2004.

[15] V. Casoulli. Semi-implicit finite difference methods for the two-dimensional shallow water equations. *Journal of Computational Physics*, 86:56–74, 1990.

[16] M.J. Castro, S. Ortega, M. de la Asunción, J.M. Mantas, and J.M. Gallardo. GPU computing for shallow water flow simulation based on finite volume schemes. *Comptes Rendus Mécanique*, 339(2):165 – 184, 2011.

[17] D. Caviedes-Voullième, P. García-Navarro, and J. Murillo. Influence of mesh structure on 2D full shallow water equations and SCS Curve Number simulation of rainfall/runoff events. *Journal of Hydrology*, 448–449(0):39 – 59, 2012.

[18] D. Caviedes-Voullième, P. García-Navarro, and J. Murillo. Influence of mesh structure on 2D full shallow water equations and SCS Curve Number simulation of rainfall/runoff events. *Journal of Hydrology*, 448-449(0):39 – 59, 2012.

[19] L. Cea, M. Garrido, and J. Puertas. Experimental validation of two-dimensional depth-averaged models for forecasting rainfall-runoff from precipitation data in urban areas. *Journal of Hydrology*, 382(1-4):88–102, 2010.

[20] H. Darcy. Les fontaines publiques de la ville de dijon. Technical report, Dalmont, Paris, 1957.

[21] Z.-Q. Deng, J.L.M.P. de Lima, M.I.P. de Lima, and V.P. Singh. A fractional dispersion model for overland solute transport. *Water Resources Research*, 42(3), 2006.

[22] K. Diethelm. *The analysis of fractional differential equations*, volume 2004 of *Lecture Notes in Mathematics*. Springer-Verlag, Berlin, 2010. An application-oriented exposition using differential operators of Caputo type.

[23] P. Garcia-Navarro, F. Alcrudo, and A. Priestley. An implicit method for water flow modelling in channels and pipes. *Journal of Hydraulic Research*, 32(5):721–742, 1994.

[24] P. García-Navarro, F. Alcrudo, and A. Priestley. An implicit method for water flow modelling in channels and pipes. *Journal of Hydraulic Research*, 32(5):721–742, 1994.

[25] P. García-Navarro and A. Priestley. The application of an implicit tvd method for water flow modelling in channels and pipes. Technical report, University of Reading, 1993.

[26] P. García-Navarro and M.E. Vázquez-Cendón. On numerical treatment of the source terms in the shallow water equations. *Computers & Fluids*, 29:951–979, 2000.

[27] J. García-Ruiz, N. Lana-Renault, S. Beguería, T. Lasanta, D. Regüés, E. Nadal-Romero, P. Serrano-Muela, J.I. López-Moreno, B. Alvera, C. Martí-Bono, and L.C. Alatorre. From plot to regional scales: Interactions of slope

and catchment hydrological and geomorphic processes in the spanish pyrenees. *Geomorphology*, 120(3-4):248 – 257, 2010.

[28] D.N. Gerasimov, V.A. Kondratieva, and O.A. Sinkevich. An anomalous non-self-similar infiltration and fractional diffusion equation. *Physica D: Nonlinear Phenomena*, 239(16):1593 – 1597, 2010.

[29] W.H. Green and G.A. Ampt. Studies on soil physics: 1. flow of air and water through soils. *Journal of Agricultural Science*, 4:1–24, 1911.

[30] Gaël Guennebaud, Benoît Jacob, et al. Eigen v3. http://eigen.tuxfamily.org, 2010.

[31] Z. He, W.Y. Wu, Yuan, and S.S.Y. Wang. *Simulation of Rainfall-Runoff in the Deep Hollow Lake Watershed Using an Integrated Surface-Subsurface Flow Model*. 2007.

[32] C. Juez, A. Lacasta, J. Murillo, and P. García-Navarro. An efficient GPU implementation for a faster simulation of unsteady bed-load transport. *Journal of Hydraulic Research*, 54(3):275–288, 2016.

[33] W. Jury and R. Horton. *Soil Physics*. John Wiley and Sons, 2004.

[34] C. Karpf, S. Hoeft, C. Scheffer, L. Fuchs, and P. Krebs. Groundwater infiltration, surface water inflow and sewerage exfiltration considering hydrodynamic conditions in sewer systems. *Water Science & Technology*, 63(9):1841 – 1848, 2011.

[35] F. Kerger, P. Archambeau, S. Erpicum, B. J. Dewals, and M. Pirotton. An exact riemann solver and a godunov scheme for simulating highly transient mixed flows. *Journal of Computational and Applied Mathematics*, 235:2030–2040, 2010.

[36] G. Kesserwani and Q. Liang. RKDG2 shallow-water solver on non-uniform grids with local time steps: Application to 1D and 2D hydrodynamics. *Applied Mathematical Modelling*, 39(3–4):1317–1340, 2015.

[37] A.A. Kilbas, H.M. Srivastava, and J.J. Trujillo. *Theory and applications of fractional differential equations*, volume 204 of *North-Holland Mathematics Studies*. Elsevier Science B.V., Amsterdam, 2006.

[38] Christopher G. Koutitas. *Elements of Computational Hydraulics*. Pentech Press, USA: Chapman and Hall, New York, 1983.

[39] T. Kärnä, B. de Brye, O. Gourgue, J. Lambrechts, R. Comblen, V. Legat, and E. Deleersnijder. A fully implicit wetting–drying method for dg-fem shallow water models, with an application to the scheldt estuary. *Computer Methods in Applied Mechanics and Engineering*, 200(5-8):509–524, 2011.

[40] A. Lacasta, M. Morales-Hernández, J. Murillo, and P. García-Navarro. An optimized GPU implementation of a 2D free surface simulation model on unstructured meshes. *Advances in Engineering Software*, 78:1–15, 2014.

[41] A. Lacasta, M. Morales-Hernández, J. Murillo, and P. García-Navarro. GPU implementation of the 2D shallow water equations for the simulation of rainfall/runoff events. *Environmental Earth Sciences*, 74(11):7295–7305, 2015.

[42] N. Lana-Renault. *Respuesta hidrológica y sedimentológica en una cuenca de montaña media afectada por cambios de cubierta vegetal: la cuenca experimental de Arnás, Pirineo Central*. PhD thesis, Universidad de Zaragoza, 2007.

[43] N. Lana-Renault, J. Latron, and D. Reguees. Streamflow response and water-table dynamics in a sub-Mediterranean research catchment (Central Pyrenees). *Journal of Hydrology*, 347:497–507, 2007.

[44] A.S. León, M.S. Ghidaoui, A.R. Schmidt, and M.H. García. Application of godunov-type schemes to transient mixed flows. *Journal of Hydraulic Resources*, 47:147–156, 2009.

[45] A.S. León. *Improved Modeling of Unsteady Free Surface, Pressurized and Mixed Flows in Storm-sewer Systems*. PhD thesis, University of Illinois at Urbana-Champaign, 2007.

[46] A.S. León, M.S. Ghidaoui, A.R. Schmidt, and M.H. García. Application of godunov-type schemes to transient mixed flows. journal of hydraulic research. *Journal of Hydraulic Research*, 47(2):147–156, 2009.

[47] S. Li and C.J. Duffy. Fully-coupled modeling of shallow water flow and pollutant transport on unstructured grids. *Procedia Environmental Sciences*, 13:2098 – 2121, 2012.

[48] P.L.-F. Liu, H. Yeh, and C. Synolakis. *Advanced Numerical Models for Simulating Tsunami Waves and Runup. Advances in Coastal and Ocean Engineering*, volume 10. World Scientific, 2008.

[49] D. López-Barrera. *Desarrollo de un modelo hidrológico/hidrodinámico de simulación de procesos de erosión y sedimentación.* PhD thesis, Universidad de Zaragoza, 2011.

[50] D. López-Barrera, P. García-Navarro, and P. Brufau. Sources of uncertainty in the validation of a coupled hydrological-hydraulic simulation model with sediment transport. *La Houille Blanche*, 3:17–22, 2011.

[51] I. MacDonald, M.J. Baines, and N.K. Nichols. Comparison of some steady state saint-venant solvers for some test problems with analytic solutions. Numerical Analysis Report 2/95, University of Reading, 1995.

[52] Ian MacDonald. *Analysis and computation of steady open channel flow.* PhD thesis, University of Reading, 1996.

[53] J.T. Machado, V. Kiryakova, and F. Mainardi. Recent history of fractional calculus. *Commun. Nonlinear Sci. Numer. Simul.*, 16(3):1140–1153, 2011.

[54] F.S.J. Martinez, Y.A. Pachepsky, and W.J. Rawls. Modelling solute transport in soil columns using advective-dispersive equations with fractional spatial derivatives. *Advances in Engineering Software*, 41(1):4 – 8, 2010. Civil-Comp Special Issue.

[55] M.G. McDonald and A.W. Harbaugh. A modular three-dimensional finite-difference ground-water flow model. *USGS Numbered Series*, 83-875, 1984.

[56] S.C. Medeiros and S.C. Hagen. Review of wetting and drying algorithms for numerical tidal flow models. *International Journal for Numerical Methods in Fluids*, 71(4):473–487, 2013.

[57] R.G. Mein and C.L. Larson. Modeling infiltration during a steady rain. *Water Resources Research*, 9(2):384–394, 1973.

[58] R. Metzler and J. Klafter. The random walk's guide to anomalous diffusion: a fractional dynamics approach. *Phys. Rep.*, 339(1):77, 2000.

[59] S.K. Mishra and V.P. Singh. *Soil Conservation Service Curve Number (SCS-CN) Methodology*. Kluwer Academic Publishers, 2003.

[60] M. Morales-Hernández, M.E. Hubbard, and P. García-Navarro. A 2D extension of a Large Time Step explicit scheme (CFL>1) for unsteady problems with wet/dry boundaries. *Journal of Computational Physics*, 263:303–327, 2014.

[61] M. Morales-Hernández, A. Lacasta, J. Murillo, and P. García-Navarro. A Large Time Step explicit scheme (CFL>1) on unstructured grids for 2D conservation laws: Application to the homogeneous shallow water equations. *Applied Mathematical Modelling*, 47:294 – 317, 2017.

[62] J. Murillo and P. García-Navarro. Weak solutions for partial differential equations with source terms: Application to the shallow water equations. *Journal of Computational Physics*, 229:4327–4368, 2010.

[63] J. Murillo and P. García-Navarro. Augmented versions of the hll and hllc riemann solvers including source terms in one and two dimensions for shallow flow applications. *Journal of Computational Physics*, 231:6861–6906, 2012.

[64] J. Murillo and P. García-Navarro. Wave riemann description of friction terms in unsteady shallow flows: Application to water and mud/debris floods. *Journal of Computational Physics*, 231:1963–2001, 2012.

[65] J. Murillo, P. García-Navarro, J. Burguete, and R. Brufau. The influence of source terms on stability, accuracy and conservation in two-dimensional shallow flow simulation using triangular finite volumes. *International Journal for Numerical Methods in Fluids*, 54:543–590, 2007.

[66] United States Department of Agriculture (USDA). Urban hydrology for small watersheds. Environment agency report, United States Department of Agriculture (USDA), 1986.

[67] United States Department of Agriculture (USDA). National engineering handbook part 630 hydrology. Technical report, United States Department of Agriculture (USDA), 2004.

[68] K.B. Oldham and J. Spanier. *The fractional calculus*. Academic Press [A subsidiary of Harcourt Brace Jovanovich, Publishers], New York-London, 1974. Theory and applications of differentiation and integration to arbitrary order, With an annotated chronological bibliography by Bertram Ross, Mathematics in Science and Engineering, Vol. 111.

[69] Task Committee on Hydrology Handbook of Management Group D of the American Society of Civil Engineers. *Hydrology Handbook*. American Society of Civil Engineers (ASCE), 2nd edition, 1996.

[70] D. Osei-Kuffuor, R.M. Maxwell, and C.S. Woodward. Improved numerical solvers for implicit coupling of subsurface and overland flow. *Advances in Water Resources*, 74:185 – 195, 2014.

[71] Y. Pachepsky, D. Timlin, and W. Rawls. Generalized Richards' equation to simulate water transport in unsaturated soils. *Journal of Hydrology*, 272(1-4):3 – 13, 2003. Soil Hydrological Properties and Processes and their Variability in Space and Time.

[72] S. Panday and P.S. Huyakorn. A fully coupled physically-based spatially-distributed model for evaluating surface/subsurface flow. *Advances in Water Resources*, 27(4):361 – 382, 2004. A Tribute to George F. Pinder.

[73] Y. Park, E.A. Sudickya, S. Pandayb, and G. Matanga. Implicit subtime stepping for solving nonlinear flow equations in an integrated surface–subsurface system. *Vadose Zone Journal*, 8(4), 2009.

[74] V.M. Ponce. Diffusion wave modeling of catchment dynamics. *Journal of Hydraulic Engineering*, 112:716–727, 1986.

[75] A. Preissmann. Propagation des intumescences dans les canaux et les rivières. In *Premier Congrès De L'association Française De Calcul*, pages 433–442, 1960.

[76] W.J. Rawls and D.L. Brakensiek. A procedure to predict green and ampt infiltration parameters. In *Proceeding of ASAE Conferences on Advances in Infiltration*, pages 102–112, Chicago, Illinois, 1983.

[77] W.J. Rawls, D.L. Brakensiek, and N. Miller. Green-ampt infiltration parameters from soils data. *Journal of Hydraulic Division*, 109(1):62–70, 1983.

[78] W.J. Rawls, P. Yates, and L. Asmussen. Calibration of selected infiltration equation for the georgia coastal plain. Report ARS-S-113, Agriculture Research Service, 1976.

[79] P.L. Roe. Approximate riemann solvers, parameter vectors, and difference schemes. *Journal of Computational Physics*, 43(2):357 – 372, 1981.

[80] M. Rubinato, R. Martins, G. Kesserwani, J. Leandro, S. Djordjevic, and J. Shucksmith. Experimental calibration and validation of sewer/surface flow exchange equations in steady and unsteady flow conditions. *Journal of Hydrology*, 552:421–432, 2017.

[81] S.G. Samko, A.A. Kilbas, and O.I. Marichev. *Fractional integrals and derivatives*. Gordon and Breach Science Publishers, Yverdon, 1993. Theory and applications, Translated from the 1987 Russian original, Revised by the authors.

[82] A. Serrano-Pacheco. *Simulación numérica bidimensional de procesos hidrológicos e hidráulicos sobre lecho irregular deformable*. PhD thesis, Universidad de Zaragoza, 2009.

[83] Naser Shokri, Masoud Montazeri Namin, and Javad Farhoudi. An implicit 2d hydrodynamic numerical model for free surface–subsurface coupled flow problems. *International Journal for Numerical Methods in Fluids*, 87(7):343–357, 2018.

[84] V. Singh and S. M. Bhallamudi. Conjunctive surface-subsurface modeling of overland flow. *Advances in Water Resources*, 21(7):567 – 579, 1998.

[85] N. Su. Theory of infiltration: Infiltration into swelling soils in a material coordinate. *Journal of Hydrology*, 395(1-2):103 – 108, 2010.

[86] N. Su. Distributed-order infiltration, absorption and water exchange in mobile and immobile zones of swelling soils. *Journal of Hydrology*, 468-469:1 – 10, 2012.

[87] N. Su. Mass-time and space-time fractional partial differential equations of water movement in soils: Theoretical framework and application to infiltration. *Journal of Hydrology*, 519, Part B:1792 – 1803, 2014.

[88] David G. Tarboton. *Rainfall-Runoff processes*. Utah State University, 2003.

[89] M. Tavelli and C.I. Dumbser. A high order semi-implicit discontinuous galerkin method for the two dimensional shallow water equations on staggered unstructured meshes. *Applied Mathematics and Computation*, 234:623–644, 2014.

[90] V. Te Chow, D.R. Maidment, and L.W. Mays. *Applied Hydrology*. McGraw-Hill Civil Engineering Series. MCGRAW-HILL Higher Education, 1988.

[91] Sally E. Thompson, Gabriel G. Katul, and Amilcare Porporato. Role of microtopography in rainfall-runoff partitioning: An analysis using idealized geometry. *Water Resources Research*, 46(7):W07520, 2010.

[92] W. Tian, X. Li, G.-D. Cheng, X.-S. Wang, and B. X. Hu. Coupling a groundwater model with a land surface model to improve water and energy cycle simulation. *Hydrology and Earth System Sciences*, 16(12):4707–4723, 2012.

[93] E.F. Toro. *Riemann Solvers and Numerical Methods for Fluid Dynamics: A Practical Introduction*. Springer, 1999.

[94] B. Trajkovic, M. Ivetic, F. Calomino, and A. D'Ippolito. Investigation of transition from free surface to pressurized flow in a circular pipe. *Water Science and Technology*, 39(9):105, 1999.

[95] H.A. van der Vorst. BI-CGSTAB - A fast and smoothly converging variant of BI-CG for the solution of nonsymmetric linear-systems. *SIAM Journal on Scientific and Statistical Computing*, 13(2):631–644, 1992.

[96] V.R. Voller. On a fractional derivative form of the green-ampt infiltration model. *Advances in Water Resources*, 34(2):257 – 262, 2011.

[97] C.B. Vreugdenhil. *Numerical Methods for Shallow Water Flow*. Kluwer Academic Publishers, Dordrecht, The Netherlands, 1994.

[98] Y. Wang, Q. Liang, G. Kesserwani, and J.W. Hall. A positivity-preserving zero-inertia model for flood simulation. *Computers & Fluids*, 46(1):505 – 511, 2011. 10th ICFD Conference Series on Numerical Methods for Fluid Dynamics (ICFD 2010).

[99] A.M Wasantha Lal. Performance comparison of overland flow. *Journal of the Hydraulic Engineering*, 124(4):342–349, 1998.

[100] A.M Wasantha Lal. Weighted implicit finite-volume model for overland flow. *Journal of the Hydraulic Engineering*, 124(9):941–950, 1998.

[101] A.M. Wasantha Lal and G. Toth. Implicit TVDLF methods for diffusion and kinematic flows. *Journal of Hydraulic Engineering*, 139(9):974–983, 2013.

[102] S. Whitaker. Flow in porous media I: A theoretical derivation of Darcy's law. *Transport in Porous Media*, 1(1):3–25, 1986.

[103] D.C. Wiggert. Transient flow in free-surface, pressurized systems. *the Hydraulics Division, Proceedings of the American Society of Civil Engineers*, 98(1):11–26, 1972.

[104] N. Wintermeyer, A.R. Winters, G.J. Gassner, and T. Warburton. An entropy stable discontinuous galerkin method for the shallow water equations on curvilinear meshes with wet/dry fronts accelerated by GPUs. *Journal of Computational Physics*, 375:447 – 480, 2018.

[105] J.R. Wixcey. Tan investigation of algorithms for open channel flow calculations. Technical report, University of Reading, 1990.

[106] H.C. Yee, R.F. Warming, and A. Harten. Implicit total variation diminishing (TVD) schemes for steady-state calculations. *Journal of Computational Physics*, 57:327–360, 1985.

[107] B.C Yen and C.W.-S Tsai. On noninertia wave versus diffusion wave in flood routing. *Journal of Hydrology*, 244(1):97 – 104, 2001.

[108] Y. Zhou and W. Li. A review of regional groundwater flow modeling. *Geoscience Frontiers*, 2(2):205 – 214, 2011.

Appendices

Appendix A: 1D Pressurized flow governing equations

The instant response for changes in a pipe flow is closely related to the elastic compresibility of both the fluid and the pipe wall material. Unsteady flow in pipes is commonly described by the cross-section integrated mass and momentum equations:

$$\frac{\partial H}{\partial t} + v\frac{\partial H}{\partial x} + v\sin\theta + \frac{c_{WH}^2}{g}\frac{\partial v}{\partial x} = 0 \tag{1}$$

$$\frac{\partial v}{\partial t} + v\frac{\partial v}{\partial x} + g\frac{\partial H}{\partial x} + \frac{4\tau_0}{\rho D} = 0 \tag{2}$$

in which $H(x,t) = \frac{p(x,t)}{\rho g} + z(x)$=elevation of the hydraulic grade line, being p the pressure, $v(x,t)$=local cross-section averaged flow velocity, $\theta(x,t)$=angle between the pipe and the horizontal level, D=diameter, ρ=fluid density, τ_0 is the boundary shear, typically estimated by means of a Manning or Darcy-Weissbach friction model. The magnitude c_{WH} accounts for the elastic waves speed in the pipe:

$$c_{WH} = \sqrt{\frac{K/\rho}{1 + \frac{DK}{eE}}} \tag{3}$$

being e the pipe thickness and E, K the elastic modulus of the pipe material and fluid, respectively. By neglecting convective terms, it is possible to reach a linear

hyperbolic equation system:

$$\frac{\partial H}{\partial t} + \frac{c_{WH}^2}{g}\frac{\partial v}{\partial x} = 0 \tag{4}$$

$$\frac{\partial v}{\partial t} + g\frac{\partial H}{\partial x} + \frac{4\tau_0}{\rho D} = 0 \tag{5}$$

These equations conform a hyperbolic system, analogous to the 2D Shallow water equations, considering the pressure and the velocity as the conserved variables.

Appendix B: Some additional calculations

2D Shallow water equations eigenvalues and eigenvectors

In this section the set of real eigenvalues and eigenvectors for 2D SW equations are obtained. The Jacobian matrix of the flux in the normal-pointing direction is:

$$\mathbf{J}_n = \frac{\partial \mathbf{En}}{\partial \mathbf{U}} = \begin{pmatrix} 0 & n_x & n_y \\ -u(\mathbf{u}\cdot\mathbf{n}) + c^2 n_x & \mathbf{u}\cdot\mathbf{n} + un_x & un_y \\ -v(\mathbf{u}\cdot\mathbf{n}) + c^2 n_y & vn_x & \mathbf{u}\cdot\mathbf{n} + vn_y \end{pmatrix} \tag{6}$$

Then, the characteristic polynomial is:

$$|\mathbf{J}_n - \lambda I| = \begin{vmatrix} -\lambda & n_x & n_y \\ -u(\mathbf{u}\cdot\mathbf{n}) + c^2 n_x & \mathbf{u}\cdot\mathbf{n} + un_x - \lambda & un_y \\ -v(\mathbf{u}\cdot\mathbf{n}) + c^2 n_y & vn_x & \mathbf{u}\cdot\mathbf{n} + vn_y - \lambda \end{vmatrix} = 0 \tag{7}$$

By solving the above determinant matrix we get:

$$
\begin{aligned}
&-\lambda\left[\left(\mathbf{u}\cdot\mathbf{n}+un_x-\lambda\right)\left(\mathbf{u}\cdot\mathbf{n}+vn_y-\lambda\right)-uvn_xn_y\right]-\\
&\qquad n_x\left[\left(-u\mathbf{u}\cdot\mathbf{n}+c^2n_x\right)\left(\mathbf{u}\cdot\mathbf{n}+vn_y-\lambda\right)+un_y\left(v\mathbf{u}\cdot\mathbf{n}-c^2n_y\right)\right]+\\
&\qquad\qquad n_y\left[\left(-u\mathbf{u}\cdot\mathbf{n}+c^2n_x\right)vn_x+\left(\mathbf{u}\cdot\mathbf{n}+un_x-\lambda\right)\left(v\mathbf{u}\cdot\mathbf{n}-c^2n_y\right)\right]=0
\end{aligned}
\tag{8}
$$

By expanding the parentheses:

$$
\begin{aligned}
&-\lambda\Big[\left(\mathbf{u}\cdot\mathbf{n}\right)^2+\mathbf{u}\cdot\mathbf{n}vn_y-\lambda\mathbf{u}\cdot\mathbf{n}+\mathbf{u}\cdot\mathbf{n}un_x+\cancel{uvn_xn_y}-\\
&\qquad\qquad-\lambda un_x-\lambda\mathbf{u}\cdot\mathbf{n}-\lambda vn_y+\lambda^2-\cancel{uvn_xn_y}\Big]-\\
&\qquad n_x\Big[-u\left(\mathbf{u}\cdot\mathbf{n}\right)^2-\cancel{uv\mathbf{u}\cdot\mathbf{n}n_y}+\lambda u\mathbf{u}\cdot\mathbf{n}+c^2n_x\mathbf{u}\cdot\mathbf{n}+\\
&\qquad\qquad c^2vn_xn_y-\lambda c^2n_x+\cancel{uv\mathbf{u}\cdot\mathbf{n}n_y}-c^2un_y^2\Big]+\\
&\qquad n_y\Big[\cancel{-uv\mathbf{u}\cdot\mathbf{n}n_x}+c^2vn_x^2+v\mathbf{u}\cdot\mathbf{n}^2-c^2\mathbf{u}\cdot\mathbf{n}n_y+\\
&\qquad\qquad\cancel{uv\mathbf{u}\cdot\mathbf{n}n_x}-c^2un_xn_y-\lambda v\mathbf{u}\cdot\mathbf{n}+\lambda c^2n_y\Big]=0
\end{aligned}
\tag{9}
$$

Simplifying and grouping terms:

$$
\begin{aligned}
&-\lambda\left[2\left(\mathbf{u}\cdot\mathbf{n}\right)^2-3\lambda\mathbf{u}\cdot\mathbf{n}+\lambda^2\right]+\left(\mathbf{u}\cdot\mathbf{n}\right)^3-c^2\mathbf{u}\cdot\mathbf{n}-\lambda\left(\mathbf{u}\cdot\mathbf{n}\right)^2+\lambda c^2=\\
&\qquad-\lambda^3+3\lambda^2\mathbf{u}\cdot\mathbf{n}+\left[c^2-3\left(\mathbf{u}\cdot\mathbf{n}\right)^2\right]\lambda+\mathbf{u}\cdot\mathbf{n}\underbrace{\left[\left(\mathbf{u}\cdot\mathbf{n}\right)^2-c^2\right]}_{(\mathbf{u}\cdot\mathbf{n}+c)(\mathbf{u}\cdot\mathbf{n}-c)}=0
\end{aligned}
\tag{10}
$$

The equation 10 conforms a third order polynomial in λ. Its zeros will correspond to the eigenvalues of the shallow water Jacobian and they can be easily obtained factorizing the indenpendent term (as shown above) and applying Ruffini's rule:

	-1	$3\mathbf{u}\cdot\mathbf{n}$	$c^2-3\left(\mathbf{u}\cdot\mathbf{n}\right)^2$	$\left(\mathbf{u}\cdot\mathbf{n}\right)\left(\mathbf{u}\cdot\mathbf{n}+c\right)\left(\mathbf{u}\cdot\mathbf{n}-c\right)$
$\mathbf{u}\cdot\mathbf{n}$		$-\mathbf{u}\cdot\mathbf{n}$	$2\left(\mathbf{u}\cdot\mathbf{n}\right)^2$	$c^2\mathbf{u}\cdot\mathbf{n}-\left(\mathbf{u}\cdot\mathbf{n}\right)^3$
	-1	$2\mathbf{u}\cdot\mathbf{n}$	$c^2-\left(\mathbf{u}\cdot\mathbf{n}\right)^2$	0

	-1	$3\mathbf{u}\cdot\mathbf{n}$	$c^2-3\left(\mathbf{u}\cdot\mathbf{n}\right)^2$	$\left(\mathbf{u}\cdot\mathbf{n}\right)\left(\mathbf{u}\cdot\mathbf{n}+c\right)\left(\mathbf{u}\cdot\mathbf{n}-c\right)$
$\mathbf{u}\cdot\mathbf{n}+\mathbf{c}$		$-\mathbf{u}\cdot\mathbf{n}-c$	$2\left(\mathbf{u}\cdot\mathbf{n}\right)^2-c^2+c\mathbf{u}\cdot\mathbf{n}$	$-\left(\mathbf{u}\cdot\mathbf{n}\right)\left(\mathbf{u}\cdot\mathbf{n}+c\right)\left(\mathbf{u}\cdot\mathbf{n}-c\right)$
	-1	$2\mathbf{u}\cdot\mathbf{n}-c$	$-\left(\mathbf{u}\cdot\mathbf{n}\right)^2+c\mathbf{u}\cdot\mathbf{n}$	0

	-1	$3\mathbf{u}\cdot\mathbf{n}$	$c^2-3\left(\mathbf{u}\cdot\mathbf{n}\right)^2$	$\left(\mathbf{u}\cdot\mathbf{n}\right)\left(\mathbf{u}\cdot\mathbf{n}+c\right)\left(\mathbf{u}\cdot\mathbf{n}-c\right)$
$\mathbf{u}\cdot\mathbf{n}-\mathbf{c}$		$-\mathbf{u}\cdot\mathbf{n}+c$	$2\left(\mathbf{u}\cdot\mathbf{n}\right)^2-c^2-c\mathbf{u}\cdot\mathbf{n}$	$-\left(\mathbf{u}\cdot\mathbf{n}\right)\left(\mathbf{u}\cdot\mathbf{n}+c\right)\left(\mathbf{u}\cdot\mathbf{n}-c\right)$
	-1	$2\mathbf{u}\cdot\mathbf{n}+c$	$-\left(\mathbf{u}\cdot\mathbf{n}\right)^2-c\mathbf{u}\cdot\mathbf{n}$	0

Hence, the set of real eigenvalues of the shallow water system is:

$$\lambda^1=\mathbf{u}\cdot\mathbf{n}+c,\qquad \lambda^2=\mathbf{u}\cdot\mathbf{n},\qquad \lambda^3=\mathbf{u}\cdot\mathbf{n}-c \tag{11}$$

Wave strenghts and source terms coefficients for 2D Shallow water equations

In this section, a basic calculation of wave strengths α and source terms coefficientsβ is presented. For the sake of consistency, it's important to take into account that the calculation order of eigenvalues and eigenvectors influences in the order of all of these coefficients. The next coefficients correspond to 3.121 and 3.122 order. The α coefficients correspond to the coordinates of the difference in vector $\mathbf{U}$ projection onto the eigenvectors matrix basis:

$$\delta\mathbf{U}_w=\tilde{\mathbf{P}}_w\mathbf{A}_w=\sum_{m=1}^{3}\alpha_w^m\tilde{\mathbf{e}}_w^m \tag{12}$$

where $\mathbf{A}_w=(\alpha^1,\alpha^2,\alpha^3)_w^T$ is the vector of the wave strenghts.

These coefficients are computed by means of the inverse of the eigenvectors matrix:

$$\mathbf{A}_w=\tilde{\mathbf{P}}_w^{-1}\delta\mathbf{U}_w=\frac{1}{2\tilde{c}_w}\begin{pmatrix}\tilde{c}-\tilde{\mathbf{u}}\cdot\mathbf{n} & n_x & n_y\\ 2(\tilde{u}n_y-\tilde{v}n_x) & -2n_y & 2n_x\\ \tilde{c}+\tilde{\mathbf{u}}\cdot\mathbf{n} & -n_x & -n_y\end{pmatrix}_w\begin{pmatrix}\delta h\\ \delta(hu)\\ \delta(hv)\end{pmatrix}_w=\cdots$$

$$\cdots=\frac{1}{2\tilde{c}_w}\begin{pmatrix}(\tilde{c}-\tilde{\mathbf{u}}\cdot\mathbf{n})\delta h+\delta(hu)n_x+\delta(hv)n_y\\ 2(\tilde{u}n_y-\tilde{v}n_x)\delta h-2\delta(hu)n_y+2\delta(hv)n_x\\ (\tilde{c}+\tilde{\mathbf{u}}\cdot\mathbf{n})\delta h-\delta(hu)n_x-\delta(hv)n_y\end{pmatrix}_w=\cdots$$

$$\cdots = \begin{pmatrix} \frac{\delta h}{2} + \frac{1}{2\tilde{c}}[\delta(hu)n_x + \delta(hv)n_y - \tilde{\mathbf{u}}\cdot\mathbf{n}\delta h] \\ \frac{1}{\tilde{c}}[(\tilde{u}n_y - \tilde{v}n_x)\delta h - \delta(hu)n_y + \delta(hv)n_x] \\ \frac{\delta h}{2} - \frac{1}{2\tilde{c}}[\delta(hu)n_x + \delta(hv)n_y - \tilde{\mathbf{u}}\cdot\mathbf{n}\delta h] \end{pmatrix}_w \tag{13}$$

Then

$$\alpha_w^{1,3} = \frac{\delta h_w}{2} \pm \frac{1}{2\tilde{c}_w}[\delta(hu)n_x + \delta(hv)n_y - \tilde{\mathbf{u}}\cdot\mathbf{n}\delta h]_w = \frac{\delta h_w}{2} \pm \frac{1}{2\tilde{c}_w}(\delta\mathbf{q}_w - \tilde{\mathbf{u}}_w\delta h_w)\mathbf{n} \tag{14}$$

$$\alpha_w^2 = \frac{1}{\tilde{c}_w}[(\delta(hv) - \tilde{v}\delta h)n_x - (\delta(hu) - \tilde{u}\delta h)n_y]_w \tag{15}$$

Following the same proceeding, the source term (slope and friction) coefficients calculation is discussed here. By projecting onto the eigenvectors matrix:

$$\mathbf{S} = \begin{pmatrix} S^1 \\ S^2 \\ S^3 \end{pmatrix} = \begin{pmatrix} 0 \\ gh(S_{0x} - S_{fx}) \\ gh(S_{0y} - S_{fy}) \end{pmatrix} \longrightarrow \tilde{\mathbf{S}}_w = \begin{pmatrix} \tilde{S}^1 \\ \tilde{S}^2 \\ \tilde{S}^3 \end{pmatrix}_w \tag{16}$$

$$\tilde{\mathbf{S}}_w = \tilde{\mathbf{P}}_w\mathbf{B}_w = \sum_{m=1}^{3} \beta_w^m \tilde{\mathbf{e}}_w^m \tag{17}$$

where $\mathbf{B}_w = (\beta^1, \beta^2, \beta^3)_w^T$ is the vector of the source terms strenghts. Inverting the system:

$$\mathbf{B}_w = \tilde{\mathbf{P}}_w^{-1}\tilde{\mathbf{S}}_w = \frac{1}{2\tilde{c}_w}\begin{pmatrix} \tilde{c} - \tilde{\mathbf{u}}\cdot\mathbf{n} & n_x & n_y \\ 2(\tilde{u}n_y - \tilde{v}n_x) & -2n_y & 2n_x \\ \tilde{c} + \tilde{\mathbf{u}}\cdot\mathbf{n} & -n_x & -n_y \end{pmatrix}_w \begin{pmatrix} 0 \\ \tilde{S}_2 \\ \tilde{S}_3 \end{pmatrix}_w = \frac{1}{2\tilde{c}_w}\begin{pmatrix} \tilde{S}_2 n_x + \tilde{S}_3 n_y \\ -2\tilde{S}_2 n_y + 2\tilde{S}_3 n_x \\ -\tilde{S}_2 n_x - \tilde{S}_3 n_y \end{pmatrix}_w \tag{18}$$

Then, the source terms coefficients are:

$$\beta_w^{1,3} = \pm\frac{1}{2\tilde{c}_w}(\tilde{S}_2 n_x + \tilde{S}_3 n_y)_w \quad , \qquad \beta_w^2 = \frac{1}{\tilde{c}_w}(-\tilde{S}_2 n_y + \tilde{S}_3 n_x)_w \tag{19}$$

Following the upwind philosophy, the inward component will be kept:

$$\beta_w^{m-} = \frac{1}{2}\tilde{\beta}_w^m[1 - sign(\tilde{\lambda}_w^m)] \tag{20}$$

Consider both the slope and the friction source terms:

$$\tilde{\mathbf{S}}_{z,w} = \begin{pmatrix} 0 \\ \left(-g\tilde{h}\delta z - g\tilde{h}S_f d_n\right) n_x \\ \left(-g\tilde{h}\delta z - g\tilde{h}S_f d_n\right) n_y \end{pmatrix}_w \tag{21}$$

where d_n is the normal distance between neighbour centers, $\tilde{h}_w$ is the arithmetic face-average water depth:

$$\tilde{h}_w = \frac{h_i + h_j}{2} \tag{22}$$

and $S_{f,w}$ represents the energy grade line for the bidimensional case:

$$S_{f,w} = \frac{\tilde{n}_w^2 \tilde{\mathbf{u}} \cdot \mathbf{n} \left|\tilde{\mathbf{u}}\right|}{\max\left(h_i, h_j\right)^{4/3}} \tag{23}$$

being

$$\tilde{n}_w = \frac{1}{2}\left(n_i + n_j\right) \tag{24}$$

Then, the source terms strenght coefficients are:

$$\beta_w^1 = \frac{1}{2\tilde{c}_w}\left(-g\tilde{h}\delta z - g\tilde{h}S_f d_n\right)_w = -\frac{1}{2}\tilde{c}_w\left(\delta z + S_f d\right)_w = -\tilde{\beta}_w^3, \qquad \tilde{\beta}_w^2 = 0 \tag{25}$$

It was taken into account that:

$$\tilde{c}_w = \sqrt{g\tilde{h}_w} = \sqrt{g\frac{h_i + h_j}{2}} \tag{26}$$

Upwinding:

$$\beta_w^{1-,3-} = \frac{1}{2}\tilde{\beta}_w^{1,3}[1 - sign(\tilde{\lambda}_w^{1,3})], \qquad \tilde{\beta}_w^2 = 0 \tag{27}$$

Appendix C: Picard iteration method

Picard iteration is a simple method for dealing with non-linear systems of equations:

$$\mathbf{A}(\mathbf{x})\mathbf{x} = \mathbf{b}(\mathbf{x}) \tag{28}$$

If the matrix is invertible:

$$\mathbf{x} = \mathbf{A}(\mathbf{x})^{-1}\mathbf{b}(\mathbf{x}) \tag{29}$$

A starting guess value x^0 is chosen and the process start:

$$\mathbf{x}^1 = \mathbf{A}(\mathbf{x}^0)^{-1}\mathbf{b}(\mathbf{x}^0), \qquad \mathbf{x}^2 = \mathbf{A}(\mathbf{x}^1)^{-1}\mathbf{b}(\mathbf{x}^1), \qquad \cdots \tag{30}$$

Hence the iteration stencil is:

$$\mathbf{x}^{k+1} = \mathbf{A}(\mathbf{x}^k)^{-1}\mathbf{b}(\mathbf{x}^k) \tag{31}$$

The linearized system of equations can be written as follows:

$$\mathbf{A}(\mathbf{x}^k)\mathbf{x}^{k+1} = \mathbf{b}(\mathbf{x}^k) \tag{32}$$

The solution of Equation 32 is obtained by means of a linear solver within the Picard iterations loop until convergence is achieved. The method converges if $\|\mathbf{A}^{-1}\mathbf{B}\| < 1$, where $B_{ij} = \partial b_i / \partial x_j$

Appendix D: List of publications

This section presents a list of journal published papers and conference contributions until the presentation of this thesis.

Journal articles

[1] **Towards transient experimental water surfaces: A new benchmark dataset for 2D shallow water solvers.** Martínez-Aranda, S., Fernández-Pato, J., Caviedes-Voullième, D., García-Palacín, I. and García-Navarro, P. *Advances in Water Resources* 121, 130-149, 2018.

[2] **Development of a new simulation tool coupling a 2D finite volume overland flow model and a drainage network model.** Fernández-Pato, J. and García-Navarro, P. *Geosciences* 8(8), 288, 2018.

[3] **Cellular Automata and Finite Volume solvers converge for 2D shallow flow modelling for hydrological modelling.** Caviedes-Voullième, D., Fernández-Pato, J. and Hinz, C. *Journal of Hydrology* 563, 411-417, 2018.

[4] **A fractional-order infiltration model to improve the simulation of rainfall/runoff processes.** Fernández-Pato, J., Gracia, J.L. and García-Navarro, P. *Journal of Hydroinformatics* 20(4), 898-916, 2018.

[5] **Application of a 2D overland flow model for rainfall/runoff and erosion simulation in a Mediterranean watershed.** Juez, C., Tena, A., Fernández-Pato, J., Batalla, R. and García-Navarro, P. *Cuadernos de Investigación Geográfica* 44(2), 615-640, 2018.

[6] **Implicit finite volume simulation of 2D shallow water flows in flexible meshes.** Fernández-Pato, J., Morales-Hernández, M. and García-Navarro, P. *Computer Methods in Applied Mechanics and Engineering* 328(1), 1-25, 2018.

[7] **Rainfall/runoff simulation with 2D full 2D Shallow water equations: Sensitivity analysis and calibration of infiltration parameters.** Fernández-Pato, J., Caviedes-Voullième, D. and García-Navarro, P. *Journal of Hydrology* 536, 496-513, 2016.

[8] **Simulación numérica de inundación de valles fluviales mediante un modelo difusivo implícito.** Fernández-Pato, J. and García-Navarro, P. *Ingeniería del agua* 20(3), 115-126, 2016.

[9] **A 2D zero-inertia model for the solution of overland flow problems in flexible meshes.** Fernández-Pato, J. and García-Navarro, P. *Journal of Hydrologic Engineering* 04016038, 2016.

[10] **Finite volume simulation of unsteady water pipe flow.** Fernández-Pato, J. and García-Navarro, P. *Drinking Water Engineering and Science* 7, 83-92, 2014.

In review

[?] **Simulación de avenidas mediante un modelo hidráulico/hidrológico distribuido en un tramo urbano del río Ginel (Fuentes de Ebro).** Fernández-Pato, J., Sánchez-Lallana, A. and García-Navarro, P. *Ribagua* (in review).

[?] **The 2D Shallow water equations and their application to realistic cases.** García-Navarro, P., Murillo, J., Morales-Hernández, M. and Fernández-Pato, J. *Journal of Environmental Fluid Mechanics* (in review).

Conference papers

[1] **Towards high-performance Hydraulic/Hydrologic numerical simulations in fluvial environments using RiverFlow2D GPU.** Fernández-Pato, J., García, R., Morales-Hernández, M., Brufau, P., Murillo, J. and García-Navarro, P. *Spain Water 2018*, 15 Nov 2018.

[2] **On the application of novel techniques to model hydrologic partitioning in 2D overland flow models.** Fernández-Pato, J., Gracia, J.L. and García-Navarro, P. *15th International Conference Zaragoza-Pau on Mathematics and it Applications*, 10-12 September 2018.

[3] **Implicit 2D surface flow models performance assessment: 2D Shallow water equations vs. Zero-Inertia Model.** Fernández-Pato, J., Morales-Hernández, M. and García-Navarro, P. *9th International Conference on Fluvial Hydraulics, River Flow 2018*, 5-8 September 2018.

[4] **Towards transient 2D experimental water surfaces: strengthening SW model validation.** Martínez-Aranda, S., Fernández-Pato, J., Caviedes-Voullième, D., García-Palacín, I., García-Navarro, P. *13th International Conference on Hydroinformatics, HIC 2018*, 1-6 July 2018.

[5] **Implicit schemes for 2D non-linear problems: Performance and efficiency assessment of two solvers.** Fernández-Pato, J. and García-Navarro, P. *Computational Methods in Water Resources, CMWR 2018*, 3-7 June 2018.

[6] **Analysis of the performance of two strategies for shallow water simulation using CFL>1.** Morales-Hernández, M., Fernández-Pato, J. and García-Navarro, P. *Computational Methods in Water Resources, CMWR 2018*, 3-7 June 2018.

[7] **Zero-Inertia vs full 2D Shallow water equations: a comparison for rainfall-runoff modelling.** Caviedes-Voullième, D., Fernández-Pato, J. and Hinz, C. *Computational Methods in Water Resources, CMWR 2018*, 3-7 June 2018.

[8] **Measuring 2D transient shallow water surfaces: raising the benchmark challenges for 2D shallow water solvers.** Caviedes-Voullième, D., Martínez-Aranda, S., Fernández-Pato, J., García-Palacín, I., García-Navarro, P. *Tag Der Hydrologie 2018*, 22-23 March 2018.

[9] **Simulación numérica de flujo superficial acoplado con redes de drenaje.** Fernández-Pato, J. and García-Navarro, P. *V Jornadas de Ingeniería del Agua 2017*, 25-26 October 2017, Poster presentation.

[10] **Modelling infiltration in 2D distributed hydraulic simulations using fractional spatial derivatives.** Fernández-Pato, J., Gracia, J.L. and García-Navarro, P. *Workshop on Fluid Mechanics 2017*, 20-21 July 2017, Poster presentation.

[11] **2D free surface steady and unsteady flows: 3D-sensing device measurements and finite volume simulation.** Martínez-Aranda, S., Caviedes-Voullième, D., Fernández-Pato, J., García-Palacín, I., Gordillo, G. and García-Navarro, P. *Workshop on Fluid Mechanics 2017*, 20-21 July 2017, Poster presentation.

[12] **Aplicación de las derivadas fraccionarias a la simulación hidrológica.** Fernández-Pato, J., Gracia, J.L. and García-Navarro, P. *Congress on Numerical Methods in Engineering*, 5-7 July 2017.

[13] **Analysis of the efficiency of an implicit upwind finite volume scheme for 2D shallow flow simulation on unstructured meshes.** Fernández-Pato, J., Morales-Hernández, M. and García-Navarro, P. *4th International Symposium of Shallow Flows*, 26-28 June 2017.

[14] **A numerical study on the influence of microtopography on rainfall-runoff-infiltration partitioning.** Caviedes-Voullième, D., Domin, A., Fernández-Pato, J. and Hinz, C. *4th International Symposium of Shallow Flows*, 26-28 June 2017.

[15] **Simulation of runoff generation and erosion in a Mediterranean watershed using 2D 2D Shallow water equations.** Fernández-Pato, J., Juez, C., Tena, A., Batalla, R.J. and García-Navarro, P. *HydroSenSoft 2017*, 1-3 March 2017.

[16] **Modelling the role of allelopathy on semiarid ecosystems controlled by plant-water feedbacks.** Pueyo, Y., Kéfi, S., Caviedes-Voullième, D., Fernández-Pato, J. and Alados, C.L. *14th International Conference MEDECOS 2017*, Poster presentation.

[17] **Challenges and improvements on high-performance river flow numerical modelling. Road to a new era of computing using RiverFlow2D GPU.**

Lacasta, A., Morales-Hernández, M., Juez, C., Caviedes-Voullième, D., Fernández-Pato, J., Murillo, J. and García-Navarro, P. *8th International Conference on Fluvial Hydraulics, River Flow 2016*, 11-14 July 2016.

[18] **An implicit method for the simulation of unsteady shallow water flow problems on flexible meshes.** Fernández-Pato, J. and García-Navarro, P. *Workshop on Advances in Numerical Modelling of Hydrodynamics*, 24-25 March 2015.

[19] **A pipe network simulation model with dynamic transition between free surface and pressurized flow.** Fernández-Pato, J. and García-Navarro, P. *12th International Conference on Computing and Control for the Water Industry, CCWI2013, Procedia Engineering* 70, 641-650, 2014.